Institute of Nuclear Physics,
Polish Academy of Sciences, Kraków, Poland

A prototype apparatus for measurement of the correlation coefficients in the β-decay of a free polarized neutron - BRAND-0 experiment

Author

mgr Karishma Dhanmeher

Supervisor

dr hab. Krzysztof Pysz, prof. IFJ PAN

This dissertation is submitted for the degree of

Doctor of Philosophy

in

Physics

Kraków, 2023

Abstract

The small-scale prototype apparatus of the BRAND experiment has been constructed and commissioned at the cold neutron beam facility PF1B in ILL Grenoble, France. The BRAND experiment aims at examination of Beyond Standard Model (BSM) components of weak interaction via simultaneous measurement of conventional and exotic correlation coefficient in β-decay of free neutron.

The construction and performance of the part of prototype setup responsible for detection and determination of energies, momenta and spin orientation of electrons from β-decay of neutrons is presented in details. Moreover, the experimental environment, beam parameters and possible sources of experimental background are extensively treated. The crucial methods for data processing and analysis of the electrons are developed. The obtained characterization of prototype components permits the necessary modifications and improvements for the next version of detection apparatus and signal readout system of the BRAND experiment. The feasibility of determination of the A, N and R correlation coefficients from the collected data has been tested.

Streszczenie

Zbudowano prototyp aparatury detekcyjnej eksperymentu BRAND. Był on testowany na wiązce zimnych neutronów PF1B w instytucie ILL, w Grenoble, Francja. Eksperyment BRAND ma na celu zbadanie składowych oddziaływań słabych, które nie są przewidywane w Modelu Standardowym. Odbędzie się to poprzez jednoczesny pomiar konwencjonalnych i egzotycznych współczynników korelacji w rozpadzie β swobodnego, spolaryzowanego neutronu.

Szczegółowo opisano budowę i działanie tej części układu prototypowego, która służy do rejestracji i pomiaru energii, pędów i orientacji spinów elektronów pochodzących z rozpadu β neutronów. Ponadto przedstawiono środowisko eksperymentalne w ILL, parametry wiązki zimnych neutronów i możliwe źródła tła eksperymentalnego. Wypracowano też procedury do redukcji i analizy danych doświadczalnych dotyczących elektronów. Otrzymane charakterystyki poszczególnych detektorów prototypu pozwolą na wprowadzenie koniecznych modyfikacji i ulepszeń w kolejnej wersji aparatury detekcyjnej i elektronice odczytu sygnału eksperymentu BRAND. Sprawdzono też możliwość wyznaczenia wspólczynników korelacji A, N i R na podstawie zebranych danych.

Contents

Chapter 1

Introduction

In the contemporary physics some significant problems remain unsolved. Among them are the reason for observed matter/antimatter asymmetry in the universe, unknown mechanisms responsible for CP violation, the origin and hierarchy of lepton masses, the number of fundamental hadron/lepton generations and the mysterious nature of dark matter and dark energy [1–3].

It is not clear if those fundamental issues can be explained still within a Standard Model (SM) of interaction or discoveries of new physics beyond Standard Model (BSM) are necessary.

Intensive experimental examinations conducted in high energy physics, astronomy, astrophysics and cosmology are undertaken in order to provide new information, which could drive the development of new theories. Usually these are a large-scale enterprises involving huge infrastructure, large collaborations, great founding (see e.g. [4, 5]).

Alternative approach consists in performing small-scale, but very precise experiments [6–9]. They are focused at observation of tiny effects hidden under bulk processes. For this aim the high precision of the apparatus and deep understanding of collected data are necessary.

A contemporary theoretical description of weak interaction provides the explicit terms, which are not foreseen in SM. Thus, when the search for BSM physics is of interest the examination of weak interaction is the most straightforward option. A suitable field for precision examination of a structure of weak interaction is the β-decay of free neutron [8, 9]. Decay of free neutron, being a purely weak interaction phenomenon, provides a distinctive opportunity to delve into the intricate dynamics of weak interactions. Shadowing processes present when β-decay of atomic nuclei is examined, in this case are absent.

Measurement of correlation coefficients of β-decay is the motivation of the BRAND project. Some of these coefficients, if different than zero, would provide an evidence of exotic components of weak forces. They could be the sources of still not identified processes responsible e.g. for time-reversal (T) violation and combined charge conjugation-parity symmetry (CP) violation.

The BRAND experiment is foreseen for many years. The apparatus will gradually be extended and refined based on the performance of previous version. Ultimately, the precision and accumulated statistic demanded to conclude about existence of exotic terms in weak interaction will be attained.

This thesis describes very initial step of the BRAND development. The first, still very limited prototype apparatus has been build and the commissioning runs were performed.

This work provides the description of the apparatus, performed tests and developed analysis methods. Encountered problems and identified deficiencies of current prototype are shown as well. Since this thesis is a first larger presentation of the very ambitious new experimental project the individual subtopics are explained extensively.

It is needed to mention as well that the preparation phase of BRAND-0 and first experiments unfortunately coincided with the COVID-19 pandemic what created significant problems, delays and multiple uncertainties for the Collaboration.

This thesis is organized in following way: next chapter provides necessary theoretical and experimental information respective for this work. In Chapter 3 the presentation of the experimental setup of BRAND-0 and the overall experimental environment at ILL is provided. Chapter 4 describes development of the main components of prototype apparatus. Large amount of material is provided in chapter 5, where employed methods of data analysis are presented. In Chapter 6 the specific tests performed on the crucial components of the experimental setup after the experiment are described. It is followed by examination of sources of the experimental background in chapter no 7. The feasibility of determination of three correlation coefficient is checked in chapter 8. The work is concluded in the Summary. Thesis is supplemented with appendix where employed BRAND-0 model of Geant4 is outlined.

Chapter 2

Experimental and theoretical background

2.1 Very short introduction to formalism of weak interaction

The most general formulation of weak interaction Hamiltonian was provided in 1956 and 1957 by Tsung-Dao Lee and Chen-Ning Yang [10–12]. It was the modification and extension of former formulation of theory of β-decay. The first one was proposed by Enrico Fermi in 1934 [13]. It has been supplemented by George Gamow and Edward Teller in 1936 [14].

The continuous development of the theory of β-decay was needed in order to adapt the crucial experimental facts, which at that time extended the knowledge about the nature of weak interaction. The most important was the evidence of parity violation in the weak interaction [15].

The generalized Hamiltonian (eq. 2.1) of Lee and Young contains the terms including all theoretically contributing the current-current interactions: scalar (S), vector (V), pseudoscalar (P), axial vector (A) and tensor (T). Each of them has both parity conserving as well as parity violating component. Their strength is given by coupling constant C_S, C_V, C_P, C_A, C_T (parity conserving terms) and $C_S^{'}, C_V^{'}, C_P^{'}, C_A^{'}, C_T^{'}$ (parity violating terms):

$$\begin{aligned} H = \; & \bar{\psi}_p \psi_n (C_S \bar{\psi}_e \psi_\nu + C_S^{'} \bar{\psi}_e \gamma^5 \psi_\nu) \\ & + \bar{\psi}_p \gamma_\mu \psi_n (C_V \bar{\psi}_e \gamma_\mu \psi_\nu + C_V^{'} \bar{\psi}_e \gamma^\mu \gamma^5 \psi_\nu) \\ & + \bar{\psi}_p \sigma^{\mu\nu} \psi_n (C_T \bar{\psi}_e \sigma^{\mu\nu} \psi_\nu + C_T^{'} \bar{\psi}_e \sigma^{\mu\nu} \gamma^5 \psi_\nu) \\ & + \bar{\psi}_p \gamma_\mu \gamma^5 \psi_n (C_A \bar{\psi}_e \gamma^\mu \gamma^5 \psi_\nu + C_A^{'} \bar{\psi}_e \gamma^\mu \psi_\nu) \\ & + \bar{\psi}_p \gamma^5 \psi_n (C_P \bar{\psi}_e \gamma^5 \psi_\nu + C_P^{'} \bar{\psi}_e \psi_\nu), \end{aligned} \tag{2.1}$$

The transformation properties of the individual current-current components are explained in table 2.1.

Bilinear Covariant	$\bar{\psi}\psi$	$\bar{\psi}\gamma^{\mu}\psi$	$\bar{\psi}\gamma^{\mu}\gamma^{5}\psi$	$\bar{\psi}\sigma^{\mu\nu}\psi$	$\bar{\psi}\gamma^{5}\psi$
Type	Scalar (S)	Vector (V)	Axial Vector (A)	Tensor (T)	Pseudo-scalar (P)

Table 2.1 The bilinear covariants and their properties under Lorentz transformation

The general form of the coupling constants C_i and $C_i^{'}$ are complex, yet certain symmetries can constrain them [6]. Maintaining parity (P) is possible if only one constant from the pair $(C_i, C_i^{'})$ is non-zero, implying either $C_i = 0$ or $C_i^{'} = 0$. Additionally, the maximum violation of parity occurs when $|C_i| = |C_i^{'}|$. Considering time-reversal symmetry (T), all these constants must be real. Concerning charge conjugation (C), the C_i constants must be real, and the $C_i^{'}$ have to be purely imaginary, with an overall phase.

It has to be highlighted that for the description of all contemporary known experimental observations related to weak interaction, sufficient are only the vector and axial vector components of weak Hamiltonian. The so-called (V-A) theory published in 1958 by Feynman and Gell-Mann [16] and Sudarshan and Marshak [17] is the current commonly accepted formulation of weak interaction problem. The (V-A) theory is a part of Standard Model (SM).

Papers of Lee and Young as well as later papers of Jackson, Treiman, and Wyld [18, 19] and Ebel and Feldman [20] provided calculations of specific differential decay rates of polarized nuclei. The authors of those theoretical papers suggested the measurements of decay rates at various kinematical conditions. The dependence of decay rates on different available observables (energies and momenta of outgoing particles, their spins) should be sensitive for various sectors of weak interaction. For example, in experiment where the polarized neutron decays and registered are four-momenta of electron and proton together with transversal components of the electron spin, the relevant form of the differential decay rate is:

$$
\begin{aligned}
\frac{d^3\Gamma}{dE_{\mathrm{e}}d\Omega_{\mathrm{e}}d\Omega_{\upsilon}} \sim 1 &+ a\frac{\mathbf{p}}{E_{\mathrm{e}}}\cdot\frac{\mathbf{q}}{E_{\upsilon}} + b\frac{m_{\mathrm{e}}}{E_{\mathrm{e}}} + \frac{\langle\mathbf{J}\rangle}{J}\cdot\left[A\frac{\mathbf{p}}{E_{\mathrm{e}}} + B\frac{\mathbf{q}}{E_{\upsilon}} + D\frac{\mathbf{p}}{E_{\mathrm{e}}}\times\frac{\mathbf{q}}{E_{\upsilon}}\right] \\
&+ \sigma_{\perp}\left[H\frac{\mathbf{q}}{E_{\upsilon}} + L\frac{\mathbf{p}}{E_{\mathrm{e}}}\times\frac{\mathbf{q}}{E_{\upsilon}} + N\frac{\langle\mathbf{J}\rangle}{J} + R\frac{\langle\mathbf{J}\rangle}{J}\times\frac{\mathbf{p}}{E_{\mathrm{e}}}\right. \\
&\left. + S\frac{\langle\mathbf{J}\rangle}{J}\frac{\mathbf{p}}{E_{\mathrm{e}}}\cdot\frac{\mathbf{q}}{E_{\upsilon}} + U\frac{\langle\mathbf{J}\rangle}{J}\frac{\mathbf{p}}{E_{\mathrm{e}}}\cdot\frac{\mathbf{q}}{E_{\upsilon}} + V\frac{\mathbf{q}}{E_{\upsilon}}\times\frac{\langle\mathbf{J}\rangle}{J}\right],
\end{aligned}
\tag{2.2}
$$

where $\frac{\langle\mathbf{J}\rangle}{J}$ is the polarization of neutron beam, $\sigma_{\perp}$ represents the transverse component of electron spin (orthogonal to its momentum vector), E_{e} and $\mathbf{p}$ are the energy and momentum of the electron, respectively, and the E_{υ} and $\mathbf{q}$ are energy and momentum of anti-neutrino. (The latter ones need to be reconstructed from the decay kinematics). The quantities *a*, *b*, *A*, *B*, *D*, *H*, *L*, *N*, *R*, *S*, *U* and *V* are the correlation coefficients.

As mentioned, from experimental point of view the decay rate is very useful. With selection of specific experimental conditions the access to various components of weak interaction is possible. It is due to the fact that aforementioned correlation coefficients (except of a) can be expressed as a linear combination of coupling constants of weak decay Hamiltonian. In the first-order approximation, they can be expressed as:

$$X = X_{\text{SM}} + X_{\text{EM}} + c_{ReS}\text{Re}S + c_{ReT}\text{Re}T + c_{ImS}\text{Im}S + c_{ImT}\text{Im}T, \tag{2.3}$$

where:

$$S \equiv \frac{C_S + C_S^{'}}{C_V},\ T \equiv \frac{C_T + C_T^{'}}{C_A} \tag{2.4}$$

As it is visible, besides of terms foreseen in Standard Model (X_{SM}) and those which are effects of electromagnetic interactions in final state (X_{EM}) the exotic (from beyond V-A theory) scalar (S) and tensor (T) components are involved.

This approach opens the doors to delve into physics beyond the Standard Model (BSM), addressing the significant challenges in contemporary physics. One of them is the exploration of time-reversal (T) violation. Among the above mentioned correlation coefficients, *D* and *R* hold potential for investigating violation in time-reversal symmetry [21]. Under the assumption of absolute conservation of the combined CPT symmetry, the discovery of processes that break T symmetry would also signify a source of CP violation. It is directly relevant to the search of processes responsible for observed dominance of matter over antimatter, as outlined in Sakharov's postulates [22]. A broad explanations of relevant physics and justification of precise measurement of neutron decay could be found in [23, 24].

2.2 The BRAND project

The BRAND experiment proposed by prof. K. Bodek [25] is a low-energy precision experiment. It is motivated at intense search for new physics beyond the standard model (BSM). The method consists in seeking the tiny deviations in low-energy observables that are linked to the nonexistent in SM exotic interactions [7].

It is planned that the BRAND experiment, in its ultimate form, will simultaneously measure 11 correlation coefficients of eq. 2.2: *a, A, B, D, H, L, N, R, S, U, V*. The β-decay of free cold neutron will be used for this aim [26]. Seven of those correlation coefficients (*H, L, N, R, S, U, V*) depend on the transverse component of spin polarisation of emitted electrons. Five coefficients (*H, L, S, U, V*) were never measured before.

The planned setup of the ultimate BRAND experiment (as proposed in 2022) is shown in fig. 2.1. It will be a cylindrical detection system surrounding the cold polarized neutron beam. Individual detection elements will be optimized for measurement of the transverse component of electron polarization and the four momenta of charged decay products. Event-by-event reconstruction of the decay kinematic will be performed. The momenta of electrons and protons will be measured in their dedicated detectors, whereas an anti-neutrino momenta shall be calculated by reconstructing the three-body kinematics of the decayed event.

The key features of the setup are:

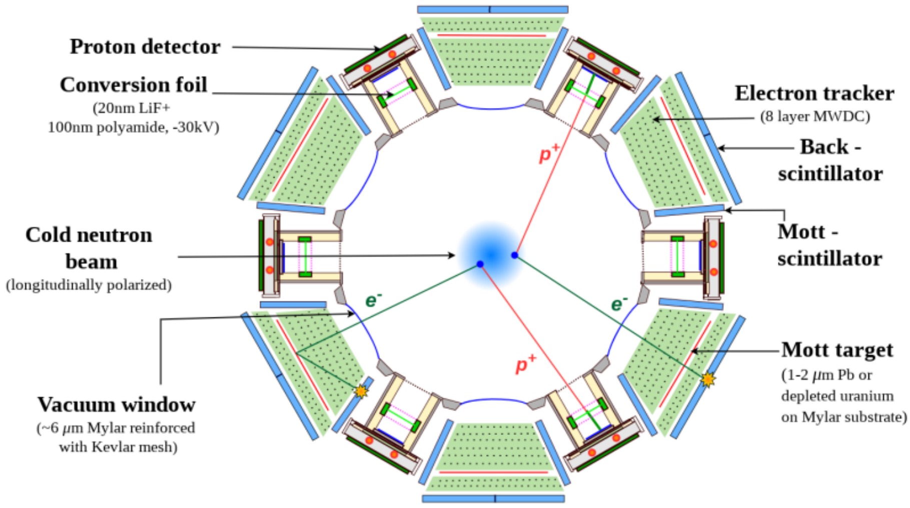

Figure 2.1 The ultimate BRAND experimental setup as proposed in 2022: cross-section perpendicular to the beam axis. It illustrates reconstruction of the decay events by registration of electrons and protons in coincidence. The red and green lines represent protons' and electrons' trajectories, respectively. The plot is reprinted from [26].

1. Azimuthal detection acceptance of 360° around highly polarised (99.5%) cold neutron beam.
2. Tracking of electrons in helium-based, low density Multi-Wire Drift Chamber (MWDC).
3. Utilization of Mott scattering for measurement of transverse polarisation component of emitted electrons.
4. Energy/momentum measurement of direct and Mott-scatted electrons in plastic scintillators.
5. Proton-electron conversion method for detection of the low energy protons.
6. Registering of the proton-electron coincidence for the vertex reconstruction and unambiguous identification of β-decay events.

The BRAND experiment is a continuation and extension of very successful experiment nTRV performed in Paul Scherrer Institute (PSI), Villigen, Switzerland [27, 28]. Experimental program of nTRV experiment utilized the detection of β-particles from neutron decay. Both the energy and the spin orientation of electrons were recorded. This permitted to provide the first ever measured limits on correlation coefficients N and R. They were consistent with the values foreseen in SM. In the BRAND experiment, the planned list of to be measured correlation coefficient is significantly extended. This will be attained through the simultaneous registration of β-decay electrons and protons along with the vertex reconstruction of the event. Very difficult and tricky method of low energy proton (< 750 eV) detection is under development. The details are available in [29, 30].

It is estimated that ultimately, with the sufficient collected statistics of events (10^5 decays/s for six months) the sensitivity of about 5×10^{-4} for the coefficients dependent on transverse electron polarization will be attained. With such precision of measurement the experimental limits on the strength of possible time-reversal symmetry-violating processes can be significantly improved. The results of the BRAND experiment will also be utilized for constraining the leptoquark exchange models and to tune the parameters of effective field theories (EFT), which provide the common formalism both for high and low-energy fundamental research. In order to accomplish this ambitious goal, the experiment performed initially at the Institute Laue-Langevin (ILL), Grenoble, France will be transferred to the new intense neutron beam at the European Spallation Source (ESS) in Lund, Sweden.

2.3 Mott polarimetry

Mott polarimetry is a crucial tool for the determination of the transverse components of electron spin. Determination of their magnitude is needed for calculation of those correlation coefficients, which are of BSM sector of weak interaction. For this reason, the method of Mott polarimetry needs to be concisely introduced here.

Mott polarimetry, was first described by N. F. Mott in the early 20-th century [31, 32]. This experimental technique is widely used for extracting the transverse polarization of electrons. It relies on the spin-orbit coupling between an electron and the Coulomb field of a spinless, high-Z nucleus. Mott polarimetry involves observation of the left-right asymmetry in the angular distribution of electrons back-scattered on a target made of high-Z material. The extracted asymmetry would be exclusively sensitive to the transverse component of electron polarization.

Mott polarimetry is a versatile technique applicable to electron beam energies ranging from a few keV to a few MeV. Thus, it is well-suited for studying the electrons emitted in free neutron β-decay. Its effectiveness is attributed to the significant mass difference between the incident electron and the heavy nucleus, resulting in minimal energy transfer to the target. As a result, the energy of scattered electrons remains nearly unchanged.

Asymmetry of scattering is quantified by the analyzing power of the target described by Sherman function (S) [33, 34].

The Sherman function is related to the square of the nuclear charge and the scattering angle measured in the scattering plane. It would be valid for a single scattering event in a very thin target (ideally just of one atom layer). However, when dealing with a finite target thickness, the multiple/plural scattering deteriorates the accuracy of polarization measurements. To address this effect, the effective Sherman function (S_{eff}) needs to be calculated or measured in a dedicated experiment. The calculations have to account for actual target thickness and all possible scattering processes. Nowadays, the calculations of effective Sherman functions can be supported with Monte Carlo simulations [35–37].

Chapter 3

Experiment at ILL, Grenoble: BRAND-0 stage

As presented in the previous chapter, the scientific program of BRAND project is very ambitious and its realization will take many years. Up to now only the very initial stage of the experimental program was partially accomplished. This work presents the performance of the small scale prototype of the BRAND setup developed for feasibility study of techniques, methods and algorithms intended for implementation in the next stages of development of BRAND experiment.

Moreover, since the author of this thesis has been involved in a development and tests of this part of detection system, which is devoted to the registration of electrons, the performance of prototypes of proton detectors will not be discussed here. Information about construction and performance of the proton detectors can be found in [29, 30, 38].

A small-scale prototype of BRAND apparatus (called BRAND-0) was build and installed at the polarised cold neutron beam facility (PF1B) at ILL Grenoble, France. With this setup two experiments have been performed: 6 days in October '20 [29, 39] and four weeks in September-October, 2021.

The first experiment, excluding the time needed for installation, safety measurement, and de-installation has effectively lasted 3 days. This time was devoted for tuning of the setup parameters. For this reason the measurement conditions were not clean and collected statistic was limited. The beam polarization was not provided as well.

The second experiment, to great extent, was also spent for the optimization of the setup (mainly of Mott detectors and proton detectors). However, collected statistics of events permitted the studies and first conclusions about the performance of electron part of detection system, signal readout and data acquisition (DAQ) system, the beam quality and experimental background. Results of analysis of these data are enclosed in this work.

Below presented is the experimental place of PF1B devoted for cold neutron physics at ILL and the prototype setup of BRAND-0 experiment used during the 2021 experimental run.

3.1 The cold neutron facility at ILL

For measurements of most of the correlation coefficients intended in the BRAND experiment the polarized neutron beam is demanded. For precise measurements the highly polarized neutron beam is important prerequisite (cf. eq. 2.2). Nowadays, the best quality of intense, cold and polarized neutron beam is provided by Institut Laue–Langevin (ILL), Grenoble, France [40].

At ILL, the neutrons are generated in a high-flux research reactor through a fission process in a compact-core fuel element. With a thermal power of 58.3 MW, it provides the most intense neutron source in the world. Initial neutrons are thermalized in the reactor moderator (heavy water). They have mean temperature $T \simeq 294$ K and mean velocity $v \simeq$ 2200 m/s. Further moderation of neutrons is done by means of liquid deuterium kept at temperature of -248 °C. Both cold ($v \simeq 800$ m/s) and ultracold neutrons ($v \simeq 10$ m/s) are achievable. Also the faster - epithermal neutrons ($v \simeq 10000$ m/s), moderated by means of graphite maintained at a temperature of 2600 °C are provided on demand.

Neutrons of desired energies are extracted and transported by means of beam-tubes towards the experimental areas. About 40 different research instruments devoted to various kinds of fundamental and applied science are served with the neutron beams at ILL. Research spectrum includes solid state physics, biology, medicine, fundamental properties of matter, engineering and industrial applications.

PF1B is one of the experimental areas at ILL, which is dedicated for particle and nuclear physics experiments. Provided there neutrons are extracted from cold neutron source (liquid deuterium moderator).

The PF1B experimental area is located around 72 m away from the reactor. Beam is transported via so-called ballistic supermirror neutron guide H113 [41]. Supermirror is a multi-layer structure of Ni/Ti (typically 100 double layers) of varying thicknesses and varying cross-sections along its length. This allows for highly efficient reflection of cold neutrons while minimizing their losses. At its exit window of the cross-section of 20×6 cm^2 the H113 supermirror guide provides the neutron capture flux density $\Phi_C = 1.35 \times 10^{10}$ cm^{-2} s^{-1} . (For explanation of beam parameters referred to as "capture" or "actual" cf. sec. 3.3).

In the PF1B station, depending on the demands of the experiment, various further arrangements of the beam transport are done. A schematic diagram showing the components of the beam transport arrangement at PF1B during BRAND-0 experiment is shown in figure 3.1. Apart from the BRAND-0 decay chamber, the following components were in use:

1. **Polarizer**
   In the polarizer, the incident neutrons of demanded spin orientation are transferred whereas those of wrong spin orientation are absorbed. This effect is achieved in the properly aligned stack of thin, single-crystal sapphire wafers, coated on both sides

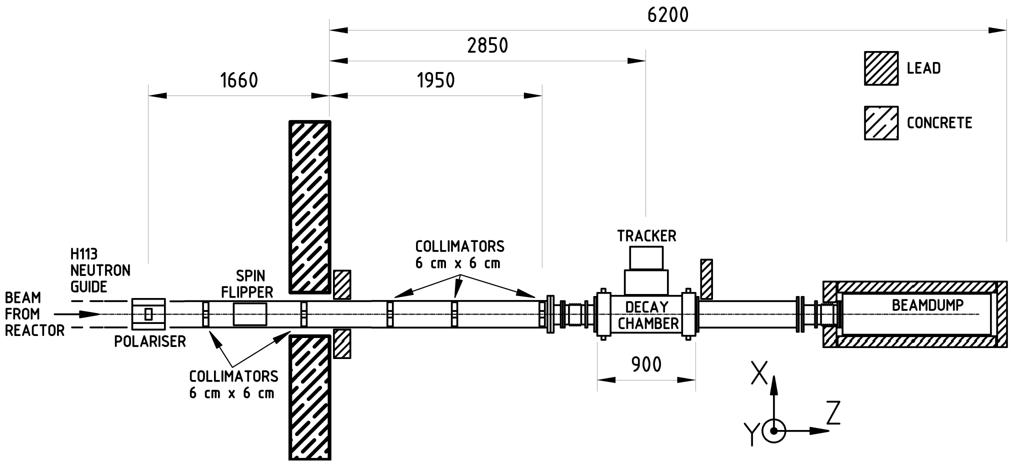

Figure 3.1 Components of neutron beam transport at PF1B areal during BRAND-0 experiment.

with Gd/Ti thin surfaces called polarizing mirrors. They form a structure similar as a supermirror of H113 neutron guide.

The present neutron polarizer installed at ILL is operated since 2020. It provides a downstream beam polarization of 0.997 (99.7% polarization) [42]. This value is averaged over the whole spectrum of the wavelength bandwidth of 0.3 – 2.0 nm. To achieve a high polarization efficiency, the polarizing mirrors are placed inside a magnetic housing with permanent magnets. These magnets generate a strong vertical field (B > 0.3 T). The neutrons leaving the polarizer have spins aligned along the Y-axis, orthogonal to their momentum direction. Some properties of the PF1B polarizer are discussed in more details in sec. 7.1.

2. **Spin flipper**
   Collection of data for two well defined but opposite orientation of neutron beam polarization, which are periodically swapped, is crucial for precision experiment. It permits significant reduction of influence of any asymmetries present in the setup geometry or in performances of detection system.

   Device which handles this task is called a neutron spin flipper. The spin flipper at PF1B is localized behind polarizer at distance about 3 m from the BRAND-0 setup. It utilizes superposition of static magnetic field gradients and oscillating magnetic field of specific frequency. They are mutually orthogonal. Oscillating field is created by solenoid driven with radio frequency current generator. Spin flipper can be in two states: (*i*) passive state - only static field is present and neutron spin remains unaffected, and (*ii*) active state - RF generator is on and resulting magnetic field causes adiabatic rotation of neutron spin. Efficiency of this process is close to 1 in broad range of neutron wavelengths. Idea of such spin flipper was introduced and is explained in [43].

3. **Collimators**
   Ideally, the neutron beam in the fiducial volume of the detection system should be narrow and of low divergence. The uncertainty in the beam position contributes to the uncertainty of the track origin and misidentification of the measured reaction. The beam halo can interact with the component of experimental apparatus and generate adverse experimental background.

   In order to define the demanded beam dimensions in the decay chamber of BRAND-0 the five collimators have been installed between the polarizer exit and PF1B entrance. They are constructed as a round lead layers of 5 cm thickness. Their outer diameter is about 18 cm and fits to the neutron guiding tube. The collimators have an aperture with an inner opening of 6×6 cm^2. The first collimator is installed 0.4 m and the fifth one 3.9 m from the polarizer exit. The distance of last collimator to the center of BRAND decay chamber is 0.9 m.

4. **Spin guiding fields**
   Maintaining of the neutron beam polarization on its way to the experimental area is extremely important. This task was realized by the arrangement of various magnets along the beam path. For this purpose dipole magnets and solenoids were used. They are visible in the photo presented as fig. 3.2. This arrangement of magnets allowed adiabatic spin rotation by 90° from vertical one to aligned along the Z-axis.

5. **Beam stop**
   After passing the BRAND-0 decay chamber the neutron beam is stopped at the beam dump. It is constructed as an aluminum box of the length of 1.5 m and side of 0.5 m. Its back side is at the distance of 3.5 m from the center of decay chamber. At the rear wall of beam dump neutrons are suppressed in 2 mm thick padding made out of LiF rubber. For this aim the reaction: $n + {}^6\text{Li} \rightarrow {}^3\text{H} + {}^4\text{He} + \gamma$ is utilized. The ^{6}Li content in this material is enriched to 80%. The position and geometry of beam dump is selected such, that particle created during neutron conversion (electrons, γs) can not be registered in the BRAND detection system.

3.2 BRAND-0 setup

Figure 3.2 shows the top view of actual assembly of the prototype setup at the ILL site. The main components are labeled. In the center the decay chamber with two solenoids maintaining the neutron spin and two Helmholtz solenoids (rectangular, yellow) for compensation of the Earths magnetic field are visible. Close to the decay chamber, the Mott polarimeter was installed. The beam comes from left side of the picture. On the right-front side of the beam dump, cased with lead blocks, is visible. In vicinity of the Mott polarimeter, the electronics and hardware for DAQ system were placed.

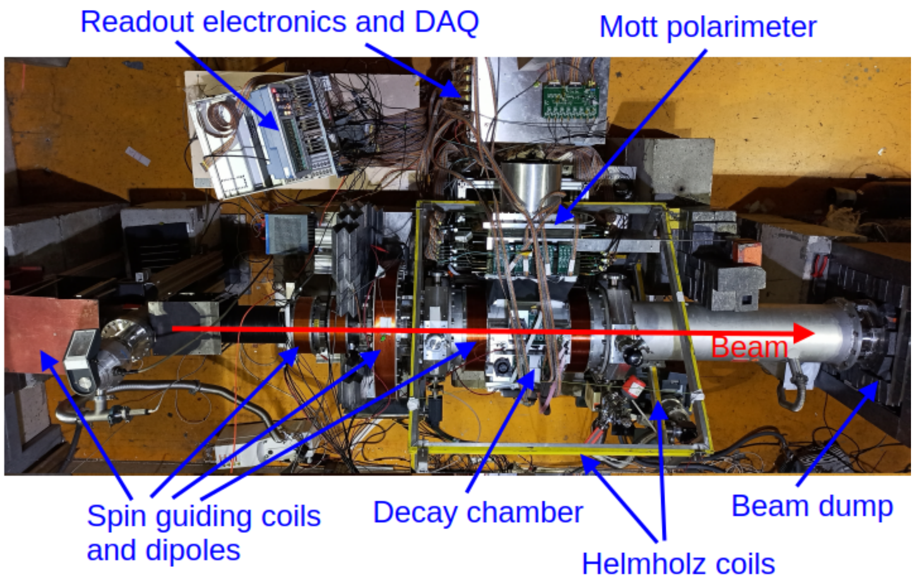

Figure 3.2 PF1B experimental area with the BRAND-0 prototype apparatus.

A Cartesian coordinate reference system is used in the BRAND experiment. Its origin (0,0,0) is located in the center of the decay chamber. Coordinate X points toward the Mott polarimeter, coordinate Y is directed up and coordinate Z is oriented along the beam direction.

Components of the actual BRAND detection system are presented in fig. 3.3. The sketch of cross section perpendicular to the beam axis at the origin of BRAND coordinate system is plotted.

3.2.1 Decay chamber

Decay chamber is an aluminum tube of inner radius of 165 mm and wall thickness of 10 mm. Its total length along Z-axis is 90 cm. Four openings - one for vacuum window (24×10 cm^2) and three for proton detectors (each 29×10 cm^2) are made at the chamber wall at 0°, 90°, 180° and 270°. Attached there are ports made from aluminium, permitting installation of window frame and assemblies of proton detectors.

The vacuum window had a shape as presented in the fig. 3.5 and dimension of 22×8 cm^2. A thin, vacuum tight foil reinforced with the Kevlar threads was used for this purpose. Kapton and Mylar foils of various thicknesses were tested against their long term mechanical endurance and vacuum tightness under 1 bar pressure difference on their both sides. Finally, the Mylar foil of the thickness of 12 μm has been used during data taking. For more details about vacuum window construction and foil selection see sec. 4.2.

Three identical units containing the proton detectors were installed at their ports outside of the decay chamber.

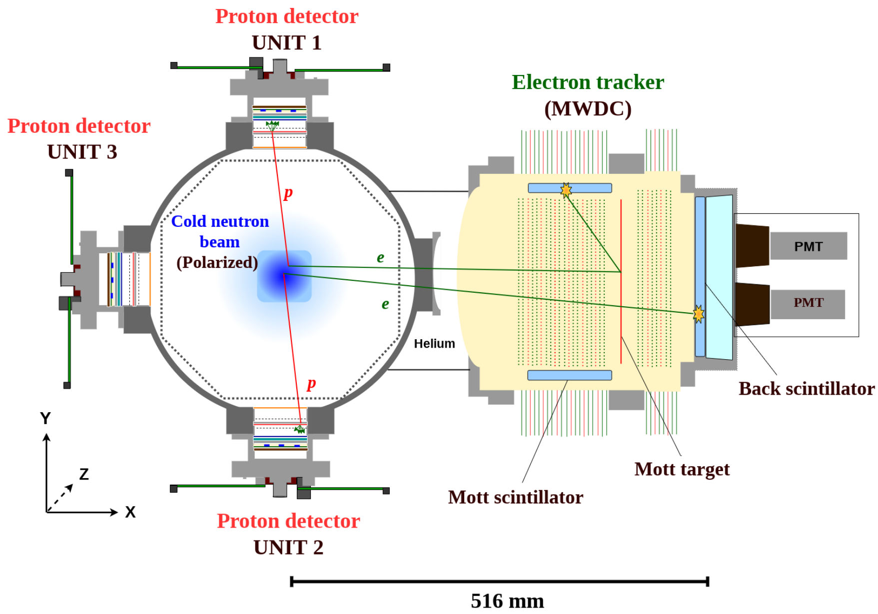

Figure 3.3 Front cross-section view of the BRAND-0 experimental setup.

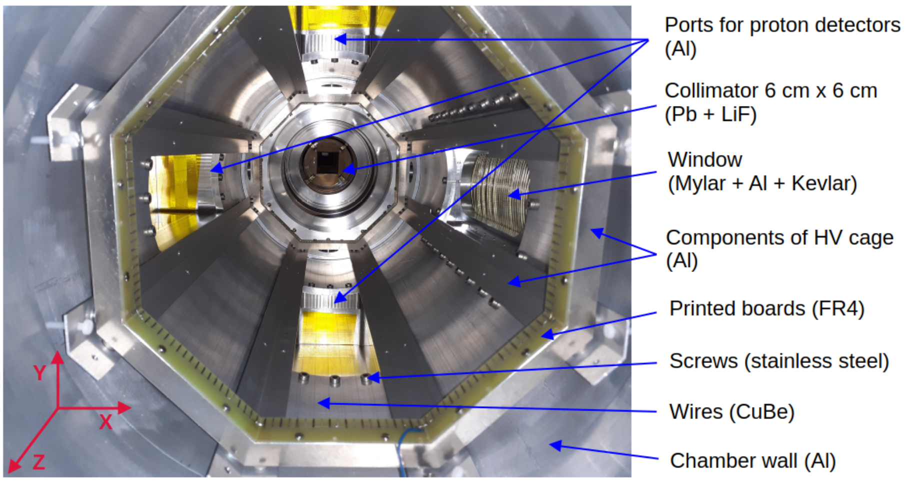

Figure 3.4 A picture showing interior of the BRAND-0 decay chamber. Respective elements important for beam guiding and background creation are labeled. See text for details.

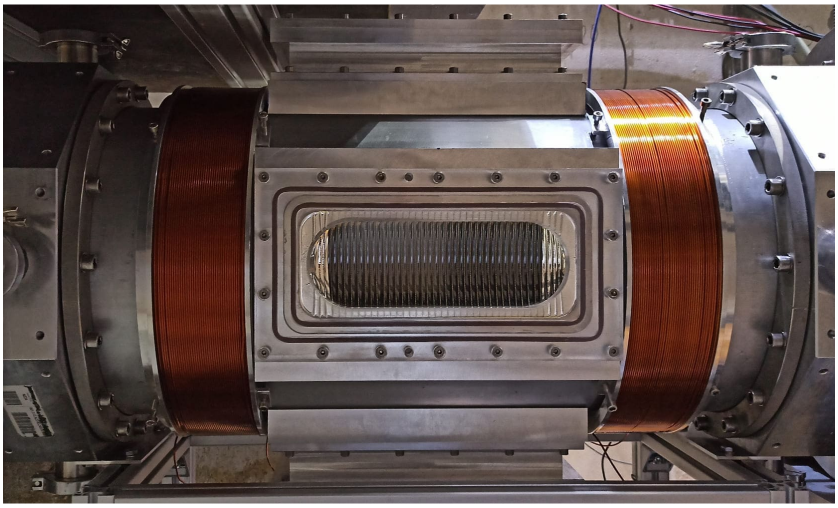

Figure 3.5 Side view of the decay chamber showing the position and shape of vacuum window. A Mylar foil stretched on aluminum/Plexiglas frame has been reinforced with the Kevlar threads. Two coils creating an axial magnetic field intended for maintaining the neutron spin orientation are visible at the sides of the vacuum window. Octagonal endcaps installed at most external sides of the chamber are visible as well. At the top, bottom and rear side, aluminium ports for the proton detectors were attached.

Inside the chamber, close to its wall a potential cage (HV cage) has been installed. Construction of this cage is visible in fig. 3.4. It is made as a mesh of parallel CuBe wires of 75 μm diameter stretched at the frame made of aluminum profiles and printed boards. The purpose of the potential cage was to define the zero-field drift volume for protons from neutron decay and to suppress the detection of low energy electrons reflected at the chamber walls.

Throughout the run, the vacuum in the decay chamber has been maintained at the level of $5 \cdot 10^{-4}$ mbar.

The BRAND-0 decay chamber has been designed and constructed in IFJ PAN. The design has been optimized with the use of the finite element model calculations [44].

To maintain the polarization inside the fiducial volume of the decay chamber, two magnetic coils have been installed around the chamber. They were made as 600 turns of 2 mm diameter copper wire wound on the aluminium torus. With the electric current of a few Amperes a demanded strength of axial magnetic field in the decay chamber was achievable.

Two large Helmholtz coils were used as well to compensate for the Earth's magnetic field. They had square shape of the edge equal to 1.16 m. Helmholtz coils have been fixed around the decay chamber at most suitable angular orientation.

3.2.2 Mott polarimeter

The electron detection system of BRAND-0 prototype form so-called Mott polarimeter. It is an ensemble of detectors which should provide the crucial information about transverse components of the electron spin together with its four-momentum. For the former, the

Mott scattering is utilized what define the name of the detection system. The method of determination of energy, momentum and spin of electron is also referred to as Mott polarimetry [45].

The Mott polarimeter was situated at the side, in front of the vacuum window of decay chamber. It consists of the following elements:

1. Tracker - a low-density Multi-Wire Drift Chamber (MWDC) with hexagonal cells. It is operated at normal pressure with a gas mixture of He:CO2 (85:15) + trace of ethanol vapor. 3D trajectory reconstruction of electrons is possible.

2. A thin Pb coated Mylar film working as a Mott scattering target (refereed to as "Mott foil" or "Mott target"). It is installed in the active volume of MWDC for the measurement of transverse electron polarization.

3. A disk-shaped (thickness 10 mm and diameter 200 mm) plastic scintillator (referred to as Back scintillator or "Back_scint") for the detection and energy measurement of direct electrons.

4. A pair of rectangular plastic scintillators (thickness of 10 mm and dimension of 100×200 mm^2) called "Mott detectors" or "Mott_Dets" for the registration and energy measurement of electrons scattered by the Mott target.

The Mott detectors were placed inside the active volume of MWDC and have been read out with SiPM sensors. The signal from the Back scintillator (situated behind the tracker) was provided by four conventional PhotoMultiplier Tubes (PMTs). For 3D tracking, a track position of the electrons in the XY-plane was extracted from the drift-time measurement. To derive the hit position along the length of the wire (Z-direction) the charge-division method was applied. The principle of the tracking mechanism was partially adopted from the miniBeta project ([46, 47]). All the scintillator detectors used in the BRAND-0 system provided the trigger signals for DAQ.

Multi-Wire Drift Chamber (MWDC)

The BRAND-0 electron tracker was built at IFJ PAN. It is an eight-layer drift chamber of 24 cm $\times$ 24 cm active area. Each layer contains 11 cells of hexagonal shape. They are formed by sandwich structure of printed boards, where anode (signal) and cathode (field) wires were soldered. Anodes were kept at positive potential, whereas cathodes have been grounded. The field wires are 75 μm diameter CuBe wires (98% of Cu and 2% of Be). For the signal wires, which are intended to provide not only the electron drift time but also the hit position along their length, the high resistance wires of NiCr alloy (80%-20%) and diameter of 25 μm have been used. The hit position along the wire was estimated from the charge asymmetry collected at its both ends.

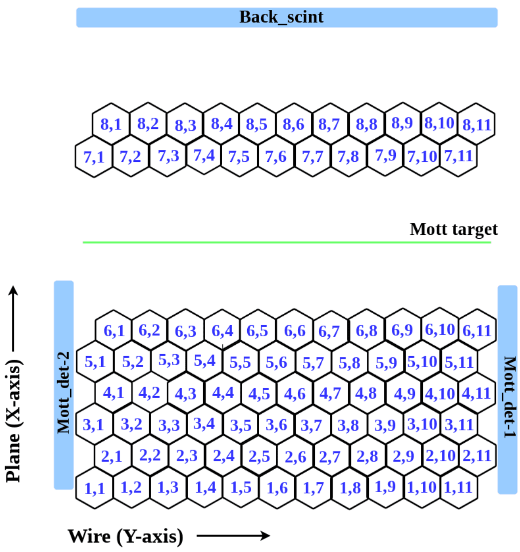

Figure 3.6 Distribution of drift cells in the XY-plane of MWDC along with positions of other crucial elements within the Mott polarimeter. A matrix of 8×11 cells is visible. Their centers are defined by positions of anode wires. The corners of each cell are formed by cathode wires. Each cell is uniquely identified by its corresponding layer called plane (P) and wire (W) number, denoted as cell (P, W).

With the proper sequence of stacking of field and signal boards the demanded hexagonal structure of high compaction has been formed (see fig. 3.6). The effective radius of drift cell was 8.66 mm, whereas the cell corners were at 10 mm distance from the cell's center.

The active volume of the tracker was limited at one side by the entrance window and on the other side by the face of Back scintillator. For the entrance window as well as for the light screening of Back Scintillator the 12 μm thick aluminized Mylar foil was used. Entrance window and housing of Back scintillator were connected to the solid aluminium frames embedding the tracker. All components were sealed with the rubber o-rings making the whole construction tight. The active volume of tracker was filled with helium-based gas mixture, continuously flowing and kept at small overpressure.

The modules of preamplifiers (developed at the Jagiellonian University, Kraków (JU)) have been connected directly to the outputs of signal boards.

Active volume of MWDC has been divided into two parts by Mott foil compartment installed between layer 6 and 7 (cf. fig. 3.7).

More information about assembly of the MWDC, performed tests and optimisation of the working parameters is provided in sec. 4.1.

Mott target

The Mott target is essential for analyzing the transverse component of the electron spin. Considering that the cross section for this purely electromagnetic process scales with the square of the nucleus charge, materials with high atomic number are strongly preferred.

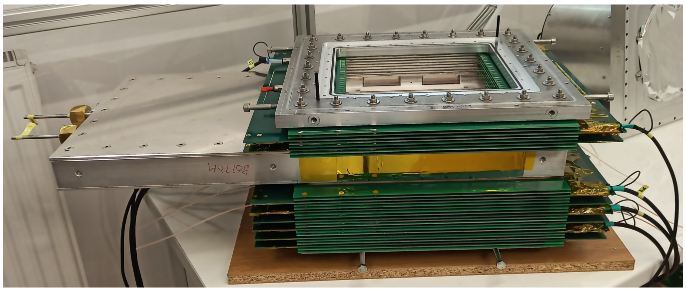

Figure 3.7 A photo showing the construction of MWDC as a sandwich of interlaying PCB boards. Signal (anode) boards, which are longer, are surrounded by pairs of field (cathode) boards. Between layer 6 and 7 the Mott foil compartment is installed (see next subsection). HV supply cables are soldered to individual signal layers. Upper aluminum frame is removed permitting observation of electrode wires inside detector.

The Mott target used in the BRAND-0 setup was a ~2 μm thin layer of lead evaporated on the 4 μm Mylar foil.

To keep the angular sensitivity uniform in the Mott scattering process, the Pb coating on the foil should be even. Also, any kind of sagging or deformation of the Mott foil surface deteriorates the homogeneity of its effective analyzing power. In case of the BRAND-0, the old foil, used initially in nTRV experiment, was utilized. Due to ageing process and slow flow of Pb against Mylar surface the thickness of lead film was no more constant over the whole area of the target. Nevertheless, for the initial experiment, devoted rather for troubleshooting of the apparatus than for precise measurement, the quality of the Mott foil was sufficient. The best possible area of the available foil was selected. To keep the Mott foil surface as plain as possible the foil was stretched uniformly in all directions and glued to an aluminum frame (from the side of Mylar).

The Mott target has been installed inside the tracker, permitting registration and unique identification of the scattered electron tracks (triggered by Mott detectors). Particles which were unaffected by the lead layer and have been registered in the Back scintillator are called "direct electrons". The last case is by far the dominant one, as merely a small fraction of electrons (about 1 in 1000) resulting from neutron decay could be back-scattered from the Mott target towards the Mott scintillator [26].

The parameters of the Mott target used in the BRAND-0 experiment (effective Sherman function, distribution of Pb material on the surface of the Mylar film) are well know since the foil have been adopted from the nTRV experiment [48].

In order to facilitate its mechanical fixation and moving in/removing of the Mott target, the so called Mott foil compartment has been constructed. It is an air tight aluminum box permitting inserting and removing the Mott target without disturbing of the current conditions of tracker (gas flow, electric field). Additional benefit of using the Mott foil compartment is the possibility to store there an aluminium plate with slits, utilised for the position calibration in Z-directions (cf. sec. 5.1.4), which can be moved in/out in the same manner as the Mott target. The photos presenting the standing alone and open Mott foil compartment equipped with the Z-position calibration plate and Mott target are shown in fig. 3.8 and 3.9 respectively.

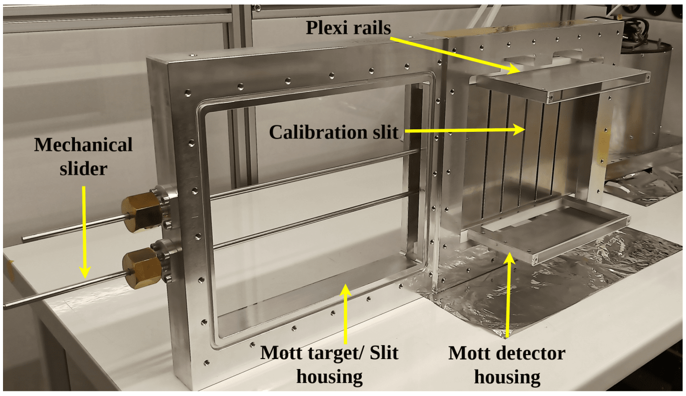

Figure 3.8 Mott foil compartment with Z-position calibration plate in working position. Manual drives and Mott scintillator housings are visible as well.

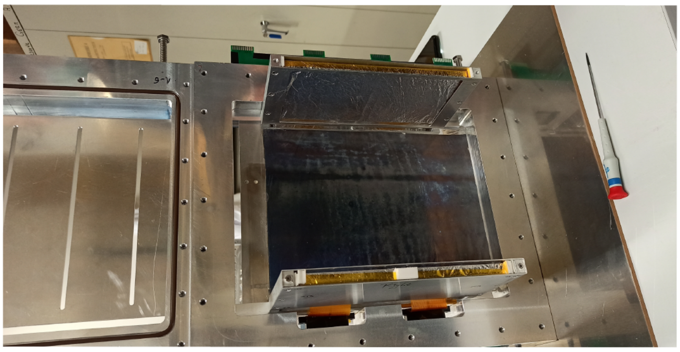

Figure 3.9 Similar view as in fig. 3.8 but here the calibration plate is removed to the parking position permitting observation of the Mott target at its working position.

Back scintillator

The Back scintillator is intended for the registration of dominant fraction of the electrons from neutron β-decay, measurement of their energies, providing the reference time for the drift-time measurement in the tracker, and providing the trigger signal. It was also used to suppress the high-energy background, and together with the last two planes of the drift chamber, it provided a veto signal for the selection of Mott-scattered events.

The detector consisted of 1 cm thick plastic scintillator disc (EJ-200) of 20 cm diameter, attached to a conical light-guide with the use of optical grease (cf. fig. 3.10). The scintillation light was gathered on the opposite side of the light guide, using four 3-inch XP3330 photomultiplier tubes (PMTs). All PMTs were individually screened from magnetic field by mu-metal shielding and the whole assembly was enclosed inside a cylindrical, light tight Faraday cap made of aluminum.

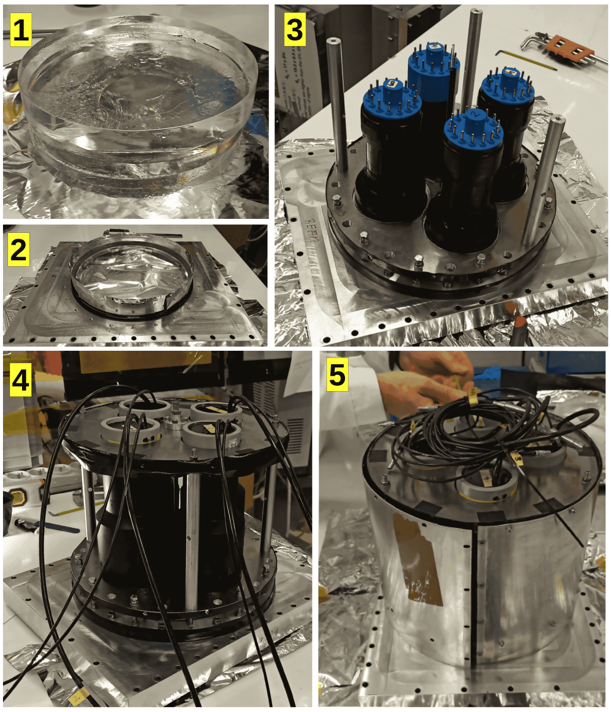

Figure 3.10 Pictures presenting the components and assembly steps of the Back scintillator.

Mott scintillators

Two Mott scintillor detectors installed inside the active volume of the tracker should provide an energy and trigger signal for the electrons which underwent the scattering on the Mott target. They were made of rectangle blocks of plastic scintillator (BC400), each of 20 cm $\times$ 10 cm $\times$ 1 cm, wrapped with thin aluminum foil. The light was readout by the rows of 14 SiPM sensors of 6 mm $\times$ 6 mm dimension attached to each short side of the detector. Their readout electronics was also kept inside the MWDC.

The way of installation and the positions of Mott detectors in the MWDC can be seen in figs. 3.3, 3.8 and 3.9. Mott detectors of BRAND-0 setup have been provided by group from Jagellonian University. Unfortunately they could not be tested before the experiment at ILL. The fully assembled Mott polarimeter is shown in fig. 3.11.

3.2.3 Proton detector

The low energy of β-decay protons ($<$ 750 eV) makes them very difficult for direct detection. For their registration in BRAND experiment the method proposed in [49] has been adopted. It relies on initial acceleration of emitted protons in the external electric potential (25-30 kV) and their subsequent conversion into bunches of secondary electrons. For this purpose a thin foil formed by depositing a 20 nm thick LiF layer onto a thin polyamide film will be used. Electrons ejected from the conversion foils are accelerated by the same electric potential and detected in a very thin plastic scintillator (thickness $\sim 25\mu$m).

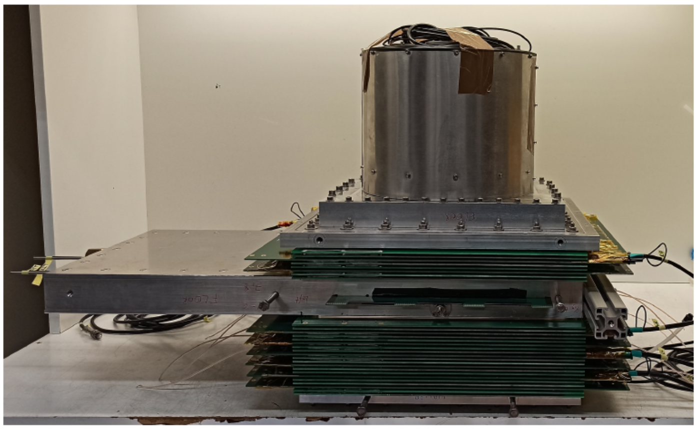

Figure 3.11 Fully assembled Mott polarimeter. Visible are: tracker composed of stacked PCB-boards with the Mott foil compartment installed between the layer 6 and 7, and the Back scintillator shielded with cylindrical Faraday cup at the top. Mott target and Mott detectors are installed inside tracker and are not visible in the picture.

During the experimental run in 2021, the apparatus intended for proton registration was still in the R&D phase. Description of performance of those detectors is beyond the scope of this thesis. Details about construction of the BRAND proton detectors and information about current status of their development can be found in [29, 30, 38].

3.2.4 Readout electronics and data acquisition (DAQ)

The signal readout and processing system comprises the custom made analog electronics and commercial time digitizers (CAEN V1190A [50]). The aim of the analog electronics is to convert the important quantities generated by detectors (energy, time, drift time, charge) to the timing signals and digitize them by means of Time-to-Digit Converters (TDC). In this way one could reduce the total cost of readout electronics by avoiding application of dedicated Analog-to-Digital Converters (ADC). The idea is similar as for commonly used Time-over-Threshold method where the value of a signal amplitude is derived from a length of properly shaped analog signal [51, 52]. In the case of BRAND-0, for each channel, two separate time signals were generated. The first one provides information about actual time of particle passage. The subsequent signal has the width proportional to the amplitude. In order to be registered by the multi-hit TDC, both signals (with their leading and trailing flanks) have to fit into the time window of the digitizer.

This method was directly used for signals of the Back scintillator, Mott scintilators and for proton detectors. Also for the measurement of charge collected at both ends of tracker wires this conversion technique was applied. In this case, however, the signals were divided into two branches - one for measurement of the drift-time, and second - for charge to time conversion.

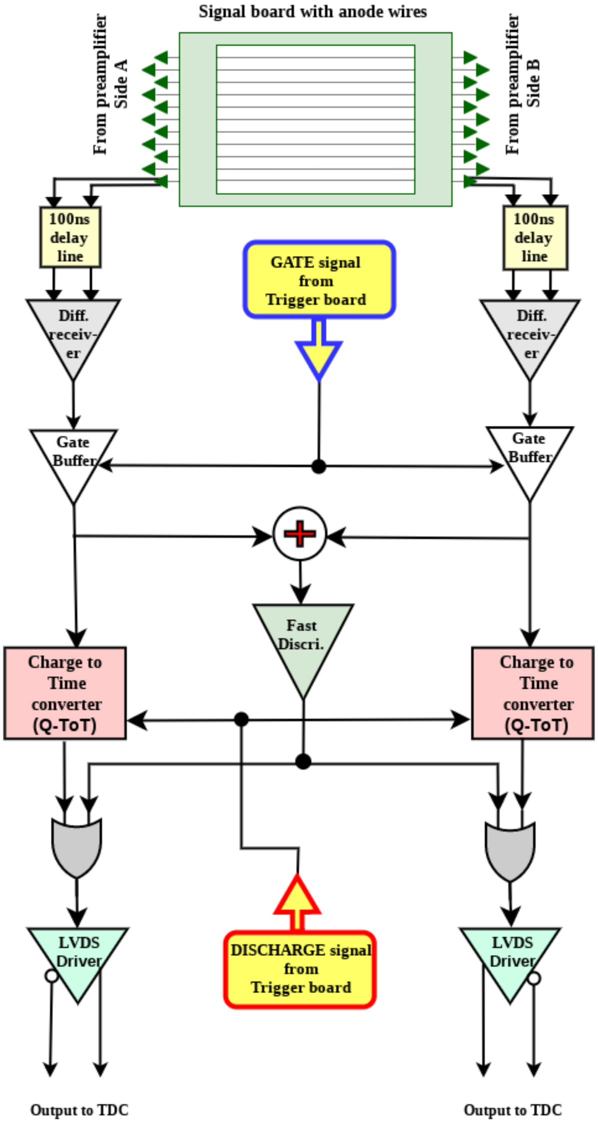

Figure 3.12 Block diagram of the signal processing chain of MWDC.

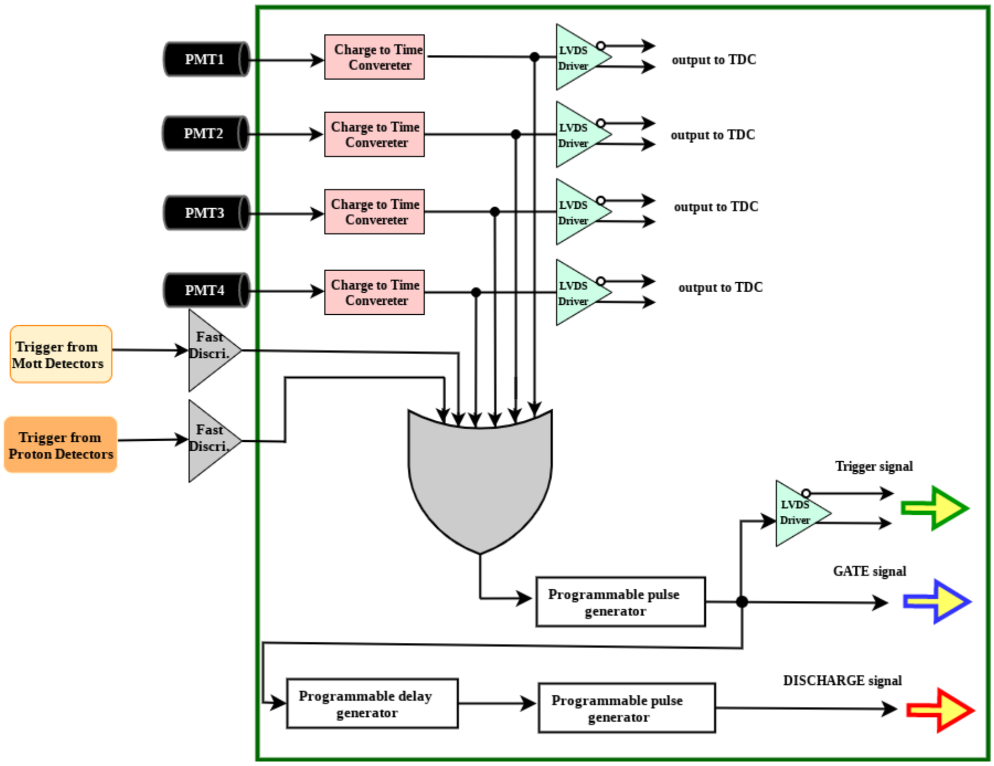

Figure 3.13 The simplistic schematic of trigger board used in the BRAND-0 setup.

Figure 3.12 contains the block diagram presenting the logic of MWDC signal processing. The amplified analog pulses from both sides of the signal wire are received at the Gate Buffer. The signals are only accepted for the further processing if both of them coincides with the GATE signal provided by the trigger board and generated by the TRIGGER signal. This trigger is produced by the fastest signal of scintillators or proton detectors. The onset of the TRIGGER signal is also the reference for drift time measurement.

Once the both wire-ends signals are accepted, the sum of them is fed into discriminator and provides the STOP signal of drift time. Signals from parallel branches are acquired by the Charge-to-Time conversion circuit in order to provide timing signals proportional to the the charges collected at both sides of the wire. Signals are integrated until the DISCHARGE signal is sent by Trigger Board.

The created LVDS timing signals are fed into CAEN V1190 128-channel multihit TDC modules.

The scheme of the Trigger Board unit is shown in fig. 3.13. The trigger for Data Acquisition (DAQ) have been constructed by OR of signals of individual photomultipliers of Back scintillator, Mott detectors or proton detectors. Selection of trigger component was done by hard connection of appropriate cable to the Trigger Board input.

The gates length, discriminator thresholds and discharge limits for charge-to-time conversion were remotely programmed with the use of Minicom protocol.

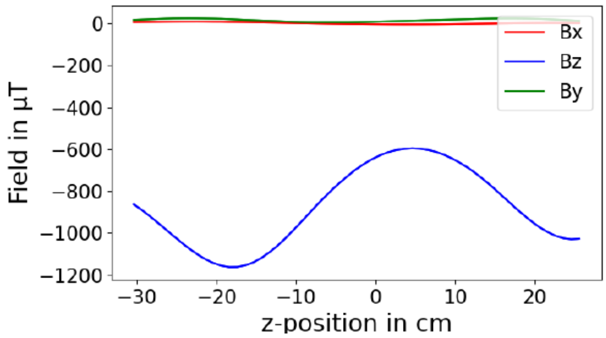

Figure 3.14 Distributions of the X, Y, Z components of the magnetic field along Z-axis, in the decay chamber during BRAND-0 experiment measured at various positions by means of the Hall sensor. Reprinted courtesy of D. Ries, N. Yazdandoost and M. Engler (Univ. of Mainz).

During data taking with only Back- and Mott scintillators as a trigger sources the dead-time of DAQ was of the order of 5%.

The accepted data were recorded on the storage disc. A custom made software was used for the data acquisition, visualisation and analysis. As it was described above, only the TDC devices were used for digitizing of the signals. But in order to distinguish between amplitude-related and time-related quantities, throughout the thesis the former ones will be provided in "AU", which in fact are "TDC units".

3.2.5 Magnetic field

In addition to dipoles and solenoids maintaining and rotating the neutron spin along the PF1B neutron transportation system, two solenoids to maintain the spin orientation in the decay chamber was prepared by group from University of Mainz (Germany). Moreover, two large Helmholtz coils were installed around the decay chamber at most suitable orientation in order to compensate the magnetic field of Earth (yellow squares in fig. 3.2). Real distribution of the magnetic field in the decay chamber has been measured using 3-axial sensor based on the Hall effect. It has been driven automatically along Z-axis of decay chamber at 9 different positions selected in XY-plane. The results of this measurements is presented in fig. 3.14. As it can be seen, Z-component (along the neutron beam line) by far exceeds both transversal components. This ensures longitudinal orientation of neutron polarization, with maximal deviation of about 1.5 degree. The sinusoidal variation of the field intensity reflects the position of the coils and is irrelevant for the neutron spin direction.

3.3 Cold neutron beam at PF1B

Profiles of beam

The polarized neutron beam has been provided to the BRAND decay chamber (cf. sec. 3.2.1) via the collimator (last beam collimator) of the square opening of 6 cm edge. It was installed upstream of BRAND chamber, inside the beam vacuum pipe, at the distance of 90 cm from the center of the decay chamber. The photo of collimators used for PF1B beam transportation is shown in fig. 3.15.

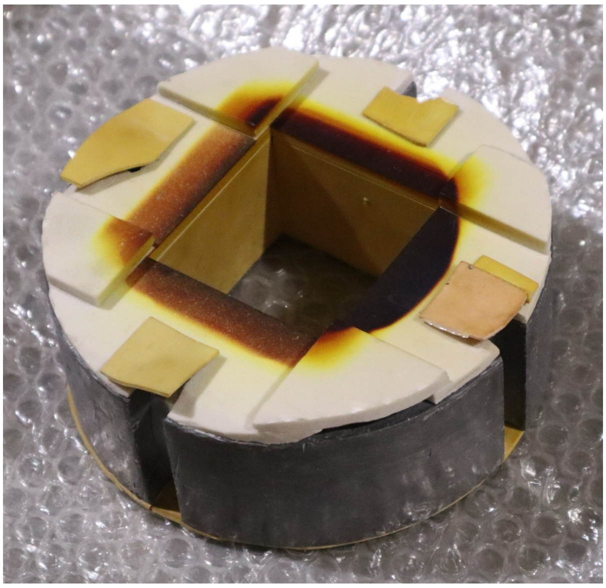

Figure 3.15 The beam collimator used for the beam shaping at PF1B experimental place. It is made as a lead block of 5 cm thickness and outer diameter of 18 cm. The lead orifice is a square of 7 x 7 cm^2 The walls of the collimators are additionally covered with the 5 mm LiF ceramics (front side and inside the opening) and 2 mm LiF rubber (back side). Thus, the effective orifice for neutrons is 6 x 6 cm^2, whereas for the γs it remains 7 x 7 cm^2.

The beam collimators are made as 5 cm thick lead block with square opening of 7 cm x 7 cm. Their front sides and walls inside opening are covered with 5 mm thick layer of LiF ceramic material, where the ^{6}Li is enriched to 96%. The back side of collimator are covered with 2 mm thick LiF rubber, where ^{6}Li is enriched to 80%. The effective aperture of the colimators for the neutrons is 6 cm x 6 cm $(2d_0$ x $2h_0)$. The lead layer is sufficient to stop almost 100% of all γs produced in the neutron transport system upstream of the collimator [53]. Thus, it is justified to assume that only those γ particles, which travel through the aperture of a collimator can be transferred further toward the PF1B area. For γs the effective aperture is equal to the oppening in the lead (7 cm x 7 cm).

The neutrons outside the aperture of collimator are suppressed in the LiF materials via reaction:

$$n + {}^6Li \rightarrow {}^3H + {}^4He + \gamma$$

The neutron absorption cross-section for thermal neutrons in ^{6}Li is equal to 940 barn [54]. For cold neutrons the cross section is larger by factor ~ 3. Resulting reaction products and γs of other origin are stopped inside the thick lead volume.

For the ideal case of non-divergent beam the beam profile inside the decay chamber should be flat over square shape area of 6 x 6 cm^2, with the homogeneous flux density (Φ - the number of beam neutrons per 1 cm^2 per 1 s) along the axis of the decay chamber. According to [41, 55] in such case the beam intensity, I, defined as the number of beam neutrons per second, is the simple product of area of collimator and the constant flux density $\Phi(0)$:

$$I = 4d_0h_0\Phi(0), \tag{3.1}$$

A flux density, $\Phi(0)$, is the number of beam neutrons per 1 cm^2 per 1 s, in the axis of the beam.

The actual beam profile during BRAND '21 experiment has been measured with the method of gold foil activation. The two sets of round spots of Au foil of 1 cm diameter, 10 spots each, kept within the rectangular Al frame (cf. fig 3.16), were used for this aim. They have been installed horizontally and vertically at the end of decay chamber (Z = +40 cm). Each set of Au foils was subsequently activated with the neutron beam over the time period of 10 minutes. The neutron capture reaction with subsequent γ and β emission is utilized:

n + ^{197}Au $\rightarrow$ ^{198}Au $\rightarrow$ γ, β $\rightarrow$ ^{198}Hg

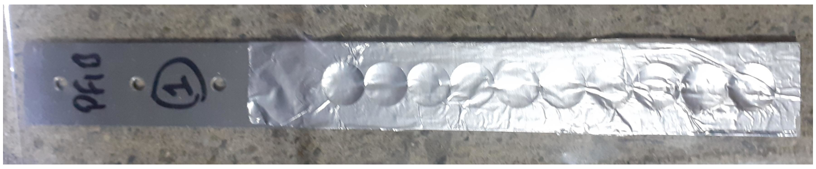

Figure 3.16 The gold foil embedded within the aluminum frame forming 10 circular areas. The gold foil is additionally protected by a layer of Al film. The circular spots of gold foil are used for the beam profile measurement via the neutron induced activation with the reaction: n + ^{197}Au $\rightarrow$ ^{198}Au $\rightarrow$ γ, β $\rightarrow$ ^{198}Hg

The subsequent measurement of induced activation of these Au spots permitted to establish the horizontal and vertical beam profiles and their absolute flux densities in the middle of the decay chamber.

Conventionally, the parameters of cold neutrons beams are given as "thermal equivalent". It means that they are re-scaled to the corresponding values, as they would be measured for thermal neutrons (of the velocity v^{th} = 2200 m/s, and λ^{th} = 0.18 nm). They are referred to as "capture flux" or "capture intensity" and should be labeled with the index "C". When the actual parameters of cold neutron beam are of interest they have to be calculated taking into account the ratio of actual and "capture" neutron wavelengths λ [41, 55].

Measured inside decay chamber of BRAND the capture flux densities for horizontal and vertical directions, $\Phi_C(x), \Phi_C(y)$, respectively, are presented in fig. 3.17.

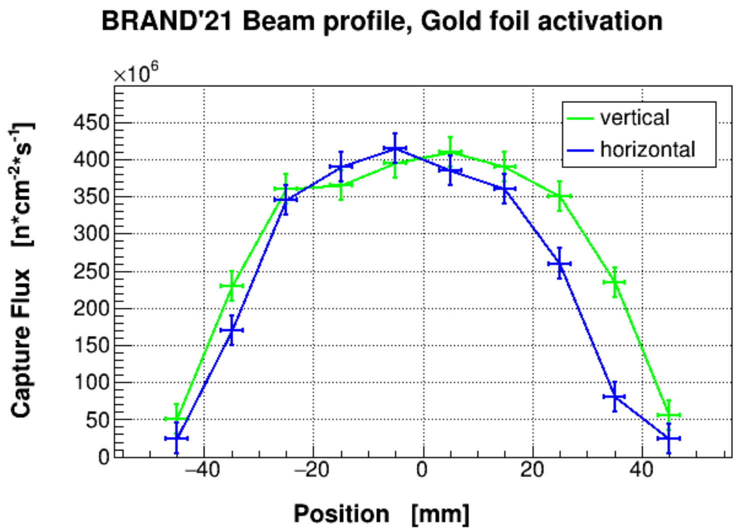

Figure 3.17 Beam profiles in vertical (green line) and horizontal (blue line) direction during BRAND-0 experiment. Data courtesy of T. Soldner (ILL).

The actual beam profiles in the decay chamber of BRAND are no more rectangular. Due to the divergence of the beam the flux density decreases with increase of the distance from beam axis. The beam core extends beyond the initial ±3 cm (aperture of collimator) both in vertical and in horizontal direction, for another ±2 cm. That is consistent with the knowledge gained from other experiments performed at the PF1B beam station where it was estimated that the beam divergence is slightly larger than 1.8 cm/1 m, both in vertical and horizontal directions [56] .

Beam intensity

From the measured beam profiles the mean quantities of $\Phi_C(x) = 2.45 \cdot 10^8$ n $\cdot$ cm^{-2} $\cdot$ s^{-1}, and $\Phi_C(y) = 2.84 \cdot 10^8$ n $\cdot$ cm^{-2} $\cdot$ s^{-1} were calculated. The resulting mean capture beam flux density, Φ_C^m, in the decay chamber is an arithmetic average of the last two values and is equal to:

$$\Phi_C^m = 2.65 \cdot 10^8 \text{ cm}^{-2} \cdot \text{s}^{-1}, \tag{3.2}$$

In order to obtain the average beam intensity, I_C^m in the BRAND decay chamber the mean capture beam flux density, Φ_C^m, has to be multiplied by the actual beam cross-section in the decay chamber, which is, according to measurement, 10 cm x 10 cm. This gives:

$$I_C^m = 2.65 \cdot 10^{10} \text{ s}^{-1}, \tag{3.3}$$

Neutron energy spectrum

The energy spectrum of the cold neutron beam at PF1B station has been measured with the time-of-flight technique described in [41, 55]. Conventionally, in neutron physics, the wavelength, λ spectra are measured (fig. 3.18 - left panel). The energy E and velocity v spectra of PF1B beam were calculated as well and shown in this figure.

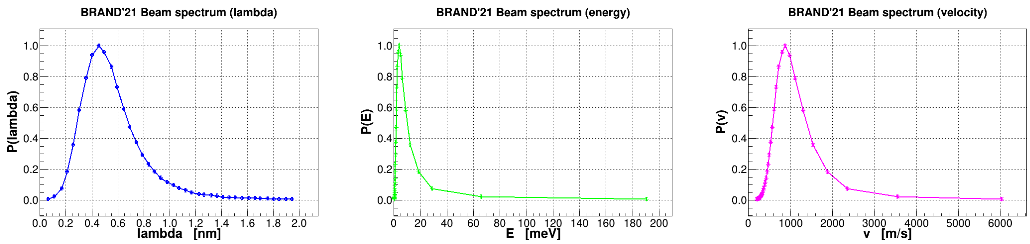

Figure 3.18 Spectra of the cold neutron beam measured during BRAND-0 experiment. Left panel: wavelength spectrum measured with the time-of-light method; middle panel: calculated energy spectrum; right panel: calculated velocity distribution.

From fig. 3.18 the following mean parameters (marked with "m") of the beam can be calculated:

$\lambda^m = 0.57$ nm,

$E^m = 4.18$ meV,

$v^m = 803$ m/s.

Neutron decay rate

Knowing the beam capture intensity and the beam velocity the expected decay rate of neutrons in the decay chamber can be calculated. But first the actual beam intensity has to be established. According to [41, 55] the scaling factor is just the ratio of the actual cold neutron wavelength ($\lambda^m = 0.57$ nm) to the average thermal neutron wavelength, λ^{th}, equal to 0.18 nm. The ratio of these quantities is 3.17. In order to obtain the actual parameters of the cold neutron beam in BRAND experiment the measured "capture" flux and all relative parameters have to be divided by this number.

Thus, the actual mean cold neutron flux, Φ^m, in the BRAND chamber is:

$$\Phi^m = \Phi^m_C \cdot \frac{\lambda^{th}}{\lambda^m} = 8.36 \cdot 10^7 \text{ cm}^{-2} \cdot \text{s}^{-1}, \tag{3.4}$$

Accordingly, the average beam intensity is:

$$I^m = I_C^m \cdot \frac{\lambda^{th}}{\lambda^m} = 8.36 \cdot 10^9 \text{ s}^{-1}, \quad (3.5)$$

The average neutron density, ρ^m, in the decay chamber is given as:

$$\rho^m = \frac{\Phi^m}{v^m} = 1040 \text{ cm}^{-3}, \quad (3.6)$$

where v^m is the average velocity of the neutrons in the beam.

The expected average neutron β-decay rate, R_β^m, per cubic cm and per second is given by formula:

$$R_\beta^m = \frac{\rho^m}{\tau} = 1.2 \text{ cm}^{-3} \cdot \text{s}^{-1}, \quad (3.7)$$

where, τ = 879.6 s is the mean lifetime of free neutron.

In the decay chamber (DC) of BRAND-0, which is 90 cm long, and with the beam cross section of 10 x 10 cm (as deduced from direct measurement - cf. fig. 3.17) the total average decay rate, R_β^{DC} is :

$$R_\beta^{DC} = R_\beta^m \cdot 9000 \; cm^3 = 10800 \text{ s}^{-1}, \quad (3.8)$$

All the quantities presented in this subsection are based on experimentally measured capture flux of neutron, the shape of beam profiles in the BRAND decay chamber and the energy spectrum of cold neutrons in PF1B station. The rectangular shape of the beam profiles is assumed and average value of neutron flux is calculated. Moreover, the shape of energy spectrum of neutron is neglected. Instead a mean value of neutron energy is taken for further considerations. It is justified at this stage of analysis of beam properties, when significant uncertainties of BRAND apparatus are dominating the measurement precision. Taking into account also the limited precision of Au activation method and neutron energy spectrum measurements the conservative estimation of total systematic error of calculated decay and detection rates is of 30%.

Detection rate of Back scintillator

An actual geometrical acceptance of the Back scintillator for β-particles of neutron beam decay has been determined by Geant4 simulations. (Detailed information about Geant4 model of BRAND-0 will be given in Appendix A.2.1). For this aim, $4 \cdot 10^8$ neutrons have been randomly distributed in the volume of 10 cm $\times$ 10 cm $\times$ 90 cm, located in the center of the model of the decay chamber. Neutrons were let to undergo a β-decay. Fig. 3.19 left panel shows the resulting raw energy distribution of the Back scintillator and number of registered electron tracks, N_β^{geom} = 620000. Those electrons were produced in neutron decay, have traversed the decay chamber window, entered the tracker and were detected in the Back Scintillator. The ratio of $N_\beta^{geom}/(4 \cdot 10^8)$ is the energy integrated geometrical acceptance, A_β^{geom}, of the tracker + Back scintillator for the β-particles originating from cold neutron beam present in the decay chamber of BRAND :

$$A_\beta^{geom} = 620000/(4 \cdot 10^8) = 0.00155 \tag{3.9}$$

It is assumed here that the tracker and the Back scintillator detection efficiency are equal to 100 % what is justified for this kind of simulations.

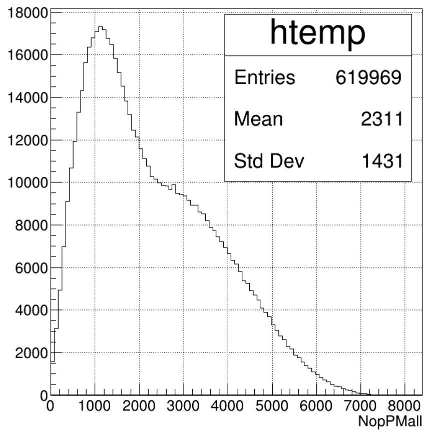

Figure 3.19 Simulated raw energy spectrum (in arbitrary units) collected in PMTs of the Back scintillator for the β-particles emitted in decay of neutron beam in the decay chamber of BRAND-0. The indicated event count is utilized to compute the experimental acceptance of the Back scintillator and tracker system for the simulated process.

Multiplying the R_β^{DC} (eq. 3.8) by the geometrical acceptance A_β^{geom} the expected detection rate of β-particles in the Back Scinillator, R_β^{BS}, is obtained:

$R_\beta^{BS} = 16.7 \cdot s^{-1}$

Taking into account uncertainties of the measured neutron flux and the unavoidable simplification of the Geant4 model the calculated β-particles rate in Back scintillator of BRAND-0 experiment is

$$R_\beta^{BS} = (17 \pm 5) \cdot s^{-1} \tag{3.10}$$

The problems of the sources and event rates of the experimental background will be addressed in chapter 7.

Beam polarization

The beam polarization during the BRAND-0 experiment was measured before the data collection using the established methodology and equipment at ILL, Grenoble. The results of the neutron beam polarization are presented in fig. 3.20.

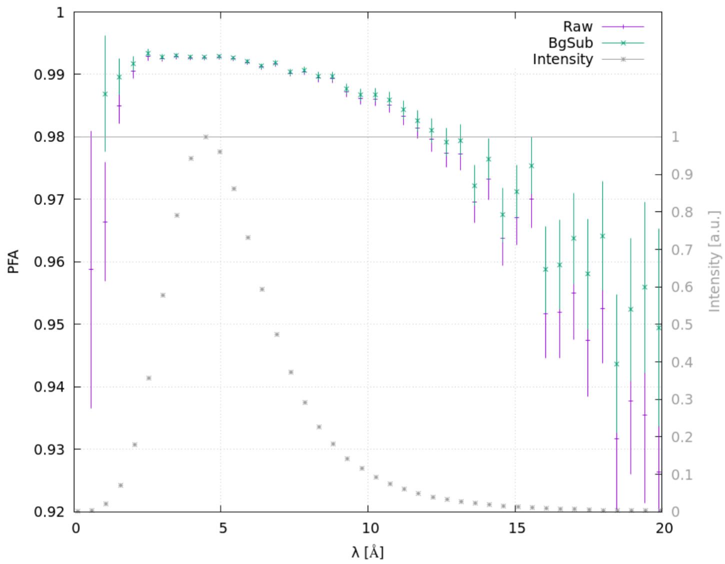

Figure 3.20 Raw and background corrected neutron beam polarisation during BRAND-0 experiment. Grey points provide reference distribution of beam spectrum. Reprinted courtesy of T. Soldner (ILL).

For the dominant part of neutron spectrum (grey points in fig. 3.20) the background corrected beam polarization (PFA, green points) is of the order of 0.992.

Chapter 4

Development of the setup components

This chapter is intended as an extension of the previous one, in order to provide more information about development of those components of BRAND-0 setup, which were done at IFJ PAN and demanded extended efforts and large time consuming tests. Development and optimisation of the MWDC and vacuum window of the decay chamber will be described.

4.1 Construction and optimization of MWDC

The detectors forming the Mott polarimeter are Back scintillator, two Mott detectors and MWDC. They are used to register electrons from neutron β-decay. The electron energy of interest ranges from $\sim$100 keV to 782 keV. The energy demanded to create one optical phonon in the scintillating material used for BRAND-0 scintillators is lower than 4 eV. Thus, even for electrons of the lowest energy the dozens of thousands optical photons will be created in the scintillaors. Taking into account the light quenching and all possible photon losses the expected efficiency of the scintillators remains still very close to 100%.

It is not a case for the MWDC. The helium gas of a low mass and low charge of its atoms is selected as the base for gas mixture of the tracker. Helium-based low-mass gas mixtures are well known for their low scattering properties and relatively long drift time which makes them one of the best options for MWDC when detection of low energy particles is planned. [57]. In this way the angular straggling of detected β-particles is minimized. But due to relatively high ionization potential of helium (average energy needed for ion-electron creation, W = 41.3 eV) and low density of electrons in the gas medium the number of electrons from primary ionization is low. Thus, it is important to create most favorite conditions inside a gas volume, to minimize the electron recombination, assure effective secondary ionization and permit electron multiplication sufficient to induce the anode signals of detectable amplitude. The working conditions (electric field, composition of gas mixture, rate of gas flow) have to be chosen in a way that ensures a high detection efficiency across the entire volume of the detector.

The possible deficiencies in detector construction, poisoning of gas mixture with electronegative dopants or wrong balancing of working conditions may significantly reduce the detection efficiency or create working instabilities (discharges) already before demanded detection efficiency is attained.

For these reasons the design, construction and assembly process of the MWDC have to be very careful. After construction of detector the most optimal working conditions need to be established by the tests.

4.1.1 Assembling of MWDC

The BRAND-0 tracker is build as a stack of PCB-boards. The anode (signal) and cathode (field) wires are soldered to pads on PCBs. During soldering of signal and field wires the optimal tension forces was applied. They were selected experimentally, to avoid breaking of the wires but provide sufficient tension eliminating any sag or displacement of the wires. Selecting of the proper force was especially important and difficult for very delicate and brickle signal wires. Finally, the signal wires were stretched with 47 g before soldering and the weight applied to field wires was 98 g. Wires have been soldered with the help of transferring frames, permitting positioning and soldering of the wires on the pads of PCB-boards with precision better than 0.3 mm.

Before installation, the selection of the PCB-components for their reliability was done. The soldering of wires and other components was performed with great care. It was followed by cleaning of the signal and field layers with alcohol in order to remove from their surfaces any dirt and remaining rosin.

The assembly of the whole Mott polarimeter has been performed inside a cleanroom with continues vertical flow of filtered air (from top to bottom) and with preserving strict demands of cleanliness.

4.1.2 Optimization of working conditions

Long time has been spend to select and optimize the best operation parameters of tracker. The aim was to attain a long-lasting, discharge-free stability of all layers of MWDC together with their high detection efficiency, under illumination with electrons at the rate similar to that expected during experiment at ILL. Radioactive β-source of ^{90}Sr and electron conversion source of ^{207}Bi (where electrons constitute only less than 10% among dominating γ radiation) have been used for this purpose. Detection efficiency has been measured by counting the hit numbers of individual layers of tracker. Counting was performed independently for signals devoted for drift-time measurement (for track position in XY-plane) and for signals used for charge-division method (track position in XZ-plane). The leakage current has been continuously monitored.

In multi-wire drift chambers, without perfect electrical separation of neighboring cells, the gas amplification of a specific sense wire depends on its neighborhood. In order to attain

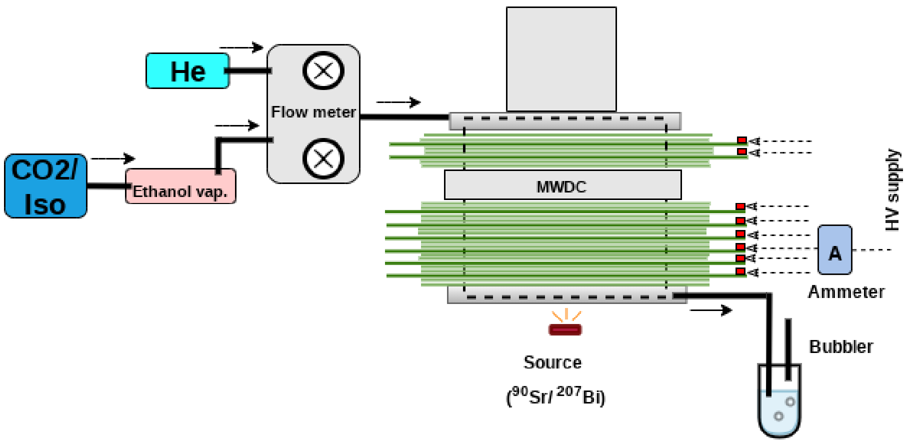

Figure 4.1 Gas flow system used for optimization of working conditions of MWDC and also during experimental runs of BRAND. For details see text.

the same signal height from the side cells and the cells closer to the chamber interior, different voltages have to be applied. This effect have been easily compensated for the whole layer, since each layer was on separate high voltage (HV). But for side wires in a single layer, from practical reasons, such voltage tuning was done only for the most extreme cells. Thus some indication of not perfectly adjusted voltages for some cells was still visible. For the optimal settings the difference between the highest and lowest voltage was about 140 V.

4.1.3 Selection of the gas mixture

Helium alone is not able to assure efficient and stable operation of drift chamber. Admixture of gasses of lower ionization potential and more complicated molecular structure is needed. Their presence increases both, the primary and secondary ionization. On the other hand, those admixtures act as a quenchers absorbing undesired ultra-violet photons, created abundantly during avalanche multiplication of electrons close to anode wire, where the electric field is the highest.

Hence, for the ultimate BRAND setup, the admixture of helium with isobutane (iso-C_4H_{10}) is considered. Another option of the quencher is the carbon dioxide (CO_2). Helium based mixtures with various proportions of these two dopants have been tested with the prototype tracker in order to provide information about their usability, both at present and also at the future stages of the experiment. Additionally, to ensure long-term stability of the tracker, a small amount of alcohol vapor (C_2H_5OH) was introduced to the gas mixture.

Fig. 4.1 presents the scheme of the gas flow system used both for mixture optimization as well as in regular experiments. A two-channel analog gas flow regulator permitting the mixture composition with precision better than 1% was used. At the detector gas outlet, a gas bubbler filled with a silicon oil was installed. It permits a fast control of gas flow and assures a small overpressure inside the tracker ($\sim$ 0.3 mbar).

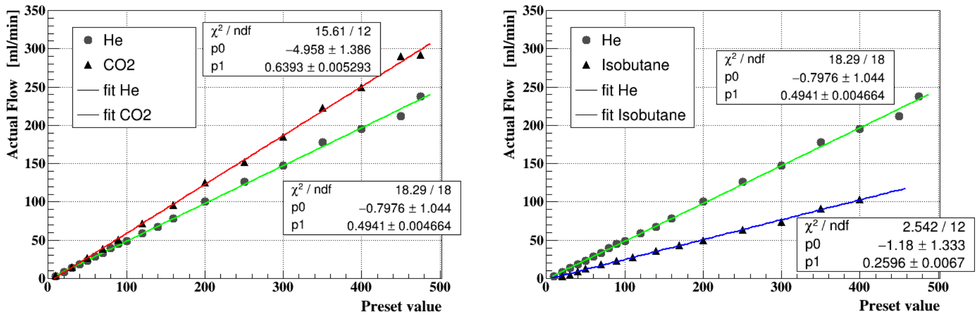

Figure 4.2 Calibration curves of the used flow meters for helium, carbon dioxide and isobutane.

Both channels of a flow meter had to be calibrated for various gasses of use. As presented in fig. 4.2 the calibration curves for gasses of interest in this work are well linear in the whole ranges of the flow regulators.

Three kinds of gas mixtures have been tested:

1. He/CO_2;
2. He/C_4H_{10};
3. He/C_4H_{10} premixed at 97% of helium and 3% of isobutane.

For each of them, different proportions of helium and quencher or ethanol vapors were tested.

The ethanol has been dosed by means of gas bubbling trough the liquid alcohol at normal temperature, as shown in fig. 4.1.

The results are presented in the form of plots and histograms - see figs. 4.3, 4.4, 4.5. In the left panels the dependencies of measured leakage current (I) of one selected layer (always the same) on the applied voltage is shown. With the constant illumination of the detector with the radioactive sources the voltages were increased and the current of the layer was observed. The region of a strong rise of the current was determined as the limit of applicable HV for this mixture. The actual working voltage has been kept at least 20 V lower than the this limit. Indicated in the figures a fraction of alcohol vapours admixed to the gas does not show actual percentage of alcohol in the mixture but informs, which fraction of the gas was bubbled through the ethanol.

For the fast estimation of detection efficiency at given conditions, the plots of hit multiplicities were used (shown in right panels of figs. 4.3, 4.4, 4.5). They have been measured separately for signals providing the drift-time information, charge information and their logical AND conjunction. Since the charge-division method requires the coincidence of signals from both ends of wire, it always performed worse than that for the drift-time measurement. The forth subplot - lower-right, permits to calculate the detection efficiency of individual layers and of whole tracker. Bins from 1 to 8 contain the hit rates (for drift-time signals) for the individual layers. Efficiency of individual layer is a ratio of its rate and the reference rate of bin 9. The counts of reference bin 9 are accepted only if coincidence between the Back scintillator and at least two layers of tracker took place. These layers must be either among the first two (layer 1 or layer 2) and the last two (layer 7 or layer 8):

Back scintillator **AND** (L1 **OR** L2) **AND** (L7 **OR** L8)

Such coincidences are most likely to indicate the actual electron trajectory within the tracker.

This method does not allow a strict calculation of efficiency but it is biased with only small uncertainty. It permits a fast estimation of detection efficiency and instant control of its variation.

Shown here reference plots of hit multiplicities are selected for such conditions, when the long-term working stability of the whole MWDC was obtained.

He/CO_2

Various proportions of He/CO_2 were tested. The example in fig. 4.3 is given for cases when He/CO_2 was 83%/17% and 85%/15%. In both cases also the vapours of ethanol were added via bubbling with CO_2 gas.

The latter mixture shown the best efficiency among ones of He with CO_2. The hit multiplicity and efficiency plots as described above are presented in right panel of figure 4.3. The detection efficiencies for β-electrons of individual layers of tracker calculated from subplot no 4 are in the range of 83% (L2) to 95% (L7). Hit mutiplicities for drift-time branch are of 6-8, whereas for charge-division method they are of 5-7.

Also a long-term stability of detector with He/CO_2 of 85%/15% proportion and with ethanol vapours was quite decent, but only for moderate particle rates of up to 500 Hz.

For higher detector load (1 kHz), the frequent breakdowns have been realized which caused the trip of single or multiple HV channels.

He/C_4H_{10}

Much better detector performance was achieved when isobutane was added to helium as a quencher. This can be attributed to much more complicated molecular structure of isobutane as compared to CO_2. As it is shown in fig. 4.4, the leakage current rise is slow in broad range of voltages. The critical value of HV, where electron multiplication starts a fast increase is well defined. The pure helium with some amount of alcohol have been tested as well (yellow graph), but, as expected, the stable working point of tracker with this mixture could not be attained. The best optimal behaviour of the tracker (high detection efficiency, stable operation over long time with high detector load) was obtained for 96.5% of helium with 3.5% of isobutane and alcohol. As it is presented in the right pannel of fig. 4.4, with this mixture the detection efficiency of all layers was higher than 95% and hit mutiplicities are high: 7-8 for "drift-time" signals and 6-8 for "charge" signals.

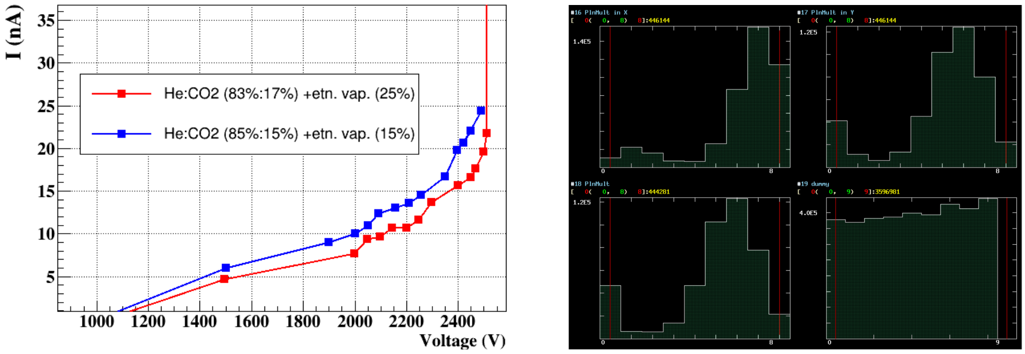

Figure 4.3 Test of tracker performance for He/CO_2 gas mixture. Left panel: dependence of a leakage current on the high voltage supplied to the anodes for a selected mixtures of helium and CO_2. In both cases the vapours of ethanol have been added as well. Percentage indicated for ethanol tells which fraction of the gas was bubbled through the alcohol. Right panel: hit multiplicities and efficiency plots obtained for the best optional mixture of 85%/15% + ethanol, and at the maximal possible supply voltage. Upper left: hit multiplicity for drift-time measurement; upper right: the same for charge asymmetry measurement; lower left: product of previous two done event-by-event; lower right: efficiencies of the individual layers (bin 1-8). See text for explanation.

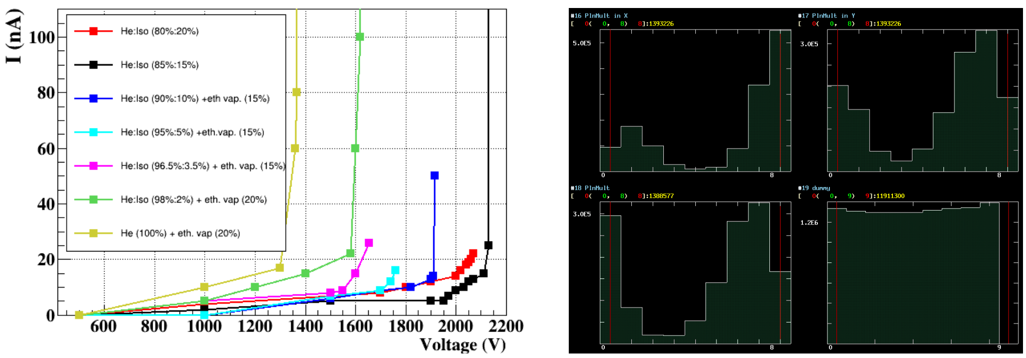

Figure 4.4 The same as in fig. 4.3 but for various proportions of He/C_4H_{10}. Plots in right panel are obtained for He/C_4H_{10} of 96.5%/3.5% and with trace amount of ethanol vapours.

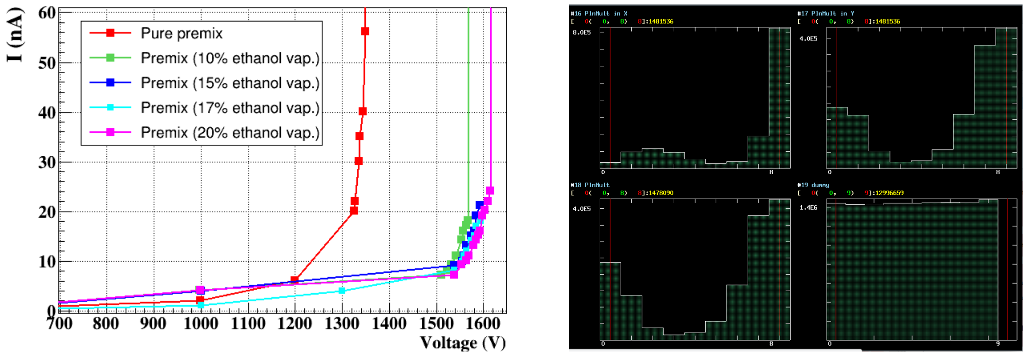

Figure 4.5 The same as in fig. 4.3 but for premixed composition of He/C_4H_{10} of of 97%/3% Various mixtures differ only by amount of ethanol. Plots in right panel are obtained for He/C_4H_{10} of 97%/3% and with ethanol vapours carried by 17% of the gas.

Premixed He/C_4H_{10}

3.5% of C_4H_{10} in a mixture is very close to the maximal amount of C_4H_{10} in the air which can be considered as non-flammable (3%). In order to comply with strict safety rules at ILL, the already premixed He/C_4H_{10} of 97%/3% have been purchased and tested in the IFJ PAN detector laboratory for its performance.

The I-V characteristics obtained for different amounts of doped ethanol are shown in fig. 4.5. This study shows a critical role of even small admixture of ethanol. When it is absent the onset of critical electron-multiplication appears at much lower voltage. The best operation of the tracker was determined for the case when 17% of the gas mixture was let to flow through the alcohol. For this condition the relative amount of alcohol can be estimated to about 0.8%. As presented in right panel, the obtained hit multiplicities peaked at 8 for both kinds of signals and detection efficiencies are very high - close to 100%.

Although the premixed He/isobutane of 97%/3% with 17% gas flow through the ethanol was selected as the best gas medium for BRAND-0 experiment, finally it could not be used due to organizational issues at ILL. Unfortunately, the experiment had to be performed with much less efficient and less stable gas mixture of He/CO_2 (85%:15%) + ethanol vapor (15%).

Nevertheless, the performed studies of performance of BRAND-0 prototype MWDC and its dependence on the selected gas medium are important contribution to development of the further versions of tracking detectors for BRAND project. Identified as the lightest yet highly effective mixture, a combination of 97% helium and 3% isobutane, along with ethanol, can be employed in future BRAND trackers.

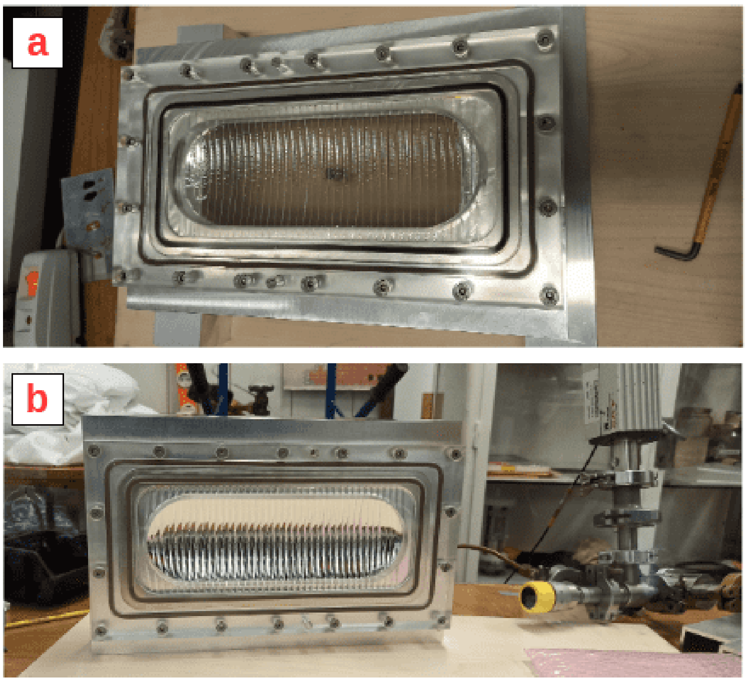

Figure 4.6 Test setup for development of vacuum windows for BRAND-0 decay chamber: foils under pressure: [a] Toray foil (thickness 4.5 μm); [b] aluminum coated Mylar foil (thickness 6 μm)

4.2 Development of decay chamber window

In the BRAND-0 setup, electrons from β-decay of neutrons are registered in the Mott polarimeter which is situated outside the vacuum chamber. In order to reach the Mott polarimeter they have to leave the decay chamber via the vacuum window. In optimal case the shape and dimension of this window should not restrict the emission solid angle for β-particles defined by the shape, dimension and position of Back scintillator. This would impose a large area of vacuum window of the decay chamber.

The development of such window, which is mechanically able to withstand the pressure of 1 bar, assures low difusion of air and helium into decay chamber and, at the same time, being sufficiently thin to diminish the angular and energy straggling of low-energy electrons was a crucial task. The confidence about durability of the window had to be high, since in case of sudden break of the window the delicate, ultra thin conversion foils of proton detectors, the tracker entrance window and the vacuum system of PF1B could be affected and even damaged.

The geometrical restrictions impose abandoning the idea of circular shape of the window, which would be mechanically optimal. Instead, the elongated shape with round ends and with lengths of Y- and Z-axis of 80 mm and 220 mm, respectively, was selected.

The idea was to develop a window of a thin foil reinforced with a Kevlar mesh. A mini-vacuum chamber was prepared to check performance of the possible solutions. The foils were

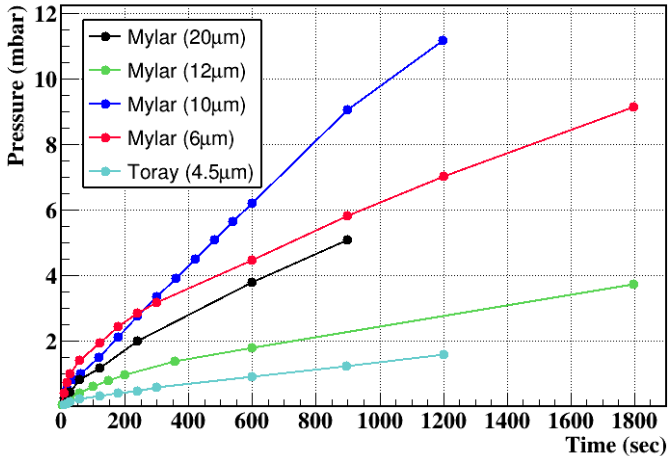

Figure 4.7 Test of vacuum tightness of Mylar and Toray windows of various thicknesses. Plot presents the pressure increase in the test chamber after pumping shut off. The best vacuum stability was observed for 4.5 μm thick Toray foil.

glued on a thin aluminum frame, whereas the Kevlar mesh of 0.3 mm diameter, twine-thread was woven and fixed on a separate frame. Both frames were fixed to the test chamber with a use of vacuum-tight O-rings pressed against a thick Plexiglass frame. The test setup is shown in fig. 4.6. Initially, the Kevlar mesh was woven in both directions (vertically and horizontally). Later it was realized that the shorter threads (vertical one) provide most of the necessary support and the presence of nodes is disadvantageous for the foil stability. Hence the longer threads (horizontal) were removed. The spacing between the vertical threads was optimized to 6 mm. With larger spacing of threads, the tendency to their breaking was observed. A similar mechanical endurance of the window was obtained when the distance between threads was increased to 10 mm. But then the mesh had to be made of double threads.

Foils of Toray and aluminized Mylar of different thicknesses were tested. The bare Toray film needed additional electricity conducting coating in order to avoid any possible buildup of charge on its surface during the experiment. For this aim a chemical of Clevios^{TM}, provided by Heraeus company [58] was used. This liquid was disposed on "vacuum side" of the foil an then dried in the oven at temperature of 120 °C.

During the test, the mini-vacuum chamber with the installed window was pumped down to the vacuum of about 10^{-4} mbar. Both the pumping time and a mechanical behavior of the window were controlled. After the pump was shut off the rate of vacuum deterioration in the chamber was observed. The results are presented in fig. 4.7.

In the laboratory tests, among all tested materials, the Toray foil of 4.5 μm thickness could keep the best vacuum in the chamber as compared to other foils. Windows made of this material shown also the long-lasting stability of performance. With continuous pumping and the vacuum level of 10^{-4} mbar in the chamber no any vacuum deterioration over 4 days was observed.

4.5 μm thick Toray window was selected for regular experiment. Astonishingly, in the real experimental conditions, such window caused fast deterioration of the vacuum in the BRAND decay chamber already after 4-5 hours of operation. Such effect was observed for 3 subsequently installed Toray windows. This regularity suggests a systematic effect, which was not present during laboratory test. It is likely that in presence of significant radiation, the electrostatic cladding on the foil was not sufficient to remove collected there charge. Thus, some mini punctures due to discharges could appeared what deteriorated the window tightness.

Finally, during data taking the 12 μm thick aluminized Mylar foil was used for decay window. With this window a 10 days trouble-less operation of decay chamber at demanded vacuum level was performed.

Besides the above described developments of the MWDC and vacuum window, the author of this work has prepared the Mott target and position calibration plates, and took part the in the design, construction and tests of the Mott compartments together with the driving system for the Mott target and position calibration plates.

Chapter 5

Methods of data analysis and calibrations

5.1 Reconstruction of particle trajectory in MWDC

The MWDC of the BRAND-0 setup permits 3D particle trajectory reconstruction through the application of two distinct track reconstruction methods. In the XY-plane, track position is derived from the drift-time information collected in a set of drift cells traversed by the particle. In XZ-plane the charge-division method is employed. For this reason, throughout this thesis frequently the XY-plane is referred to as "drift-time plane" and XZ-plane as "charge-division plane".

The following sections provide description of the principles and methodologies employed for the reconstruction of particle trajectories in the MWDC. The cells pattern of BRAND-0 tracker and their naming is explained in fig. 3.6.

5.1.1 Track reconstruction methods

The drift-time plane

Operation principles of drift chambers are well known and successfully utilized in many experiments. They undergone extensive studies and development since they were proposed as a tool in experimental physics. Information regarding the working principle of the drift chambers can be found e.g. in [59–61].

Charged particle passing through a gaseous medium ionize the atoms and gas molecules along its path. Considering the relativistic velocities of detected particles (in this case the electrons emitted in the β-decay), the ionization is assumed to occur instantaneously throughout the entire trajectory in the detection volume. At the same time particle is registered in any of fast detectors associated with the MWDC. Electrons generated in the ionization process undergo multiplication. They gradually migrate toward the positively charged centers of the drift chamber cells of the highest electric potential. Simultaneously, positive ions are drawn towards the grounded field wires (c.f. fig. 5.1).

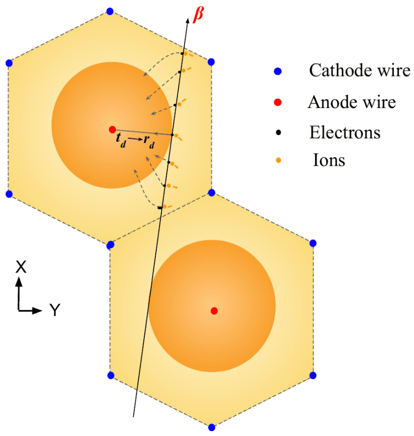

Figure 5.1 Illustration of operation principle of the drift cells in BRAND-0 tracker: When a relativistic charged particle traverses a drift chamber it induces ionization along its trajectory. Ion-electron pairs are generated. They drift in electric field towards their corresponding electrodes. Primary electrons interact with gas molecules inducing a secondary ionization. Close to the anode a fast electron multiplication process occurs due to the development of a Townsend avalanche. A detectable electric signal is created. The arrival time to anode of earliest clusters of electrons is measured as drift-time t_d. After time-position calibration the closest drift radius r_d can be established. The drift time of ions is typically 3 orders of magnitude larger than that of drifting electrons [62]. Information carried by them is disregarded.

A "hit" is defined as an occurrence of ionization within a single cell, resulting in a generation of an anode signal. For each hit the arrival time of first bunches of drifting electrons to the anode of individual cell is measured. The reference time is provided by fast external detector. In case of BRAND-0 it was realised by the Back or Mott scintillators. In this way the electron drift-times t_d for individual hits are measured and stored by DAQ system. Hits from different detector channels, associated with the same scintillator signal form an "event".

Positional calibration is conducted to establish the relationship between the t_d and the drift distance, r_d. This calibrated relationship is utilized for trajectory reconstruction in the drift-time plane. X- and Y- coordinates of trajectory are determined.

The charge-division plane

The third component (along Z-axis) for 3D trajectory, is determined from the hit position along the length of anode wire. The anode wires ($\phi = 25$ μm) are made of nickel-chromium alloy (8/2) distinguished by their high resistivity. It is about 66 times higher than for conventional copper wires of the same diameter. It is sufficient to observe the hit position dependent asymmetry in collected charge on both sides of the wire.

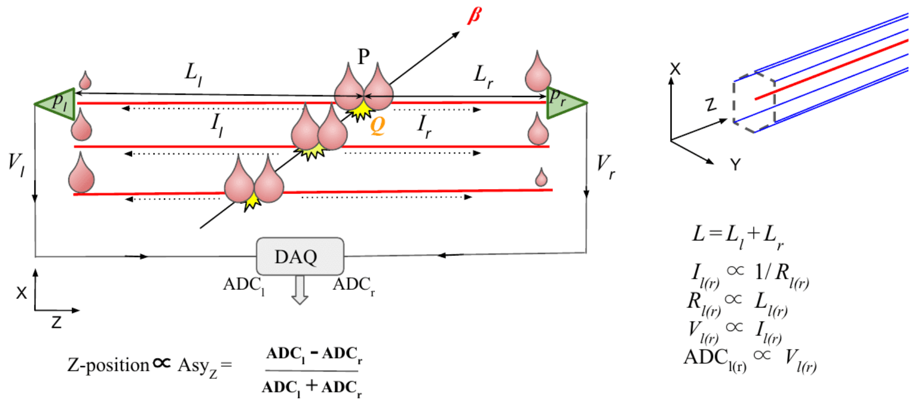

Figure 5.2 A simplified illustration of the idea behind the charge-division method. It uses the relation between the hit position along the wire length and the asymmetry of the charge collected at the two ends of the wire. At hit point P, the collected charge Q induces the currents flowing toward ends of the wires $I_{l(r)}$. They are inversely proportional to the resistances of the wire fractions to the right and to the left of the hit position, $R_{l(r)}$, and hence to their fractional lengths $L_{l(r)}$. Thus, connected at both wire ends the current preamplifiers generate the voltage signals, which are related to the length of respective wire fraction $L_{l(r)}$ and hence to the initial division of collected charge. The asymmetry Asy_z between these two quantities is utilized to determine the hit position in the XZ-plane.

The concept of the charge-division technique is illustrated in fig. 5.2. The total current I induced on the anode wire is proportional to the collected ionization charge Q. This current is split into currents flowing toward left and right side of the wires:

$$I = I_l + I_r \tag{5.1}$$

Currents experienced by the preamplifiers connected at both wire ends are inversely proportional to the respective resistances of the wire fraction, and thus to its length:

$$I_{l(r)} \propto 1/R_{l(r)} \propto 1/L_{l(r)} \tag{5.2}$$

The generated signals and recorded "ADC" values preserve the relation to the respective fraction of the wire length and hence to the initial division of collected charge:

$$\mathrm{ADC}_{\mathrm{l(r)}} \propto V_{l(r)} \propto L_{l(r)} \tag{5.3}$$

The asymmetry relations between ADC_l and ADC_r are further utilized to determine the hit position in the charge-division plane.

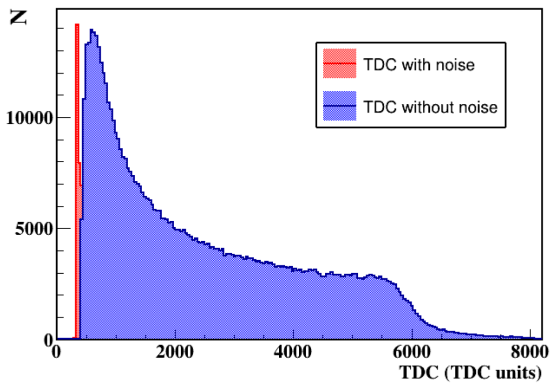

Figure 5.3 Typical drift-time spectrum (in TDC units) of a single cell of MWDC; (red) the raw spectrum; (blue) filtered from events of TDC < 420.

5.1.2 Preprocessing of raw data

Before proceeding with the analysis of the data obtained from the MWDC, their preprocessing was conducted in order to identify and remove any events present in raw data that exhibited significant deviations from the reasonable hit number or from monotonic shape of respective spectra. In general, the events of hit number lower than 3 and higher than 32 were disregarded. Only events triggered by the Back- and Mott scintillators were processed in the present analysis.

Inspection of raw spectra

In case of BRAND-0 only the time information are recorded. The multihit TDC modules (cf. sec. 3.2.4) are used for this aim. Nevertheless, information about amplitudes are derived from properly converted time signals. Thus, in the following both the TDC spectra of drift-times will be discussed as well as the signal amplitude spectra called here ADC_l and ADC_r for signal amplitudes detected on left and right side of the anode wires, respectively.

Figure 5.3 shows a typical drift-time spectrum of a single cell. For most of the cells a distinct sharp peak was present at the very beginning of the spectrum (approximately at TDC < 420), clearly correlated with the trigger pulse. This was most likely caused by insufficient delay of the analog signals compared to the trigger pulse. Signals from those peaks had to be removed. Unfortunately, with this operation the information about onset of drift-times and some part of spectrum was lost. Also from ADC spectra (cf. fig. 5.4) a small number of noisy events, typically occurring at $ADC_{l(r)} < 200$, needed to be removed from further analysis.

Amplitude spectra of some the most external cells exhibit additional noise as it is shown on fig. 5.5. In such cases in order to, at least, partially remove the undesired events, significantly higher cut-off threshold (1100 units) for spectra of each side of the wire was applied.

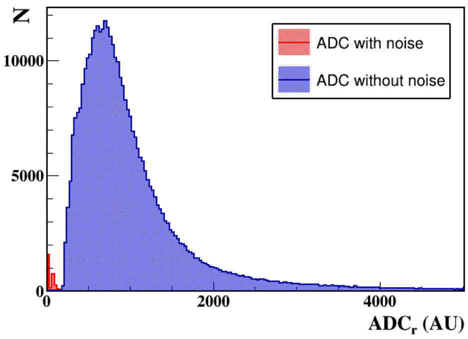

Figure 5.4 An example of amplitude spectrum recorded from right side of anode wire. Event filtering by removing signals of $ADC_r < 200$ have been applied.

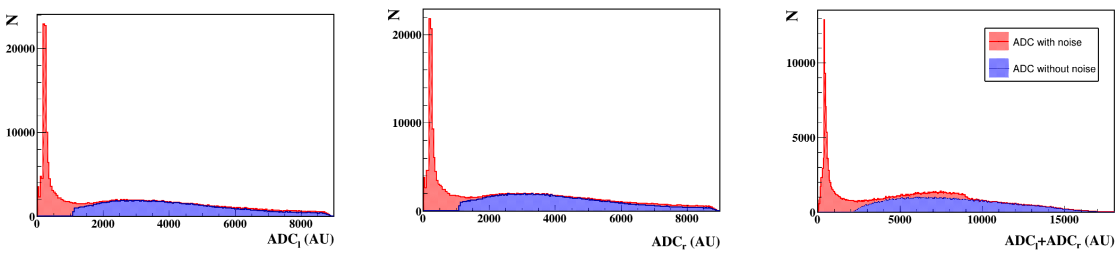

Figure 5.5 The ADC spectra of the outer cell (3,1) that experiences higher amplification due to partial shielding from neighboring cells. The left and middle distributions represent the ADC values obtained from the left and right sides of the wire, respectively. The rightmost distribution corresponds to the added spectra where event is only accepted when both side of ADC are above the threshold. To filter out noise for such cells, a high ADC cut-off threshold of 1100 units on each side of the wire was applied; (red) the raw spectrum; (blue) cleaned spectrum.

During the experiment an observation was made regarding the presence of additional noise in the drift-time spectra of the outer cells. Those cells are in close proximity to the Mott detectors. In fig. 5.6, examples of scatter plots of ADC vs. TDC for cell (2,11) are presented. It is noteworthy that the noisy pattern only emerges in the drift-time distribution when the events are trigger by Mott detectors. The only plausible explanation for the origin of this noise could be the interference of SiPMs used for light collection in Mott detectors with the electric circuitry of the drift cells. The outer cells, being important for tracking of Mott scattered electron tracks, are susceptible to the impact of such noise. This effects deteriorate the tracking resolution for those significant events. The spectra of inner cells did not show any harmful effect while being triggered by the Mott detectors.

It was found as well that for the cells (1,2), (7,5), (7,8), and (8,3) only one side of the ADC spectrum was recorded. As a result, these specific cells had to be deemed unusable and excluded from the reconstruction process. In effect the detection efficiency for XZ-plane has been decreased.

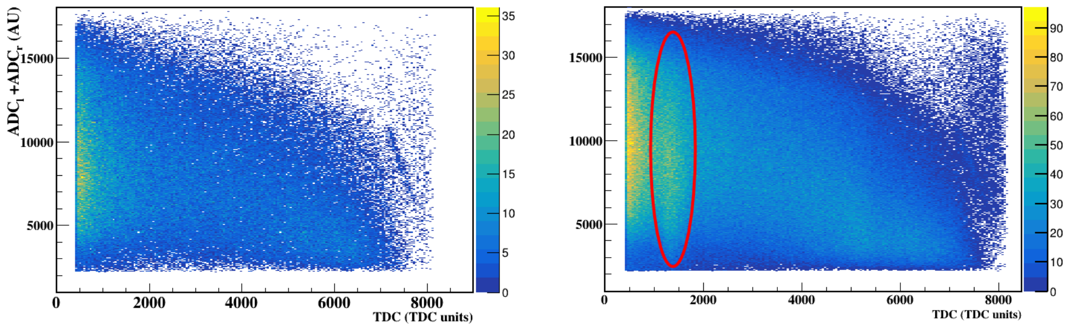

Figure 5.6 Correlation plot of ADC vs. TDC for cell (2,11). It shows the unexpected influence of the Mott_dets on the TDC spectra. Left panel: events triggered by the Back_scint; right panel: events collected in the same time period, but triggered by the Mott_det. The additional noise component in drift-time spectrum induced by Mott_dets is indicated with a red ellipse. Notably, the ADC spectra remained unaffected.

Topological track selection algorithm

In the BRAND experiment, identification of two classes of electron trajectories originating from decay of neutrons is of main interest:

- those which undergo back-scattering on the surface of the Mott target and form two tracks with a common vertex. They are called "Mott scattered electrons";
- those which are transmitted through the Mott target and are registered in the Back scintillator. They form one track trajectory and are called "direct electrons".

All other event classes contribute to the experimental background, which needs to be identified and suppressed from analyzed data.

For track identification and selection, a dedicated topological track-finding algorithm (TTFA) was developed. It relies entirely on the granularity of the MWDC. Individual hits of event are tested if they can form a linear trajectory. In this way a track candidates are identified and used in subsequent track-fitting procedures.

The main features of TTFA are listed below:

1. For each accepted event the matrix of cells (cf. fig. 3.6) is scanned along the layers searching for the hit. Scan starts from cell (1,1).
2. Found hits of the layer are checked for their spatial distance. If they are in direct neighborhood they are appointed to the same track. If not, they are appointed to different tracks.
3. The same is done in following layers, but the proximity to already identified hits is checked as well.
4. At the end of scanning procedure a few tracklets (parts of the tracks) are identified.

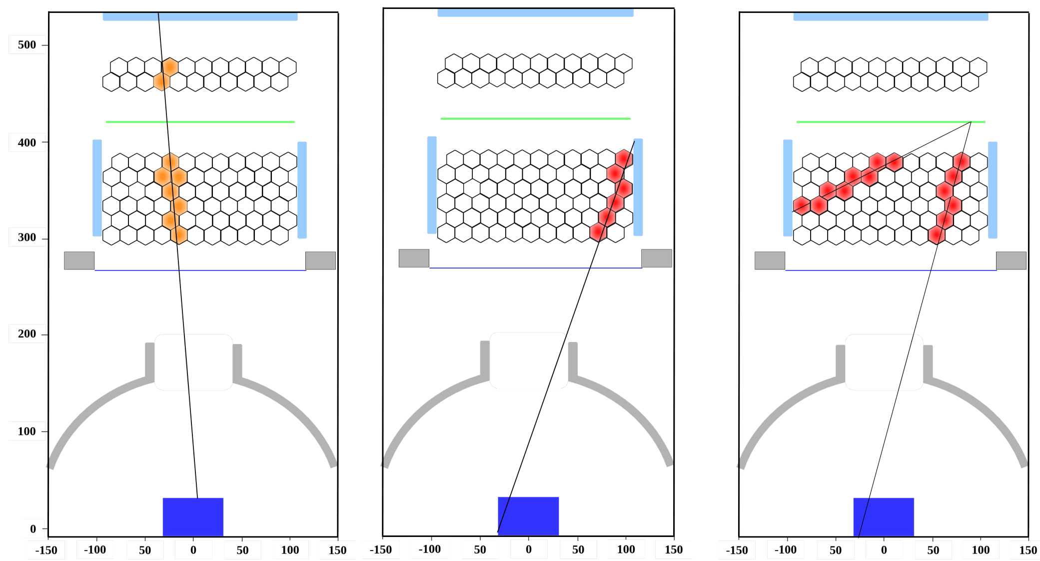

Figure 5.7 Illustration of a different cell patterns resulting from an electron propagating through the MWDC (black lines) and registered in one of the scintillators. The left and middle panels present the "direct track" registered in the Back_scint and Mott_det1, respectively. The track of Mott scattered electron "V-track" registered in Mott_det2 is shown in the right panel. Tracks originate from the core of the beam (blue area).

5. Linear alignment of tracklets is checked and they are appointed to form an individual track candidates. Only one-, two- and tree track candidates are allowed.

6. The worst track candidate is treated as noise or background and is not considered in further analysis.

7. In this way a one-track and two-track event candidates are selected. They are subject of track fitting procedure.

With full detection efficiency of all hit cells the algorithm operates efficiently and complete tracks are identified already after scanning procedure. Unfortunately many cell have reduced detection efficiency (due to lower efficiency of whole layer, damage of readout circuit, noise). Than, the algorithm can be misled, resulting in incorrect track selection. In such cases, the refinement of track identification is done during tracking procedure (cf. sec. 5.1.3).

5.1.3 Reconstruction of particle trajectory in drift-time plane

In this section the methods employed for fitting the trajectory of the particle will be explained. Problems related to the position calibration of a single cell will be addressed as well.

Fitting procedure in the drift-time (XY) plane

The drift cells provide the information that do not directly correspond to the actual coordinates of the hit position. Rather, they provide information about the coordinates of the firing wires and associated drift-times. To extract the actual (X, Y) hit coordinates from this data, a track-fitting procedure which uses the the drift-times information is needed. It encompasses two sequential steps called Pre-fit and Re-fit.

Pre-fit: This initial step involves the determination of a straight line, $L_d : y = a + bx$, which passes as close as possible to the centers of the hit cells belonging to the selected track. A least-squares fitting technique is used to minimize the function:

$$D_{\perp} = \sum_{i=1}^{\mathrm{N}} d_i, \tag{5.4}$$

where N is the number of firing cells and d_i is the distance of the center of drift cell (x_i, y_i) to the line L_d. The parameters of this line serve as the initial parametrization for the re-fit function. The equations involved in the minimization can be found in [63].

Although TTFA cleans the cells outlying the track, during the pre-fit still the test of misguided hits is done. If for any hit, $d_i >$ 10 mm (maximal distance within the cell from its center), this hit is removed from the track and pre-fit starts again.

Re-fit with "Minuite": Further optimization of the fitted track accounts for the measured drift-times and is performed using Minuit package from the root software [64]. The function to be minimized is:

$$\chi^2 = \frac{1}{\mathrm{N}-2} \sum_{i=1}^{\mathrm{N}} \left(\frac{\Delta_i}{\sigma_r} \right)^2 \tag{5.5}$$

where N is the number of accepted hits and Δ_i is the tracking residuum of i^{th} cell, defined as:

$$\Delta_i = d_i - r_i \tag{5.6}$$

In the above equation, r_i is the computed drift radius (see next subsection). The parameter σ_r is associated with the drift radius measurement. Its distribution along the cell radius is equivalent to the position resolution of the respective cell. Example of such distribution is is presented in fig. 5.11.

Similarly as for pre-fit the check for outlying hits is performed but with higher precision. Outlying cell is removed from further fitting when Δ_i exceeds 5 mm (half of the maximal distance in the cell).

After final re-fit the best fit parameter (a, b) are obtained. They define the determined trajectory of particle through the MWDC in XY-plane.

Calculated closest-approach points of the trajectory to the centers of the cells provide the coordinates used later for particle trajectory reconstruction in XZ-plane.

Position calibration The position calibration of a single cell in the drift-time plane involves establishing the relationship $r(t)$ between the drift-time t_d and drift radius r_d. The recorded drift-time spectra are used for this aim. Calibration process consists of two stages: initial calibration and its iterative tuning.

As a principle, the data used for $r(t)$ calibration should be collected when each cell of the tracker is uniformly irradiated. The best option is to perform a long lasting run with detection of cosmic muons. Due to time constrains such run was not possible prior or during the experiment. Instead, for the position calibration of tracker the selected data sets collected during neutron beam had to be used. Since both the window of MWDC as well as triggering scintillators are of large area, the stream of direct and scattered β-particles from neutron decay was uniform enough to obtain initial calibration in the drift-time plane.

- **Initial calibration**: The drift cells of the BARND-0 tracker have hexagonal shape defined by arrangement of the field wires. While this design offers advantages for tracking of low-energy particles, it also introduces some challenges for precision tracking. Due to the deviations from cylindrical symmetry and the lack of physical boundaries at the cell edges, the electric field there is not well defined. In effect the drift-time spectra are smeared and have extended tails at higher TDC values. This fact affects the accuracy of position measurements.

  For cells with cylindrical cross section, the shape of drift-time spectrum can be fitted with the empirical formula provided e.g. in [65]. Then, both the onset of the spectrum (t_0) as well as its limit at large values (t_{max}) can be precisely determined. For drift-times of BRAND-0 tracker fitting the function of [65] caused ambiguities in drift-time ranges. (Also missing the onset of the spectrum which needed to be cut off in data preprocessing - cf. sec 5.1.2 was adverse for this kind of fitting).

  Thus, for BRAND-0 data the upper ranges of drift-time spectra (t_{max}) of individual cells were selected arbitrary. After optimization it was found that the best calibration and position resolution is obtained when the drift-time spectra are cut at the time bin where the amplitude drops to 5% of maximal amplitude of the spectrum.

  After fixation of t_0 = 420 (in TDC unit - cf. 5.1.2) and t_{max} the commonly used method for establishing a $r(t)$ dependency was utilized. According to [66] and as explained in [46], the $r(t)$ is calculated by the following integration:

$$r(t) = \frac{R_{cell}}{N_{tot}} \int_{t_0}^{t} \frac{dn}{dt'} dt' \tag{5.7}$$

N_{tot} and R_{cell} represents the total number of tacks through the drift cell and the radius of the drift cell, respectively. Practically, the integration is replaced by summation of integer numbers of entries (Δn) in the discrete time bins, $dt^{'} \rightarrow \Delta t$.

The drift-time-to-radius relation, $r(t)$, was calculated for each individual cell. Analytical forms of these distributions have been obtained by application of TSpline class from the Root toolkit [67]. Example of such initial calibration function is shown in fig. 5.9.

- **Iterative procedure:**

  Tracking precision obtained with initial calibration $r(t)$ can be enhanced by an iterative procedure using the distributions of tracking residua calculated along the cell radius.

  The total drift-time range for each cell was divided into 57 bins of variable width. Widths were adjusted to assure sufficient statistics of events in each bin. For each bin the distribution of tracking residua was created. Gaussian fit to this distribution provided the mean value and the standard deviation used further as a local correction to the calibration.

  The iterative procedure involves the following steps:

  1. Using the calibration of previous step the tracks are fit.
  2. Distribution of reconstruction residua are built. Fig. 5.8 left panel shows the example of such distribution as a function of the drift-time obtained with the initial calibration. Deviation of the mean values of the residual distribution (Δ) from zero for almost whole drift-time range is clearly visible.
  3. Values of deviation are added as a correction to the calibration curve for respective bin of the drift-time.
  4. The corrected $r(t)$ curve was fitted using the "SmoothSuper" class from the Root toolkit [68] in order to obtain analytical form of the function. It was used as a new calibration in the next step of iteration.

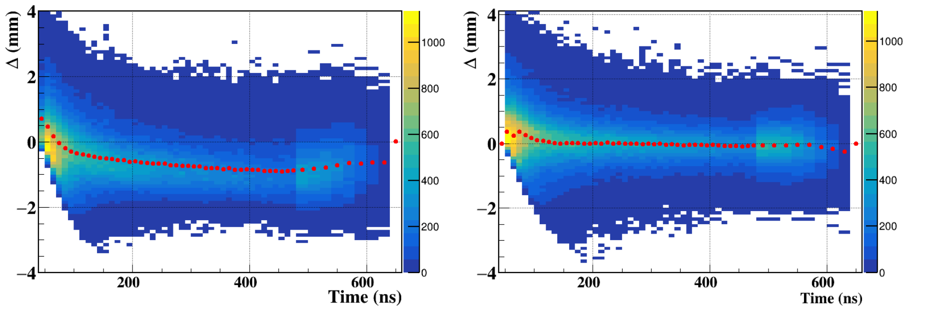

Figure 5.8 Distributions of the residua calculated for individual bins along drift-time range. Examples for cell (3,5). Red dots show the mean value of Gaussian fit applied for distribution in respective time bin. Left panel: obtained after performing initial calibration; right panel: final distribution achieved after 4 iteration of correction procedure.

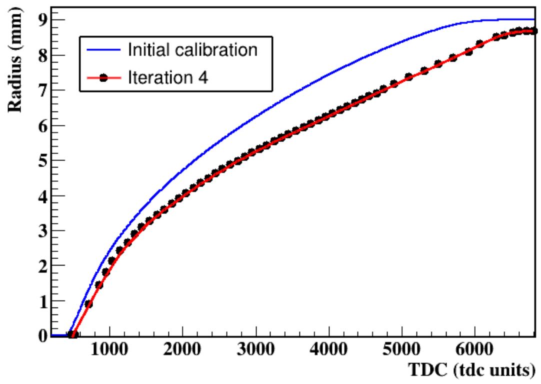

Figure 5.9 Initial (blue line) and final (red line) $r(t)$ calibration functions for the exemplary cell (3,5). The red line is the fit of the discrete histogram presented by black dots. For fitting the "SmoothSuper" class from the Root toolkit [68] was used.

The described procedure was repeated until no further improvement of residua distribution was observed. Conducting 3 to 4 iterations were usually sufficient to achieve a satisfactory calibration. Figure 5.8 right panel shows the example of residua distribution along drift-time obtained after the final iteration step. In presented case of cell (3,5) four iterations were performed.

Both initial and final drift-time to drift-distance relations are presented in fig. 5.9.

Tracking quality parameters: The tracking quality was assessed after each iteration step by examining the respective distribution of the χ^2 calculated for each track. Example is given in fig. 5.10. The tracking quality improves in each step of $r(t)$ correction. χ^2 distribution for the final iteration is peaked around 1, indicating a dominance of well reconstructed trajectories. Also some amount of tracks of large χ^2 value contribute. Events with such reconstructed trajectories should be treated with caution.

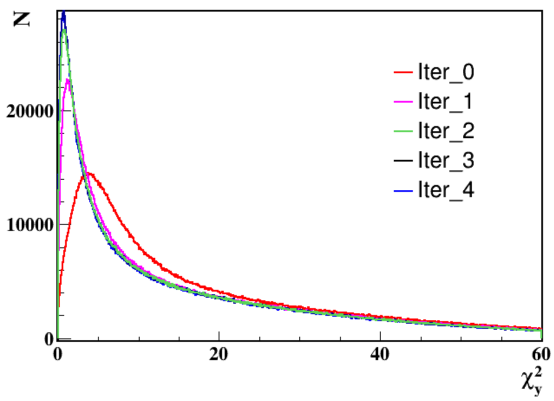

Figure 5.10 Distributions of χ_y^2 for the fitted trajectories in XY-plane calculated for subsequent iteration of $r(t)$ calibration. Continues improvement is observed. For the final iteration step (Iter_4) the χ_y^2 is peaked at 1, as expected for good tracking.

Reconstructed tracks of low quality are caused by:

- presence of Mott target which causes significant angular straggling for traversing electrons;
- noise misidentified as a hit still present in the data despite of data cleaning and application of TTFA;
- decreased efficiency of tracker due to use of not the most optimal gas mixture (cf. 4.1.3);
- partially- or totally nonfunctional readout of some cells.

To diminish the influence of doubtful tracks on the results of experiment the limits need to be applied on the acceptable range of χ_y^2 distributions. For this aim also the tracking resolution and tracking efficiency have to be taken into account.

To determine the optimal limit of the χ_y^2, the estimation was done with the assumption of 8-hit track and average 0.7 mm resolution of tracking (from initial estimation of resolution). With Δ = 2.1 mm (equivalent to 3 standard deviations of tracking resolution), it yields a χ_y^2 limit of 12 (eq. 5.5).

For events of χ_y^2<12 the tracking efficiency, $\eta_y(\Delta r)$, is calculated across the radius r for each cell. Δr are the selected segments across the cell radius. For each event, the cells expected to fire are defined by the fitted track parameters. Numbers of tracks traversing those cells are calculated separately for each bin of Δr, providing value of $N_{all,\Delta r}$. If the individual cell was actually hit and track was reconstructed within Δr, the number of $N_{fired,\Delta r}$ was incremented by 1.

Efficiency $\eta_{y,i}(\Delta r)$ for cell i and radius range Δr is given by equation:

$$\eta_{y,i}(\Delta r) = \frac{N_{fired,\Delta r}}{N_{all,\Delta r}} \tag{5.8}$$

The position resolution of individual cell, σ_y, is determined by analysis of residua distributions across the cell radius. For each Δr a standard deviation σ_y is taken from Gaussian fit. Figure 5.11 presents the example of tracking efficiency distribution (left panel) and position resolution (right panel) along the cell radius, for the selected events with $\chi_y^2 < 12$. Efficiency drop is realized close to anode wire (due to lack of initial part of the drift-time spectrum). Also approaching the edge of the cell the tracking efficiency significantly deteriorates.

If not stated otherwise, the limit of $\chi_y^2 < 12$ was used throughout the data analysis in this work.

5.1.4 Track reconstruction in charge-division plane

The principle of position measurement by charge-division method has already been explained in section 5.1.1. In the following the problems concerning the position calibration and implementation of charge-division into trajectory reconstruction will be addressed.

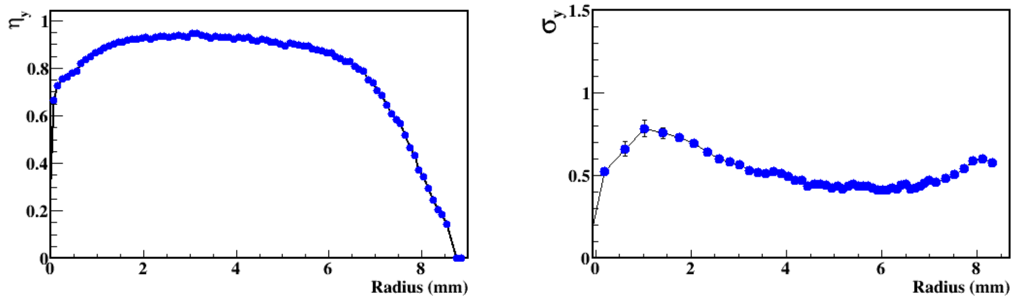

Figure 5.11 Distribution of tracking efficiency (η_y) (left panel) and position resolution (σ_y) (right panel) as a function of the distance to the sense wire for an exemplary cell. Only events with $\chi_y^2 < 12$ were taken for the calculations.

Trajectory fitting method in XZ-plane

Performed tests and analysis have shown that in BRAND-0 the trajectory reconstruction based on charge-division method is less accurate than those utilizing measurement of drift-times. Thus, in the analysis of experimental data only those hits which were accepted by the final tracking in the drift-time plane have been later used for the tracking in the charge-division plane. Besides this restriction the trajectory fitting in the XZ-plane follows a similar methodology as it was employed for the drift-time plane.

1. **Pre-fit**:

   A straight line $L_c : z = c + dx$ is fitted. $x = x_{i,L}$ are obtained from the drift-time reconstruction as a closest-approach points of the trajectory to the center of the cell. Values of z are extracted from the charge asymmetry-to-Z-position calibration (described later). In pre-fit the determination of initial fit parameters is done. They are used in the subsequent re-fit algorithm.

2. **Re-fit**: During iterative re-fit the track was fitted by minimizing the residual distribution using the "TMinuit" class [64]. Similarly as for XY-tracking also here the outlying hits were removed from the track. The limiting value of residuum was $\Delta < 30$ mm. After re-fit, the reconstructed track parameters c and d for XZ-plane have been determined.

Position calibration along anode wires

In order to extract position along a wire using the charge-division method, dedicated calibration procedure has to be applied. The calibration data for the Z-axis were collected during the experiment, using the ^{207}Bi source and two calibration plates with slits (as explained in fig. 5.12).

Two 3 mm thick aluminum plates, each with 3 slits cut perpendicular to orientation of wires were used. Width of each slit is 4 mm. Their position along Z-axis are centered around 0 mm, -60 mm and +60 mm. First plate was fixed at front of the tracker window. Second one was inserted into the tracker volume between planes 6 and 7. Plates and slits were positioned

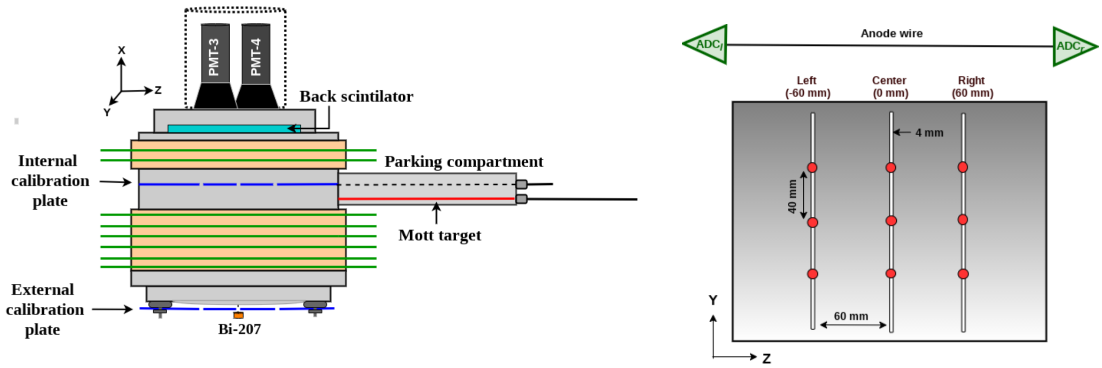

Figure 5.12 Setup arrangement for position calibration in Z-direction. ^{207}Bi electron source along with the two calibration plates were used. Each plate had 3 slits (each with width 4 mm and length 20 mm), cut perpendicularly to the orientation of the anode wires. Left panel: side view of the setup; right panel: 9 positions of the bismuth source (red spots) selected during calibration runs.

co-linearly. During the calibration runs, the Mott target was removed from tracker into the parking compartment.

A bismuth source was positioned at various places along the slits at the external calibration plate. In order to illuminate all wires in the tracker, 9 source positions were used during calibration runs (see right panel of fig. 5.12).

Gain balance of preamplifier pairs: Bismuth data collected when the source was positioned along the central slit were used to balance possible differences in preamplifier gains of both sides of each anode wire. For this aim the method described in [46] was adopted. It is illustrated in fig. 5.13. Ideally, if both preamplifiers had the same gain, the distribution of amplitudes measured left side and right side of anode wire, ADC_l vs. ADC_r, would exhibit symmetry along the line $\mathrm{ADC}_l = \mathrm{ADC}_r$. After fitting a straight line to the ridge of actual distribution, parameters p_0 and p_1 of the fit can be utilized for gain corrections of each pair i of preamplifiers:

$$\mathrm{ADC}_{r_{corr}} = p_{i,0} + p_{i,1}\mathrm{ADC}_r \tag{5.9}$$

For the fit the orthogonal distances regression (ODR), which minimizes residua along both axes was utilized.

Figure 5.13 displays the scatter plot of the amplitudes measured at left side and right side wire of cell (4,10). In left panel the collected distribution before any correction is shown. The ridge of distribution (white line) is displaced from expected orientation at 45° (red line). After correction the amplitudes measured on both sides of wire are balanced and ridge of ADC_l vs. ADC_r is oriented along 45° line.

After gain balance the asymmetry used to extract the hit position along Z-axis, $\mathrm{Asy_z}$ was calculated as:

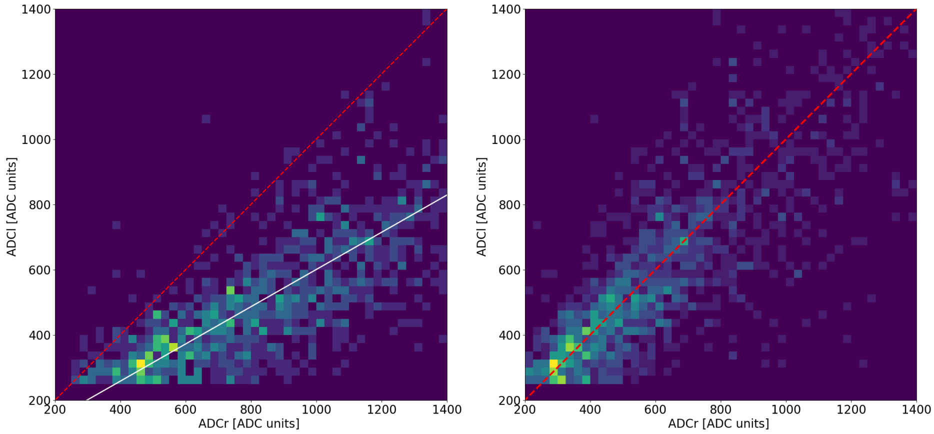

Figure 5.13 Left panel: scatter plot of amplitudes measured at left and right side of anode wire of the cell (4,10). For this cell one of the largely imbalanced gains on ADC signals were observed. Measurement was done when bismuth source was positioned at Z = 0 mm. The red dashed line indicates the expected $ADC_l = ADC_r$ relationship. The solid white line presents the actual orientation of ridge of the distribution. It was obtained by fit with the use of orthogonal distance regression (ODR). Right panel: Distribution corrected by means of obtained regression parameters. $ADC_l = ADC_r$ is achieved.

$$\mathrm{Asy_z} = \frac{\mathrm{ADC}_l - \mathrm{ADC}_{r,corr}}{\mathrm{ADC}_l + \mathrm{ADC}_{r,corr}} \tag{5.10}$$

Event selection with signal asymmetry of PMTs Fig. 5.14 presents the projection of the source on the Back_scint when placed at different positions on the external calibration plate. Only tracks, which are perpendicular to the wires provide information useful for position calibration. The inclined tracks have to be disregarded.

Selection of those tracks is supported with the information provided by the Back_scint. PMT3 and PMT4 are positioned parallel to the Z-axis, symmetrically around the center of Back_scint. Asymmetry, $\mathrm{Asy}_{PMT3,4}$, of their signals, ADC_{PMT3} and ADC_{PMT4} provides information about particle hit position on the surface of Back_scint along Z-axis. (Of course the gains of PMTs must be first properly balanced). $\mathrm{Asy}_{PMT3,4}$ is calculated according to formula:

$$\mathrm{Asy}_{PMT3,4} = \frac{\mathrm{ADC}_{PMT3} - \mathrm{ADC}_{PMT4}}{\mathrm{ADC}_{PMT3} + \mathrm{ADC}_{PMT4}} \tag{5.11}$$

Figure 5.15 presents the distributions of $\mathrm{Asy_{PMT3,4}}$ for the various positions of the source along Z-axis. The cuts applied in order to select only tracks perpendicular to Back_scint are indicated as red lines.

After event selection described above, the $\mathrm{Asy_z}$ distributions for charge-division calibration could be created. The examples for various source position are shown in fig. 5.16. It was realized that the resolution of asymmetry measurement is the best in the center of the wire and deteriorates along the wire towards its ends. The range of asymmetry is very

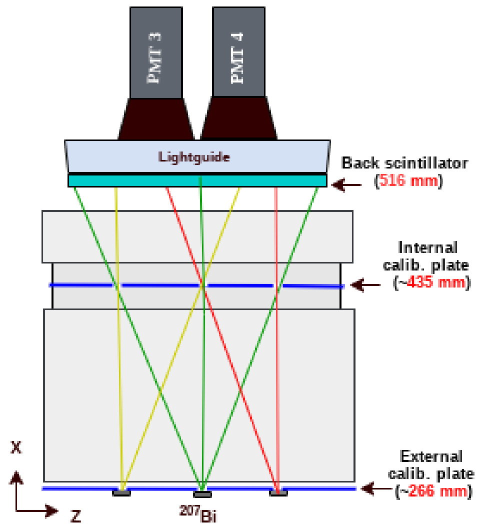

Figure 5.14 Projections of the ^{207}Bi source placed at different positions at the external calibration plate on the surface of Back_scint during position calibration runs for charge-division method. In addition to demanded perpendicular tracks registered in Back_scint also the inclined tracks penetrating through neighboring slits contribute to the spectra. In calibration the latter tracks are suppressed by cuts applied on the spectra of Back_scint.

much restricted. For the source positions of ± 60 mm (what is half of the wire length) the asymmetry vary only as ± 0.13. It indicates that the resistances of the signal readout circuits dominate over the resistance of anode wires. This is adverse effect. For such short dynamic range of measured $\mathrm{Asy_z}$ the position resolution must be damped.

Standard calibration Utilizing the calculated asymmetries for different Z-position of the source, a simple linear position calibration has been obtained. Fig. 5.17 shows the example of such calibration for the cell (4,6). A straight line was fitted and extrapolated to cover the whole expected range of asymmetry. The physical range of the wire (± 120 mm) is indicated. In linear calibration, for these extreme positions, the $\mathrm{Asy_z}$ should be of about ± 0.25. As it was already mentioned the actual resistive "length" of the anode is longer than the wire itself. The resistance of whole signal readout circuitry has to be added. From the observed range of asymmetry distribution it is clear that this component dominates the total resistance of anode. It should, however, be noticed that the decrease of detection efficiency near the end of the wire has to be accounted as well. It is due to geometrical constrains of Back_scint (which is of circular shape and 200 mm diameter).

However, as shown in right panel of fig. 5.17, where asymmetry measured for the whole length of wire is presented it extends beyond ± 0.25 and reaches ± 0.5. This distribution was measured with electrons from beam decay, without presence of calibration plates.

This observation may suggest that the function of position calibration along the wire is not linear. This hypothesis is examined in the following.

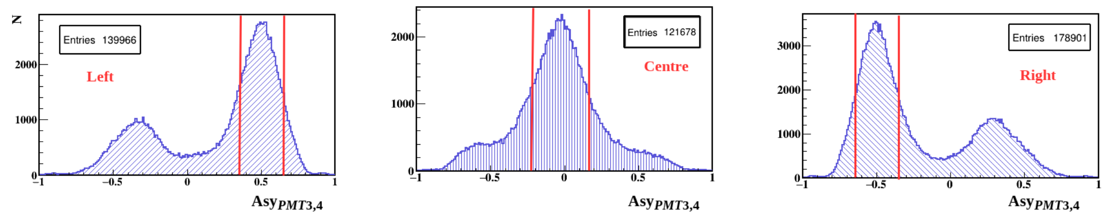

Figure 5.15 The asymmetry distributions between the signal amplitudes of PMT3 and PMT4 measured during Z-position calibration runs, respectively for left, central and right slit position of source at the outer calibration plate. The main peaks are from tracks perpendicular to the surface of Back_scint. Other components of the distributions are result of inclined tracks traversing the adjacent slits of the inner calibration plate. Selection cuts of events used for position calibration in charge-division method are indicated with red lines.

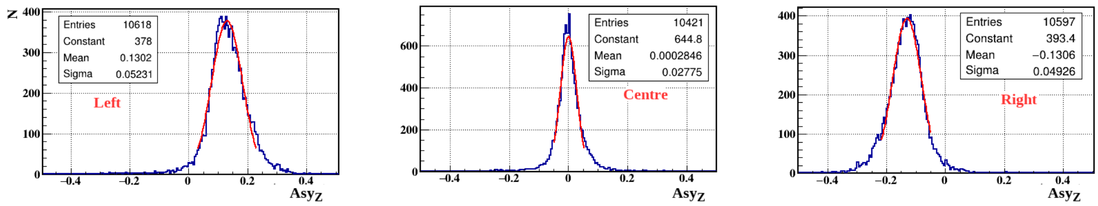

Figure 5.16 Examples of distribution of asymmetry Asy_Z calculated after selection of perpendicular tracks. Histograms in left, middle and right panels contain distribution collected when bismuth source was positioned at left, middle and right slit of external calibration plate, respectively.

Extension of calibration range Some extension of calibration range along the Z-direction is possible for wires of Layer 7 and 8. The geometry of calibration plates can be utilized for this aim as it is presented in fig. 5.18. For the central wire of layer 8 (cell (8,6)) the images of internal slits exposed to bismuth source localized at external slit are at Z = -75, -60, -15, 0, 15, 60, and 75 mm. Thus, four additional points for calibration are gained. Two of them extends more toward the end of the wire (± 75 mm) than for standard calibration of tracker (± 60 mm).

In such range of wire length the calibration remains linear. It is presented in fig. 5.19 left panel.

Even larger extension of calibration range is possible for central wires of most upper layer of tracker. For this aim data recorded during beam operation have been used. For track reconstruction of those events the selected anode wire of cell (8,6) is divided into 10 mm segments centred at Z = -83, -60, -40, -23, 0, 23, 40, 60 and 83 mm. More extended segments are not reasonable due to maximal radius of Back_scint and its round shape. Tracking was performed with layer 1 - 7 only and in Z-direction the standard calibration was assumed. If the calculated trajectory has fallen into any of the selected segments of cell (8,6), the corresponding experimental asymmetry have been calculated. Effect is shown in fig. 5.19 right panel.

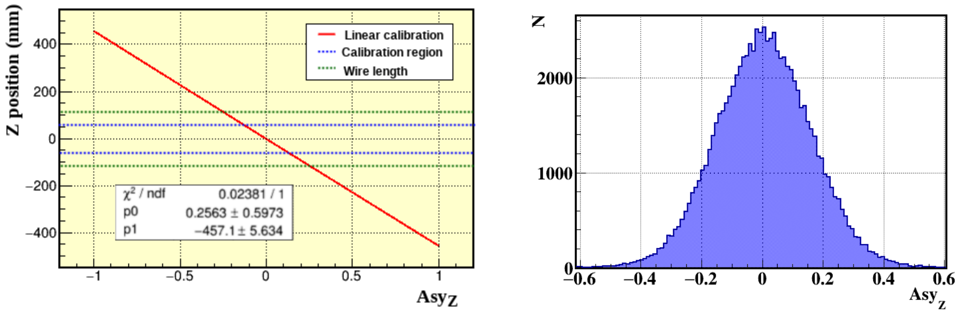

Figure 5.17 Left panel: simple linear Z-position calibration for cell (4,6) (red line). Blue lines indicate the length of the wire used for the position calibration while green line presents the limit of the physical length of the wire. Right panel: Asy_Z measured for the same cell but for beam data (without calibration plates). Asymmetry ranges in ±0.4 with extended tails

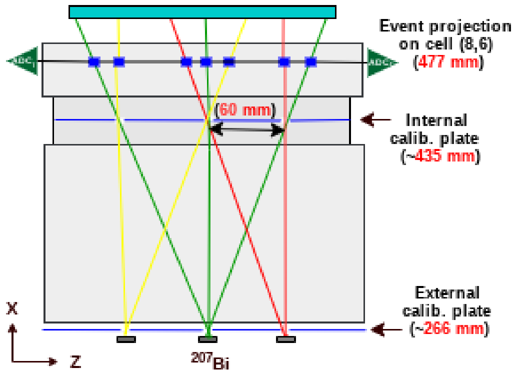

Figure 5.18 Utilization of geometrical alignment of calibration plates and radioactive source for extension of Z-position calibration range for central anode wire of layer 8, cell (8,6). Blue squares indicate points for which the charge asymmetry can be calculated. Calibration can be performed within ±75 mm range.

Also in this case no non-linearity of calibration curve is observed. Rather the tendency of calibration function to bend in reverse than expected direction is realized. Thus, also for the wire range of ±83 mm a non-linearity of calibration was not observed.

Test of non-linear calibration Performed checks indicated that in the range of Z=±83 mm the position calibration for anode wires is linear. More outer ranges of the wires are not accessible for sufficiently precise measurement of charge asymmetry. Nevertheless, the issue of possible non-linearity in Z-position calibration in outer regions of wires has been addressed. In view of lack of calibration points beyond Z = ±83 mm a shape of non linear function for the whole length of anode wires has been assumed. In fig. 5.20 left panel this function is plotted with red line. It provides smooth transition of linear range between Asy_Z = ±0.2 and the whole range of Asy_Z = ±1.

Initially assumed shape of calibration function was a subject of modification with iterative process of minimizing the tracking residua. It was tested for each cell of MWDC. The example

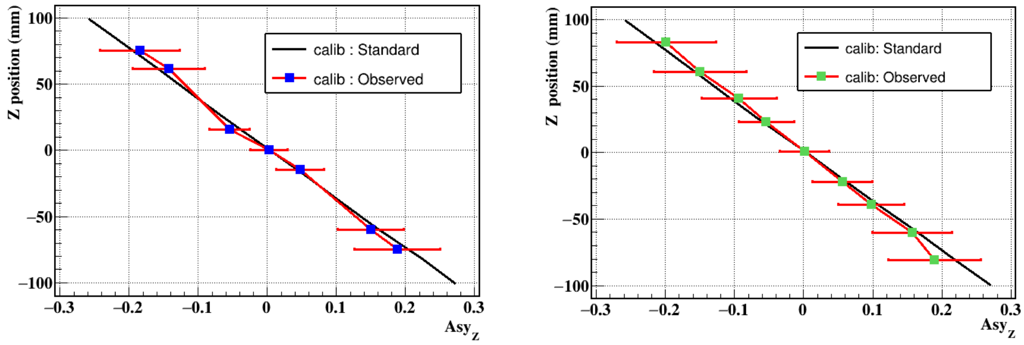

Figure 5.19 Position calibration along Z-direction for central wire of layer 8, cell (8,6). Calibration range was extended as compared to the standard calibration of tracker. Left panel: calibration range is extended to ±75 mm. Geometrical effect of alignment of calibration plates and radioactive source was utilized. Right panel: calibration range is extended to ±83 mm. Trajectories of electrons originating from the neutron beam and reconstructed with the help of planes 1 to 7, have been used to obtain this dependence.

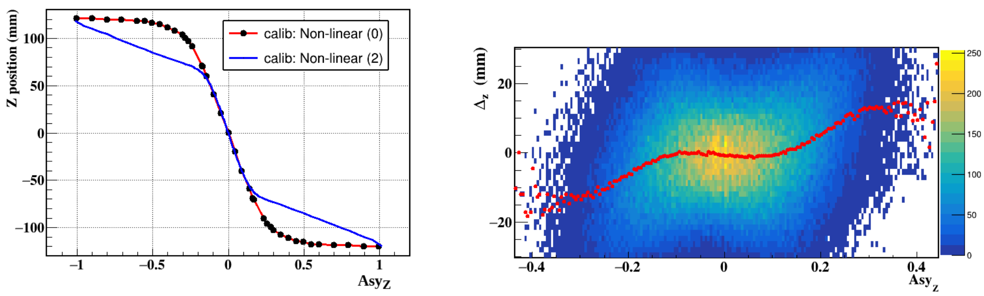

Figure 5.20 Left panel: assumed initial shape of non-linear Z-position calibration function (red line) extending beyond observed range of measured asymmetry $\mathrm{Asy_Z}$. This function was a subject of modification with iterative process of minimizing the tracking residua for each cell of MWDC. In effect the modified distribution plotted with blue line was obtained. Resulting curve is for sure not physical. Tracking performed with the use of this distribution lead to undesired deterioration of source position reconstruction. Right panel: example of distribution of tracking residua in XZ-plane used in iterative calibration for modification of the initial shape of calibration curve.

of distribution of residua as a function of signal charge asymmetry measured along the anode wires is shown in fig. 5.20 right panel. The distribution of residua in the charge-division method indicates significantly worse position resolution compared to the drift-time plane. Outside the central region of wire (-0.15 $< \mathrm{Asy_z} <$ 0.15) the residua are very large, up to $\sim \pm 15$ mm. This causes a small modification of calibration curve in the middle of the wire but very strong at outer part. In effect hits recorded in external part of wires during calibration process are artificially "shifted" toward center of the wire. Effect of such calibration can be observed in plots of fig. 5.21.

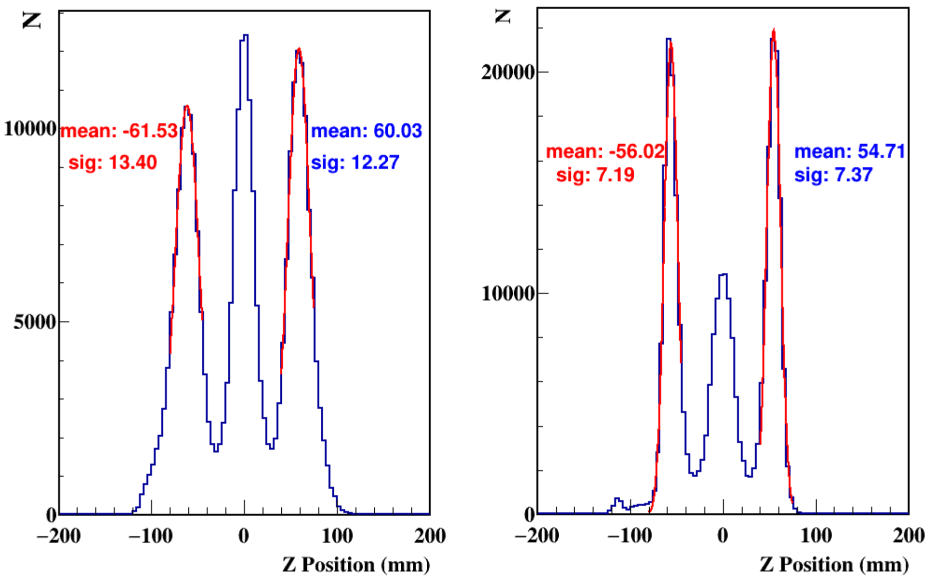

Figure 5.21 Reconstruction of the slits positions of internal calibration plate along Z-direction. Data collected for 2 positions of bismuth source at the external calibration plate Z = ± 60 mm (cf. fig. 5.12) are added. The presence of middle peak is a result of contribution from middle slit. Left panel: performed with initial shape of non-linear calibration. Reconstructed positions of the source are correct (means values about ± 60 mm) but the resolution is poor ($\sigma \sim 13$ mm); Right panel: reconstructed source position with non-linear calibration modified in iteration procedure. Visible is significant improvement of resolution of source reconstruction ($\sigma \sim 7$ mm) but on the expense of systematic shift of source position (mean values about ± 55 mm). Central peak remained unaffected (note different vertical scales). Described effect illustrates the failure of the iterative correction procedure applied for the non-linear calibration of charge-division method.

As a result of this analysis, it was concluded that solid information about position calibration in Z-direction currently can be obtained only for central part of the wire in Z ± 85 mm. In this range calibration is linear. Assumption about possible non-linearity of Z-position calibration in more outer regions of anode wires can not be verified. Due to limited dimension of the Back_scint (R = 100 mm) and its round shape, the event statistics close to wire end is small and shape of measured charge asymmetry is biased by geometry.

Hence, it was decide that in this work the track reconstruction in Z-direction will be performed using only linear calibration.

Control of tracking quality in charge-division plane

As presented in fig. 5.22 right panel (and also can be concluded from residua distribution of right panel of fig. 5.20) the position resolution in Z-direction is poor. For all cells the σ_z in the center of the wire is about 12-13 mm. It spoils towards wire ends and can reaches even 20 mm. In the left panel of fig. 5.22 the typical distribution of tracking efficiency along the wire length is presented. It is much worse than those derived for drift-time plane. Here it reaches 78% at maximum in the central part of the wire and decreases toward wire end.

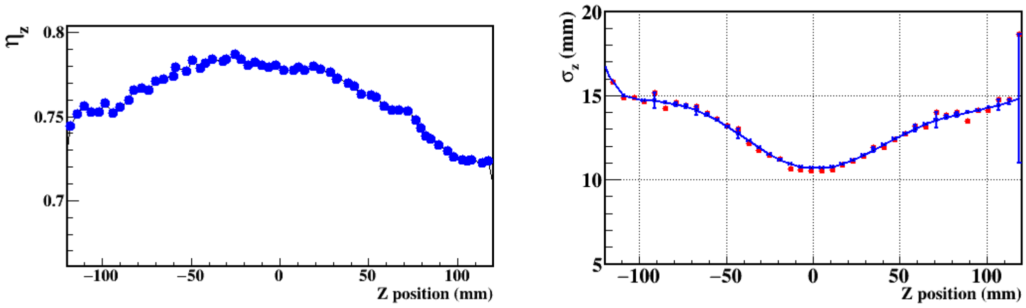

Figure 5.22 Examples of distributions for selected cell. Left panel: tracking efficiency along the wire length; right panel: position resolution (σ_z) along the wire length (red circles). For calculation of χ_z^2 the smoothing with the "SmoothLowess" function [69] was used (blue line).

The χ^2 distribution for tracking in XZ-plane is presented in fig. 5.23. The hits used for reconstruction in charge-division method were already approved in XY-tracking. Thus, the probability, that they belong to real events is high. For the standard quality tracking in XZ-direction the χ_z^2 limit was selected as 3. With such limit the tracks of lower quality from the tail of distribution are avoided.

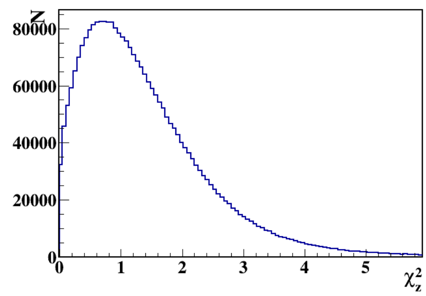

Figure 5.23 Distribution of χ_z^2 in the charge-division plane obtained by reconstruction of neutron beam data.

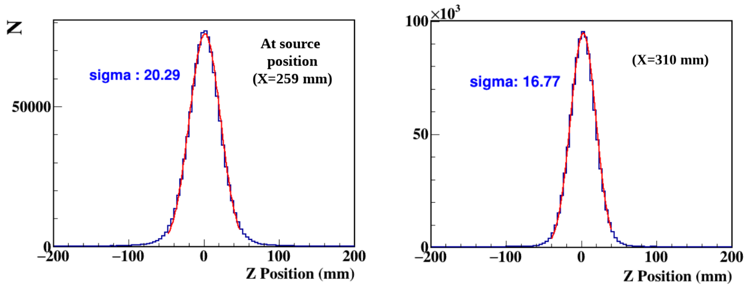

Figure 5.24 Reconstruction of the calibration source at its nominal X-position (left). For this study the inner calibration plate was removed. Even better focusing (narrower distribution along Z-coordinate) is obtained for X=310 mm, as presented in right panel. This was identified as one of the systematic effects of wrong determination of slope parameter for charge-division tracking method in BRAND-0 experiment.

Taking into account the lower efficiency associated with the charge division method, all events with $\chi_z^2 < 3$ are taken for reconstruction. This limit avoid the events from the extended tail.

Reconstruction of position of the calibration source with the charge-division method provided its nominal place (X = 259 mm). But astonishingly, as illustrated in fig. 5.24, its more sharp image (smaller σ) has been observed for other position (X = 310 mm). It may indicate at some systematic effect of the charge-division method used in the experiment. It consists in misidentification of the slope of a track in XZ-plane. As it will be shown later (c.f. sec. 5.2.2) in similar way affected is also the reconstructed position of the Mott target. Despite of undertaken efforts for understanding and elimination of this effect it could not be corrected in this analysis.

In conclusion of 3D-tracking reconstruction methods employed for MWDC of BRAND-0, it has to be written that this detector can be used for tracking of low energy electrons from the neutron decay. The tracking method based on the drift-time measurement and the r(t) calibration (XY-plane) provided satisfactory average position resolution of 0.6 mm. This result agrees with the expectation for this kind of the detector. The average single cell efficiency was of the order of 0.8, what needs to be improved. For this aim the front-end electronics must be modified in order to accept the whole range of the drift-time spectrum.

The results obtained with the charge-division method (XZ-plane) are of much worse quality. The single cell resolution ranges from 12 mm to 20 mm, depending on hit position along the wire.This indicate at a need of significant improvements. The average single cell efficiency for charge-division method, which is of 60% is clearly influenced by low quality of tracking in XZ-plane. A possible source of relatively low position resolution of this method will be addressed later in the next chapter.

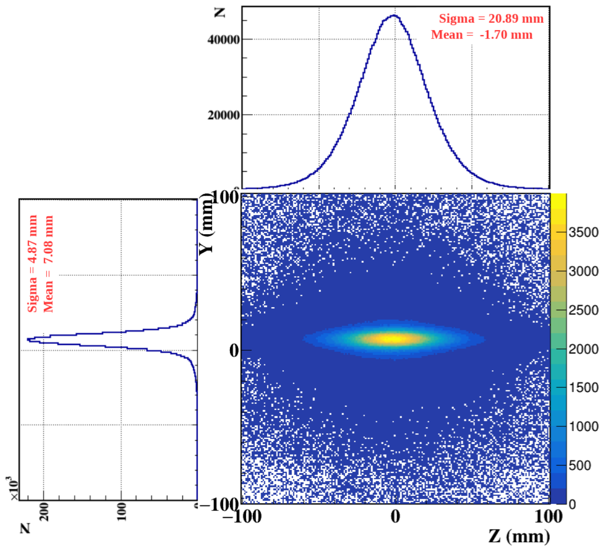

Figure 5.25 Distribution of the electrons from 207-Bi source reconstructed at the source position (the internal calibration plate was absent).

5.2 Single tracks in the Mott polarimeter

Single track events are by far the dominant kind of events collected in BRAND-0 experiment. They carry information about energy distribution of β-particles and asymmetry in β-emission. In the ultimate version of this experiment they can be used also for the studies and control of most of systematic effects. For these reasons the single track events have to be carefully identified and analyzed. It is also the case for current examination of BRAND-0 data. The example of single track event is shown in fig. 5.7, left panel.

5.2.1 Single tracks studies with ^{207}Bi radioactive source

Fig. 5.25 presents the reconstructed position of ^{207}Bi source of electrons registered in coincidence of the tracker and the Back_scint. The internal calibration plate was not present. The source has been placed at the center of the external calibration plate (X, Y, Z) = (259, 7, 0) mm. The spot of the source was of 5 mm diameter. Independent track reconstruction have been performed for XY-plane and XZ-plane. For tracking with the drift-time information, the reconstructed source position is satisfactory ($\sigma < 5$ mm), whereas the reconstruction in charge-division plane exhibits notably worse resolution ($\sigma \sim 21$ mm).

Another deficiencies in the performance of the tracker are well visible in fig. 5.26, presenting the distribution of electrons from ^{207}Bi source reconstructed at the surface of Back_scint. Destructive influence of missing readout channels of the cells closest to the Back_scint (in layer 7 and 8) is well identified. It results in the areas of low tracking efficiency around Y $\sim$ -30 mm and 60 mm. Finer strip-like pattern also along the Y-axis is caused by deterioration of tracking efficiency close to the centers and ends of the cells (cf. fig. 5.11).

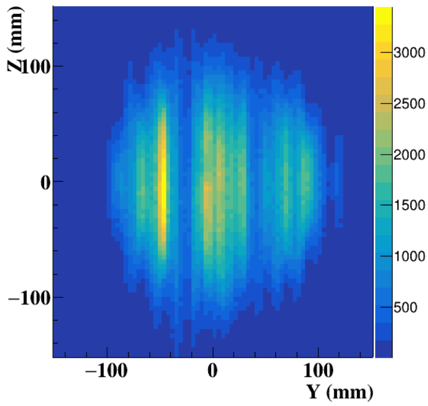

Figure 5.26 Distribution of electrons from ^{207}Bi source reconstructed at the surface of the Back_scint. A clear influence of not working channels for drift cells can be identified around Y∼30 and 60 mm. Furthermore, fine strip-like pattern along the Y-axis appeared due to the decreased efficiency close to the centers and at the end of the drift cells.

5.2.2 Track reconstruction for beam events

Features of track reconstruction observed for electrons emitted from the ^{207}Bi radioactive source can also be identified in the results of reconstruction of electrons emitted from the decay chamber during the beam operation. With the drift-time information, the reconstruction of the beam position and the decay chamber window is sufficiently precise (cf. fig. 5.27 left and right panel, respectively). It even allowed for the identification of a tiny displacement of reconstructed beam spot in Y-direction. Which about 10 mm in negative Y-direction. This effect can be explained as a combination of presence of the magnetic field, causing curvatures of the electron track inside the chamber and the displacement of the whole Mott polarimeter with respect to the vacuum chamber. Reconstructed image of the decay chamber window reproduces well both the shape and dimensions of the window. The image is quite sharp in Y-direction, whereas the poor resolution in XZ-plane is reflected in very fuzzy edges of the reconstructed window in Z-direction.

5.3 "V-tracks" in the Mott polarimeter

Detection of electrons back-scattered on the Mott target is the principal issue of the Mott polarimeter. Such events contain two tracks reconstructed both in in XY- and XZ-planes. In both projections, the tracks should cross in a common vertex, coinciding with the position of Mott target. In the following, this event topology will be referred to as "V-track". It is clear that V-tracks can be created also on other setup elements like MWDC walls, wires, gas mixture, scintillators, etc.. Another processes which shadow the searched for Mott scattering are elastic electron-electron interactions where, in output channel, two electrons propagate from one vertex (Møller scattering [70, 71]).

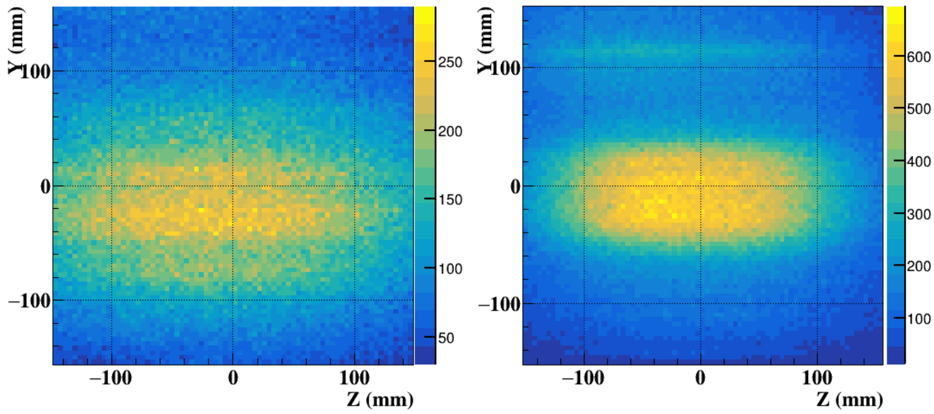

Figure 5.27 Reconstructed distribution of trajectories in the YZ-plane of particles emitted from the decay chamber when the neutron beam was on. Left panel: position track distribution reconstructed at the beam axis. Tiny shift in the beam position from 0 has been identified as the effect of the magnetic field and displacement of the Mott polarimeter. The fuzzy edges of the beam are due to scattering of electrons on the window frame, beam halo and presence of background events. Right panel: reconstruction of the decay chamber window. Much worse resolution along Z-direction than along Y-direction is visible. The component occurring around Y $\sim$120 mm has been identified as a background component originating outside the decay chamber window. This particular contribution is effectively eliminated from further analyses through the cuts on reconstructed trajectories.

Reconstruction of the vertices of all double-track events is crucial for selection of true Mott scattered electrons from a background processes. Method of selection of double track events and their vertex reconstruction was presented in sec 5.1.1. But it is worth to remind that the tracks and vertex reconstruction in both detection planes (XY - drift-time plane and XZ - charge-division plane) are done independently. However, since charge-division method is less precise in determination of hit position, only events correctly reconstructed in the drift-time plane are utilized for the subsequent reconstruction in the XZ-plane. For reconstruction of vertices only events triggered by one of the Mott detectors are considered.

5.3.1 Scattering of electrons emitted from ^{207}Bi

Before the studies of Mott-scattering of β-particles from neutron beam decay, the performance of vertex reconstruction method was tested using the data collected for ^{207}Bi radioactive source.

Fig. 5.28 presents the examples of two most dominant double-track event classes recorded for this case. In left panel the two track originate from vicinity of the source. Such events are identified as Møller scattering of conversion electron from the source on the electron of calibration aluminum plate or housing of the source. In the right panel there is example of regular back-scattering of conversion electron on the Mott target.

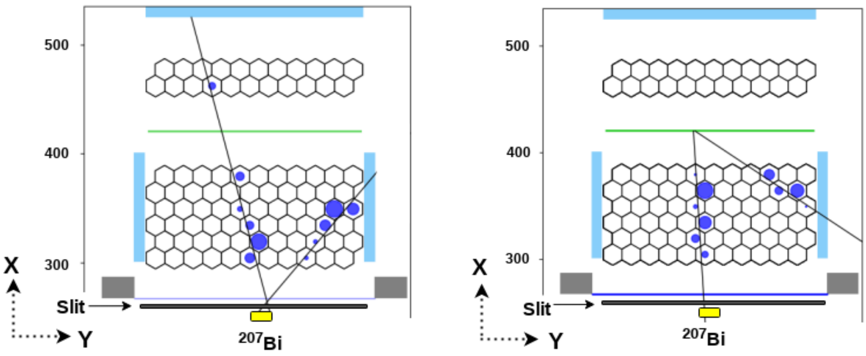

Figure 5.28 Visualization of examples of two most dominant classes of double-track events recorded when ^{207}Bi radioactive source illuminated the Mott polarimeter. Tracks are reconstructed in XY-plane. Left panel: Møller scattering of conversion electron emitted from the source on electron at the construction material surrounding the source. In effect two electrons propagate from one vertex. Right panel: back-scattering of electron on the Mott target.

Vertex reconstruction in drift-time plane (XY)

The resulting distribution of vertices along X-axis of the setup is shown in fig. 5.29

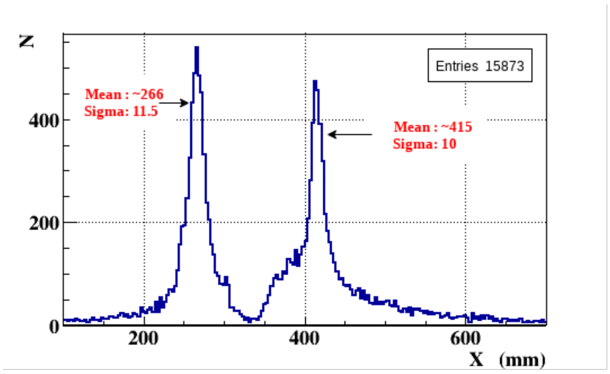

Figure 5.29 Vertex distribution along X-direction reconstructed using drift-time information and obtained from the two-track events recorded when ^{207}Bi source was used to illuminate a Mott spectrometer.

Two components are well distinguished. Their position along X-axis agree well with actual position of calibration plate placed between the source and the tracker (265 mm) and Mott target (418 mm). For the selected events of those two components (in the range of $\pm 2\sigma$ of fitted Gaussian function) the distribution of reconstructed vertices along Y-axis is presented in fig. 5.30.

For Møller scattered electrons the source position is perfectly reconstructed (left panel) whereas scattering of direct electrons is distributed over the whole surface of the Mott target and its frame (right panel). The contribution from frames can be easily separated.

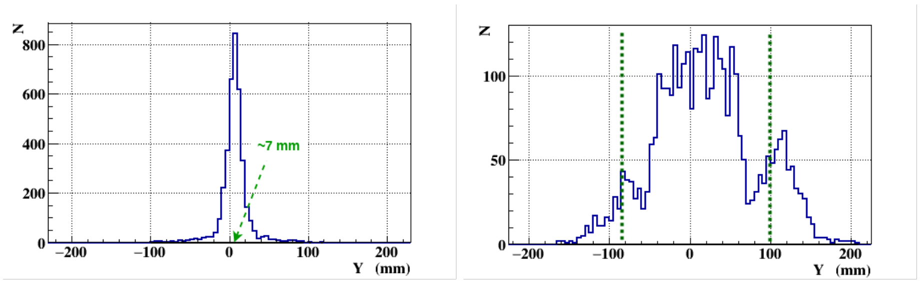

Figure 5.30 Distributions of reconstructed vertices along Y-direction for events selected from two dominant components presented in fig. 5.29. In each case a $\pm 2\sigma$ cut have been applied to the individual peak. Left panel: events from the peak corresponding to calibration plate position. Reconstructed vertices indicate a bismuth source position displaced from 0 by 7 mm as in actual setup. Right panel: Events from the component at ~415 mm. Their vertices spread across the Mott target surface and its frame. Dotted green lines indicate the position of aluminum frame of Mott target in Y-direction. The spiky structure visible in this distribution appears due to variation of detection efficiency along the layers of tracker (cf. fig. 5.11).

Vertex reconstruction in charge-division plane (XZ)

Figure 5.31 presents the quality of position reconstruction of vertices for two-track events using the charge-division method. Unlike the vertex distribution in the drift-time plane (fig. 5.29), the presence of a two-peak structure is not visible for charge-division plane. Instead a very broad peak is observed with a maximum located inside the tracking volume of MWDC around X = 350 mm.

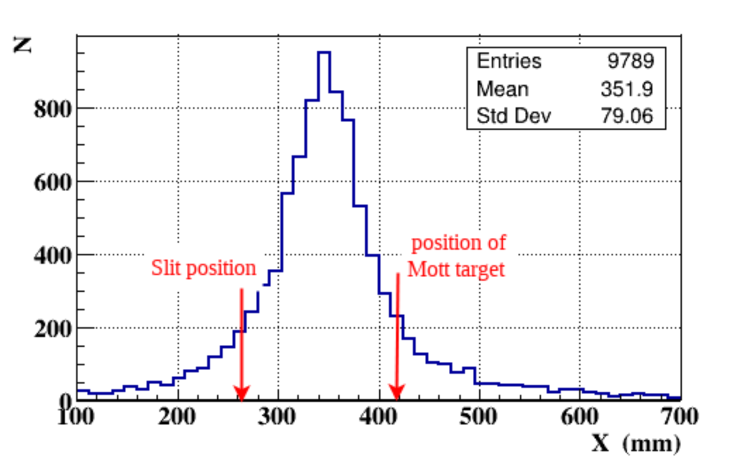

Figure 5.31 Distribution of vertices of two-track events along X-direction obtained with the charge-division method for electrons emitted from ^{207}Bi source.

This failure in resolving of the two components, so clearly distinguished by the drift-time reconstruction, can partially be attributed to the position resolution, which is much worse in case of charge-division method than for drift-time method. Due to much lower detection and tracking efficiencies for XZ-plane the resulting statistics of accepted events is reduced to 60% in comparison to result for XY-plane.

In order to separate contributions from Møller and Mott scattering of electrons in the vertex distribution measured with the charge-division method, again the event selection with $\pm 2\sigma$ cuts on peaks in distribution of fig. 5.29 have been applied. Figure 5.32 presents the vertex distributions of selected in this way different event classes both along X- and Z-direction.

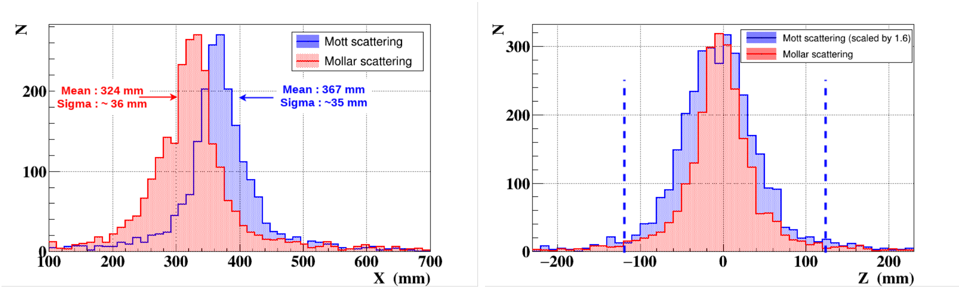

Figure 5.32 Distributions of reconstructed vertices using the charge-division method for two-track events selected separately for Mott scattering (blue histograms) and Møller scattering (red histograms). Selection was done by application of $\pm 2\sigma$ cut on separated components of distribution presented in fig. 5.29. Left panel: distributions along X-direction; right panel: distribution along Z-direction. Vertical dashed lines indicate the frame position of Mott target in Z-direction.

The left panel of the fig. 5.32 reveals that for both classes of events the resulting distributions still are very broad. Their positions however, are slightly displaced towards the real positions of the calibration plate and the Mott target. But this shift is by factor of about 3 too small to correctly reproduce the origin of both event classes. This fact indicates at a systematic effect affecting the slope of trajectories reconstructed in the charge-division method. It should be noted that despite of many attempts with different calibration functions and assumption of different position dependent resolution no explanation of this effect has been found.

The right panel of fig. 5.32 displays the distribution of vertices in the XZ-plane separately for Møller and Mott events. They both are symmetric around zero. Distribution formed by Mott scattered electrons does not cover the whole width of Mott target in Z-direction. This can be explained by the presence of calibration plate with vertical slit at the tracker entrance. Also, contribution from scattering on the frames can not be distinguished. Distribution attributed to Møller scattering is much broader than expected ($\sim$4 mm) and indicate that the resolution of vertex reconstruction in Z-direction is of the order of 35 mm.

The conclusions from the analysis of V-tracks induced by the conversion electrons from ^{207}Bi source are following:

- position resolution of vertex reconstruction in the XY-plane (with use of measured drift-times) is sufficient to provide crucial physical information, like identification of external background sources and distinguishing them from the events of interest for the final analysis;

- it is not the case for the vertices reconstruction in XZ-plane (charge-division method), which suffers from low efficiency, low resolution and systematic error in the determination of trajectory slope. This method is not sufficient for the reliable selection of true events.

It must be concluded that identified deficiencies of the charge-division method significantly deteriorate the general performance of the Mott polarimetry in BRAND-0 setup. They prevent a reliable determination of physical results, which require full 3-dimensional trajectory reconstruction.

5.3.2 Mott scattering of β-particles from neutron decay

Fig. 5.33 illustrates the reconstructed vertex distribution along X-axis for the data collected during beam operation. It is done for all well-reconstructed, two-track events, separately in the drift-time plane (left panel) and charge-division plane (right panel).

The distribution obtained by applying the drift-time method demonstrates a prominent peak at the actual position of the Mott target. Also smaller peaks at various positions along X-axis are present. They are attributed to electron scattering on the internal components of the MWDC.

Similarly as it was in case of electrons from ^{207}Bi (cf. sec. 5.3.1), the distribution shown in right panel, reconstructed using the charge-division method, does not exhibit clear evidence of scattering on the Mott target. Instead, it peaks at the center of the tracking volume at $\sim$ 360 mm, which is about 60 mm away from the actual position of the target.

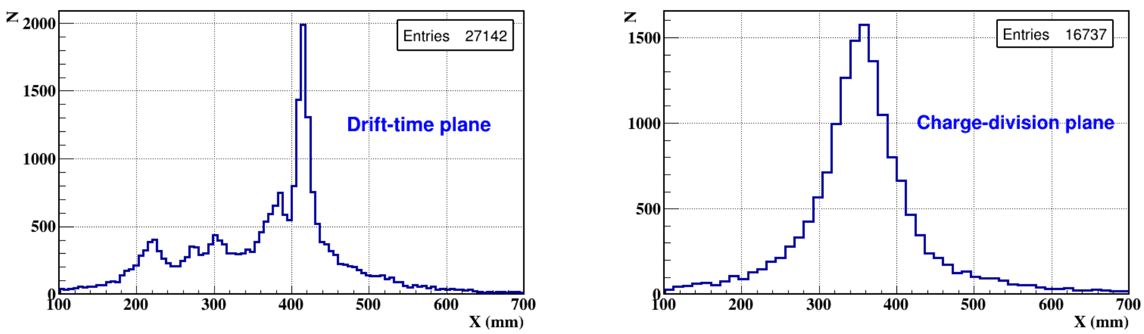

Figure 5.33 Vertex reconstruction along X-direction for all well-reconstructed two-track events recorded during beam operation. Left panel: done with tracking in XY-plane (drift-time); right panel - tracking with charge-division method in XZ-plane. Prominent peak visible at X $\sim$ 420 mm in left panel coincide with actual position of the Mott target. It is not a case when charge-division method is used (right panel), where broad distribution of vertices with maximum around the position of plane 3 of MWDC was obtained.

Further refinement of this analysis was obtained by applying geometrical conditions for both reconstructed tracks: (*i*) track more orthogonal to the Mott target (called "source-track") must originate from inside of the decay chamber and traverse the surface of decay chamber window; (*ii*) track more tangential to the Mott target ("scint-track") should point to the surface of the one of the Mott detectors. This track selection relied on the reconstruction only in the drift-time plane.

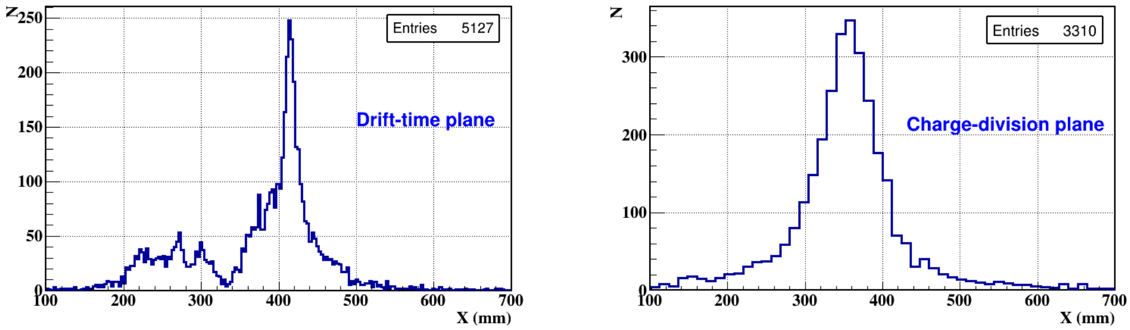

Figure 5.34 The same as in fig. 5.33 but for refined event selection: from the reconstructed tracks one points to the surface of the decay chamber window and second to the surface of one of the Mott detectors.

Under such conditions improvement in identification of scattering vertices on the Mott target is observed. In the distribution presented in left panel of fig. 5.34, where tracking is done in the XY-plane, on cost of significant loss of the statistics, the relative contribution of Mott target vertices is increased in comparison to the distribution in left panel of fig. 5.33. For the distribution obtained by tracking in XZ-plane no any improvement is realized.

For completeness, the vertex distributions along Y- and Z-direction are shown in fig. 5.35. Whereas for the Y-direction, beside the expected back-scattered electrons from the Mott target also the contribution of the Mott target frame (and possibly also frame of the Mott detectors) can be identified, it is not visible along the Z-direction. Asymmetry in contributions of aluminum frames at Y = +100 mm and Y = -100 mm results from combined effects of: (*i*) displaced from zero position of the whole tracker, (*ii*) effective beam position displaced from zero due to the magnetic field, and (*iii*) different detection efficiencies of both Mott detectors.

Estimation of the amount of V-tracks from sources different than the Mott target in the distributions presented in fig. 5.34 can be done by comparison of the data collected during beam operation but with- and without Mott target inserted to the tracker. In fig. 5.36 the time-normalized and dead-time-corrected distributions of vertices reconstructed for both cases are superimposed.

For the drift-time plane (left panel), it is evident that the peak associated with scattering on Mott target (at X∼415) is nearly absent when the Mott target was removed from the detection volume. This indicates that the presence of the Mott target significantly contributes to the observed vertex distribution. Also the components of vertex distribution recorded

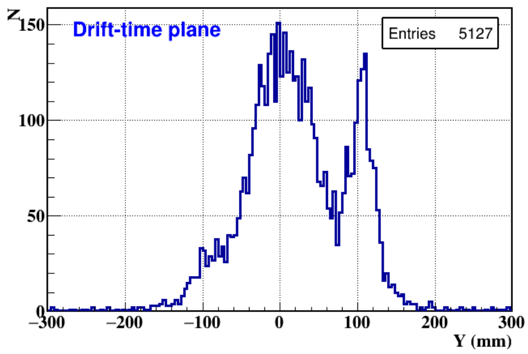

Figure 5.35 Distribution of vertices for the same events as in fig. 5.34 but along Y-direction (left panel) and Z-direction (right panel).

in absence of the Mott target reproduce almost perfectly the background present in the spectrum of fig. 5.34 left panel. Thus, position cuts along X-direction can, to great extent, improve selection of true events of electron scattered on the Mott target.

For the charge-division plane (right panel), the presence of the Mott target appears to result in a slight shift of the whole distribution towards actual position of the target. It is however not sufficient to enhance the identification of Mott scattering vertices in XZ-plane.

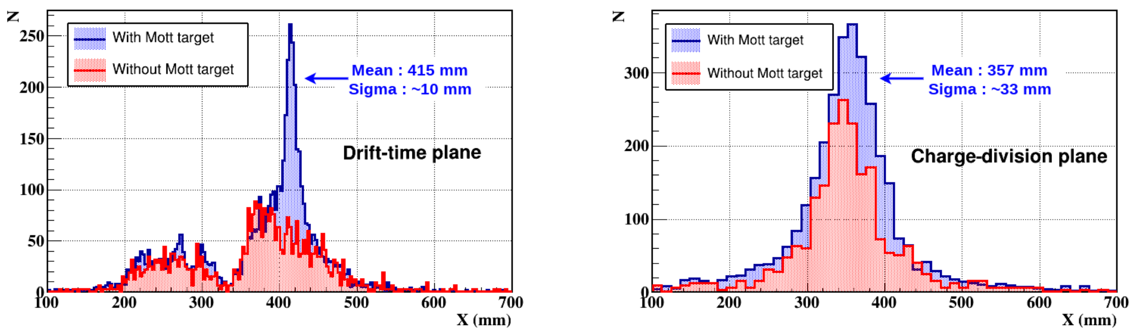

Figure 5.36 Time-normalized and dead-time corrected distribution of reconstructed vertices of V-tracks along X-direction for beam events collected when Mott target was inserted to the tracker (blue histograms) and Mott target was removed (red histograms). Clear impact of Mott target can be identified in case of drift-time tracking in XY-plane (left panel), whereas almost no effect (except increase in statistics) is visible when tracking based on charge division in XZ-plane is used (right panel).

5.3.3 Event selection for physics analysis

A large contamination of selected V-tracks with background events have been realized. Thus, for the determination of data set which can be finally used for calculation of correlation coefficients depending on orientation of electron spin (i.e. N and R) all possible selection criteria have to be applied. In addition to those already introduced the following should considered:

(i) projection of "source-tracks" at the beam axis must be contained within range of -40 mm $<$ Y $<$ 20 mm (effective shift of the beam in the vertical direction (-10 mm) is taken into account). It assures that track comes from beam core, at least in Y-direction;

(ii) projection of "source-tracks" at the decay chamber window must be comprised in range of -30 mm $<$ Y $<$ 30 mm in order to minimize influence of window frame (dimension of widow in Y-direction is 80 mm);

(iii) the same is demanded in Z-direction, where the accepted range is -80 mm $<$ Z $<$ 80 mm (dimension of widow in Z-direction is 220 mm);

(iv) only events within $\pm 3\sigma$ cut on Mott vertex peak obtained for both tracking planes are accepted (cf. fig. 5.36);

(v) contribution from the frame of Mott target is excluded.

The resulting distributions along X-direction for both tracking planes are shown in fig. 5.37.

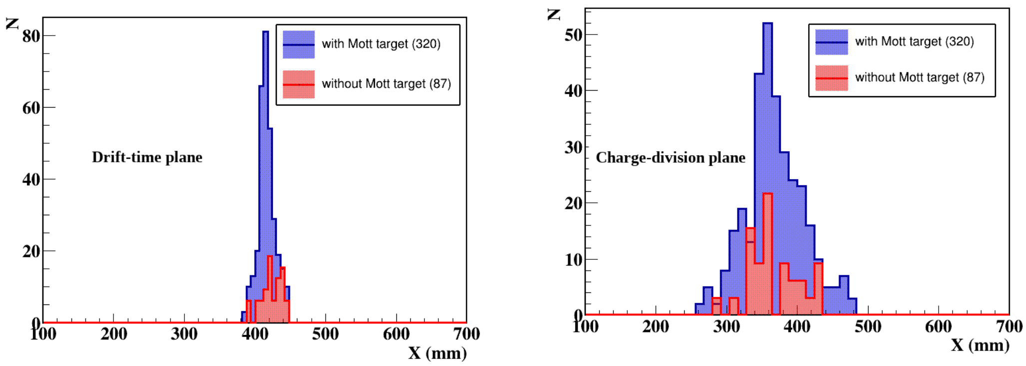

Figure 5.37 The same as in fig. 5.36 but obtained with the most stringent selection criteria explained above. The distributions are time-normalized and dead-time corrected. The numbers in brackets provide statistics of events. Events selected in this way should be used for determination of β-correlation parameters N and R.

It is observed that despite of stringent cuts applied, still some contribution of unresolved background remains in vicinity of the Mott target position. Thus, the vertices which form the dominant peak can not be unambiguously identified as originating from Mott-scattering of β-particles of beam neutron on the Mott target. Distributions of fig. 5.37 permits an estimation of the ratio of electrons actually back-scattered from Mott target (signal) to all other V-track events (background) registered in this region. Unresolved contamination of spectrum with vertices from other sources has to be considered as systematic effect. Among obtained candidate events of Mott-scattering, the ratio of background-to-signal, is 27 $\pm$10 %.

Fig. 5.38 presents the distributions of reconstructed vertices at the surface of the Mott target for final set of the selected events: along Y-direction (left panel) and Z-direction (right panel).

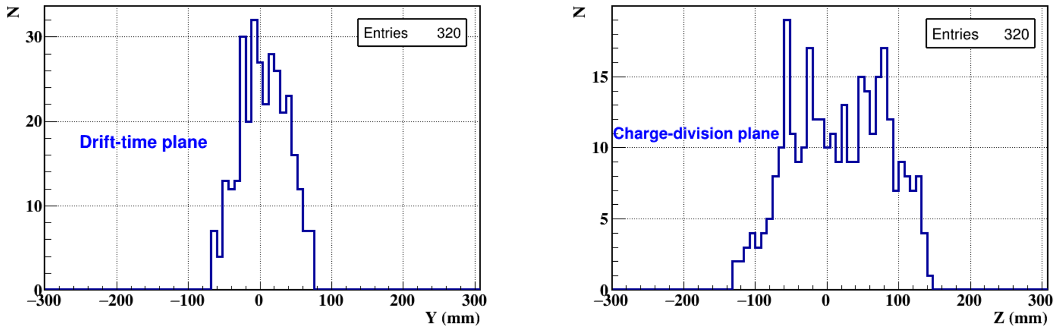

Figure 5.38 Vertex distributions along Y-direction (left panel) and Z-direction (right panel) of Mott foil surface. Only event of most stringent selection criteria are used.

Events presented in figs. 5.37 and 5.38, selected with the most stringent conditions available for the BRAND-0 data, should be used for the determination of the β-decay correlation parameters N and R. From the analysis of the V-track events, it was concluded that the event selection method works well in the drift-time plane. But to achieve the required confidence level in the determination of correlation coefficients, the currently available resolution in the charge-division method is insufficient. Also, the available statistics is very low-only 320 events. Among them still 27 $\pm$10 % are events not originating from back-scattering on the Mott target, obscuring the information from neutron decay. Additionally, some part of electrons identified as originating from the beam, in fact was produced on the aluminum walls of the decay chamber and also must be considered as a background.

The obtained event statistics can be doubled if the results of analysis of less credible data sets will be included. However those data have been identified as even more affected by electronic noise correlated with the Mott or proton detectors operation.

5.4 Energy measurement

The precise determination of energy of electrons originating from β-decay of neutron is the next crucial task in the BRAND project. It is needed for calculation of some correlation coefficient (A, N, R), for reconstruction of neutrino energy (together with measured energy of proton) and for reconstruction of whole kinematics of neutron decay. Moreover, cuts applied on energy spectra support filtering of true events from experimental background.

In the BRAND-0 setup, the energy of electrons is measured in Back_scint (direct electrons) and in Mott_dets (Mott-scattered ones). The subsequent section focuses on energy measurement and energy calibration in those scintillator detectors.

5.4.1 Position dependence of signal amplitude distribution

Energy measurement in scintillating detector is based on the light collection of photons produced in scintillating material by the incident particle. This process strongly depends on the properties and geometry of scintillating material, presence and geometry of light guide, kind and position of light collecting sensors and finally on the hit position of the incident particle. Reproduction of true energy spectrum from the raw data is in general a tough task which needs a careful calibrations.

For calibration of energy and its dependency on hit position in the BRAND-0 scintillators the ^{207}Bi calibration source was used. The information about the electron energy spectrum of ^{207}Bi is given in appendix A in fig. A.6. The discrete electron energy lines of this source of $\sim$500 keV and $\sim$1000 keV are in the range of measured energy of β-particles in the BRAND experiment ($<$ 782 keV). The γs abundantly emitted from ^{207}Bi were suppressed by demand of coincidence of the scintillating detectors and tracker signals. Calibration runs were performed during the experiment at ILL with the source positioned centrally at the front of the tracker window at (X, Y, Z) = (259 mm, 7 mm, 0 mm). Measurement of electron hit position on the surface of the scintillators was supported by tracking with the MWDC.

Signal amplitude calibration for Back_scint

Collection of the light created in the Back_scint was carried out by four 3-inch photomultipliers (PMTs). Their positions at the rear side of the light guide of Back_scint is shown in fig. 5.39. Optical contact of light guide and PMTs was done by means of silicone grease. The gains of the involved PMTs were coarsely equalized by applying the working voltages selected during the initial tests. The fine tuning of PMTs gain was balanced by matching the shape of the spectra collected only for hits from the central part of the scintillator. For this purpose the area of 14×14 mm^2 indicated as a red square in fig. 5.39 has been selected. From symmetry of the system and huge number of photons emitted isotropically within the scintillator, it follows that each photomultiplier should detect similar number of photons and produce signal of the same amplitude - provided their gains are the same. This procedure allows to obtain more accurate gain matching (see fig. 5.40).

In order to study the dependence of light collection on the hit position, the area of Back_scint was divided into a grid of squares of dimension 10×10 mm^2. Energy spectra of each square was extracted by summing the signal contributions from all four PMTs. In view of the geometry of the scintillator and PMT read-out this approximation was considered as

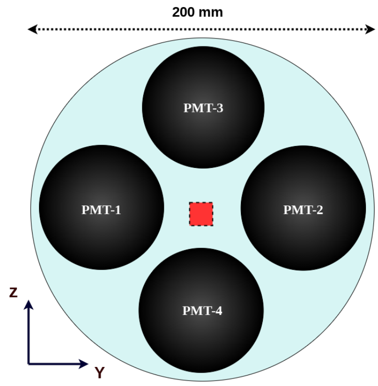

Figure 5.39 Positions of entrance windows of four 3" PMTs at rear side of light guide of Back_scint (black circles). Red square in the middle indicates the area in the center of the Back_scint defined for selection of hits used for fine tuning of PMTs gain balance.

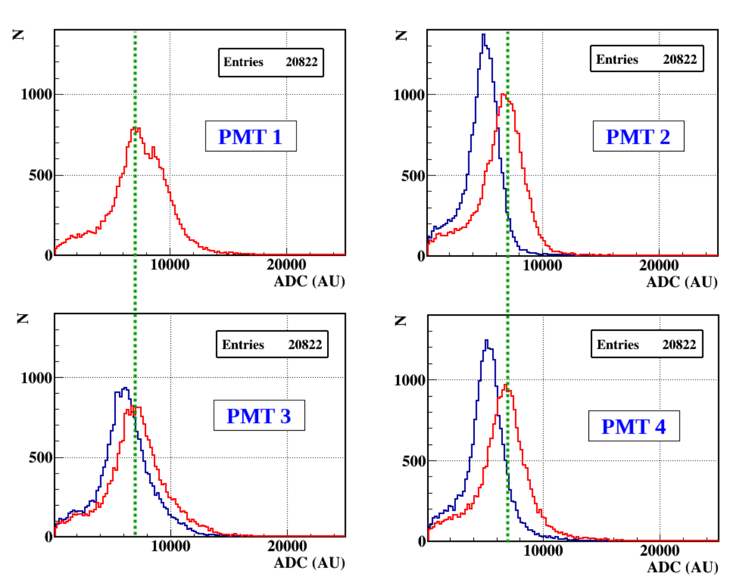

Figure 5.40 Gain balance of four PMTs used to collect the light from the Back_scint. Energy spectra of individual PMTs created only for events recorded in the central area of the Back_scint are considered. Blue lines - initial distributions. Red lines - distributions after the modification with relevant balancing factors. For PMT1 initial and corrected spectra overlap. Vertical green lines indicate the same positions of maxima of each distribution.

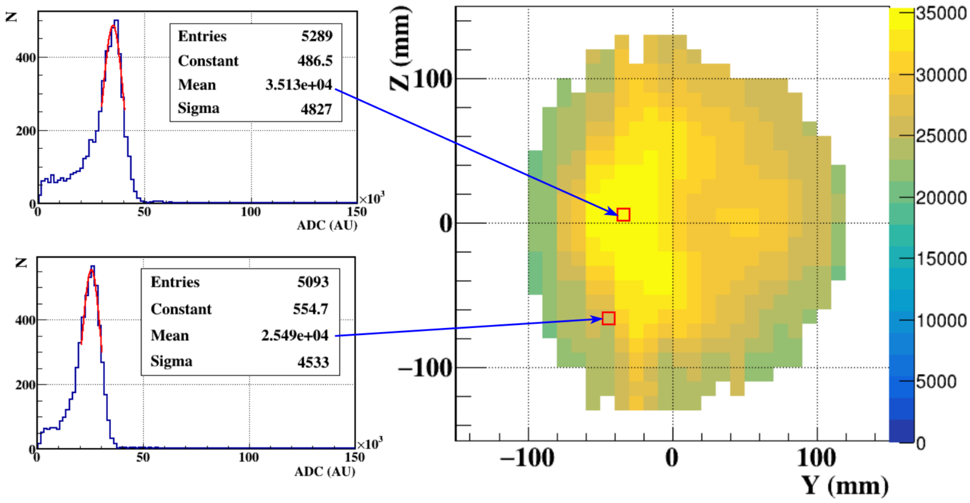

Figure 5.41 Initial "gain map" of the Back_scint surface. It shows that, even after exact matching of all four PMTs, the accumulated signal depends on particles hit position on the scinitillator surface. Maxima of histograms prepared for each square correspond to the higher energy line of ^{207}Bi electron source. Examples of spectra are shown for the squares marked with red symbols. The extension of the plot beyond the geometrical dimension of Back_scint (ϕ = 200 mm) is due to the limited tracking precision.

the most appropriate. The gain attributed to each bin of surface has been parameterized by the position of Gaussian function fitted to the maximum of the spectra. It corresponds to energy line of 1 MeV of bismuth electron source. This way a "gain map" along the surface of the Back_scint was established. It is shown in fig. 5.41.

Comparing the positions of maxima of individual energy spectra, position sensitive energy correction factors for each square on the Back_scint surface were calculated. After application of them, the gains of whole surface of the Back scintillator have been properly equalized (cf. fig. 5.42).

Having those correction factors the energy spectrum for the whole area of the Back_scint can be prepared. It should be of the same shape as those collected for individual small squares of detector surface. It is confirmed in fig. 5.43, where energy spectrum of ^{207}Bi restricted only to the central square of the surface (left panel) is compared to the spectrum accumulated by the whole scintillator (right panel). The positions as well as the widths of both distributions are very similar what illustrates the well-balanced position dependent calibration.

As already mentioned, only one group of the conversion lines of electrons around 980 keV is visible. The absence of low energy lines concentrated around 480 keV was observed already during the experimental run at ILL. As it could indicate at too high threshold of the front-end electronics, it triggered a series of high voltage adjustments of all four photomultipliers. But increase of the PMT's voltages only scaled the spectrum, without noticeable change in its

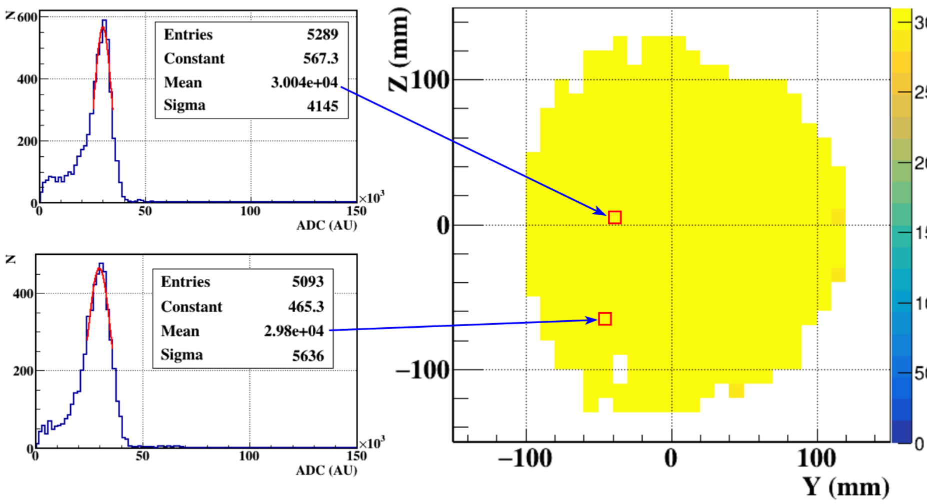

Figure 5.42 The same as in fig. 5.41 but after application of correction factors for hit position dependence of light collection.

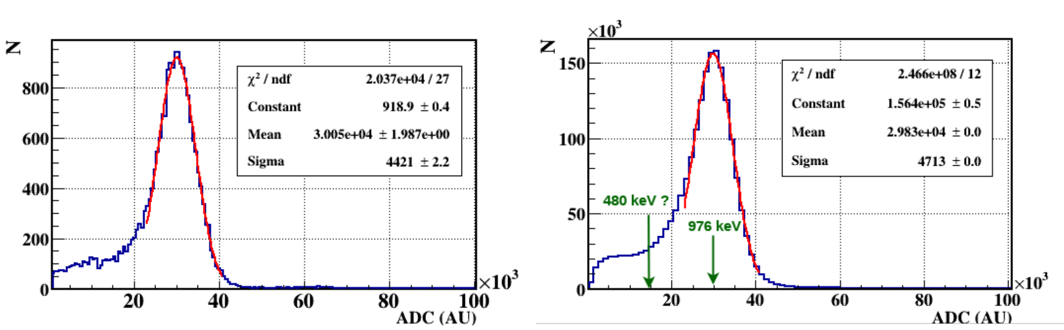

Figure 5.43 Energy spectra of ^{207}Bi with Gaussian fit at ~980 keV electron line. Left panel: for the events collected at the small region in the center of Back_scint surface; right panel: for the hits covering the whole scintillator surfaces and after applying the calculated position-energy-balancing factors. The arrows represent the positions of expected calibration line from ^{207}Bi, assuming that high energy line corresponds to the visible peak and energy threshold is consistent with zero. Due to the missing lower component of ^{207}Bi energy spectrum, only one calibration point is available.

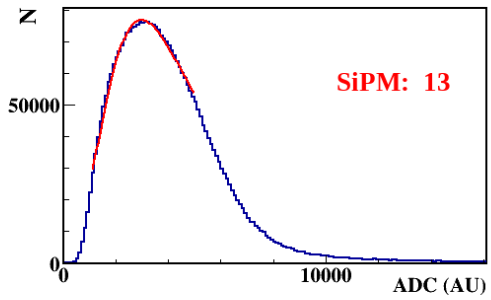

Figure 5.44 Example of signal amplitude spectrum obtained for one SiPM sensor when Mott_det was exposed to electrons emitted from ^{207}Bi source.

shape. Thus, the suppression of the lower energy component of ^{207}Bi at $\sim$ 480 keV has been attributed to poor amplitude resolution of the system, which deteriorates even more for low signal amplitudes. Other responsible factors are imprecise tracking, preventing more accurate accounting for the position dependence of the PMT response, and enhanced energy and angular scattering of low energy electrons in the windows of the setup, specially on the surface of the Mott target. The problem of low resolution of amplitude measurements in BRAND-0 will be addressed in the next chapter (c.f. sec. 6.2).

The total energy spectrum (right panel of fig. 5.43) was used to tune the parameters of Geant4 model when response of the Back_scint was simulated. The position and shape of the spectrum have been well reproduced (cf. fig. A.7).

Calibration of the Mott detectors

Each of two Mott_dets in the BRAND-0 setup was read out via 28 Silicon Photomultiplier (SiPM) sensors. A row of 14 sensors was attached to each narrow side of the plastic scintillator at its left and right side. In the BRAND-0 setup, the Mott_dets together with SiPMs were installed inside the active volume of MWDC. Their temperature monitoring was not feasible. The used SiPMs have shown large instabilities in their operation. Adjustment of their bias voltage and detection threshold was frequent and tedious task.

The data for the characterization of the Mott_dets were collected in ILL simultaneously with the Back_scint calibration using ^{207}Bi radioactive source. Calibration data analyzed in this work was collected continuously without altering the threshold and bias voltages of SiPMs.

The example of typical raw signal amplitude spectrum of an SiPM is shown in fig. 5.44. It resemble the Landau function. It was found that SiPM channels 1, 8, and 24 from Mott_det1 were non-functional. SiPMs channels 35 to 39 from Mott_det2 could not be used due to high level of noise.

Similarly as for the PMTs of the Back_scint, in analysis of the Mott_dets, the gain of the SiPMs channels were equalized by applying the gain balancing factors. They were calculated by fitting the Landau distributions to the raw amplitude spectra of individual SiPM channels.

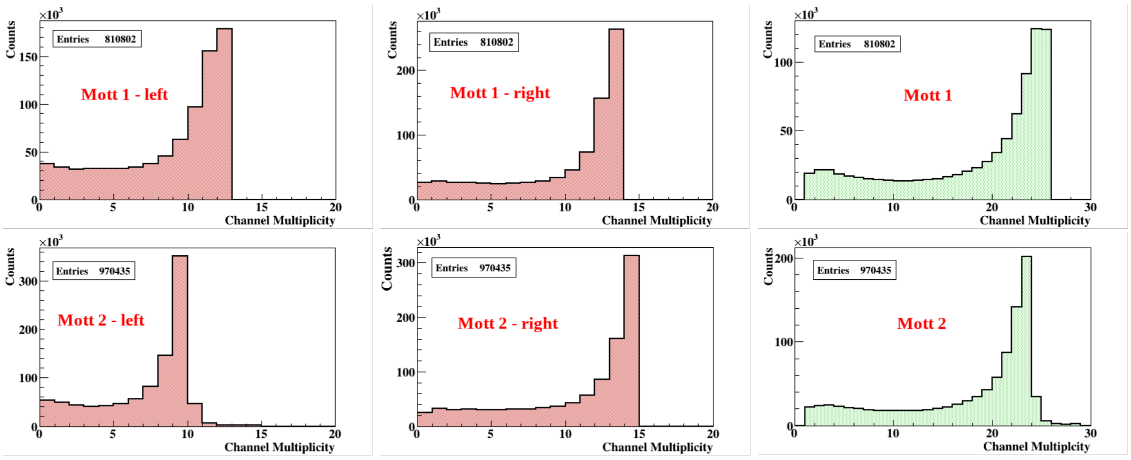

Figure 5.45 Distributions of SiPM channel multiplicity of events recorded in the Mott_dets. Presented are the distributions for left and right sides of each Mott_det extracted separately (red histograms) and the summed distributions for the individual detector (green histograms). Differences in the maximal multiplicities are result of missing/noisy channels.

The position corresponding to the maximum of the fit served as a reference for determination of the gain factors.

Channel multiplicity of events in the Mott detectors

The channel multiplicity of event indicates the number of SiPMs activated per trigger induced by the Mott_det. Distribution of channel multiplicity serves as a valuable parameter to assess the SiPM array's efficiency in collecting light. It provides as well insights into noise level within the detection system.

Figure 5.45 shows the SiPM channel multiplicity distribution of the Mott_dets for events collected in coincidence with reconstructed electron tracks.

All distributions peak at the number of well functioning attached sensors, which suggests relatively large efficiency of a single sensor. This observation is in contradiction to observed plateaux below multiplicity eight (or six for side with many dead channels). Presence of those plateaux can be partially explained by events with very low energy deposition (e.g. on the edge of scintillator and very close to some sensor), or electronic noise of the SiPMs. But it also can be an indication of some more serious malfunctioning of the front-end electronics.

For the total amplitude spectra, summed over all sensors from each side of the Mott_dets, the compensation for the missing signal contributions of the malfunctioning channels was done. An average value of signal amplitude was assumed for missing channels. By such channel number balancing, the negative impact of non-functioning channels was to large extent smoothed.

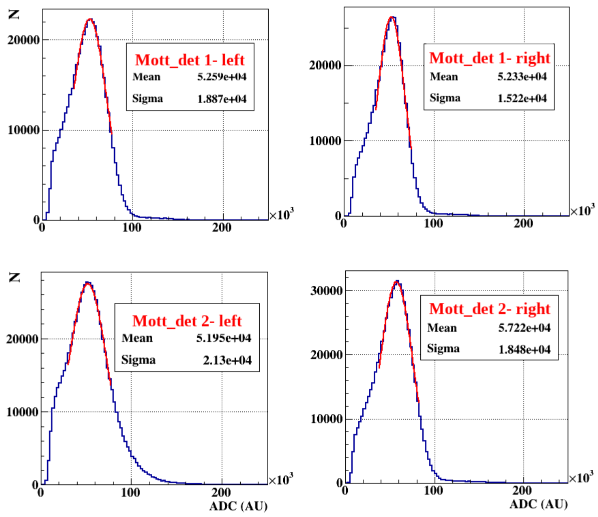

Figure 5.46 ^{207}Bi energy spectra extracted from both sides of respective Mott_dets.

^{207}Bi energy spectra of Mott detectors

For events triggered by the Mott_dets with well reconstructed tracks in the MWDC and position reconstructed within the $\pm 2\sigma$ of the actual source position, the total energy spectra of ^{207}Bi were extracted. The energy spectra extracted from the left and right SiPM arrays in the respective Mott_dets are shown in fig. 5.46.

Corresponding summed spectra for each Mott_det are presented in fig. 5.47. Correction for light attenuation effect by adding the contribution from both side of Mott_det resulted in small improvement in the energy resolution. The ratios of the widths of peaks corresponding to the high energy lines to their centers decreased in comparison to about 32% and 40% for Mott_det 1 and, 2 respectively. This improvement, however, is by far not enough to resolve both main components of bismuth energy spectrum. Similarly as in the case of the Back_scint this observation was available already during the data taking at ILL. To check for the threshold effect the analysis was performed also for larger bias voltage applied to the SiPM sensors. Except scaling, no change in the shape of the distribution was observed.

The visible discrepancy in position of maximum of spectra of both detectors is attributed to the lack of contributions of missing channels, which could not be sufficiently compensated by performed channel number balancing.

Similarly as it was realized for the Back_scint, the energy calibration with only a single calibration point makes it impossible at this stage of the analysis.

To investigate the dependency of the amplitude spectra from Mott_dets on the hit position, the energy spectra corresponding to eight rectangular regions (30 mm $\times$ 10 mm) on the detector surface (see Fig. 5.48) were extracted. These spectra are displayed in fig. 5.49. They resemble the total energy spectra obtained from the entire scintillator surface. Individual

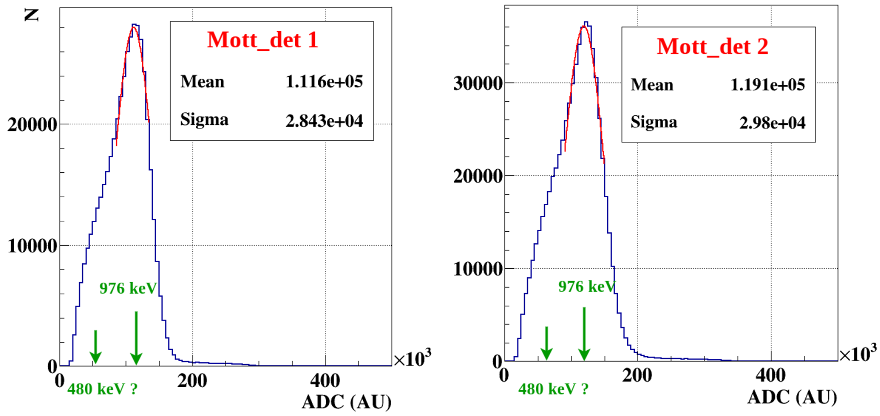

Figure 5.47 The total energy spectra of ^{207}Bi, obtained by summing the signal amplitudes for both sides of respective Mott detector. The Gaussian function is fitted to the main component of distribution, which is attributed to upper line of ^{207}Bi spectrum. Arrows indicate the calibration points expected for absolute energy calibration, assuming vanishing energy threshold. Actually, also for Mott detectors only one calibration point per spectrum is available.

energy components are not resolved. Also not any dependence of the shape of energy spectra on the hit position is observed. This subject will be scrutinized in following section.

Light attenuation in Mott detectors

The photons propagating along the scintillator volume, before they reach a photosensitive detector undergo light attenuation. This effect may result in large position dependence of the detected signal amplitude, spoiling the observed energy resolution from the extended scintillator. In the following, strength of light attenuation in the Mott_dets will be checked.

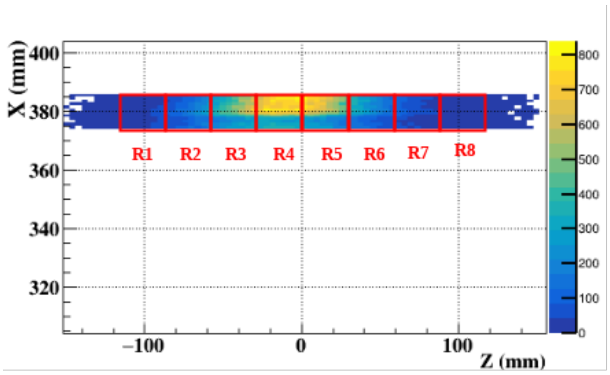

Figure 5.48 The example hit projection distribution on the surface of the Mott_det1, showing selected regions (Rn) extraction of local energy distributions. Projection extended beyond the physical limit of scintillator in Z-direction results from poor position resolution in XZ-plane.

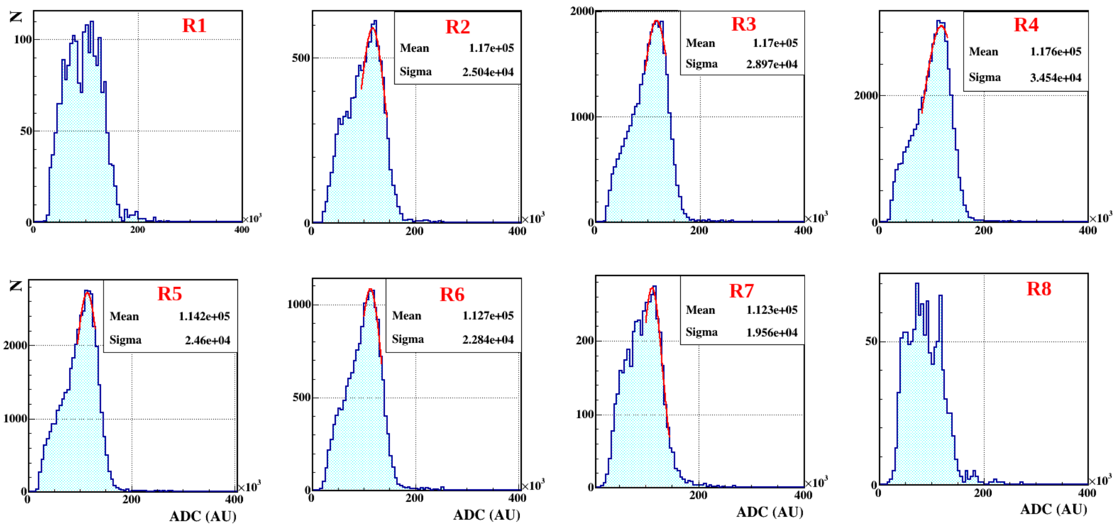

Figure 5.49 The energy spectra of ^{207}Bi extracted for the selected regions on the surface of Mott_det1 (c.f. fig. 5.48). The shapes of these spectra are simmilar as the total energy spectrum collected from the whole surface of the detector.

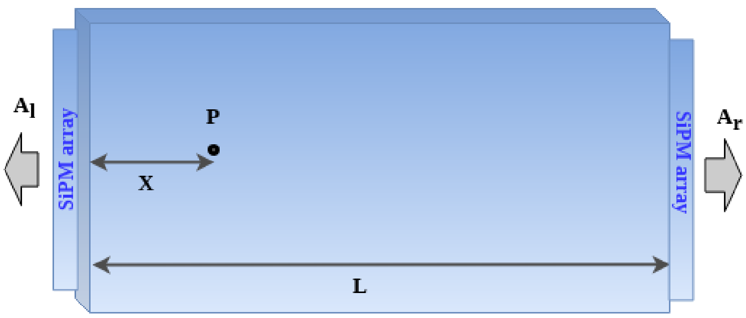

Figure 5.50 Illustration of an event with particle hit position at point P on the scintillator surface. The length of scintillator is L. A_l and A_r represent the amplitudes of signals produced by the left and right SiPM arrays, respectively.

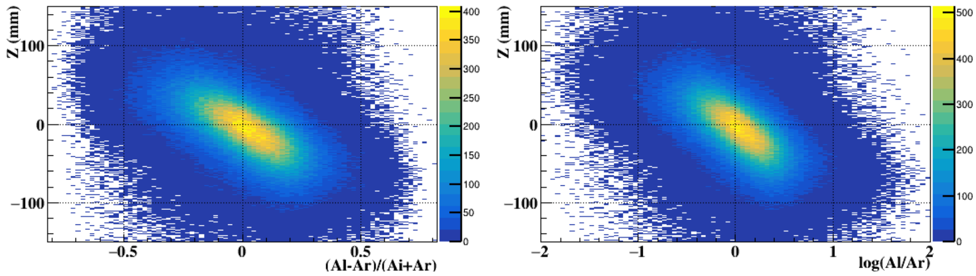

Figure 5.51 Correlation of the reconstructed position along the length of the Mott_det1 with standard asymmetry (left panel) and logarithmic asymmetry (right panel). Very similar dependence in both cases is observed.

If α is the light attenuation length for the given scintillating detector of length L and the particle hit the surface at distance X from left side of scintillator (cf. fig. 5.50) then the signal amplitudes created by light sensors at the left (A_l) and right (A_r) side of the scintillator can be written as [72]:

$$A_l(X) = A_0 e^{-X/\alpha}, \qquad A_r(X) = A_0 e^{-(L-X)/\alpha}, \tag{5.12}$$

where, A_0 is the amplitude which would be observed without light attenuation. The quantity called "logarithmic asymmetry":

$$Asy_{log} = \log(A_l/A_r) \tag{5.13}$$

which depends linearly on hit position, and is independent on the amount of light initially produced. This is not the case for the so called "standard asymmetry":

$$Asy_{stand} = (A_l - A_r)/(A_l + A_r) \tag{5.14}$$

which shows exponential depends on X.

Fig. 5.51 shows the correlation between the reconstructed Z-position of the tracks on the scintillator surface (along the length of the scintillator) and the standard and logarithmic asymmetries between the amplitudes recorded at both sides of the Mott_det. Both distributions are almost identical showing very similar degree of correlation of the plotted variables. This proves the existence of light attenuation in Mott_dets. But on the other side it indicates at other effects which are strong enough to hide the difference between both asymmetries.

This effect was further examined by comparing the geometric and arithmetic mean distributions. The geometric mean of the amplitudes from both sides of scintillator can be expressed as:

$$mean_G = \sqrt{A_l \cdot A_r} \quad = A_0 \sqrt{e^{-L/\alpha}} \tag{5.15}$$

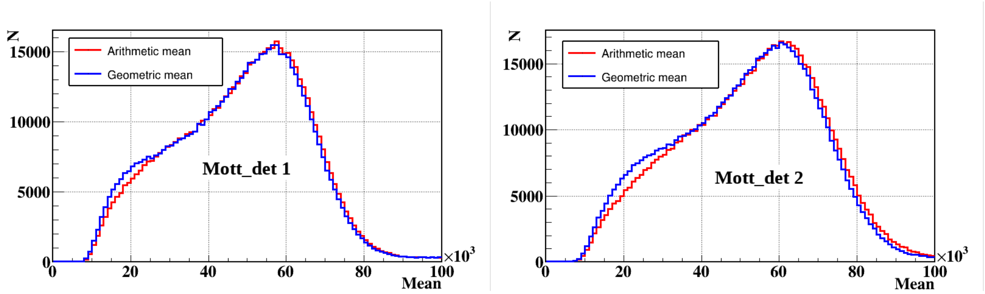

Figure 5.52 Comparison between the arithmetic and geometric means calculated for the respective Mott_dets. The plots show almost ideal equality between these two statistical quantities for both Mott detectors.

The arithmetic mean is:

$$\mathrm{mean_A} = \frac{\mathrm{A_l} + \mathrm{A_r}}{2} = \frac{\mathrm{A_0}}{2} \cdot \left(e^{-\frac{X}{\alpha}} + e^{-\frac{(L-X)}{\alpha}} \right) \tag{5.16}$$

The comparison between equation 5.15 and 5.16 shows that the geometric mean does not depend on the distance X, whereas in the case of arithmetic mean explicit dependence of the distance is observed. Hence, the application of geometric mean should remove the distance dependence from the measured total amplitude spectra and the comparison of the distributions of geometric and arithmetic means provide the information about the strength of light attenuation effect in examined scintillation detector.

Such comparison for the Mott_dets is presented in fig. 5.52. While a small differences could be realized, the overall shapes of the distributions appear to be identical for both Mott_dets. The above observations suggests that the light attenuation is not significant enough to account for low resolution of the observed energy spectrum. Most likely the latter is related to the other effects. Among such effects the following have to be considered:(i) the aspect ratio of the scintillator, which is rather wide (2:1), (ii) low accuracy of tracking, which for this component involves charge-division method, and finally (iii) low resolution of amplitude measurement. Considering the results obtained for the Back_scint, the last reason seems to be the most likely. Signals from the light sensors of both detectors were processed by identical custom made electronic circuits, working as a charge-to-time converter (see next chapter).

SiPM gain balance for the neutron beam data

Unfortunately, due to realized significant instability of the SiPMs performance during the run, the previously calculated gain balancing factors based on ^{207}Bi spectra could not be applicable for the analysis of neutron beam data. In order to account for this variability, gain balancing factors had to be calculated as a function of time. The plot shown in fig. 5.53 is an example of the gain variation over time for SiPM 0. During this time the data taking with a neutron beam was ongoing. The entire data collection period was divided into eight regions,

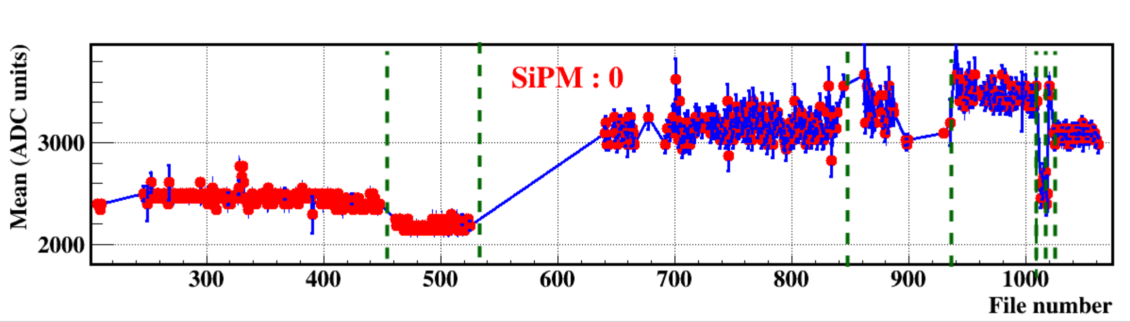

Figure 5.53 Variation the gain for a typical SiPM over the course of the run time. The bin in the horizontal axis corresponds to the file number. The plot illustrates the periods of longer work stabilities and fluctuations in the SiPM gain throughout the duration of the run.

where the working conditions of SiPMs were similar. For data collected within the specific time period the gain correction factors were calculated and applied. The method described for ^{207}Bi has been used.

5.4.2 Energy spectra of electrons from neutron decay

The following section focuses on the energy measurements of electrons collected during the beam operation. All essential gain balancing factors extracted earlier (cf. sec. 5.4.1) are utilized for this aim.

As explained in 5.4.1 the two data sets were used for analysis of results of BRAND-0 experiments. They are numbered as data set 6 and data set 7. They differ in cleanness of experimental conditions during data taking and some parameters of the setup (e.g. the HV for PMTs of Back_scint). The calibration and analysis for both data sets have been performed independently. Nevertheless methods of data treatment for both data sets are identical. In this work, in order to keep consistency between subsequent plots, the proceeding of analysis process will be explained using predominantly examples from data set no 7.

Energy measurement in the Back scintillator

The raw signal amplitude spectra registered by the individual PMTs of Back_scint during the beam operation are shown in fig. 5.54. The spectra are built only out of events for which good quality tracks have been reconstructed by the MWDC. The sharp cuts visible on the high amplitude side of the distributions are the result of the fixed width of the TDC window of DAQ, which was about 1.8 µs. It is important to notice that this limitation does not affect the high energy lines from bismuth, which are visible even below the half of the whole distribution (cf. fig 5.40). Thus, the limitations on the TDC window could not affect the β-energy spectrum from neutron decay.

The sum of signal amplitudes from all four PMTs provides better approximation of the total energy spectrum for beam data. It is shown in fig. 5.55.

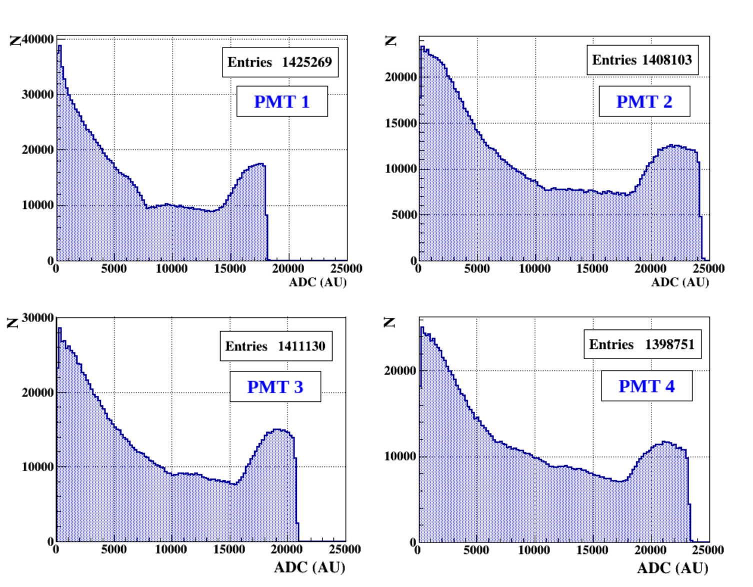

Figure 5.54 The raw signal amplitude spectra collected in the individual PMTs of the Back_scint for the neutron beam data.

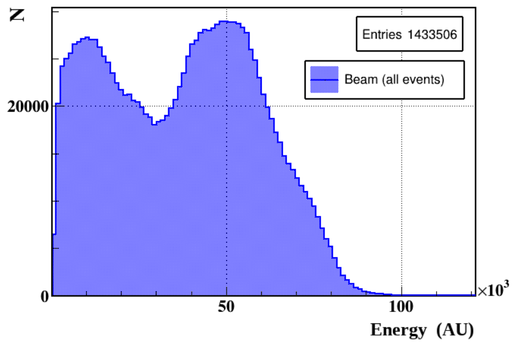

Figure 5.55 Raw total energy spectrum collected in Back_scint. The shape of the spectrum is discussed in the text.

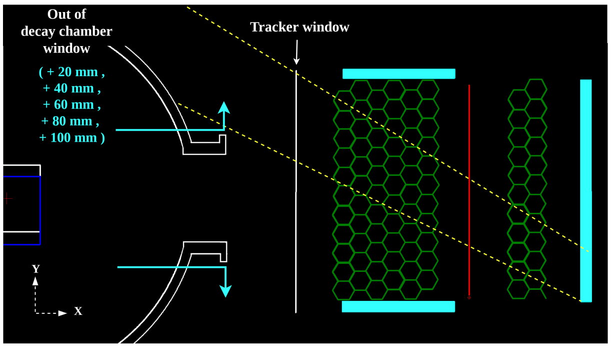

Figure 5.56 Investigation of energy spectra of events originating from the beam-activated background. The extrapolated track position falls within the tracker window but must originate from outside of the decay chamber window. For study of the spatial distribution of such events the tracks are selected with various cuts. The size of decay chamber window is excluded together with some additional offset. Theses offsets were selected as +20 mm, +40 mm, +60 mm, +80 mm, and +100 mm in the outward direction. The same offsets are applied both along Y-direction as well as Z-direction.

The spectrum consists of two components. The lower energy component is attributed to the measured β-spectrum of electrons originating from the decay of neutrons from beam. Origin of the bump visible at higher amplitude range is an effect of background electrons of energy much above 1 MeV, which deposit their energy completely or partially in the Back_scint. Maximum energy deposition for electron entering the Back_ scint perpendicularly to its surface is about 2 MeV. This is defined by the scintillator thickness (1 cm). Higher energies are allowed for inclined trajectories. Observed peak is additionally affected by the high amplitude cutoff seen in fig. 5.54. The problem of experimental background in the BRAND-0 run will be discussed later in the chapter 7.

Spacial decomposition of Back scintillator energy spectrum

Events originating from outside of the decay chamber The data collected during the run revealed events occurring when the neutron beam was active, but the reconstructed track of those particles did not originate from the decay chamber. To select such events, and to determine their contribution to the energy spectra the cuts on the positions of reconstructed trajectories were applied. Various ranges of cuts were used, as it is illustrated in fig. 5.56. The example of 2D cuts is presented in fig. 5.57.

Figure 5.58 shows the resulting energy spectra for particle trajectories within the applied positional cuts. The shape of this spectrum only weakly depends on the range of the cut. But the magnitudes change strongly indicating higher yield of the background in vicinity of the decay chamber window. Beside the dominant component, corresponding to the high energy bump seen already in fig. 5.55, a component overlapping with the energy range of the β-spectrum can be seen. Such kind of background, originating from outside of the chamber

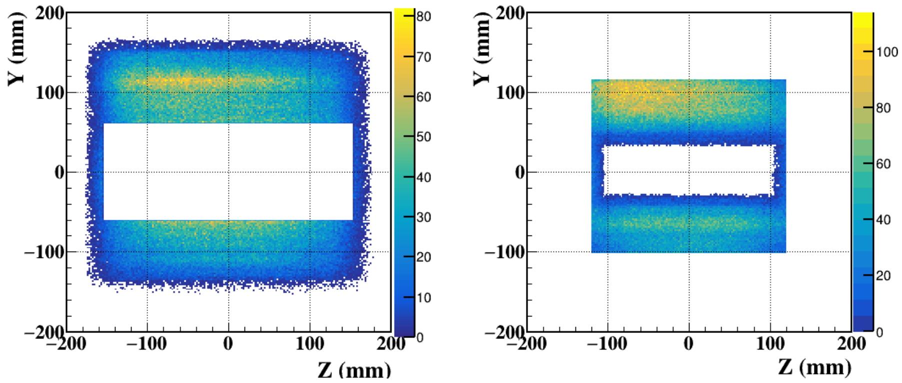

Figure 5.57 Example of the 2D cuts applied for the case of 20 mm offset of the cuts demonstrated in fig. 5.56. The left and right panels represent the cut at the decay chamber window and its image at the tracker window, respectively. Up-down asymmetry of this kind of background type is clearly visible.

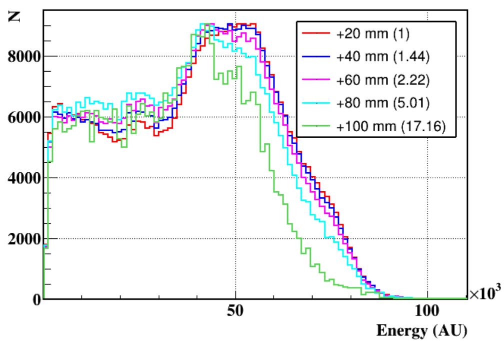

Figure 5.58 The energy spectra obtained for the position cuts shown in fig. 5.56. Each spectrum has been normalized to the largest maximum. The normalization factors are shown in brackets.

window, can be easily excluded from energy spectrum of electrons originating from decay of neutrons from the beam.

In the following part of this section, the energy spectra of events with tracks originating from inside of the decay chamber will be studied. In order to avoid contribution of particles that potentially could be scattered on the frame of decay chamber window, the positional cuts are applied as depicted in fig 5.59. Moreover, for the same reason, also the active area of tracker window is reduced for particles tracks. Dimension of MWDC window are decreased at each side by 3 mm along Y-direction and 15 mm along Z-direction. These cuts are estimated accordingly to position resolution in respective direction.

Energies of electrons emitted from the beam To further purify the neutron β-decay spectrum, the track position cuts were applied to select only those electrons which could originate from the volume of the beam core. In case of BRAND-0 data the 3D cuts of beam volume are not feasible since vertex of neutron decay can not be determined (lack of registered

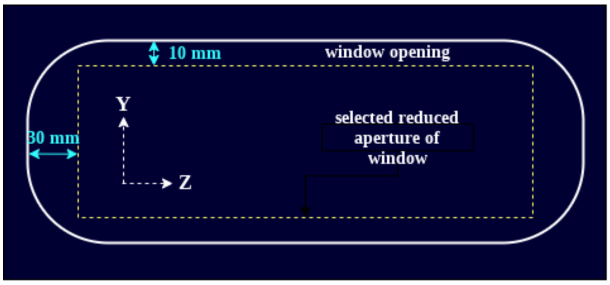

Figure 5.59 Positional cuts applied to select the events with reconstructed tracks origin within the decay chamber window. The area within the white line represents the actual opening size of the window. The area limited by the dashed yellow lines indicate the reduced aperture of the window. This cut is necessary to avoid contribution of electrons scattered on the inner surface of window frame.

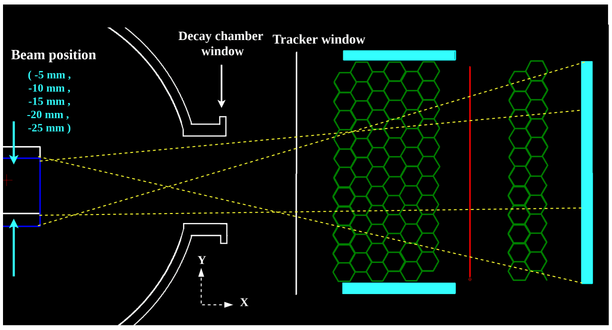

Figure 5.60 Illustration of the positional cuts applied to select the possibly pure energy spectra from neutron beam. Considered were only the tracks traversing the tracker window and the decay chamber window. At the beam position, the cuts were selected at nominal beam dimension and then restricted more with five steps of 5 mm each. The same cuts were employed both in Y- as in the Z-direction. Displacement of effective vertical beam position was taken into account: blue square shifted down from the chamber axis.

proton counterpart of decay). Thus, presented in this (and also in next one) paragraph track selection still not excludes background events created "behind" and "at front" of the beam. For selection it was made sure that the reconstructed tracks traverse both the decay chamber window and the tracker window with restrictions concerning their frames as explained above. Cuts on the beam dimension were applied along Y-and Z-direction. They were tightened in five, 5 mm steps starting from the nominal beam size (cf. fig. 5.60).

Fig. 5.61 shows the resulting energy spectra. Sharp cuts applied both in Y- as well in Z-direction significantly reduced number of accepted events. Nevertheless, the statistics in the plots is sufficient to draw the conclusions. Differently than expected, the two component shape of spectrum does not change with limiting the volume of track origin. This finding indicate that the visible background component follows similar spatial distribution as that of electrons from neutron decay. Explanation of this effect will be provided in chapter 7 where background examination is performed with Geant4 simulations.

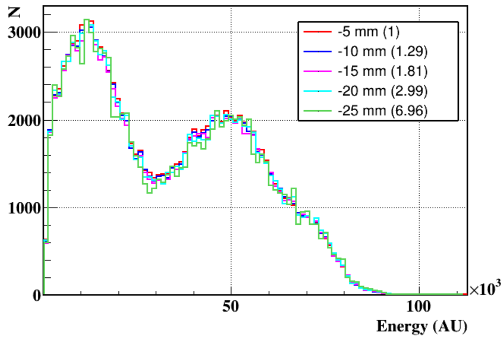

Figure 5.61 The energy spectra obtained with cuts applied on the beam size when electron tracks were reconstructed (cf. fig. 5.60). Spectra has been normalized to the largest maximum. Normalization factors are shown in the brackets. Despite of narrowing the beam size the relative background contribution to the spectrum remains constant.

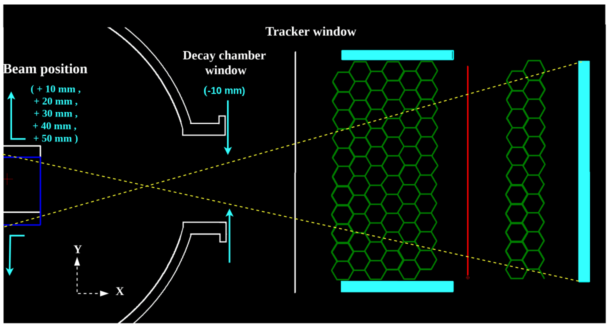

Figure 5.62 Positional cuts applied to investigate the energy spectra of events created by the beam halo. Selected tracks must traverse the tracker window and the decay chamber window, excluding their frames. At the beam position, the tracks were required to pass outside the main beam profile. Exclusion of the beam core started at its nominal dimension extended by 10 mm at both sides and continued until 50 mm at both sides, with the step of 10 mm. In Z-direction no any cuts were applied.

Contribution from beam halo The neutron beam profile measured during the run reveals a sharp decrease in neutron flux away from the beam center (cf. fig. 3.17). Nevertheless a precise shape of the beam distribution outside the beam core, so-called beam halo, is not known. It is important to consider also the interaction of the beam halo with the internal components of the decay chamber. Such interactions can generate the background events. The potential mechanisms responsible for generation of such a background are studied in chapter 7. To extract the contribution from the beam halo in the collected data, the cuts were implemented to select such events. Only events from outside of the beam core are selected with increasing of the distance from the beam center along Y-direction. It is illustrated in fig. 5.62.

The resulting energy spectra are shown in fig. 5.63. Also in case of halo events the relation of low energy component and high energy component of resulting energy spectra remains constant, independently of the applied cut. The low energy component larger than the high

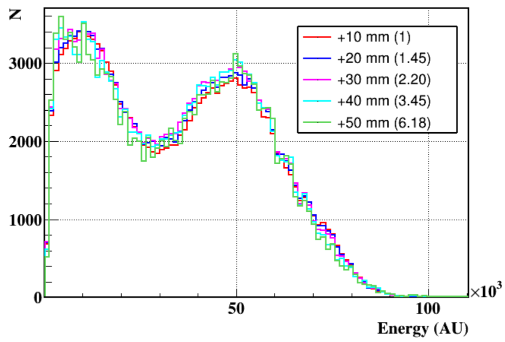

Figure 5.63 Energy spectra obtained for beam halo events. Applied cuts are explained in fig. 5.62. Spectra have been normalized to the largest maximum. Normalization factors are given in brackets.

energy component in the halo induced background might be a surprising effect. It can origin both from electrons from β-decay re-scattered from the decay chamber wall (Mott and Møller scattering) as well as from interaction of beam halo with the components of BRAND-0 apparatus inside the decay chamber. The yield of high energy electrons within applied cuts seems to be decreased.

Energy calibration of Back scintillator After identification of the main components of background which can be rejected from energy spectra by application of cuts on position of trajectories the energy spectrum of BRAND-0 experiment was created. The selected cuts are as follows: (*i*) frames of tracker and decay chamber windows are excluded; (*ii*) only tracks originating from the beam core are allowed (cut in Y-direction of $\pm$30 mm, including shift of the beam); (*iii*) no cut along Z-direction at the beam position.

The spectrum is shown in fig. 5.64 together with the spectrum collected for ^{207}Bi radioactive source. Positions of maximum of β-spectrum (at 270 keV - cf. fig. A.3) and position of maximum in bismuth spectrum (at 980 keV - cf. fig. A.6) provides 2 reference point for absolute calibration of energy axis. This way of energy calibration is not very precise since positions of those, only two, reference points are biased with large uncertainties. But observing the relative positions and the shapes of high-energy component of bismuth electron source and the β-spectrum from neutron decay, there is no doubt that low energy component of bismuth source should fit into the recorded energy range. This fact further strengthens the recognition of the poor energy resolution as the main reason of the absence of this low energy line in the obtained spectra.

Fig. 5.65 presents the already calibrated energy spectra of Back scintillator. Its left panel shows energy spectrum attributed to the beam core compared to the contribution of beam halo (for the given selection cuts). Right panel of this figure compares the same "beam" energy spectrum to the component originating from outside of decay chamber. All shown spectra were collected when restriction in track origin in Z-direction were the same. Differences was only allowed in selected range along Y-direction.

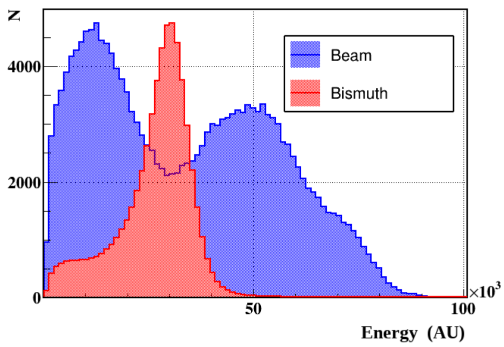

Figure 5.64 The total energy spectrum collected in Back_scint for beam data (blue histogram) and ^{207}Bi source (red histogram). Lower energy component of the "beam" spectrum is formed predominantly by electrons from β-decay of neutron beam. Position of its maximum (at 270 keV) together with position of peak in bismuth spectrum (at 980 keV) are used to perform the absolute energy calibration.

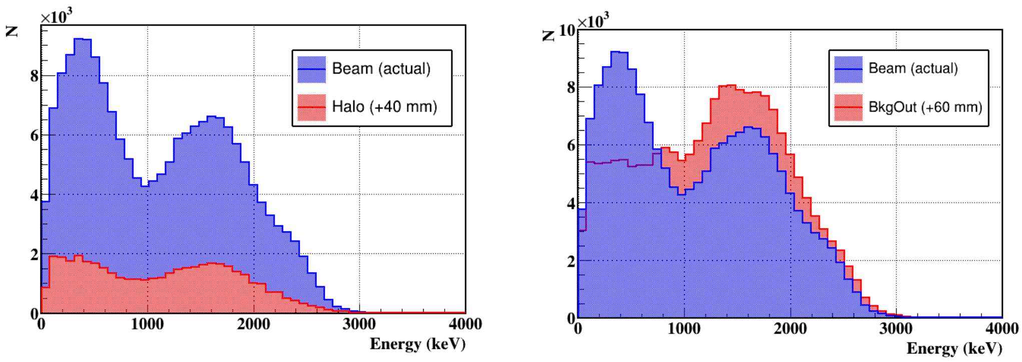

Figure 5.65 Left panel: comparison of the shapes and magnitudes between the selected spectrum of neutrons from core of the beam (blue histogram) and the background originating from the decay chamber but out of the beam region (red histogram). The later is for range of accepted events above ± 40 mm of the beam dimension along Y-direction. Right panel: the same but here "beam" spectrum is compared to background spectrum originating from outside of decay chamber window. Accepted background events stem from region above ± 60 mm from the edges of decay chamber window (in Y-direction).

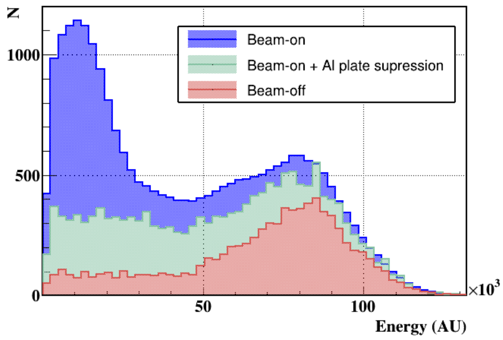

Figure 5.66 (Exceptionally, presented here spectra belong to data set no 6, where energy scaling is different than for set 7). Collection-time normalized and dead-time corrected the energy distributions of events when particles trajectories traversed the decay chamber window. Blue histogram - collected when beam was on; green histogram - collected when beam was on but vacuum window of decay chamber was covered with 3.8 mm thick aluminum plate. Despite of presence of a diaphragm still a significant background yield is recorded by the Mott polarimeter. Red histogram - time-normalized and dead-time corrected energy spectrum recorded for beam-off. Both constant and beam-induced background components are integrated. These findings indicate the importance of reliable method of background identification in BRAND experiment.

Examination of constant components of background

Spectrum of "blind window" The energy spectrum recorded during beam operation but when the vacuum window of decay chamber was covered by 3.8 mm thick aluminum plate is shown in fig. 5.66. β-decay electrons of energies lower than 800 keV can not be transferred trough such plate. In fig. 5.66 such collected spectrum is compared to the one collected without diaphragm. Trajectories from the whole window area (except the frame) were accepted. Both the low and the high energy components are present in "screened" spectrum. The low energy component, as expected, is suppressed but still remains at the level of 30% of normal "beam" spectrum. As it can be seen, the high-energy component did not move. This confirms that its shape is indeed an effect of, as previously claimed, the thickness of the Back scintillator and the limit of the TDC window. Geant4 simulations have shown that both the high and low energy components of background in this case are induced by high energy gamma propagating along the beam and also created inside the decay chamber. Detected electrons are the effect of their electromagnetic interaction (mainly Compton effect). To the low energy background visible behind the widow cover, also the neutron-induced reaction contribute. The simulations of background recorded in Back scintillator with the presence of aluminium cover of decay chamber window are especially difficult and long-lasting. Thus, collected only low statistics of simulated events prevents from precise definition of all contributions to actually recorded spectra.

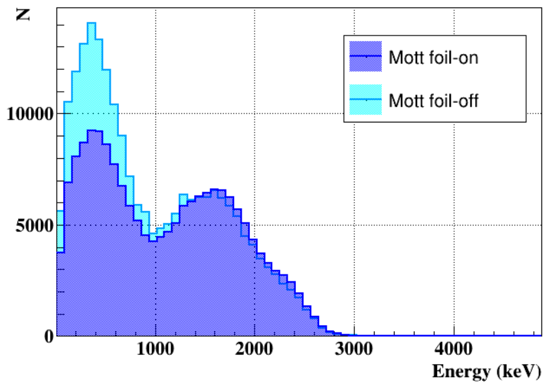

Figure 5.67 Time-normalized and dead-time corrected energy spectra recorded when Mott target was present inside tracker (deep blue histogram) and Mott target was removed (light blue histogram). Significant suppression of low energy component is realized.

Background spectrum for beam-off Fig. 5.66 also compares the time-normalized and dead-time corrected spectra collected during the periods of beam-on and beam-off. Positional cuts on the reconstructed trajectories in this case allow all events passing the decay chamber window excluding its frame. The beam-off distribution shows the expected suppression of the low energy component. However, still some amount of background events (9%) remains in the energy range of electrons from β-decay of free neutrons. The high energy background is also present. Presented beam-off spectrum contains both the component of radioactivity induced by beam in the components of BRAND-0 setup as well as the constant background component present in PF1B during routinely operation of the facility. At current stage of BRAND-0 these contributions are unresolved. Dedicated studies of the behaviour of the background spectrum and its yield after the beam stop are needed in the future experiments.

These results indicate that without detection of protons and reliable neutron decay vertex reconstruction the energy spectra measured in BRAND experiment (in ILL), in the range of measured β-spectrum can be contaminated with unresolved background events up to 30%.

Effect of the Mott target on the energy spectrum The presence of the Mott target, which is composed of heavy element of lead, influences the trajectories and energy of the β-particles. The energy losses are relatively week (cf. fig. 6.5) but the angular straggling for low energy electrons results in deviations of their original paths. This leads to deterioration of tracks quality and their possible rejection. Fig. 5.67 displays the comparison between the time-normalized energy spectra obtained with and without the presence of the Mott target in the MWDC. It can be clearly seen that the low energy part of the spectra, which is in the range of β-particles from the neutron decay, gets dampened in the presence of the Mott foil.

In BRAND experiment the knowledge of exact reaction event numbers is not of large importance since absolute cross sections are not measured. But large statistics of credible events is of high importance. Thus, increase of tracking effectiveness for low energy electrons is an important task. For the future tracker of BRAND it can be achieved by increase of amount of layers behind the Mott target. For such configuration separate tracking at both sides of Mott foil can be employed with matching of relevant tracklets.

The final energy spectrum collected in the Back_scint reveals a two component of energy. The low energy component is identified as a predominant contribution from the electrons of beam neutron decay. But admixture of even 30% of background particles in this energy range is very likely. The high energy component is in total a result of various background reaction. At the precision of current analysis the spacial origin of electrons contributing to the background created inside the decay chamber can not be differentiated from the distribution of beam itself. Some insight into background origin is provided by simulations presented in the next chapter.

Presence of the Mott target and limited precision of tracking suppress the accepted event number for energies of measured β-spectrum. This was also visible for measured spectrum of ^{207}Bi.

Events of this class are needed for control of experiment precision and for extraction of those correlation coefficients, which are not dependent on electron spin.

Angular straggling at the Mott target, when not accounted for, in case of not homogeneous thickness of the target, can impact the feasibility of measurement of β-decay asymmetry.

Energy measurement in the Mott detectors

For the energy analysis of the beam events registered in the Mott_dets, the data from time period 1 (most to the left) of fig. 5.53 was used. They exhibit higher statistical significance and lower variance in the gains of individual SiPM spectra. The shapes of the raw energy spectra collected by the selected SiPM sensors after the application of the gain balancing factors are presented in fig. 5.68.

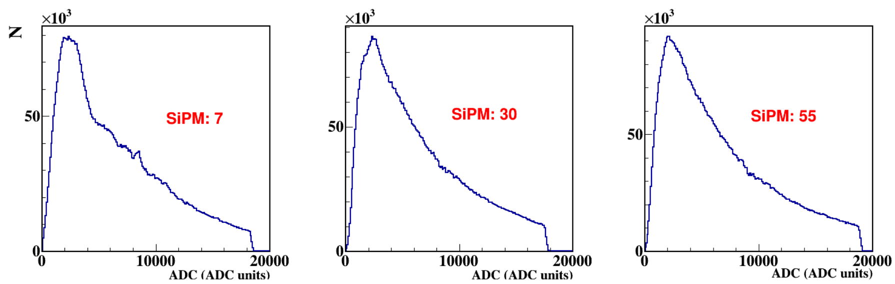

Figure 5.68 Raw signal amplitude spectra of the exemplary SiPMs collected during the beam operation. Some differences in their shapes are visible. The sharp cut at the right side of each spectrum is the result of the limited width of the TDC window.

The total energy spectra of both detectors, obtained by adding the signal amplitudes of all SiPMs of the respective Mott_dets are given in fig. 5.69. Still no any track position cuts were applied there. Those spectra do not show distinct components, which can be attributed to β-spectrum and background. Since the thickness of Mott_dets is the same as thickness of Back_scint (1 cm) the high energy component should also be present in this case.

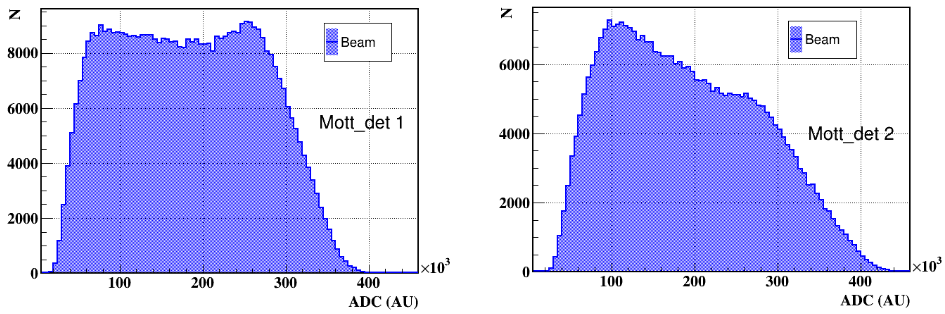

Figure 5.69 Raw spectra of beam events collected in individual Mott_dets. No positional cuts on the reconstructed track origin applied.

Similar analysis of possible spacial origin of detected track as done for the Back_scint spectra have been performed. Due to placement of the Mott_dets in MWDC, they can see deeper inside the decay chamber, away from the beam profile. They are more likely to detect any background contributions originating both above and below the nominal beam dimension. Fig 5.70 presents the positional cuts applied to the reconstructed trajectories in order to extract the energy spectra from such events. Energy spectra in the respective Mott_dets with these positional cuts is presented in fig. 5.71. Despite of reduced statistics, the shape of the spectra induced by beam halo do not differ from those of fig. 5.69.

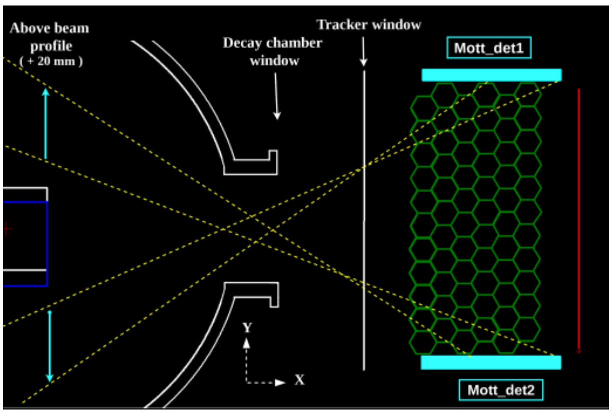

Figure 5.70 Illustration of the positional cuts applied to extract the energy spectra of the background events originating above and below the nominal beam dimension.

Due to geometry of the setup it follows that the acceptance of Mott detectors to direct electrons from the neutron decay is small (cf. fig. 5.72). It was an intentional feature, in order

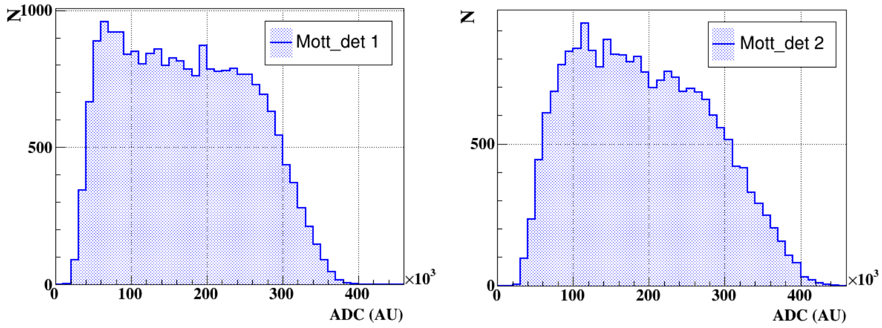

Figure 5.71 Energy spectra of background originating from beam halo.

to expose these detectors more to the electrons back-scattered from the Mott target. However, some of direct electrons from the beam core still could reach the Mott detectors.

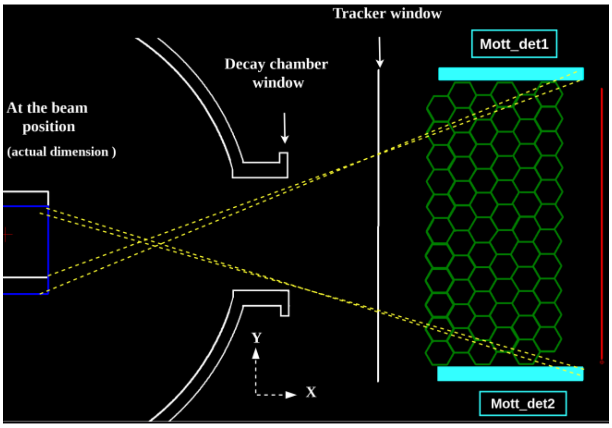

Figure 5.72 Illustration of the cuts applied to extract the energy spectra of the electrons originating directly from the beam core (dotted yellow lines). Only electrons stemming from most outer region of the beam core can contribute. Effective beam position (blue rectangle) is displaced from the chamber axis due to combined effect of magnetic field and misalignment of vertical position of Mott polarimeter (by 7 mm).

The energy spectra for such events are shown in fig. 5.73. The higher number of events registered in Mott_det1 compared to Mott_det2 is a result of the beam position being apparently shifted as explained earlier. The shape of both distributions change according to the expectations, showing clear enhancement in the lower energy range. But collected statistics and resolution is insufficient to resolve the components originating from β-decay of neutron beam and from possible background.

Direct beam events registered in Mott_dets are not of interest of BRAND physics. But their spectra can support the absolute energy calibration of Mott_dets. Unfortunately, in this case they are useless, due to reasons mentioned above. Moreover, these spectra can not be directly compared to ^{207}Bi spectrum. Variation of working conditions of SiPMs during the experiment does not permit a common energy scale for both classes of spectra.

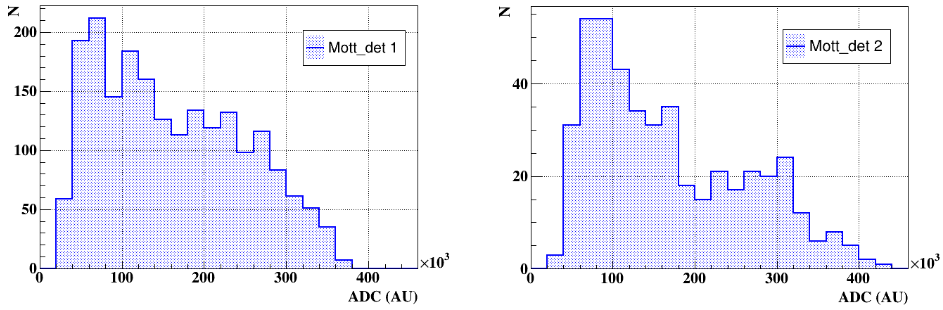

Figure 5.73 Energy spectra of the electrons originating from the beam core, which could be directly registered in one of Mott_dets. Due to very limited acceptance only low amount of such events can be collected. Difference in event number in both histograms appear due to effective shift of beam position (effects of magnetic field and physical displacement of Mott polarimeter along Y-axis by +7 mm).

Realized very poor energy resolution of Mott detectors of BRAND-0 experiment and lack of absolute calibration of their spectra makes impossible the calculation of those correlation coefficients, which are dependent on the energies of Mott scattered electrons.

Chapter 6

Performance of Mott Polarimetrer

The time available for performance tests of the prototype BRAND-0 setup was very limited. After the first very short run in October 2020, the setup underwent a significant extension and modification. It was the case for all components including the signal processing electronics. After completion of the modification permitting continuation of the tests only short time was left before second experimental run at ILL. This time was spend mainly for optimization of the working conditions of tracker. The aim was to achieve a stable and discharge-free operation with sufficient detection efficiency. Due to lack of Mott detectors and the final version of the readout electronics (which were provided only at the beginning of a second experiment), the global behavior and performance of the complete Mott polarimeter could not be tested.

Nevertheless, the basic checks of available components i.e. the tracker and Back scintillator have been performed. Both the laboratory tests and the limited data collected during the first, short run of BRAND experiment proved satisfactory position resolution of tracker derived from drift-time (in XY-plane). Position resolution in XZ-plane derived from signal charge measurement was significantly worse. The same was observed for energy spectra in the Back scintillator.

The material for detailed studies of detection system was collected only with completed apparatus during autumn ’21 experiment. These studies are presented in this work as the most actual ones. As presented in chapter 5, analysis of the data collected during the experimental run at IIL shows some peculiarity along with the low energy resolution and worsening of position resolution in Z-direction (determined with charge-division method).

Following the experiment, a certain tests were conducted in the laboratory to investigate the potential causes behind the issues observed in the data. This chapter presents a detailed account of those tests.

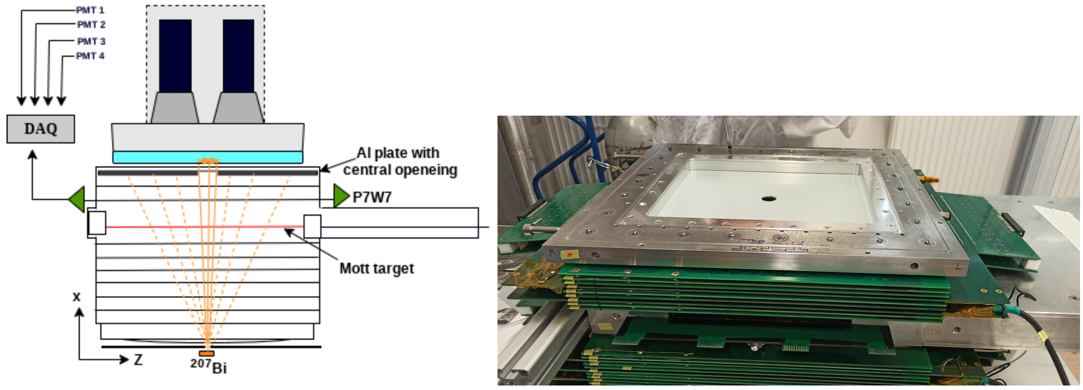

Figure 6.1 Modification of the Mott polarimeter for laboratory test of energy resolution of the Back scintillator. Left panel: schematic of the setup where orange lines (continues and dotted) present the trajectories of electrons from bismuth source in MWDC. The continues lines represent the trajectories, which can reach the scintillator surface through the circulars opening in the installed aluminum plate.; Right panel: aluminum plate with central opening installed between the tracker and Back scintillator permitting selection of electron hit position in Back scintilator is visible.

6.1 Energy resolution of the Back scintillator

As it was presented in sec. 5.4, the obtained energy resolution of all scintillators used in BRAND-0 setup is not satisfactory. The calibration data of the ^{207}Bi source taken at ILL during 2021 experiment showed low energy resolution (cf. sec. 5.4.1).

In order to identify the reason of these effects, the performance of the Back scintillator alone has been checked in the laboratory with the use of a simple ADC-based acquisition system, which is available in the detector laboratory of IFJ PAN.

6.1.1 Experimental setup and acquisition

Arrangement of the Mott polarimeter have been kept similar as during experiment at ILL. The Back scintillator has been irradiated by ^{207}Bi radioactive source placed at front of the tracker. Signals from the tracker have not been recorded, hence particle tracking could not be applied. Instead, in order to minimize the hit position dependence on the energy spectrum in Back scintillator, the 4 mm thick Al plate have been installed between tracker and Back scintillator. It had in the center an circular opening of 20 mm diameter. The γs emitted by ^{207}Bi were suppressed by requirement of coincidence of PMTs signals with tracker signal of the cell situated below the opening in Al plate. This arrangement is shown in fig. 6.1.

The circuitry of the signal processing is presented in fig. 6.2

6.1.2 Energy spectra

The shapes of the raw spectra registered by individual PMTs are presented in fig. 6.3. As expected, two main energy components formed by emission lines of electrons about 500

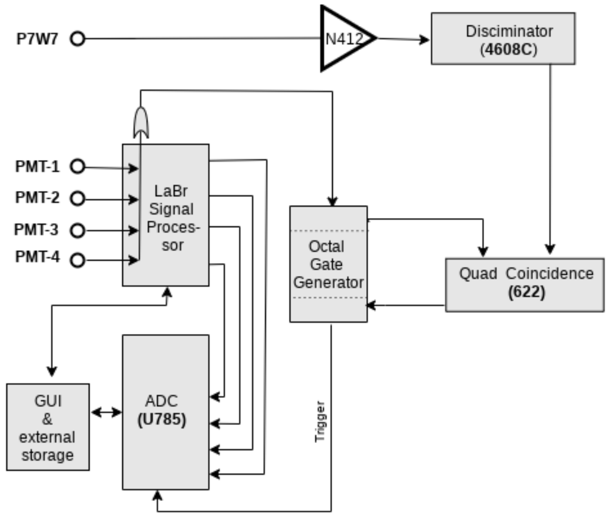

Figure 6.2 Scheme of the signal processing used during energy resolution test of Back scintillator with the use of ADC-based DAQ. Symbols: P7W7 - signal from cell (7,7), PMT-1-4 - signals from photomultipliers of the Back scintillator, other - names of electronics units.

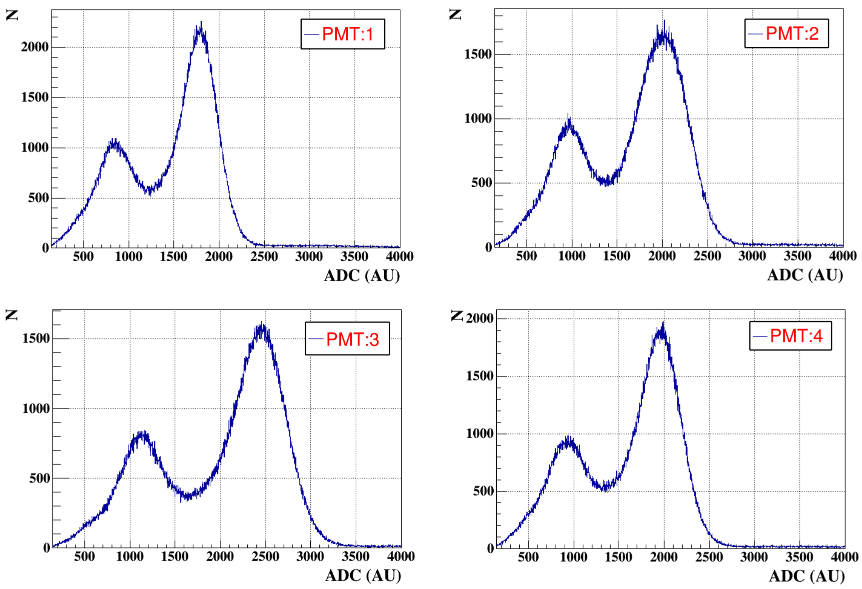

Figure 6.3 Raw energy spectra (in arbitrary units) of conversion electrons emitted from ^{207}Bi radioactive source collected by individual PMTs. Two components formed by electron energy lines around 500 keV and 1000 keV of are well resolved.

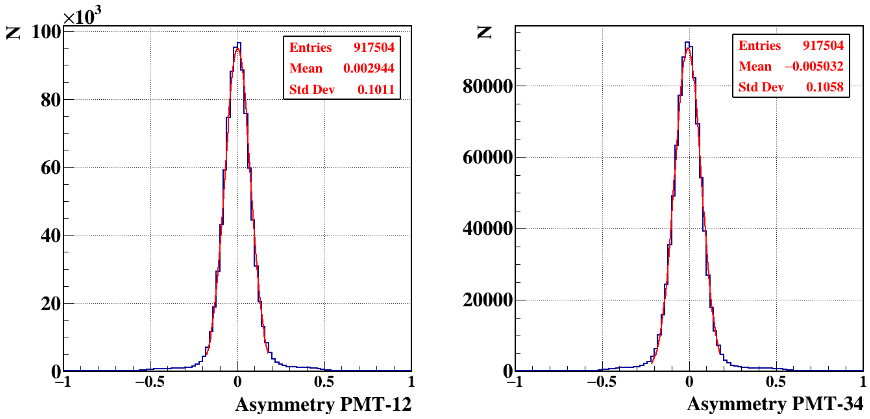

Figure 6.4 The asymmetry distribution, calculated with equation 5.11 for the amplitudes of the diagonally opposite PMTs. The left plot represents asymmetry between PMT 1 & 2 whereas the right one is for the asymmetry between PMT 3 & 4.

and 1000 keV are clearly visible. The total spectrum of electrons detected in the selected area of the Back scintillator is obtained by addition of individual PMT spectra. The proper gain balancing factor have been calculated from comparison of the peak positions in energy spectra of individual PMTs.

The correctness of applied PMT's gain compensation is proved by distributions of signal amplitude asymmetry. This quantity is calculated according to eqation 5.11 for diagonally opposite PMTs. As presented in fig. 6.4, the asymmetry distributions for PMT-1 and PMT-2 as well as PMT-3 and PMT-4 are centered at zero and are symmetric around this value.

Gain-corrected individual PMT's spectra were added event by event. The resulting ^{207}Bi spectrum registered in the center of the Back scintillator for the cases when Mott foil was present and removed is given in fig. 6.5. Presence of 2 μm thick lead layer causes a small energy losses, seen mainly for the high energy line, whereas the suppression of the lower energy component is about 5%.

Although the circular aperture allowed only a small area of exposure at the Back scintillator surface the background events (γs, cosmics) could not be completely excluded. In fig. 6.6 this background was fitted and deducted providing almost background-cleared spectral components of electron. They are at expected relative positions and their areas reflect the actual intensities of the ^{207}Bi electron lines. The energy resolution in the range of neutron decay β-spectrum (electron line at 500 keV) is of about 11%.

In the laboratory test, the energy spectrum of ^{207}Bi of the same structure have been recorded for all sets of PMT supply voltages as used during the run at ILL.

The results of the laboratory tests performed after the ILL experiment in autumn 2021, when instead of BRAND electronics and DAQ the simple ADC-based readout system was used, have proven the following facts:

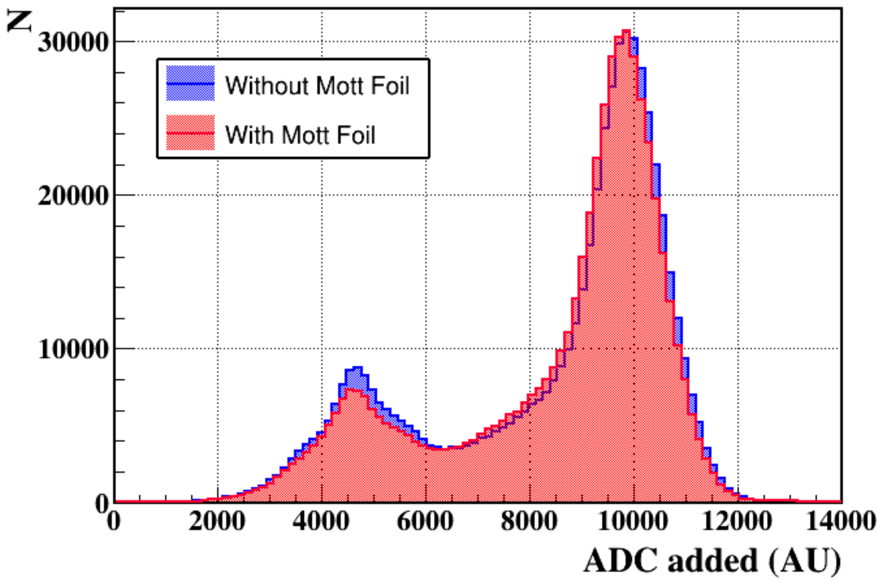

Figure 6.5 Energy spectrum of ^{207}Bi (in arbitrary units) registered in central part of the Back scintillator and recorded with a simple ADC-based acquisition system. Two well-resolved components of electron energy spectrum are visible. Modification of recorded spectrum due to electron straggling in the Mott foil is shown as well.

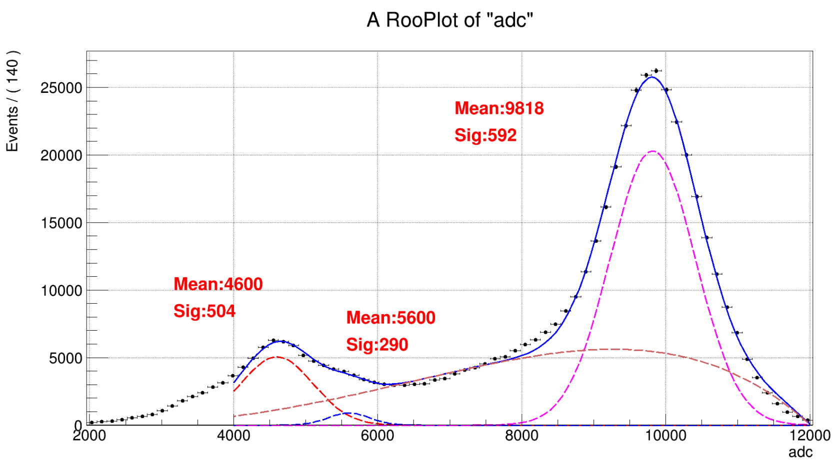

Figure 6.6 Background subtraction from recorded spectrum of electrons from ^{207}Bi. Energy resolution of Back scintillator in the range of lower component of the spectrum is equal to 11%. Arbitrary units are used.

- energy resolution of the Back scintillator is sufficient to resolve both groups of spectral electron lines ($\sim$500 and $\sim$1000 keV) of ^{207}Bi, even for events integrated over the circular area of 20 mm diameter on the scintillator surface;
- energy resolution in the energy range of β-particles from neutron decay is better than 11%;
- presence of Mott foil causes a small shift of energy spectrum of about 15 keV and suppression of low energy particles by $\sim$ 5%;
- HV values supplied to all four PMTs of the Back scintillator during experiments were always sufficient to record a β-spectrum in its range of interest.

6.2 Test of resolution of the Back scintillator with the BRAND electronics and DAQ

In the previous section it has been shown that the energy resolution of the Back scintillator should have been much better than the observed during the experimental run. In the following section, the tests of custom made front-end electronics used during the experiment, as a potential source of this problem, are presented.

6.2.1 Test of the dedicated analog front-end electronics

The analog signals of a shape similar as those delivered by the Back scintillator PMTs and of adjustable amplitude have been prepared with the help of a function pulse generator. After splitting they were fed into the dedicated signal lines of BRAND-0 electronics. The same signal from generator have been used to prepare the trigger for the DAQ system. This circuitry is shown in fig. 6.7.

The signals were processed in BRAND-0 DAQ as it was done during experimental run. Fig. 6.8 shows the screenshot from the oscilloscope with the relevant signals accumulated over 5 seconds. The yellow signals correspond to the output from one of the amplitude-to-time converters of the signal processing electronics. As it was described in sec. 3.2.4 the observed signal width should be proportional to amplitude of analog signal. Astonishingly, with ideal stability of analog input signal the signal converted into time shows a clear width variation of about 10%. Such behaviour of amplitude-to-time converter of electronics surely deteriorates the resolution of the quantities proportional to signal amplitude.

6.2.2 Baseline effect

After a closer look into a reason of observed signal width instability it was realized that the responsible are the small fluctuations of the baseline of the analog input signal. In order to quantify this effect an input signals generated with a constant amplitudes of the heights equivalent to the lower and to the higher ^{207}Bi electron energy lines were fed into PMT-signal

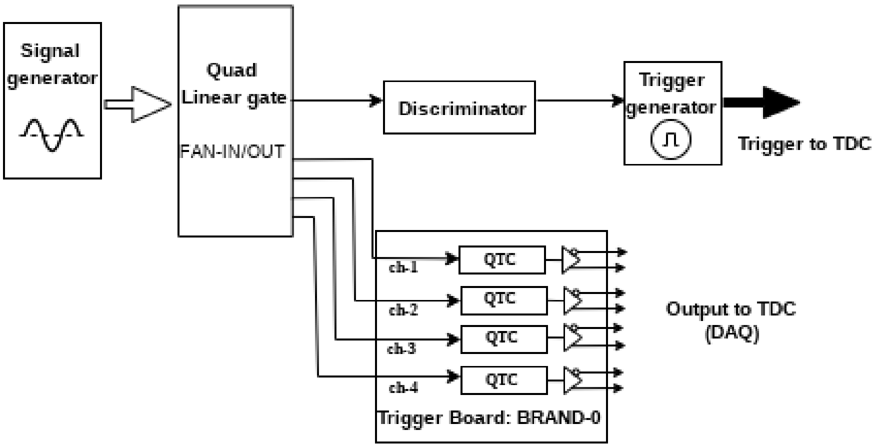

Figure 6.7 Signal circuitry used for the studies of the observed poor amplitude-resolution problem in BRAND-0 electronics. The notation "ch-n" corresponds to the ports where the inputs from the PMTs of the Back scintillator are fed into the Trigger board (cf. fig 3.13)

.

Figure 6.8 A scope screenshot showing the signals responsible for amplitude measurement via signal conversion into time as it was used in BRAND-0 electronics. Green signal - analog input from generator which mimic the PMT signal. Red signal - relevant trigger. Yellow signal - converted from amplitude the time signal intended for providing the amplitude information. 10% instability of a width of this signal is observed, whereas the amplitude of analog input signals remains stable.

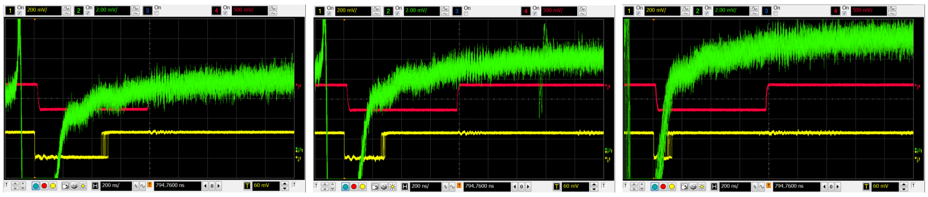

Figure 6.9 Constant input signal amplitude equivalent to lower energy component of ^{207}Bi spectrum (green). Only the lowest part of the signal is visible. Controlled variation of baseline position of input analog signal (green) with a step of 2 mV is done. Resulting drastic change of width of respective converted output pulse (yellow) is visible.

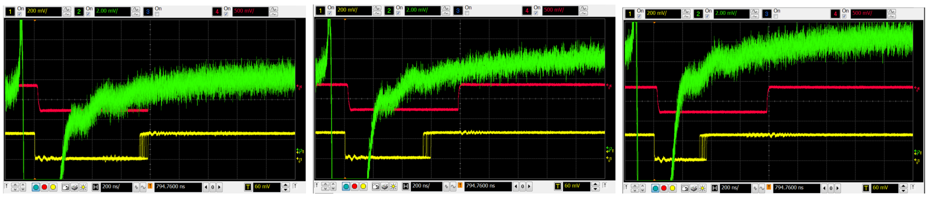

Figure 6.10 The same as in fig. 6.9 but for input signals of amplitude equivalent to higher energy component of ^{207}Bi spectrum.

inputs. The baselines of those signals were changed in the controlled way by a few mV as it is shown in fig. 6.9 and 6.10 for lover and higher electron energy lines, respectively.

Fig. 6.11 shows the amplitude distributions collected during above described tests for input signal amplitudes equivalent to lower energy component and higher energy component of ^{207}Bi spectrum. Note, that inspite of significant difference in amplitudes of signals equivalent for lower and higher component of ^{207}Bi spectrum, due to only small variation of baseline the resulting distributions can overlap.

The aforementioned results were used for calibration of baseline sensitivity of amplitude measurements in BRAND-0 experiment in autumn 2021. Calibration for lower energy region

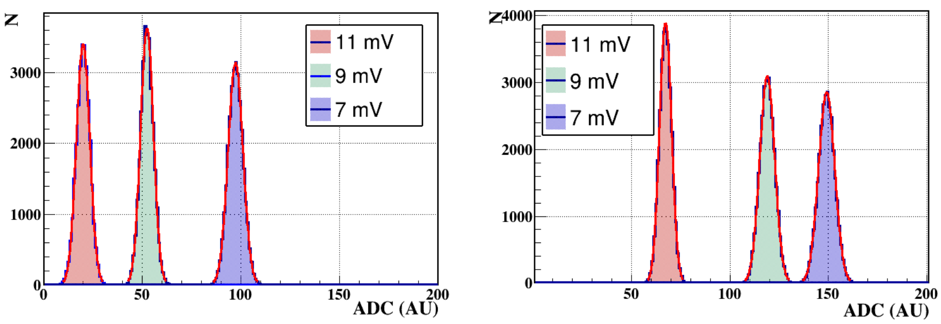

Figure 6.11 Distributions of amplitudes of generated analog signals equivalent for lower (left panel) and higher (right panel) components of ^{207}Bi spectrum. Signals were processed and recorded by the electronics and DAQ of BRAND-0. The baseline of input signals was changed by 2 mV. Arbitrary units are used.

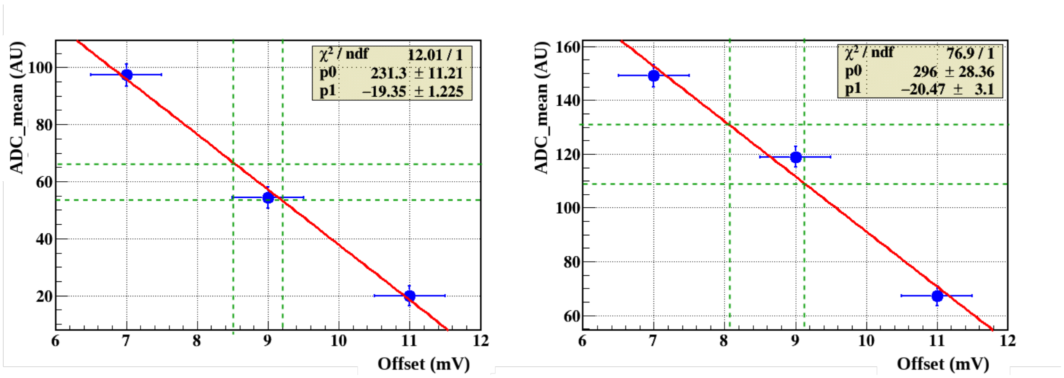

Figure 6.12 Dependence of signal amplitude on baseline position for read-out electronic system used in the BRAND-0 experiment in 2021. Left panel: dependence for energy range of lower component of ^{207}Bi spectrum registered in Back scintillator (~500 keV). 10% variation of recorded amplitude is caused by 0.7 mV displacement of baseline; right panel: the same but for energies ~1000 keV (upper component of ^{207}Bi spectrum). Here 10% deterioration of amplitude measurement is induced by 1 mV fluctuation of input signal baseline.

is shown in fig. 6.12 left panel, whereas the calibration for higher energy range is presnted in right panel of this figure.

Performed tests have shown undesired over-sensitivity of the amplitude measurement on the signal baseline position. The baseline fluctuation of only ± 0.4 mV caused an amplitude uncertainty of 10%. Low frequency oscillations of this range are hard to avoid in the experimental conditions. The presence of significant noise, as it was present during the BRAND-0 experiment, also could account for the baseline fluctuations.

This effect explains the observed low resolution of energy visible in the Back scintillator data. Since the same method of amplitude-to-time conversion was used both for Mott detectors and for charge-division method, the problems encountered for energy measurement by the Mott scintillators and poor track position resolution along the wire length can be explained by recognized effect of amplitude measurement instability.

The further studies of this effect and possible corrections of amplitude measurement method in the BRAND experiment are strongly demanded.

Chapter 7

Background studies for BRAND '21 experiment at ILL

For the measurement of correlation coefficients at the planned and demanded precision the clear signal from the actual β-decays of free polarized neutron must be distinguished from the background abundantly created in the severe radiation environment accompanying the experiments at the neutron beam facilities.

In case of PF1B experimental station at ILL special care is taken in order to diminish the undesired exposure of detection systems to the ambient radiation. It is attained by effective beam collimation, low beam divergence, construction of beam dump, but also by passive neutron and γ shielding (e.g. concrete and lead walls).

Also the BRAND-0 apparatus was constructed predominantly from light materials (with the dominance of aluminum) in order to diminish the building of γ and electron radiation sources in vicinity of sensing elements of the setup.

The philosophy of signal registration and selection in BRAND experiment is optimized for effective background rejection. Ultimately it will consists in multi stage processing, starting from the logical trigger construction, selection of multihit track with proper topology, signal discrimination based on the time and energy windows, and finally on the demanded coincidence of β-electron with the accompanying proton from neutron decay.

Unfortunately, during run of BRAND-0 in autumn of 2021 not all aforementioned functionalities of apparatus and data analysis were already available. The most effective tool for background reduction i.e. registration of proton-electron coincidence, could not be employed since the proton detectors have been still in R&D phase.

The part of apparatus dedicated for electron detection alone, is not able for complete background rejection. Thus, the electron spectra registered in Back- and Mott Scintillators are contaminated with the signals of the origin different than the studied β-decay of neutron.

Considering the origin, amount and distribution of experimental background in BRAND-0 measurement the following contributions have to be taken into account:

- contamination of neutron beam with the γ particles;

- presence of halo of neutron beam.

Their influence on the quality of BRAND results will be scrutinized in this chapter. The examination of background will be done for data collected with Back scintillator, since they provide better quality and event statistics than those obtained for Mott detectors. Nevertheless, at present stage of experiment development the background estimations valid for Back scintillator can be generalized also for other detection subsystem in BRAND setup.

7.1 Contamination of neutron beam with γs

7.1.1 Flux of γ particles in decay chamber of BRAND-0

The main source of possible γ contamination of the neutron beam at PF1B is the neutron polariser situated 4.8 m upstream of the center of BRAND decay chamber [73].

Quantities established by measuring the capture beam flux density at entrance, $\Phi_C^{pol\_in}$, and exit, $\Phi_C^{pol\_out}$, of the polarizer [56] are:

$\Phi_C^{pol\_in} = 2.11 \cdot 10^{10}\ \mathrm{n} \cdot \mathrm{cm}^{-2} \cdot \mathrm{s}^{-1}$;
$\Phi_C^{pol\_out} = 3.57 \cdot 10^{9}\ \mathrm{n} \cdot \mathrm{cm}^{-2} \cdot \mathrm{s}^{-1}$;

(For explanation of "capture" term relevant to cold neutron beam see section 3.3, page 26). The difference of these numbers is the total lost capture flux of neutrons, $\Phi_C^{pol\_lost}$, due to reactions undergoing in the polariser:

$\Phi_C^{pol\_lost} = 1.753 \cdot 10^{10}\ \mathrm{n} \cdot \mathrm{cm}^{-2} \cdot \mathrm{s}^{-1}$;

The polarization process of neutrons is in fact a filtering process where neutrons of demanded spin orientation are transmitted, and those of wrong spin direction are absorbed. Neutron are traversing a set of super-mirrors oriented along the direction of neutron beam. Mirrors are aligned such, that each neutron must undergo at least one scattering at the mirror surface. Neutron with the spin up are scattered at small angle and follow their path. Neutrons with spin down are scattered in opposite direction and absorbed in the underlying layer of gadolinium. The absorption process is realized by neutron capture reaction (n-capture):

$^{N}\mathrm{X}+\mathrm{n}\rightarrow{}^{N+1}\mathrm{X}\rightarrow \gamma, \beta \rightarrow{}^{N+1}\mathrm{X}+1$.

Neutrons in the polarizer are lost also due to their possible captures at other construction materials. Except of Ga they are: Fe, Si, N, Ti and sapphire (Al_2O_3) [42]. Compounds containing Fe/Si, Si/N and Gd/Ti form the thin surfaces of super-mirrors. Their relative abundance in the total material budget of polarizer is negligible. Most abundantly present are oxygen and aluminum nuclei. But despite of the highest abundance of oxygen among other materials in the polarizer, due to its small neutron capture cross section (0.00019 b) this reaction can be neglected when the total n-capture yield is calculated. Combining the amounts of individual isotopes and their n-capture cross sections it turns out that only Ga and Al isotopes are important for calculation of the neutron losses in polarizer.

Since the n-capture cross sections for cold neutrons are hardly known, the neutron capture cross sections used in this work are the measured or interpolated values obtained for thermal neutrons. They are provided by National Nuclear Data Center of Brookhaven National Laboratory as a Thermal Neutron Capture γ's "capgam" data base [74]. This is sufficient for calculation of relative yields of reactions induced by neutrons on individual isotopes present in polarizer or in construction of BRAND setup. When actual values of cross sections for cold neutron are needed they are calculated with the commonly accepted experimental scaling formula. It tells that n-capture cross sections scales with $1/v_n$ factor, where v_n is the neutron propagation speed. For cold neutrons supplied to PF1B this factor is equivalent to ratio of $\frac{2200m/s}{803m/s} = 2.74$.

The sapphire (Al_2O_3) is the main component of polariser used in ILL. Actually, the sapphire layers are the main medium of the super-mirror, in which the neutrons are transported. Application of sapphire instead of air, as it is used in conventional neutron polarizers, permitted to achieve an ultra-high average polarization of $P_n \geq 0.997$ and significantly decrease the volume of polarizer. The currently used polarizer form a box of $8 \times 8 \times 5$ cm^3, where 5 cm is the path length of the neutron in the polarizer [73].

The small drawback of such polarizer construction consists in a fact that transmitted neutrons are subject of additional capture at nuclei of its medium, i. e on ^{27}Al and ^{16}O. Since the capture probability on ^{16}O (0.00019 b) is 3 orders of magnitude smaller than on ^{27}Al (0.231 b), oxygen is not considered as an important component of capture reaction. But the presence of ^{27}Al nuclei is the second (after gadolinium) main reason of neutron loss in the polarizer volume.

Taking into account the total amount of Al in the polarizer, the capture beam flux density at its entrance ($\Phi_C^{pol\_in} = 2.11 \cdot 10^{10}$ n $\cdot$ cm$^{-2} \cdot$ s^{-1}) and assuming the appropriate capture cross-section for cold neutron at ^{27}Al as 0.63 barn the estimated lost neutron capture flux due to interaction in the sapphire layers of supermirror is:

$$\Phi_C^{pol\_lost\_Al} = 7.22 \cdot 10^8 \text{ n} \cdot \text{cm}^{-2} \cdot \text{s}^{-1};$$

It is only about 4 % of the total lost of neutrons in the polarimeter. It means that rest of neutron losses in polarimeter (96%) are due to capture reaction in gadolinium of the absorption layers. The latter one is estimated as:

$$\Phi_C^{pol\_lost\_Gd} = 1.681 \cdot 10^{10} \text{ n} \cdot \text{cm}^{-2} \cdot \text{s}^{-1};$$

This number is significantly larger than the half of the beam flux density entering the polarizer ($0.5 \cdot \Phi_C^{pol\_in} = 1.055 \cdot 10^{10}$ n $\cdot$ cm$^{-2} \cdot$ s^{-1}). The difference indicate that except the spin-filtering process of neutrons there are as well other occurrences when neutrons are lost at Ga nuclei.

Processes of neutron losses described above are associated with the emission of prompt γs and β-electrons. The electrons are deflected in the magnetic field of polarizer (B = 0.374 T, vertical) and efficiently dumped still inside its housing. For example the β-particles from decay of ^{28}Al have endpoint energy of 2.863 MeV. Electron of such energy curl with the radius of 4 mm in the magnetic field as this one used in polarizer of PF1B. But the γ particles remain unaffected in the direction of polarizer exit and can be transferred towards the experimental area along with the polarized neutron beam.

Since the γs in the polarizer are produced in prevailing way as the prompt deexcitations following the neutron capture, it is justified to assume that lost of each neutron in the polarizer is associated with the emission of some number of γs.

Deexcitation of the compound nucleus after the neutron capture proceeds via the emission of γ cascade. In general it might be a complex process involving many intermediate levels before the energy ground state is achieved. The resulting γ spectra may contain a number of individual energy lines of various intensities. Examples of γ spectra of ^{156}Gd, ^{158}Gd and ^{28}Al are shown in fig. 7.1.

Nucleus of ^{158}Gd, which is the dominant source of γ rays in the PF1B polarizer (see table 7.1 below), after n-capture is excited to 7937 MeV. In about 23% cases deexcitation proceeds with emission of two-three γs and led to ground state or to two low-lying excited levels [75]. Energies of these γ-rays vary in broad range. But at least one of them might be of high energy - not much smaller than that of total excitation. Emission of two γs of comparable energies, which carry almost all total excitation energy is also possible.

In other cases deexcitation undergoes via γ-cascade of higher multiplicity. Involved are more intermediate states, even more than 90. γs of such high multipliciy must carry only a small fraction of a total excitation energy. Also the secondary γs of broad energy spectrum can be created. Without detailed simulation of processes undergoing in the polariser the estimation of number and energies of created there γs is difficult and must be charged with large uncertainty. Such simulation is beyond the scope of this work.

Tentatively, for the sake of further background estimation, it is assumed that in average, each neutron lost in polariser is associated with creation of 10 γs.

Under such assumption, the estimated flux of γs in the polariser ($\Phi_{C_\gamma}^{pol}$) is one order of magnitude higher than total loss of neutrons capture flux there:

$$\Phi_{C_\gamma}^{pol} = 10 \cdot \Phi_C^{pol\_lost} = 1.753 \cdot 10^{11} \cdot \text{cm}^{-2} \cdot \text{s}^{-1};$$

This number has to be re-scaled to the actual cold neutron flux according to formula 3.4, i.e. divided by 3.17:

$\Phi_{\gamma}^{pol} = \frac{1}{3.17} \cdot \Phi_{C_{\gamma}}^{pol} = 5.55 \cdot 10^{10} \cdot \mathrm{cm}^{-2} \cdot \mathrm{s}^{-1}$

The γ beam intensity can be calculated taking into account the total active area of polarimeter equal to 8 cm $\times$ 8 cm = 64 cm^2:

$I_{\gamma} = 5.55 \cdot 10^{10} \cdot \mathrm{cm}^{-2} \cdot \mathrm{s}^{-1} \cdot 64\ \mathrm{cm}^2$

$I_{\gamma} = 3.55 \cdot 10^{12} \cdot \mathrm{s}^{-1}$

For estimation of number of γs contaminating the neutron beam at PF1B place the solid angle for their propagation along the neutron beam has to be calculated. Such flux of γ created in polarizer is not coherent and must have very large divergence. Thus, it is justified to calculate the solid angle for γs as defined by the last collimator at front of BRAND chamber. This collimator is located in the beam tube at the distance of 3.61 m from the polariser and for γ transition has square aperture of 7 cm $\times$ 7 cm. (cf. fig. 3.15).

Such calculated solid angle $(d\Omega_{\gamma})$ for polarizer's γ transmission into PF1B area is equal to $3.0 \cdot 10^{-5}$ of the 4πrad.

Taking it into account, finally, the γ beam intensity in the BRAND decay chamber (I_{γ}^{DC}) can be calculated as:

$I_{\gamma}^{DC} = I_{\gamma} \cdot d\Omega_{\gamma} = 3.55 \cdot 10^{12} \cdot \mathrm{s}^{-1} \cdot 3.0 \cdot 10^{-5}$

what makes:

$$I_{\gamma}^{DC} = 1.07 \cdot 10^{8} \cdot \mathrm{s}^{-1} \tag{7.1}$$

This value of I_{γ}^{DC} is the estimated γ intensity expected inside the BRAND-0 decay chamber during measurement of the β-decay correlations.

The calculated γ beam intensity I_{γ}^{DC}, has to be compared to the measured actual neutron beam intensity I^{m} of $8.36 \cdot 10^{9}$ n $\cdot$ s^{-1} (cf. equation 3.5). Their ratio is equal to $1.3 \cdot 10^{-2}$ what quantifies the actual contamination of cold neutron beam at PF1B facility with the γ particles.

The solid part of collimator is made as 5 cm thick lead layer. Such thickness of collimator assures high attenuation of γs. According to [53] γ of energies up to 1 MeV are suppressed there in 100%. For higher energies of γ-particles, but in the range of those created in polariser, i.e. below 8 MeV, the attenuation deceases to $\sim$ 90%. It means that some additional fraction of higher energy γs from polarizer can penetrate the lead blocks of collimators, enhancing their flux in decay chamber and modifying their spacial distribution.

It has to be stressed that processes of the neutron- and γ creation and their suppression in the polarizer and in the elements of PF1B transportation system would need a detailed simulation including complicated construction and geometry of polarizer and the rest of neutron transportation system. For the precision of the BRAND experiment foreseen ultimately, this task might be needed. At the current stage, when all systematic uncertainties are still dominated by apparatus and electronics imperfections, such precise simulations are not of highest importance.

7.1.2 γ spectrum

In the previous subsection it was estimated that the main reaction responsible for neutron loss in a polarizer is the capture process. It undergo at the materials used for construction of polarizer. They are: sapphire (Al_2O_3), Gd, Fe, Si, N, Ti [42].

Combining the amount of individual isotopes in the polarizer materials and their n-capture cross section it was shown that only the gadolinium and aluminum are important for calculation of γ spectrum. Their contribution to these processes are: Ga - 96 % and Al - 4 %.

Natural Ga is composed of 6 stable isotopes of significant abundances. For Al only isotope of ^{27}Al has to be taken into consideration.

The neutron capture properties of those Ga and Al isotopes are given in table 7.1.

Isotope	Isotopical Abundance [%]	Fractional abundance [%]	Cross-section [b]	Relative contribution [%]
^{154}Gd	2.18	2.1	85 ± 12	3.0E-3
^{155}Gd	14.8	14.2	60900 ± 500	1.76E1
^{156}Gd	20.5	19.7	1.8 ± 0.7	7.0E-4
^{157}Gd	15.7	15.1	254000 ± 815	7.83E1
^{158}Gd	24.8	23.8	2.2 ± 0.2	1.0E-3
^{160}Gd	21.9	21.1	1.4 ± 0.3	6.0E-4
^{27}Al	100	4.0		4.0E0

Table 7.1 Comparison of abundances, cross-sections for neutron capture and resulting relative contributions of individual Gd and Al isotopes to γ yield in PF1B polarizer. Fractional abundances are calculate in order to take into account the total Gd contribution of 96% and total Al contribution of 4%. Only reactions with ^{157}Gd (with relative contribution of $\sim$78%), ^{155}Gd ($\sim$18%) and ^{27}Al ($\sim$4%) are significant for production of γ background in BRAND experiment (see the last column of the table).

From table 7.1 it can be concluded that only yield of γs produced by neutron capture on ^{155}Gd, ^{157}Gd and ^{27}Al are significant as the possible neutron beam contamination. Their relative yield is of 17.6 %, 78.3 %, and 4%, respectively. Neutron capture at all other isotopes present in the polarizer contribute to the total γ yield with much less than 0.1 %.

Fig. 7.1 presents the examples of spectra of prompt γs emitted after the thermal neutron capture in ^{157}Gd, ^{155}Gd, and ^{27}Al. The spectra are adopted from database of [74], where also the numerical values of individual γ-line intensities are provided. It is assumed here that relevant γ spectra for reactions induced by cold neutrons are similar.

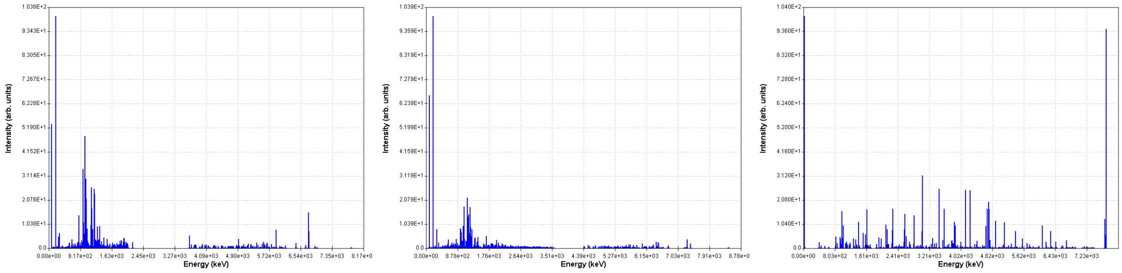

Figure 7.1 The γ spectra of reactions ^{157}Gd(n,γ)^{158}Gd (left panel), ^{155}Gd(n,γ)^{156}Gd (middle panel) and ^{27}Al(n,γ)^{28}Al (right panel) at thermal energies of neutrons. Adopted from [74].

7.2 Background simulations with Geant4

At the current stage of BRAND experiment the estimation of the rate of fake electron is possible only by means of simulations. These electrons are created by interactions of halo neutrons or γs with the components of BRAND-0 apparatus installed inside decay chamber and with internal walls of decay chamber.

7.2.1 Background rates

Two kinds of background origin are considered:

1. Undesired electrons created in the components of BRAND setup by the halo of neutron beam.

2. Charged particles created by γ particles stemming from the polarizer and propagating along the neutron beam.

Background rate induced by beam halo

Using full model of BRAND-0 setup described in appendix A the interaction of neutron beam with the BRAND setup has been performed. The beam parameters of the model were similar as those of actual beam provided to PF1B. In the simulations a neutron beam has energy of 0.004 meV - the mean of actual beam energy measured during BRAND experiment. The beam was shot on the collimator of the realistic material, dimensions and position in regard to the BRAND setup. The beam divergence in vertical and horizontal direction has been adjusted such, that the simulated beam profiles match those measured during experiment - cf. fig. 7.2 left panel. Fig. 7.2 right panel, contains a similar plot but vertical axis is presented in logarithmic scale and horizontal axis covers the whole diameter of decay chamber. In this way the shape and magnitude of simulated beam halo is shown. Simulated

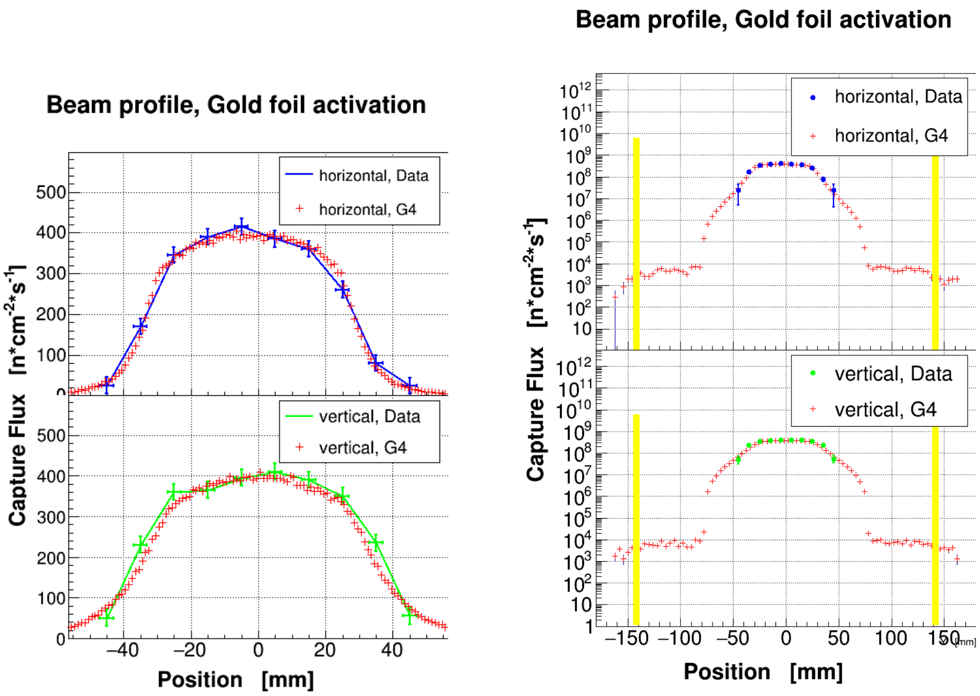

Figure 7.2 Left panel: simulated beam profiles in horizontal and vertical direction (red symbols) superimposed on measured profiles of the core of neutron beam in the decay chamber (blue/green lines and symbols). Right panel: (note the logarithmic scale) the same but for position range covering the whole radius of decay chamber. Yellow lines indicate location of the aluminum plates of HV cage inside decay chamber. Geant4 simulation provided the shape and intensity of beam halo originating from scattering of beam neutrons on the nuclei of rest gas and components of neutron transportation system. The level of $\sim 5 \cdot 10^3 \cdot \mathrm{cm}^{-2} \cdot \mathrm{s}^{-1}$ neutrons is expected at the radial position of HV cage.

beam halo is spreading over the whole radius of decay chamber and reaches value of up to $\sim 10^4 \cdot \mathrm{cm}^{-2} \cdot \mathrm{s}^{-1}$. On the plot also the radial position of the setup element closest to the beam center, i.e. HV cage, is indicated with the vertical yellow lines. According to the simulations, the solid aluminum plates and rings of HV cage are exposed to the neutron beam halo of the flux $\sim 5 \cdot 10^3 \cdot \mathrm{cm}^{-2} \cdot \mathrm{s}^{-1}$.

Since the knowledge about actual shape and magnitude of the beam halo is currently unavailable, the results of simulation of the background created by beam halo are biased with large uncertainty. But at the moment those uncertainties cannot be evaluated.

Nevertheless, it is worth to try at least to guess the components and reproduce the shape of the background visible in experimental energy spectra at energies exceeding the neutron β-spectrum ($>$ 1000 keV - cf. fig 7.7). Than, knowing the composition and magnitude of background spectrum at higher energies, indirectly, its yield in the energy range as for searched β-particles can be, hopefully, estimated.

In the Geant4 simulations the following processes were taken into account: elastic neutron scattering, neutron capture, radioactive decay of reaction products with γ and β emission, electromagnetic processes induced by secondary γ-particles (Compton scattering, photo-electric effect, e^+e^- pair creation), electromagnetic processes induced by electrons with emission of secondary electrons (ionization). The dominant material of neutron interaction is aluminum, which is a main construction material of decay chamber itself and HV cage installed inside.

$6.34 \cdot 10^9$ neutron tracks have been simulated. Their origin and distributions were identical as for simulations of the beam profiles and beam halo shown above. Neutrons traversed the whole transportation system of PF1B. Some of them (halo) interacted with the setup of BRAND-0.

Fig. 7.3 presents the two-dimensional distributions, in projection to XY-plane, of the primary and secondary interaction points for various processes acting during neutron beam transportation through the BRAND-0 setup.

Electrons created inside the decay chamber (also at its wall), which traversed through its window, entered the volume of tracker and have been detected in back scintillator, were counted. There have been 272 of such electron tracks. The resulting raw energy distribution of back scintillator is presented in fig. 7.4 left panel.

The ratio of accepted electron tracks to the total number of simulated neutrons is a product of probability of neutron beam interaction with components of BRAND setup, P^{halo} and the effective geometrical acceptance of the BRAND-0 detection system (tracker + Back scintillator) for the background induced by beam halo, A^{geom}_{halo}:

$$P^{halo} \cdot A^{geom}_{halo} = 272/(6.34 \cdot 10^9) = 4.29 \cdot 10^{-8}$$

The expected experimental detection rate of the Back scintillator due to the background induced by beam halo R^{BS}_{halo} can be calculated as:

$$R^{BS}_{halo} = I^m \cdot P^{halo} \cdot A^{geom}_{halo}$$

(I^m is the actual mean neutron beam intensity estimated in section 3.3, eq. 3.5). Thus,

$$R^{BS}_{halo} = 8.36 \cdot 10^9 \cdot 4.29 \cdot 10^{-8} = 359 \cdot s^{-1}$$

As it was already mentioned, the exact cross sections for cold neutron interactions are not well known. In the Geant4 simulations, due to lack of experimental data, the extrapolated

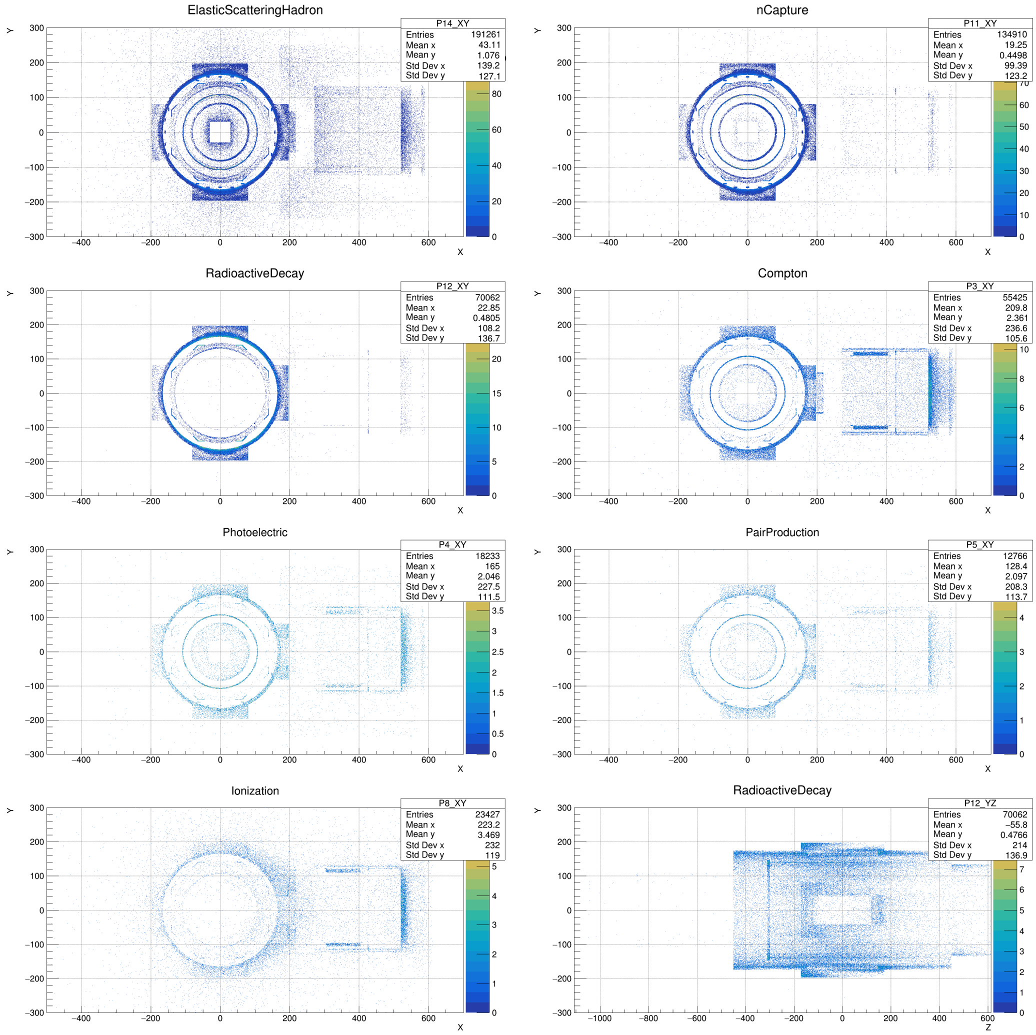

Figure 7.3 Geant4 simulations. Model of neutron beam and BRAND-0 setup was employed. Shown are distributions of interaction points for primary and secondary processes undergoing when neutron beam is transported along the BRAND-0 setup in PF1B cave. Names of processes are indicated as the histogram titles. Except the last one, presented are distributions projected to XY-plane of the setup. The last histogram (in lower right panel) is an example of interaction point distribution along the beam direction (i.e. in the YZ-plane). In this case, the distribution of secondary process of radioactive decay of exited nuclei of construction materials is shown.

values of cross sections are used. This procedure may introduce a significant error which is not under control. It is assumed here that extrapolations of interactions cross sections for cold neutrons may introduce the error of factor 2.

Another very important component of error may be caused by unknown shape of beam profiles outside the central region. Simulations with assumed beam dimensions and divergence provided well reproduced experimental profiles for the core of the beam (in the range of $\pm$ 5 cm in both directions). But visible is also an intense halo of the simulated neutron beam (cf. fig. 7.2 right panel). It is quite probable that the actual shape of the beam halo is

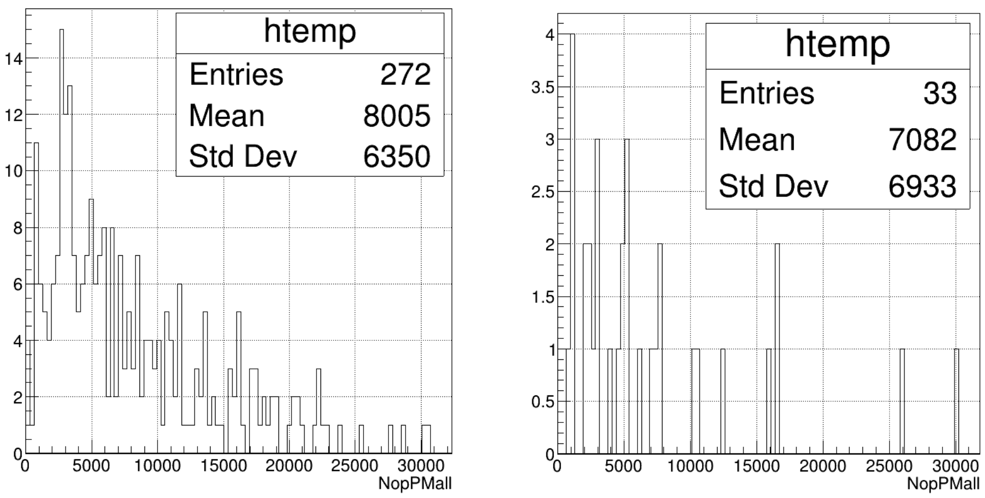

Figure 7.4 Simulated raw distributions of optical photons collected in photomultipliers of back scintillator. Left panel: for background electrons originating from interaction of beam halo with elements of BRAND setup; Right panel: the same as in left panel but for background events induced by γs propagating along the neutron beam. Indicated numbers of events are used for calculation of experimental acceptances of Back scintillator+tracker system for simulated processes.

different than this obtained from Geant4 simulations. This unclear situation with the shape of beam halo prompt to assume another component of uncertainty of beam halo induced background as another factor 2. Under those assumptions calculated rate of beam induced background is:

$$R_{halo}^{BS} = (360^{+720}_{-270}) \cdot \mathrm{s}^{-1} \quad (7.2)$$

Rate of γ induced background

Similar analysis can be conducted for spurious electrons created in the components of BRAND-0 setup by the γ particles produced in the polarizer and propagating along the neutron beam. In fig. 7.1 it is visible that the energy of the γs emitted during deexcitation of ^{158}Gd, ^{156}Gd and ^{28}Al spreads from $\sim$ 30 keV to $\sim$ 7.8 MeV. The most intense are regions of the lowest energy (but they do not contribute to background creation) and those about 1 MeV. High energy γs are less abundant but they contribute more to the background creation due to higher reaction cross section (see sec. 7.2.2 and fig. 7.6 right panel).

In order to estimate the amount of background created by γs propagating along the neutron beam a simulation similar to that describe above has been done. $2 \cdot 10^8$ γ tracks flying along the neutron beam were simulated. Their origin and divergence were randomly distributed in the same way as for the neutron beam. Their energies were randomly selected from the whole range of possible energies i.e. from 30 keV to 7.8 MeV (assuming flat distribution).

Fig. 7.5 presents the same as fig. 7.3 but for processes induced by γ contamination of the neutron beam.

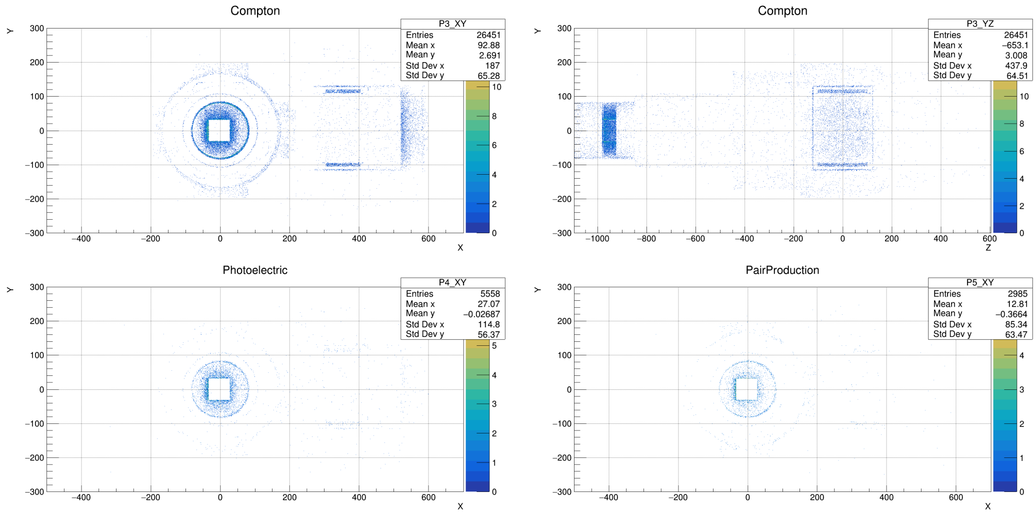

Figure 7.5 The same as in fig. 7.3 but for electromagnetic processes induced by γ particles propagating along the neutron beam. Except of distributions of vertices of three processes (Compton scattering, photoelectric effect and γ-e^{-}e^{+} conversion shown in projection to XY-plane, the one in upper right panel is an example of Compton scattering distributed in YZ-plane (along the beam direction).

Fig. 7.4 right panel shows the raw spectrum of back scintillator and number of counts for those electrons produced by γs inside the decay chamber, which traversed the decay chamber window, entered the tracker and have been registered in back scintillator. For 2 $\cdot\, 10^8$ simulated initial γ track 33 such events were recorded in back scintillator. A ratio of these numbers gives the product of electron (of sufficient energy) production probability by the γ, P^γ, and the geometrical acceptance for recording of such electrons in the tracker and Back scintillator, A^{geom}_γ :

$$P^\gamma \cdot A^{geom}_\gamma = 33/(2 \cdot 10^8) = 1.65 \cdot 10^{-7}$$

Thus, the expected experimental rate of γ induced background in the Back scintillator (R^{BS}_γ) is calculated as:

$$R^{BS}_\gamma = I^{DC}_\gamma \cdot P^\gamma \cdot A^{geom}_\gamma$$

$$R^{BS}_\gamma = 17.7 \cdot \mathrm{s}^{-1}$$

Estimated error should include the uncertainties of the the neutron flux measurement and all simplifications of the γ spectrum taken into account. It is estimated that total uncertainty in this case is of factor 2. Thus, the expected rate of γ induced background in back scintillator is:

$$R_\gamma^{BS} = (18^{+18}_{-9}) \cdot \mathrm{s}^{-1} \tag{7.3}$$

Other sources of background

Other sources of experimental background created inside or in vicinity of the BRAND-0 detection system has been also considered. Neutron capture reaction are possible also on the rest gas inside the transportation system, the CuBe wires of the HV cage or in the LiF rubber (of 80 % enriched ^{6}Li) present in the collimator and in the beam stop. But it was calculated or/and simulated that due to the trace amount of these materials (for case of N, O, Cu, Be) or due to geometrical restriction (for Li and F) the probability of recording of electrons created in these materials by the BRAND-0 detection system is negligible. Elastic interaction of transported neutrons with the nuclei of the rest gas contributes to the build up of beam halo and is included in the simulations of halo-induced background.

Summary of background simulations

Under assumption taken in order to simulate the yield and components of background (which are explained above), it can be concluded that the background registered in the detectors of BRAND-0 experiment is dominated by reactions induced by beam halo in the components of the setup. Its rate can be higher than the expected signal from β-decay of neutron beam (cf. eq. 3.10 in section 3.3). Careful studies of the collected energy spectra (cf. sec. 7.3) indicate that actual background induced by beam halo is at least one order of magnitude smaller than the value estimated here. The component of background induced by γ-particles inside the decay chamber of BRAND-0 is of the same amount as the expected signal rate (eq. 3.10) .

7.2.2 Background spectrum

Fig. 7.6 presents the simulated spectra of the background recorded by the tracker+Back scintillator. Individual components are indicated. The background induced by the interaction of neutrons with the elements of BRAND-0 apparatus is shown at left panel of fig. 7.6. In this case the highest yield of spurious electrons is induced by nuclear processes, i.e. neutron capture and radioactive decay of excited compound nuclei. Those processes are associated with γ emission, thus, some contribution of "secondary" γ-induced electromagnetic processes (Compton scattering, photoelectric effect and γ-conversions is observed as well. It is important to note that about 8% of registered background electrons are the secondary products of various electromagnetic processes. In Geant4 they are referred to as "ionization". The relative yields of individual contributions visible in left panel of fig. 7.6 follows the results of simulations.

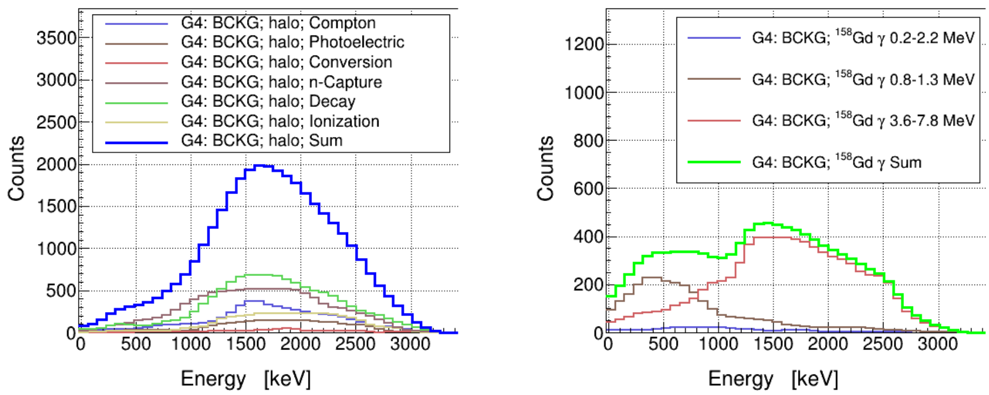

Figure 7.6 Simulated with Geant4 spectra of experimental background detected in back scintillator in coincidence with tracker. Background particles originate from interior of decay chamber. Left panel: background spectrum induced by hadronic and electromagnetic reaction of primary and secondary particles of beam halo. Right panel: sum of electromagnetic processes induced by γ particles traveling along neutron beam. Separately shown are contributions from γs of energies from three energy ranges where γ intensities are different (cf. fig. 7.1).

The background spectrum induced by "primary" γs (those propagating from polarizer along the neutron transport system) is shown in fig. 7.6 right panel. In order to take into account the varying intensities of γ of different energies (cf. fig. 7.1), three ranges of γ energies have been distinguished in the simulations. γ particles of energies 200-800 keV together with 1300-2200 keV was taken as one energy interval contributing to the background simulation with intensity of 28%. Energies of 800-1300 keV group γs with the highest relative intensity of 57%. γs with the energies of 3600-7800 keV contribute only with of 15%. Intensities of γs of individual energy ranges have been calculated in relation to the total intensity of energy spectrum integrated between 200 and 7800 keV. Spectrum of ^{158}Gd was used for this aim as having the most dominant contribution to the background. It was also checked (by simulations) that those γ particles, which are emitted with energies below 200 keV could not contribute to production of BRAND-0 detectable background.

In simulation, the energies of γ particles within given energy range have been selected randomly from the flat distributions.

As it is shown in resulting distribution in right panel of fig. 7.6, despite of much lower emission frequency, the processes induced by higher energy γs contribute more to the background production than the dominant low energy γs. In case of γ-induced background the spurious electrons are predominantly created by Compton scattering.

Simulation of experimental background in BRAND-0 experiment demands a huge amount of CPU time. Thus, for rare processes only the minimal number of counts preserving the statistic significance could be simulated. For this reason the background spectra shown in fig. 7.6 (and later on in fig. 7.7) have been smoothed with the use of TH1::Smooth() function of CERN Root toolkit [76].

7.3 Comparison of experimental data with simulations

Rate of counts in back scintillator recorded by scaler of DAQ is $R_{exp}^{BS} = (940 \pm 50) \cdot s^{-1}$. This number includes all events recorded per second. Also those when any particle, also not electrons and those electrons not originating from inside of decay chamber, was able to create a signal in back scintillator. Important is to select out of R_{exp}^{BS} only those events, when signals of back scintillator are in coincidence with tracker. Numbers of such events, created by electrons originating from inside of decay chamber and recorded in the Back scintillator in coincidence with tracker, were identified in analysis of experimental data. They are:

for the case when neutron beam was on:

$R_{exp}^{BS\&Tr\&DC\_Beam} = (49 \pm 4) \cdot s^{-1}$

and when neutron beam was off:

$R_{exp}^{BS\&Tr\&DC\_NoBeam} = (16 \pm 2) \cdot s^{-1}$

The difference of these rates gives the estimation of experimental rate of credible signal events detected in back scintilator:

$$R_{exp}^{BS\&Tr\&DC} = (33 \pm 4) \cdot s^{-1} \tag{7.4}$$

7.3.1 Signal to background ratio for back scintillator

Above calculated rate $R_{exp}^{BS\&Tr\&DC}$ comprises both events of searched for true β-particles of beam neutron decay as well as the spurious events originating from inside decay chamber. $R_{exp}^{BS\&Tr\&DC} = (33 \pm 4) \cdot s^{-1}$ agrees well with simulated sum of numbers of signal contribution ($R_{\beta}^{BS} = (17 \pm 5) \cdot s^{-1}$) (cf. eq. 3.10) and γ-induced background ($R_{\gamma}^{BS} = (18\ ^{+18}_{-9}) \cdot s^{-1}$) (eq. 7.3). Estimated contribution of beam halo induced background ($R_{halo}^{BS} = (360\ ^{+720}_{-270}) \cdot s^{-1}$) (eq. **??**) is evidently strongly overestimated. The reason of this disagreement consists most likely in nonphysical shape of simulated beam halo (fig. 7.2 right panel). Unfortunately, the results of beam halo simulation can not be verified at present stage of experiment. For the future experimental runs of BRAND it would be desirable to extend the range of beam profile measurement for the whole radius of decay chamber.

Comparison of experimental and simulated particle rates (disregarding the simulated rate of beam halo induced background) permits to conclude that out of experimentally detected events ($R_{exp}^{BS\&Tr\&DC} = (33 \pm 4) \cdot s^{-1}$) only about 50 ± 35 % could be the signals from measured β-decay. The remaining 50% most likely results from background reactions. Fortunately, comparing the background spectra of fig. 7.6, it seems that the background yield is larger for higher energies of registered events, whereas in the range of expected β-spectrum the background particles contribute less. But, due to unknown or uncertain contribution of background events a precise estimation of β-spectrum contamination with spurious events is not feasible at this stage of experiment.

The best reproduction of the shape of experimental energy distribution of back scintillator is presented in fig. 7.7. It has been obtained for the following partial yields of signal and

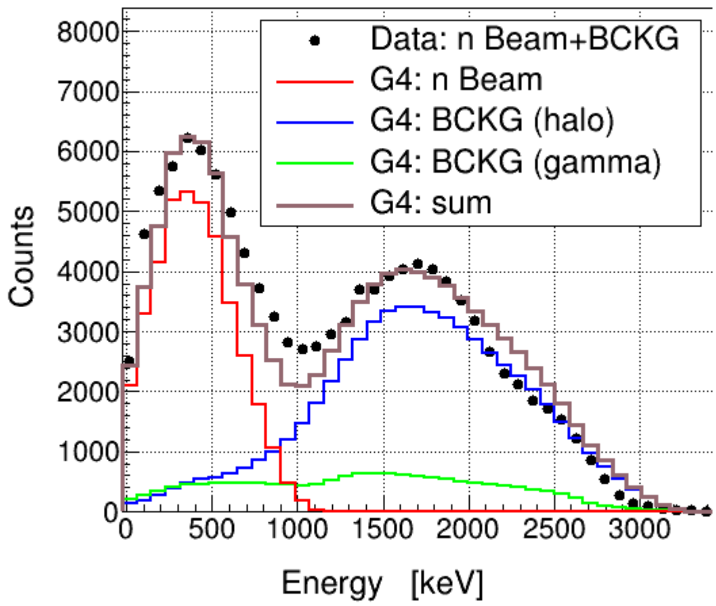

Figure 7.7 Experimental energy spectrum of Back scintillator for electrons detected in coincidence with MWDC and with tracks reconstructed as originating from interior of decay chamber (black dots). It is compared with results of Geant4 simulations of β-spectrum of electrons from neutron decay (red line), components of background reactions due to beam halo (blue line) and stray γs propagating inside the neutron transport system (green line). Despite of unavoidable simplifications and uncertainties present both in the data analysis as in the simulations, the sum of signal and background reaction well reproduces the shape of experimental spectrum. The uncertain magnitude of background has been normalized to the maximum of a bump visible in experimental spectrum above the energy of neutron decay β-spectrum (> 1000 keV).

background components:

β-decay : 35%
background (beam halo) : 52%
background (γs) : 13%

This proportions are in good agreement with above estimated signal to background ratio in the back scintillator spectrum.

The actual endpoint energy of free neutron β-spectrum is 782.35 keV. Observed in fig.7.7 tail of simulated β-spectrum extending beyond this value is mainly due to limited resolution observed for experimental spectra. The simulated energy distributions needs to be significantly smeared in order to reproduce the actual ones. (cf. sec. 5.4.1 for discussion of energy resolution of the Back scintillator and more detailed explanation.) Some uncertainty in energy distributions appears also due to limited precision of simulated light collection/attenuation processes in Back scintilator+lightguide+photomultipliers. Due to complexity of the light propagation and light collection process the experimental energy spectra of individual photomultipliers could not be exactly reproduced in simulations. When the correction of position dependence of light collection is applied, for some small fraction of simulated data an artificial shift of energy spectra toward higher values is observed.

7.3.2 Background contamination of β-spectrum for selected energy bins

From fig. 7.7 the signal to background ratio for individual energy ranges can be estimated. The results are presented in table 7.2.

Energy range [keV]	Signal+Backgr. [counts]	Backgr. (halo) [counts]	Backgr. (γ) [counts]	Backgr. sum [counts]	Backgr. percentage [%]
0-250	12490	600	828	1428	11
250-500	18012	1410	1316	2726	15
500-750	14904	1926	1409	3335	22
750-1000	9781	3057	1378	4435	45
1000-1250	8438	5424	1414	6838	81
1250-3000	52598	48019	8763	56782	100

Table 7.2 Signal and background contribution for different energy bins of energy spectrum registered in Back scintillator and shown in fig. 7.7. In the range of energies of measured β-spectrum, i.e. below ~750 keV the unresolved background contribution varies between 11% and 22%.

As expected the upper part ($>$ 1000 keV) of energy spectrum of back scintillator is entirely formed out of electrons originating from background reactions. In the energy range of 750 - 1000 keV, where no β-particles from neutron decay are expected, still 55 % of signal particles is present. It is due to above mentioned limited precision of experimental (and simulated) energy spectra and of position dependency corrections of energy in simulated data.

In the energy range of interest, i.e. below 750 keV , where collected β-spectrum is registered the signal to background ratio varies from 11% to 22%. Estimated uncertainty of signal to background ratio is 35%. These values are in agreement with the estimation of background contribution to the β-energy spectrum obtained from experimental data in sec. 5.4.2. That value was of 30%.

7.3.3 Conclusions of background simulations

Estimation of background component in the distributions measured in BRAND-0 experiment is, up to now, based entirely on the results of Geant4 simulations. It is biased with large uncertainty resulting from:

- simplification in the model of experimental geometry;
- lack of knowledge of relevant cross sections for cold neutron interactions;
- simplification of processes taking part in polarizer;
- not physical level of simulated beam halo;
- disregarding of projectiles and processes taking part outside the neutron transportation system.

Despite of these drawbacks, the obtained level of background seems to be realistic. The same amount of background has to be considered also for the Mott detectors installed inside the tracker in close vicinity of the back scintillator.

At the current stage of development of BRAND experiment the spurious electron tracks of energy below 780 keV, created in the decay chamber can not be identified and rejected. Thus, estimated level of background contamination of obtained energy spectra has to be taken into account as an systematic effect of large uncertainty in the analysis of experimental data.

Despite of limited precision of experimental background simulations performed with Geant4 for BRAND-0, they show a need of advanced modeling of experimental setup and beam transportation, which is indispensable support for data analysis and their interpretation, especially in high precision experiments. Constructed model of BRAND-0 setup and conducted simulations are the first attempts oriented in this direction.

Chapter 8

Feasibility of A, N and R measurement in BRAND-0 experiment

In order to accomplish the scientific aim of the BRAND project, i.e. to measure 11 correlation coefficients of neutron β-decay, a complete kinematics of neutron decay must be determined. For this aim both the electron's and proton's four momenta as well as all components of electron spin need to be measured.

With the present prototype of BRAND-0 setup, where protons still could not be measured, only the coefficients depending solely on electron related observables might be addressed. The general equation of the decay rate distribution of β-decay (eq. 2.2) is reduced to the following form [48]:

$$W(\mathbf{J}, \sigma_\perp, E_\mathrm{e}, \mathbf{p}) \propto 1 + \mathbf{P} \cdot \left(A\frac{\mathbf{p}}{E_\mathrm{e}} + N\hat{\sigma_\perp} + R\frac{\mathbf{p} \times \hat{\sigma_\perp}}{E_\mathrm{e}} \right) \tag{8.1}$$

Where $\mathbf{P}$ is average neutron polarisation ($\frac{\langle \mathbf{J} \rangle}{J}$). It means that only coefficients A, N and R remain in the scope of BRAND-0 experiment. Unfortunately, at the present stage of the experiment development, measurements of A, N and R are strongly affected by the low precision of track reconstruction, poor electron energy determination, insufficient collected event statistics and limitations specific to individual correlation coefficients, related to the geometry of the setup. Nevertheless, attempts to check a feasibility of estimation of those coefficients have been undertaken. Results will be presented in the following sections.

8.1 β-decay asymmetry

The non-zero electron emission asymmetry in β-decay, depending on the orientation of initial spin of decaying particle was first observed in the famous experiment of C. S. Wu et. al. [77]. In this experiment, it was realized that the electrons from spin oriented particles of ^{60}Co are preferentially emitted into hemisphere opposite to the spin direction of decaying nuclei. Measured asymmetry was of the order of 11%. It was the first observation of parity violation in weak interaction.

From that time the correlation coefficient A, which characterizes the strength of β-decay asymmetry (cf. eqs. 2.2 and 8.1), have been precisely measured in several experiments, e.g. [78–82]. It is one of the best known parameters of weak interaction. From the value of A the ratio of axial-vector and vector coupling constants in weak interaction can be determined. This is important for studies of fine components of weak force and can be used for the determination of V_{ud} element of Cabibbo-Kobayashi-Maskawa (CKM) matrix [24]. The present average experimental value of A parameter is -0.11958 $\pm$0.0002 (Particle Data Group, 2022 [62]).

For the case when only electron momentum is detectable, the decay rate of polarised neutrons from eq. 8.1 can be written as:

$$W^{\pm}(\boldsymbol{\beta}, \gamma) = W_0[1 + A\mathbf{P} \cdot \boldsymbol{\beta} \cos(\gamma)], \tag{8.2}$$

where the sign in subscript represents the state of neutron polarization with the average polarisation $\mathbf{P}$, W_0 is the decay rate of unpolarized neutrons, $\boldsymbol{\beta} = v/\mathrm{c}$ is the electron velocity normalised to the speed of light, γ is electron emission angle with respect to the direction of neutron polarisation (cf. fig. 8.9).

For the BRAND experiment the A parameter is of highest interest. Its precise measurement provides the best way of the determination of average neutron polarization which enters directly into systematic error of all other correlation coefficients. The another way of averaging would involve multidimensional integrals (neutron polarization depends on its wavelength, position in the beam, beam divergence), which, even for as good polarized beam as this available at ILL, could generate substantial systematic error.

A parameter measurement in BRAND-0 was not of primary importance. Indeed, the BRAND-0 polarimeter is situated in an unfavorable position with respect to the neutron spin orientation. When viewed from direction perpendicular to the neutron spin axis, the effect of the decay asymmetry for both states of spin flippers is the lowest in this case ($\gamma \sim 90°$, $\cos(\gamma) \sim 0$). The small solid angle of the polarimeter and circular shape of the triggering detector additionally diminish overall sensitivity of the polarimeter to the decay asymmetry. Moreover, the track position resolution in Z-direction, which is relevant for the decay asymmetry measurement, in BRAND-0 was poor (cf sec. 5.1.4).

Despite of those discouraging features of the setup, the seek for the electron emission asymmetry in BRAND-0 has been performed and its results will be presented in the following section.

8.1.1 Preliminary search for β-decay asymmetry in the data of BRAND-0

Prior to the calculation of the A parameter a preliminary analysis was conducted. This analysis focused on identifying of any asymmetry in the spacial emission of electrons recorded in the Back scintillator. For the geometry of BRAND-0 the most obvious candidate for such aim is the distributions of slope parameter of electron tracks projected onto XZ-plane. Electron emission asymmetry should be reflected in the difference in shape and/or position of slope parameter distributions obtained for opposite spin orientation of decaying neutron. Their mean values have to be different than zero and displaced in opposite direction. Comparing a slope parameter distributions of the tracks is also the most straightforward method in BRAND-0, since they are obtained directly from reconstruction of Z-component of the track.

The neutron beam's polarization was altered every 16 seconds using the spin flipper. The state of the neutron polarization was recorded for each event and stored together with all other raw data in the corresponding files.

Although the asymmetry for a given electron energy is a simple cosine function of angle (cf. eq. 8.2), it is convoluted with geometrical acceptance and experimentally accepted spectrum of electron velocities. It makes difficult to predict the real asymmetry distribution, which should be seen by this experimental setup. For this reason, the results of Geant4 simulation will be used as an introduction and illustration of the expected effects.

β-emission asymmetry simulated with Geant4

Due to unfavourable detection geometry for β-asymmetry measurement in BRAND-0 a Geant4 simulations have been performed in order to estimate a usability of current apparatus for this aim.

A model containing a full geometry of the decay chamber and Mott polarimeter has been prepared. Neutrons were randomly distributed inside the decay chamber along its longitudinal axis following the real distribution of the beam. (Beam halo is not needed to be implemented in this case). Their maximal polarization has been assumed which directed towards positive or negative direction of Z-axis. Neutrons were let to decay with nominal electron emission asymmetry. A user controlled fraction of uniformly distributed electrons accounting for background has been provided. The shape and magnitude of the magnetic field present in the decay chamber was included in the simulations as well.

The slope of the electron track through the detection system has been measured by means of its momentum orientation. Only the component of momentum lying in the XZ-plane was of interest in this study.

Considering that the presence of windows and foils in the path of electrons can cause deviations from their initial trajectories, the orientation of Z-momentum component of electron has been checked at specific places: at its creation point, after it passed window of decay chamber, after it passed tracker window and after it passed the Mott target.

Distribution of relevant track slope parameter (referred to as "sp_Z") in XZ-plane have been obtained. Example of distributions of track slopes of electrons for both polarization of neutrons are shown in fig. 8.1.

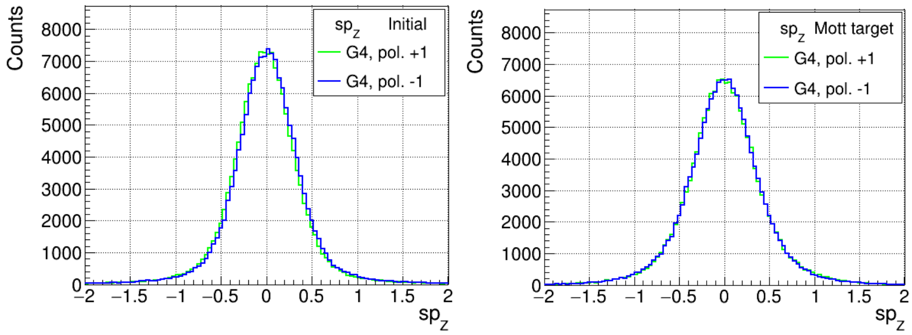

Figure 8.1 Geant4 simulation: distributions of orientation of Z-component of β-electron momentum for positive (green) and negative (blue) direction of neutron polarization. Orientation of momentum is equivalent to the slope parameter (sp_Z) of the trajectory. Left panel: for electrons just after β-decay of neutron; right panel: for electrons just after their passage through the Mott target.

The distributions of Gaussian-like shape have been obtained. As expected, for positive and negative polarization directions the distributions of electron tracks have the same shape but they are a bit displaced.

For each distribution a mean value and standard deviation of mean have been calculated. Results are presented in the comparative plots of fig. 8.2.

Examination of effect of each window/foil on the measured asymmetry has shown evidence that the asymmetry between the two spin states gradually diminishes after passing through each foil (cf. upper row of fig. 8.2). The presence of unpolarized background attenuates the overall effective asymmetry. For 20% admixture of background, as it was estimated in simulations of background level, for the BRAND-0 data, initial asymmetry is smaller and it is washed up faster along the electron trajectories. But even behind tracker entrance the electron emission asymmetry remains sufficient to be detected. Only behind the Mott target, where the probability of scattering is higher, the asymmetry in momentum distributions disappears.

By employing the tracking for simulated data the emission asymmetry can be revealed, as it is presented in lower row of fig. 8.2. Tracking process selects tracks of sufficient hit multiplicities, including layers where the asymmetry was still preserved. This makes the asymmetry distribution visible even after it was fade away by scattering at Mott target.

These results highlight the importance of minimizing the straggling effects in windows, foils, and tracker for preserving and detecting of β-decay asymmetry in the experimental setup. Also the presence of not identified and not suppressed background events have a dampening effect on the asymmetry. The same concerns measurement of all correlation coefficients, since precise event selection and momenta determination are an unavoidable prerequisites for their determination in BRAND measurements.

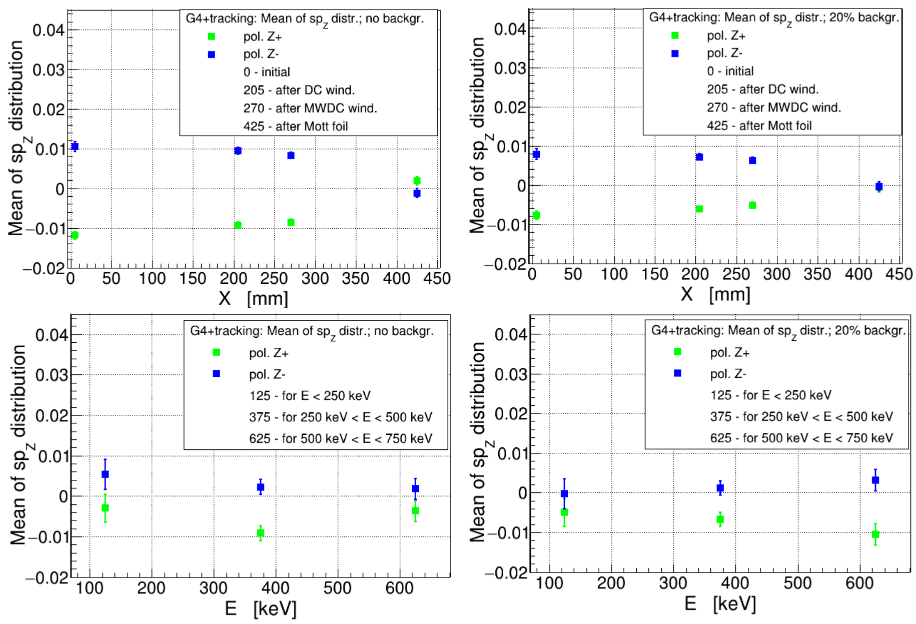

Figure 8.2 Simulated with Geant4 differences in distributions of track slope parameters for electron emitted in β-decay of longitudinally polarized neutrons. Distributions for positive and negative longitudinal polarization directions are compared. Left column: for background free experiment; right column: for 20% admixture of not polarized background; Upper row: shown are mean values of distributions obtained from the momentum vector orientation at decay vertex (0 mm), after electron has passed vacuum window (205 mm), after electron has passed tracker window (270 mm) and after electron has passed Mott target (425 mm). Lower row: mean values of distributions of slope parameter obtained by tracking and with selection of electron energy ranges: 125 - for energy bin of 0-250 keV, 375 - for 250-500 keV and 625 - for 500-750 keV.

8.1.2 Beam data analysis - event selection

For search of the β-emission asymmetry in BRAND-0 the data collected during the most stable and favourite experimental conditions have been used.

Position cuts

For the selection of most reliable events for emission asymmetry search, the two-dimensional position cuts were used. They were applied to select:

- proper track origin from the beam core in Y-direction from -40 mm to + 20 mm (nominal beam size including the shift of beam image);
- trajectory fits into the nominal decay chamber window size by avoiding the influence of its frame;
- trajectory fits into the active window of MWDC, avoiding the tracks, which could origin at the window frame.

Tracking quality

To test if the searched for asymmetry is not affected by the criterion of event quality, the analysis has been performed for two different limits of χ^2 for accepted tracks:

- standard quality - as used throughout of this work ($\chi^2_y < 12$ and $\chi^2_z < 3$), which ensures reliably of the reconstructed events;
- reduced quality - limits on χ^2 value extended as $\chi^2_y < 50$ and $\chi^2_z < 5$.

Influence of Mott target

It is worth to note that, in order to maximize the statistics available for the measurement of N and R correlation coefficients, during the data collection the Mott target was almost always inserted. Its presence inside the MWDC caused large angular straggling and had impact on the track reconstruction. In order to mitigate the influence of the Mott target on the measurement of emission asymmetry, the analysis was repeated with excluding from the tracking procedure the MWDC planes located after the Mott target (layers 7 and 8). Data collected with removed Mott target are also available, however with low statistics. They were analyzed as well by including all layers of MWDC in the tracking.

Influence of electron energy

To control the dependence of electron energy on the emission asymmetry as well as to provide reference of asymmetry value obtained for the background events, the collected energy spectrum of the Back scintillator was divided into following seven bins (given in keV): 0-250, 250-500, 500-750, 750-1000, 1000-1500, 1500-2000, and 2000-3000. In the first three bins predominantly the signal from β-decay of neutron beam is expected while the remaining bins at higher energies correspond to the observed background.

8.1.3 Results

Fig. 8.3 shows the distributions of track slope parameter in XZ-plane. Events of standard track quality of electron of the first energy bin (0 - 250 keV) are taken into account. All layers of MWDC are included into tracking. Distributions are shown for two respective spin states of the neutron beam (left and middle panels). The terms "Flip 0" and "Flip 1" correspond to polarization state of the neutron when the flipper is in passive mode (neutron spin -Z) and when the flipper was active (neutron spin flipped to +Z), respectively.

During the track reconstruction for events collected under the different flipper states, an important observation was made. For the beam data, the count of correctly reconstructed events varies between the two flipper states. For Flip 0 state, the number of normal quality events is always by 9% larger than that for Flip 1 state. When criterion for track reconstruction are relaxed as described above (for reduced quality events) this difference remains but is reduced to 7%. At the same time the neutron detection rate in the neutron monitoring system does not show any significant difference for the different spin states of the flipper. The observed variation is below 0.2% and does not explain the observed statistics difference of tracks reconstructed in MWDC. The possible reasoning behind this effect is studied later in this chapter.

In the rightmost panel of fig. 8.3, both distributions, after statistics normalization are overlapped. In order to compare the shapes of the distributions such normalization was necessary to compensate for the observed difference in the collected statistics. Both distributions are of almost identical shapes. Their mean values differ by 19% with the uncertainty of the mean value of 9%. It means that they differ only by 2 standard deviations, what is not sufficient to conclude about their distinction.

The plots of the mean values of slope parameter distributions for individual aforementioned energy bins are shows in figs. 8.4, 8.5 and 8.6. In left panels of these figures the results for standard quality events are presented whereas in the right panels - for reduced events quality.

Fig. 8.4 contains the result biased by the presence of Mott target, obtained when all layers of MWDC were used for the tracking. Tracking with only first 6 layers of MWDC was implemented for the analysis presented in fig. 8.5. Differently than expected, the results are more scattered and worse than those in fig. 8.4. This can be explained by deterioration

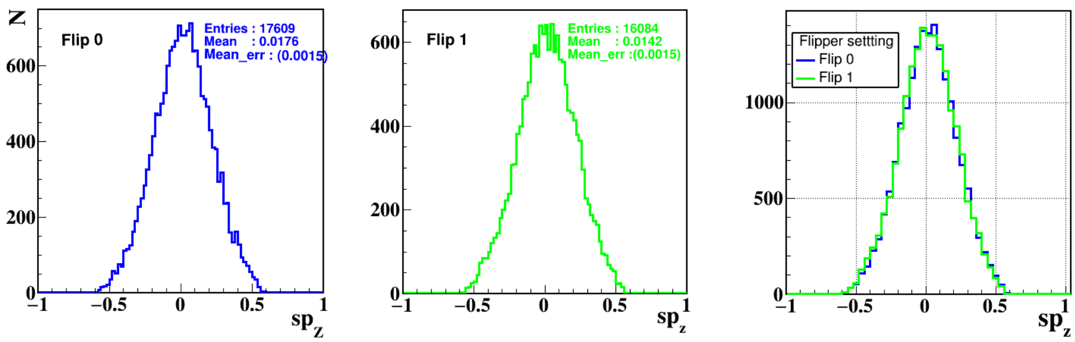

Figure 8.3 Example of distribution of slope parameter of reconstructed track in XZ-plane. They are obtained for electrons of energies lower then 250 keV recorded by Back scintillator. All tracking layers and standard quality of tracking is employed. Left and middle panel: distribution obtained for flipper state 0 and state 1, respectively; right panel: superposition of both distributions after their normalization. The mean values of both distributions differ by 19 ±9 %.

of quality and reliability of tracking when hit multiplicity is decreased. Another factor influencing the fit stability is the shorter base used for the trajectory fitting. . Note, that in "full MWDC" tracking the base is much larger since layers 7^{th} and 8^{th} are separated from the rest of MWDC by additional thickness of the "Mott foil compartment" (5.5 cm). Effect of scattering on Mott target is also not present in plots shown in fig. 8.6, since it was removed form the tracker during this data taking. All layers of MWDC are used for tracking in this case. The error bars shown in plots of figs. 8.4, 8.5 and 8.6 are equal to ±1 standard deviation of mean of sp_Z distributions.

All presented plots show the shift of mean values of the distributions towards positive sides. In an ideal detection geometry, they should be symmetrically displaced from zero to positive values (for neutron spin directed towards -Z) and to negative values (for neutron spin directed toward +Z). In reality, it is observed that, more tracks reconstructed as emitted into forward hemisphere is accepted than those emitted in backward direction. This can be explained by small misalignment of the detection setup. Another reason of this displacement of the distributions can be the presence of non isotropic background. Just for compensation of such - difficult to control - systematic effects, the spin flip method is used to measure the actual asymmetry. It permits to ignore the common displacement of the distributions and conclude only from their relative positions.

Comparing the positions of the distributions for both spin states in fig 8.4, it could be stated that, in general they follow expected trend for β-asymmetry. For standard quality of events, only for electrons of energy in 250-500 keV range, the distinction of distributions of their track slope parameter is of statistical significance. Data selected with larger limit of accepted χ^2, reveal smaller statistical errors, and are smoother. For those data the Flip 0/Flip 1 distributions for two lowest energy bins can be qualified as resolved. All these points are located in the energy range compatible with the β-energy spectrum. For other energy bins, both those of β-energy range and of higher energy the differences between positions of distributions are insignificant.

Inspection of figs. 8.5 and 8.6 indicates that data points there are charged with larger uncertainties what is a result of reduced statistics of examined distributions. The statistically significant distinction of their mean positions for both flipper states in not observed.

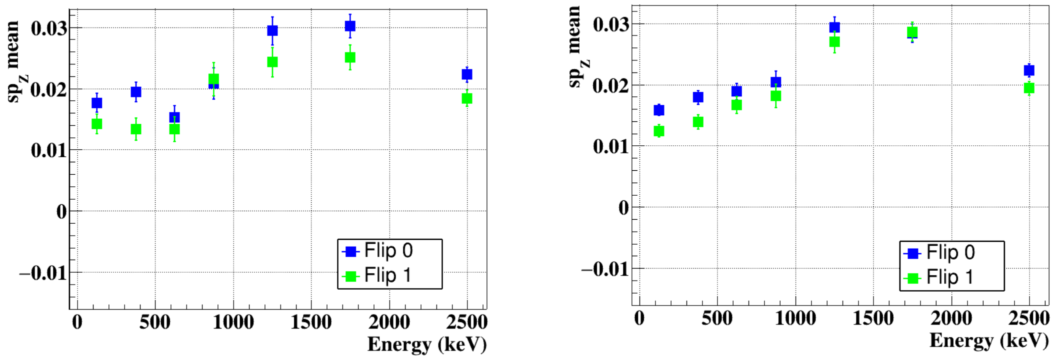

Figure 8.4 Mean track slope parameter in XZ-plane of electron trajectories selected for the determination of β-asymmetry, calculated for the seven defined energy bins. Blue squares: for electrons emitted when neutron spin was oriented towards -Z direction; green squares: for electrons emitted when neutron spin was oriented toward +Z direction. Values for energies lower than 750 keV are for events with dominant contribution of electrons from neutron decay. Values for higher energies exclusively originate from the background events. Left panel: events of standard tracking quality; right panel: for reduced tracking quality. See text for conclusion.

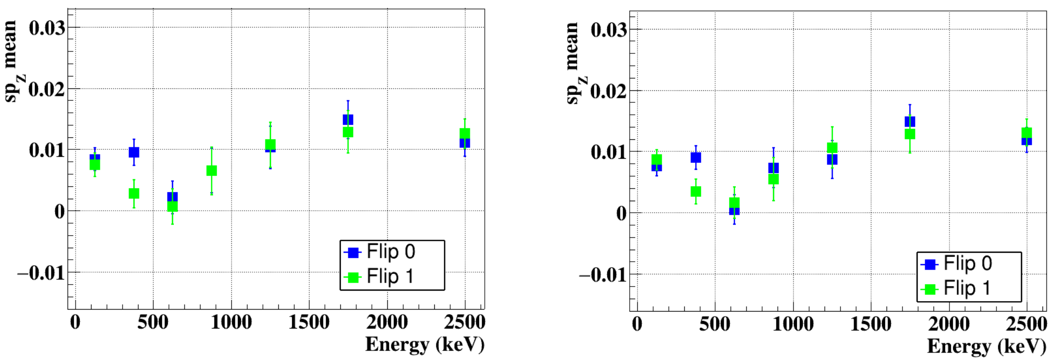

Figure 8.5 The same as in fig. 8.4 but for the case when only layers from 1 to 6 were used for track reconstruction.

8.1.4 Comparison with electrons emitted from ^{207}Bi source

In order to verify the credibility of results of β-asymmetry investigation with beam data, a similar analysis as presented above was performed, but for the electrons emitted from ^{207}Bi radioactive source. The calibration data collected in ILL during the experiment in autumn

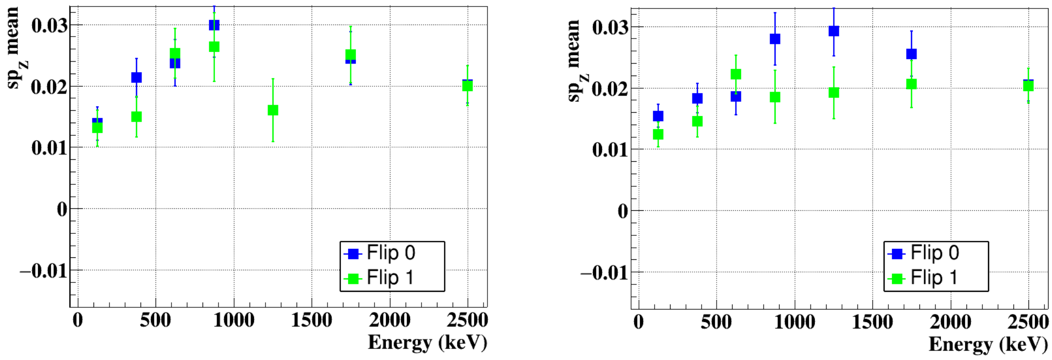

Figure 8.6 The same as in fig. 8.4 but for the data set collected with removed Mott target.

2021 were used. The source was placed close to the tracker window in its central axis. The internal position calibration plate was removed from MWDC. The spin flipper was active and operated the same way and with the same frequency as for the beam operation.

The state of a spin flipper is not expected to have any influence on the spacial distribution of electrons emitted from bismuth source and it has to remain purely isotropic. The results are presented in fig. 8.7. Astonishingly, the asymmetry in the distributions of conversion electron tracks is visible. And this asymmetry is different for flipper in Flip 0 (off) and Flip 1 (on) states. The obtained asymmetry is statistically significant for lowest energy bin (below 300 keV). In this case of mean values of distributions are predominantly negative. It can be caused by opposite misalignment of the source in regard to Mott polarimeter as it was in case of misalignment realized for the beam data (figs. 8.4, 8.5 and 8.6). The dependency of these asymmetries on energy is another astonishing finding. Its origin remains unknown.

Further investigations have been performed. The position of the ^{207}Bi source have been reconstructed separately for both flipper states. The results for Z-direction (charge-division method) are shown in fig. 8.8. In left and right panel the reconstructed distributions of the source position in Z-direction for Flip 0 and Flip 1 state, respectively, are presented. For Flip 1, the reconstructed source distribution is $\sim$50% broader than that for the data taken during passive mode of flipper (Flip 0). When examining the same distribution but for the Y-direction (drift-time measurement), no significant difference is observed.

Presented facts indicate that when flipper is in active mode it affects the quality of the registered data. This explains the observed difference in reconstructed track statistics for two states of flipper discussed earlier in this chapter. The lower numbers of accepted events and larger deterioration of track reconstruction from charge-division method during the Flip 1 state is the result of flipper interference with the detection system.

The spin flipper and the detection system should be electrically decoupled. However, some level of connection between these two systems is not excluded. Operation of flipper can also induce electromagnetic noise which is picked up by the readout electronics. Standard observation of electronic pulses, prior to the experiment, did not signal any such connection. Also proper operation of local electronic systems used for neutron beam polarization

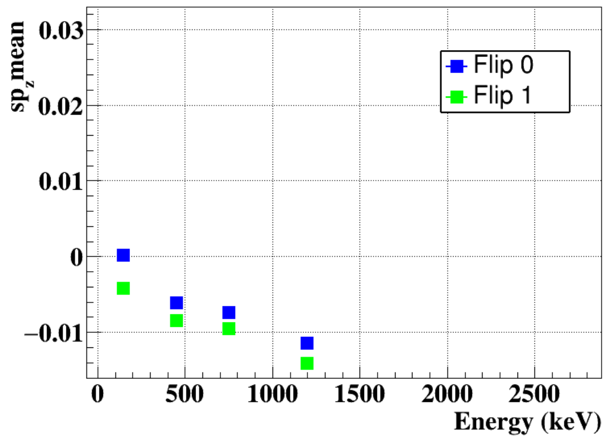

Figure 8.7 Mean values of the distributions of electron track slope parameter. They are calculated for tracks of conversion electrons emitted from ^{207}Bi radioactive source. During this measurement the neutron spin flipper was operated in the same manner as during the measurement with the beam. In this case the energy spectrum is divided into four bins: 0 - 300, 300 - 600, 600 - 900, 900 - 1200 (all in keV). standard quality tracking is applied. Error bars are smaller than the size of markers. Despite that in this case no any asymmetry in the emission distributions is expected, the results indicate the same behaviour as for the beam data. This fact puts in question the ability of the system to detect real value of β-asymmetry.

measurement indicates at a correct functioning of the flipper. Observed during experiment the interference of flipper and BRAND readout confirms the main finding from the post-experiment tests, described in chapter 6. They indicated unusually high sensitivity of the applied custom electronics to the stability of the signal base line, or in other words-to low amplitude noise picked up by this electronics. Further on-site investigations in the experimental place of PF1B are needed to understand the exact origin of the data deterioration by flipper operation and mitigate its impact on the method of amplitude measurement in the BRAND experiment.

As a final conclusion it has to be written that it is very likely that the observed above footmark of asymmetry in electron emission direction for the beam data (cf. fig.8.4) is not due to actual β-emission dependency on the neutron spin orientation but rather a systematic effect related to the flipper operation, which affects the registration and reconstruction of electron tracks.

Based on the simulations described at the beginning of this section, it becomes evident that the presence of various foils along the path of electrons and the inclusion of background events significantly diminish the actual asymmetry of β-decay. It makes it difficult to be detected in BRAND-0 setup, which was not optimized for this measurement. Nevertheless, implementation of tracking, should select some fraction of those events, where emission asymmetry is still preserved.

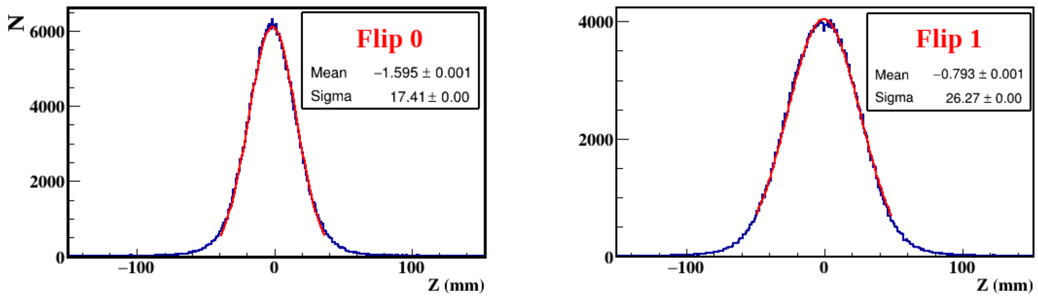

Figure 8.8 Reconstructed Z-position of ^{207}Bi source using the the charge-division method. Data were collected during operation of neutron spin flipper. Left and right panels present the source position reconstructed solely during flipper state 0 (OFF) and flipper state 1 (ON), respectively. Significant broadening of distribution for active state of flipper is realized. This influence of flipper on the track reconstruction by means of charge-division method, has not been observed in the separate readout electronics used for the study of neutron beam polarization. It is a clear indication of large sensitivity of custom front-end electronics used in BRAND-0 experiment.

In reality, the tracking procedure used for experimental data analysis is much more complex and challenging compared to the simplified tracking used for simulated data. The systematic effects observed, especially in the charge-division method, are intricate and difficult to be incorporated into the simulations. Obviously, the disturbing influence of spin flipper on the detection system could not be accounted in the simulations.

Despite of promising results of simulations, all recognized during data analysis unfavorable effects effectively hindered the extraction of any discernible β-emission asymmetry within the BRAND-0 setup. Considering all the aforementioned effects, the attempt to extract the value of asymmetry parameter A was not pursued.

8.2 Coefficients N and R

Coefficients N and R can be derived from observables related only to the emitted β-particle - its energy, momentum and spin. They are very important for detailed studies of weak interactions since they are sensitive for transverse component of electron spin. Their values, when different than expected in SM, would indicate the presence of scalar and tensor components of weak interaction. This fact would confirm existing of phenomena not foreseen in SM.

The first attempt to measure N and R coefficients in neutron decay was undertaken in nTRV experiment [83–85]. This experiment provided first experimental limits for of the N and R values. Their quantities within the uncertainty limits were consistent with the values expected in SM.

8.2.1 Feasibility of N and R determination in BRAND-0

The analysis of N and R coefficients is based on the event-by-event reconstruction of momenta and transverse polarization of those electrons emitted in neutron decay, which underwent a Mott scattering at the Mott target and were registered in one of the Mott detectors. Mott scattering process is sensitive to the spin orientation of the impinging electron. It is attributed to the influence of the spin-orbit term in the interaction potential.

In comparison to estimation of asymmetry coefficient A described above and based on analysis of single track events triggered by the Back Scintillator, for N and R coefficients the analysis of double track events triggered by Mott scintillators is needed. The methods of selection of those events were presented in sec. 5.3.3.

For the description of the kinematics relevant to the measurement of N and R correlation coefficients, additional vectors and angles have to be introduced [84]. They are presented in fig. 8.9.

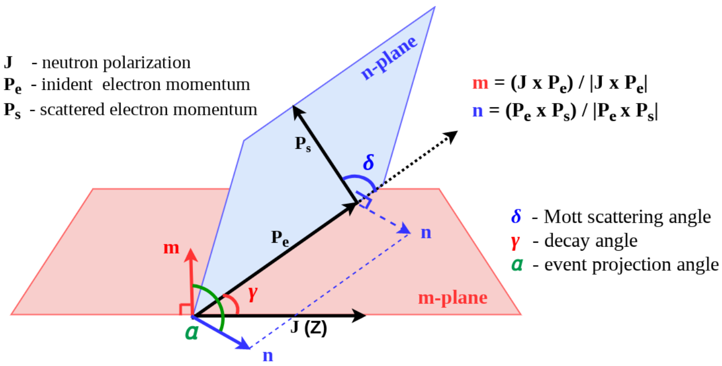

Figure 8.9 The reference frame for analysis of the transverse electron polarization by means of Mott scattering. m-plane, also known as the decay plane, is spanned by vectors **J** and $\mathbf{P}_e$. n-plane referred to as the scattering plane, is defined by the vectors $\mathbf{P}_e$ and $\mathbf{P}_s$. δ is the scattering angle between the incident and scattered track measured in the scattering plane. γ is the angle between the neutron polarization vector **J** and $\mathbf{P}_e$ in the decay plane. α is the angle between unit vectors **m** and **n** and is called event projection angle.

A unit vector $\hat{\mathbf{m}}$, perpendicular to the decay plane (m-plane) is defined as:

$$\hat{\mathbf{m}} \equiv \frac{\hat{\mathbf{J}} \times \hat{\mathbf{p_e}}}{|\hat{\mathbf{J}} \times \hat{\mathbf{p_e}}|} \tag{8.3}$$

whereas the unit vector perpendicular to the scattering plane (n-plane), is given as:

$$\hat{\mathbf{n}} \equiv \frac{\hat{\mathbf{p_e}} \times \hat{\mathbf{p_s}}}{|\hat{\mathbf{p_e}} \times \hat{\mathbf{p_s}}|} \tag{8.4}$$

The latter one is related to the transverse component of the spin vector of emitted electron by:

$$\sigma_\perp \propto S(E_e, \delta)\hat{\mathbf{n}} \tag{8.5}$$

Sherman function $S(E_e, \delta)$ describes the analyzing power of nuclei applied in Mott target. For calculation of its actual value the material and thickness of the scattering layer has to be taken into account. Due to multiple and plural scattering of electrons in the Mott target the analytical form of this function needs to be replaced by distributions obtained in simulations, depending on the target thickness, scattering angle and elemental composition of the target. It usually is referred to as effective analyzing power.

It is convenient to introduce angle α, which relates the mutual orientation of the planes explained above. Value of α can be derived from following relations:

$$\cos\alpha \equiv \hat{\mathbf{m}} \cdot \hat{\mathbf{n}}, \quad \sin\alpha \equiv \hat{\mathbf{m}} \times \hat{\mathbf{n}} \tag{8.6}$$

The geometrical form-factors relevant to individual correlation coefficient can be expressed as:

$$\mathcal{F}(\alpha) \equiv \hat{\mathbf{J}} \cdot \hat{\mathbf{p_e}}, \quad \mathcal{G}(\alpha) \equiv \hat{\mathbf{n}} \cdot \hat{\mathbf{J}}, \quad \mathcal{H}(\alpha) \equiv \hat{\mathbf{n}} \cdot (\hat{\mathbf{J}} \times \hat{\mathbf{p_e}}) \tag{8.7}$$

Substituting the above defined quantities in eq. 8.1 obtained is the decay rate for Mott scattered electrons as a function of α:

$$W(\alpha) \propto 1 + P\beta(\alpha)\{A\mathcal{F}(\alpha) + S(\alpha)[N\mathcal{G}(\alpha) + R\mathcal{H}(\alpha)]\} \tag{8.8}$$

from which the experimental number of counts for the different states of flipper can be derived as:

$$\mathrm{N}^{\pm} = \mathrm{N}_0\, \epsilon_{\mathrm{v}}^{\pm} \left\{ 1 + \eta^{\pm} P \left[A\overline{\beta\mathcal{F}(\alpha)} + N\overline{S(\alpha)\mathcal{G}(\alpha)} + R\overline{\beta S(\alpha)\mathcal{H}(\alpha)} \right] \right\} \tag{8.9}$$

Experimental conditions are characterized by quantities specific for positive and negative direction of beam polarization.

- accepted as true event number, N_0;
- accepted as true and efficiency corrected event numbers, $\mathrm{N}^{\pm}$;
- efficiency of spin flipper, $\eta^{\pm}$;
- disturbing factor caused by data deterioration due to flipper operation, $\epsilon^{\pm}$.

Quantities $\overline{\mathcal{F}(\alpha)}$, $\overline{\mathcal{G}(\alpha)}$, and $\overline{\mathcal{H}(\alpha)}$ denote the average values of relevant geometrical form-factors as a functions of α. In order to extract N and R coefficients, the asymmetry $\mathcal{A}(\alpha)$, build from the accumulated counts $\mathrm{N}^{\pm}$ is used. It allows for efficient reduction of systematic uncertainty:

$$\mathcal{A}(\alpha) = \frac{\mathrm{N}^{+}(\alpha) - \mathrm{N}^{-}(\alpha)}{\mathrm{N}^{+}(\alpha) + \mathrm{N}^{-}(\alpha)} \tag{8.10}$$

Using eq. (8.9) in (8.10) and applying Taylor explanation [48] asymmetry can be written as:

$$\mathcal{A}(\alpha) = P(1-\eta/2)\left[A\overline{\beta\mathcal{F}(\alpha)} + N\overline{S(\alpha)\mathcal{G}(\alpha)} + R\overline{\beta S(\alpha)\mathcal{H}(\alpha)}\right] - \epsilon_{\rm v}/2 \quad (8.11)$$

Assuming the first term in the square brackets of eq. 8.11 is known, the two-parameter fit of asymmetry to the distribution of event projection angle α permits to extract coefficients N and R [48].

The extracted distribution of α for the selected V-track events is presented in fig. 8.10. The shape of this distribution is defined by the relative orientation of neutron polarization and the geometrical acceptance of the tracker and Mott detectors.

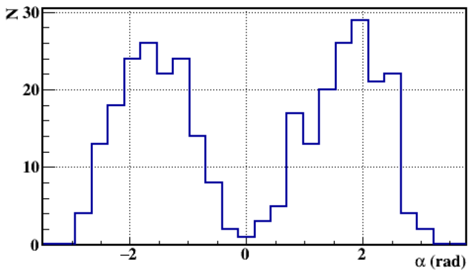

Figure 8.10 Distribution of the event projection angle α for the identified Mott scattered events.

Fig. 8.11 presents the raw energy distributions for relevant events, recorded separately for each Mott detectors. These distributions seem to be more enhanced at the lower energies than those observed for direct electrons from beam (cf. fig. 5.73). The possible enhancement of low energies can be explained by increase of the Mott scattering cross section when electron energy decreases [48]. But the low event statistics of these spectra prevent from making any strict conclusions.

Presented energy spectra, unfortunately can not be calibrated in energy units (cf. sec. 5.4.2).

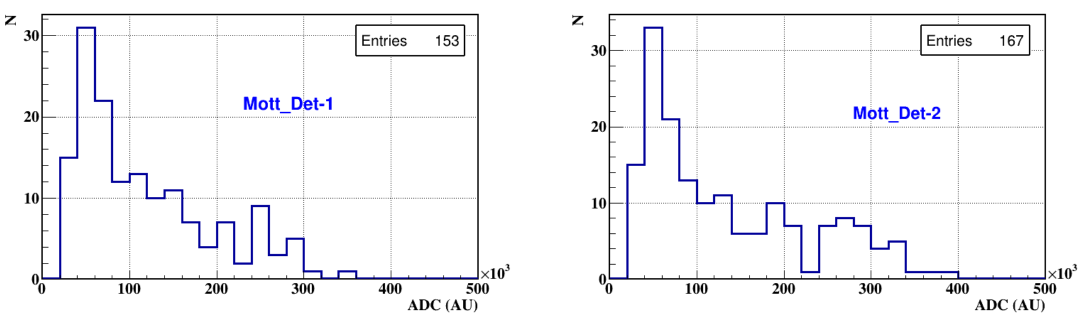

Figure 8.11 Raw energy distribution of the identified Mott scattered electrons, recorded in Mott_det1 (left panel) and in Mott_det2 (right panel).

The summary distribution of the scattering angles δ for available events is shown in fig. 8.12. The shape of the distribution is the result of current configuration of the Mott polarimeter.

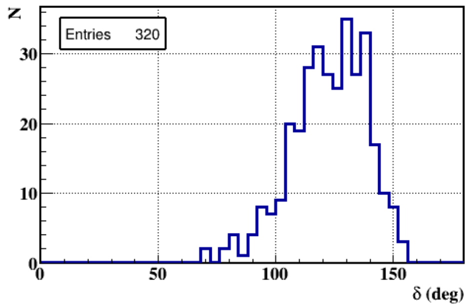

Figure 8.12 Sum of distribution of scattering angles δ for selected V-tracks recorded in both Mott detectors.

Successful attempt to extract the correlation coefficients N and R according to the formula 8.11 demands very stringent requirements for the experiment. Except precisely known neutron polarization and large statistic of well identified events $N^{\pm}$, the good energy and angle measurements have to be performed. From these observable, in BRAND-0 experiment, only polarization was known with sufficient precision. The geometry of experimental setup should also ensure high sensitivity to the measured observable. The present setup can be characterized by the minimal sensitivity to A and R correlations. However, the N correlation in principle could be measured. The main obstacles which preclude its successful measurement in BRAND-0 are: very low statistics, deterioration of reconstruction of emission angle due to influence of flipper and lack of energy calibration. All these facts together prevent the estimation of correlation coefficients A, N and R in the current work.

Chapter 9

Summary

A small-scale prototype apparatus for precise physics experiment BRAND has been constructed and tested. The BRAND experiment is an ambitious scientific project aiming at search of BSM physics by examination of a structure of the weak interaction. It will be done by means of simultaneous measurement of 11 correlations coefficients of weak interaction in β-decay of free neutron. Among them seven coefficients are sensitive for transverse component of spin of emitted electron. Their values may indicate an non-zero contribution of exotic - scalar and tenor components of weak interaction. The BRAND experiment is scheduled for many years of realization, with continuous extension of experimental apparatus, increase of measurement precision and accumulation of event statistics.

A prototype experimental setup presented in this work called BRAND-0 was devoted for initial tests and verification of general idea and some specific experimental methods planned to be implemented in the BRAND experiment. It was constructed and tested during two experimental runs conducted at PF1B cold neutron beam in ILL Grenoble, France. The first experiment performed in December 2020 was very short (3 days). The second one (September/October '21) lasted 4 weeks and was used for tests of apparatus and, to some extent, also for collection of data.

Presented thesis concerns the description of construction and performance of the part of BRAND-0 setup, which was planned for measurement of four momenta and spin orientation of electrons emitted from decaying cold neutrons of the beam. For performance studies have been utilized both the data collected in laboratory tests as well as those collected in ILL.

Also the experimental environment at ILL together with beam quality assessment and studies of possible sources of experimental background were extensively described.

Both promising features as well as deficiencies of the current setup have been realized. Confirmed was the feasibility of electron track determination with the use of drift-time measurement in hexagonal cells of MWDC filled with helium-based gas mixture. Performed test proved long lasting working stability of such detector when helium gas is admixed with 3% of isobutane and trace amount of ethanol vapours. In such configuration the detection efficiency of the tracker is close to 100%. Applied method of signal readout is suitable for attaining the demanded position resolution. Small tuning of front-end circuitry is advisable.

Realized the most significant drawback of the current BRAND-0 setup consists in over-sensitivity of the custom amplitude-to-time converter of the front-end electronics to the fluctuation of signal baseline. Even tiny displacement of baseline level of 1 mV results in 10% alternation of measured signal amplitude. This adverse effect significantly influences the quality of quantities derived from measurement of signal amplitudes. This concerns the tracking resolution along the anode wire length, where charge-division method is employed. Also the energy resolution of scintillating detectors of BRAND-0 is strongly affected. At this stage of setup verification it is impossible to judge if the correction of malfunctioning circuitry responsible for amplitude-to-time conversion would be sufficient to obtain reasonable Z-position and electron energy resolution of Back- and Mott scintillators.

Elimination of observed deterioration of drift-time spectra by operation of SiPM in vicinity of tracker cells needs a longer studies preceded with careful tuning of Mott detector readout system.

The on-site investigation in ILL of, most likely electromagnetic, coupling of neutron spin flipper to the readout and DAQ of BRAND are desired as well.

The importance of a highly effective method of registration of slow protons from neutron decay have been noticed. Their identification, precise measurement of their energy and reconstruction of their creation point are needed not only for kinematic reconstruction of events, but are also indispensable for suppression of severe multi-component experimental background.

The first version of BRAND-0 model was created and implemented into Geant4 framework. Performed simulations permitted the identification of mechanisms and reactions responsible for creation of dominant components of experimental background observed during first runs of BRAND experiment.

A feasibility of determination of an β-asymmetry parameter A as well as the correlation coefficients N and R, which are related to the electron spin orientation has been checked. In all cases it turned out that the quality of experimental data collected in BRAND-0 experiment in autumn '21 is still not sufficient for such aims.

Appendix A

Simulations of BRAND-0 setup with Geant4 framework

In the contemporary experimental nuclear physics, and especially in the so called precision physics, where the tiny effects hidden under the "bulk" processes are searched for, a support of Mote Carlo (MC) simulation is indispensable.

The Monte Carlo simulations of the well established physics permits to disentangle the components of "known" from "unknown" and obtain the more clear picture of examined processes.

Another important aim of MC simulations is to obtain the "response function" of the experimental apparatus to the processes acting during research. In view of the complexity of contemporary experimental setups, their large volume, variety of the detection and readout systems, the mapping of both the global as well the local acceptances or efficiencies of the detector setup is possible only with the simulations tools.

Nowadays the most advanced and universal toll for MC simulations in physics, chemistry, biology, medicine, engineering is the Geant4 toolkit [86–88] provided by Geant4 Collaboration and supported by CERN. It allows the simulations of processes acting during the particles passage through the matter. Geant4 contains the broad library of variety of experimentally verified physics processes.

The Monte Carlo simulation in this work were performed with the Geant4 and are oriented for:

- identification of the origin and distributions of experimental background;
- verification of energy spectra of Scintillating detectors;
- identification and compensation the unknown features of the readout and DAQ system;
- support in position calibration of MWDC;
- determination of detection acceptances;
- estimation of expected magnitude of β-emission asymmetry;

In the following the detection geometry implemented to the MC simulations, the selected physics range and the verification of the results of Geant4 simulations will be outlined.

A.1 Physics

For the purposes of this thesis, various kinds of processes had to be simulated. Implementing all of them at once and simulating with the full geometry of the setup would cause the large CPU time needed for creation of sufficient statistics of events. This would be time consuming, inconvenient, and is in fact not needed. Simulation of various classes of processes, like neutron decay, neutron transportation, electron transportation, electromagnetic processes of γs, scintillation, background origin and its propagation, can be to some extent decoupled and simulated only with the use of appropriate part of detection setup and relevant range of implemented physics.

Standard packages of G4RadioactiveDecayPhysics and G4OpticalPhysics were utilized. For processes involving electron transportation and interaction the G4EmPenelopePhysics model was used. It has advantage for low energy electromagnetic processes over the standard electromagnetic physics models of Geant4. It assures low energy cut of 50 eV for e^-, e^+ and γs.

Available in Geant4 the so called high precision neutron physics models are in fact developed for higher energy range than demanded for cold neutron beams. They are tuned predominantly with the use of data obtained for thermal neutrons. Thus, it has to be remembered that precision of simulations obtained for interaction of cold neutrons is limited.

A.2 Geometry

A.2.1 General model of BRAND-0

In fig. A.1 the most general model of BRAND-0 implemented into Geant4 simulations is shown. The model comprises:

- decay chamber filled with air at pressure of 5E-4 mbar. Inside the chamber the structure of HV cage is located. Chamber is equipped with 3 ports for proton detectors and one port for installation electron transmission vacuum window. Proton detectors are not included. Longitudinal magnetic field along Z-axis of the magnitude and shape similar as this measured during BRAND-0 experiment is implemented;
- Mott polarimeter composed of MWDC (filled with He + CO2 mixture at atmospheric pressure), two rectangular scintillators working as Mott detectors, Mott target, Back scintillator together with light guide and four photomultipliers (only their entrance windows) attached with silicon grease.
- beam dump;

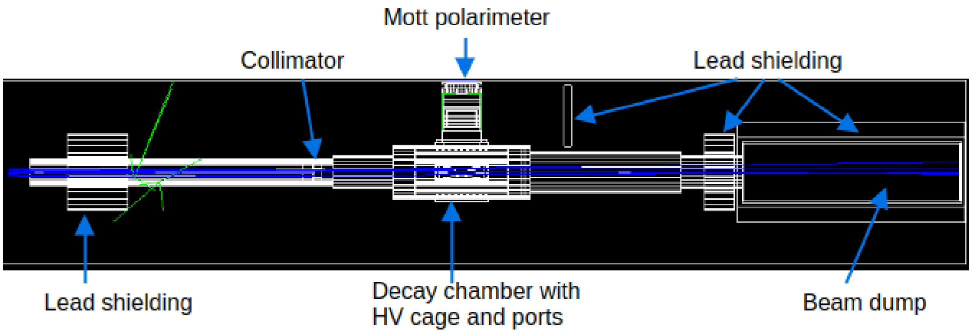

Figure A.1 The general view of the prototype BRAND-0 setup implemented into Geant4 simulations. Visible are: decay chamber with ports for proton detectors and electron transmission window; HV cage inside the decay chamber; Mott polarimeter (MWDC + Backs scintillator, Mott detectors, Mott target); one collimator, beam dump, lead shieldings, vacuum pipes. A few neutron tracks are shown as well (blue lines).

- one beam collimator closest to the decay chamber;
- shielding walls and layers of lead;
- vacuum tubes for beam transportation.

All dimension and mutual positions of components are exact as in real setup or very similar to them. It is also the case for construction materials used in the model.

This general model of BRAND-0 was used for simulation of beam profiles and beam halo as well as for simulations of experimental background. Neutrons simulating the beam or the γ particles propagating along neutron transportation system were generated upstream of decay chamber at distance about 3 m from its center. Processes acting in the neutron polarizer are not included to current model.

A.2.2 Small model of BRAND-0

For simulations of neutron beam decay the model restricted only to decay chamber and Mott polarimeter was sufficient. It is presented in fig. A.2.

This model was used to simulate the energy spectra of Back scintillator and Mott scintillators as well as for studies of β-asymmetry coefficient A. Propagation of decay products different than electron and γ particles was suppressed. Particles resulting from interaction of electrons with the setup components were tracked.

Examples of simulated initial spectra of electrons and protons from β-decay of neutron beam are shown in fig. A.3

A.2.3 Simulated spectra of radioactive source

For simulations of reference energy spectrum of ^{207}Bi and for aims of position calibration in Z-direction it was sufficient to use a model with Mott polarimeter only supplemented with

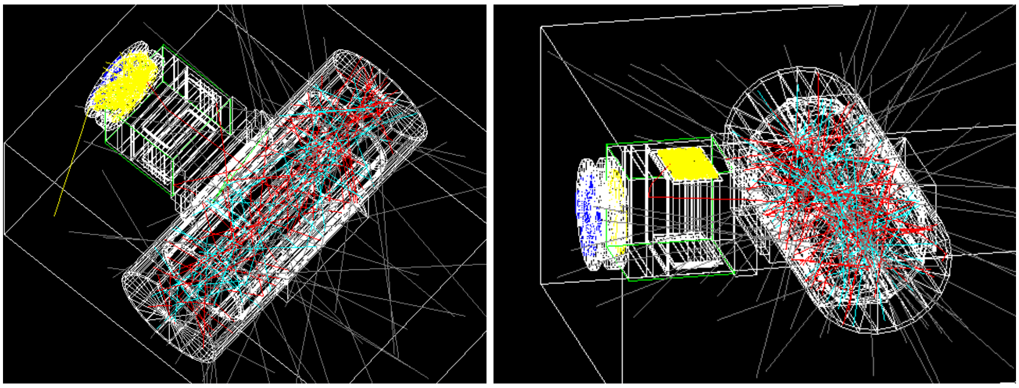

Figure A.2 Version of Geant4 model of BRAND-0 setup restricted only to decay chamber and Mott polarimeter. Such setup is sufficient to simulate decay of neutron beam and propagation of produced particles. Particle tracks: electrons, proton, antinutrino,optical photon, gamma. Left panel: example of event with electron recorded in Back scintillator; right panel: example of event where electron is scattered on Mott target and recorded in one of Mott detectors. In real simulations tracks of protons and antineutrinos are suppressed.

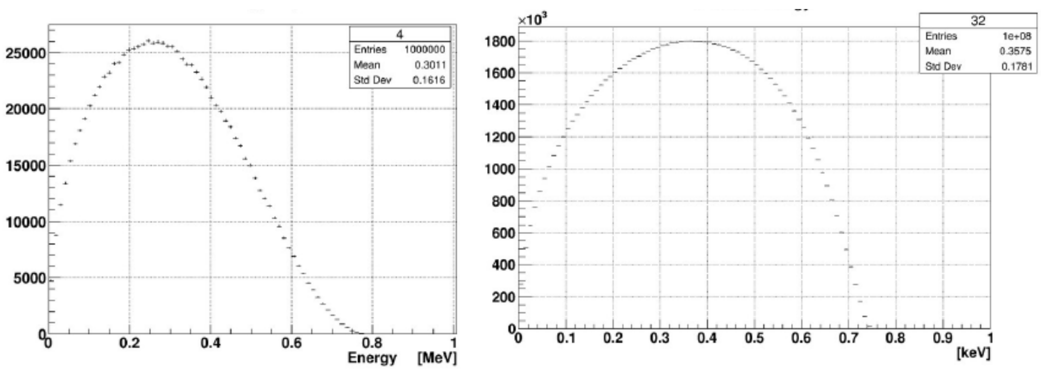

Figure A.3 Example of simulated initial energy spectra for β-particles (left panel) and protons (right panel) from neutron decay. Note different energy units in both plots.

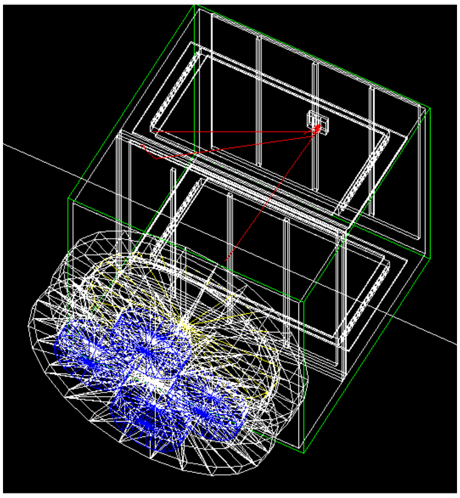

Figure A.4 Geant4 model of Mott polarimeter extended with radioactive source of ^{207}Bi and two aluminium plates. Each plate has three vertical slits of 4 mm width. One plate was installed at front of entrance window of MWDC and second one has been positioned inside MWDC, close to Mott foil. In experiment these diaphragms were used for position calibration of tracker in Z-direction. A few electron track are shown as well. γ tracks from ^{207}Bi are suppressed.

the radioactive source and two aluminium plates - one installed at front of the tracker and second, internal one - inside, close to Mott target. Each aluminium plate has 3 vertical slits of 4 mm width. They allowed to perform measurements demanded for position calibration in Z-direction. Such arrangement is shown in fig. A.4.

Fig. A.5 presents the image of the slits of internal calibration plate at the Back scintillator. It is a result of simulations with the use of ^{207}Bi source positioned at front of tracker entrance window.

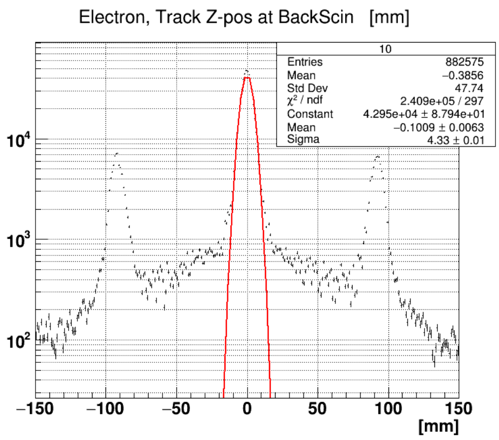

Figure A.5 Geant4 simulation: image of calibration slits of internal aluminium plate at surface of Back scintillator. Detectors were illuminated by ^{207}Bi radioactive source positioned at front of tracker entrance window.

Simulated spectrum of conversion electrons emitted from ^{207}Bi is presented in fig. A.6. In left panel of this figure the numbers of optical photons created in Back scintillator are shown. Only the hits in central part of Back scintillator - the square of 2 cm x 2 cm, are taken into account in order to avoid the position dependence in light collection. In this way a raw emission spectrum is obtained where four most intense energy lines of electron conversion spectrum are well resolved. The labels near by the individual peaks inform about energies of electrons (in keV) and percentage of their relative emission intensities. (For calculations of intensity also the γs emitted from ^{207}Bi are included). During light transportation and light collection in photomultipliers this spectrum is deteriorated and suppressed. In effect, in simulated spectrum of PMTs signals, only two component of the electron spectrum remains resolved: $\sim$500 keV and $\sim$1000 keV. This spectrum is presented in right panel of fig. A.6.

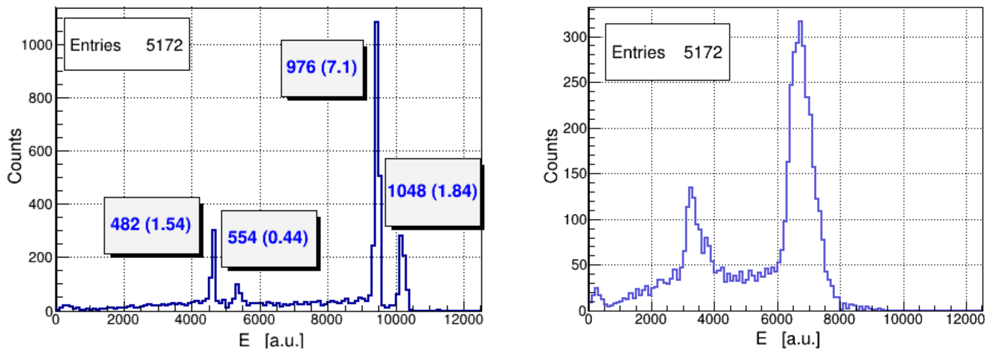

Figure A.6 Geant4 simulations. Left panel: ^{207}Bi conversion electron spectrum registered in central place of Back scintillator (in arbitrary units equal to number of created optical photons). Four resolved energy lines are visible. Labels close to respective peaks inform about energy of the electrons in keV. Values in parenthesis are the relative intensities of electron energy lines given in %. Right panel: the same spectrum but derived from sum of signals generated in photomultipliers of Back scintillator. Only two group of electron lines remain resolved. Due to losses in collection of optical photons the spectrum is shifted towards lower values. Here no gain in PMTs and no any energy smearing is introduced yet. Note the difference in vertical scales of both plots.

In order to reproduce the experimental spectra of ^{207}Bi the proper gains of PMTs and smearing of energy spectra needed to be introduced. It was done with the use of random generator with assumption of normal distribution of broadening factors. The variation of efficiencies of individual photocathodes of PMTs were assumed to be of 10%. The same value of broadening was assumed for gain stability of PMTs. Finally, those factor occurred to be not important since deterioration of energy spectra in BRAND-0 is predominated by response function of readout electronics. The best reproduction of experimental spectrum of ^{207}Bi was achieved for Gaussian distributions of simulated numbers of optical photons in individual PMTs ($NopPM_i$) when their standard deviation σ_i were expressed as:

$$\sigma_i = \sigma_0 \cdot \frac{C}{NopPM_i} \tag{A.1}$$

with $\sigma_0 = 0.022$ and $C = 360$;

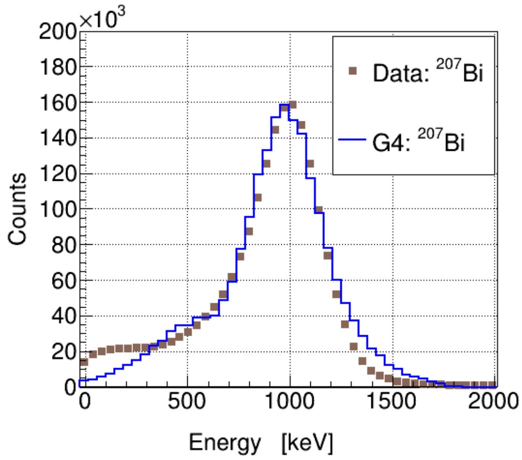

Figure A.7 Experimental spectrum of conversion electrons emitted from ^{207}Bi radioactive source and registered in Back scintillator of BRAND-0. Only component of ~1 MeV energy is visible. Component of energy ~500 keV got diffused and suppressed due to poor resolution of signal processing electronics. Simulated by Geant4 spectrum where response function of electronics was introduced is superimposed. Good agreement of data and simulations has been achieved.

With response function of electronics approximated with above mentioned width of normal distribution, the experimental spectrum of electrons emitted from ^{207}Bi have been well reproduced as it is shown in fig. A.7. Presented spectrum is obtained for whole area of Back scintillator, where position dependence of light collection was compensated with the procedure described in sec. 5.4.1. Simulated data were a subject of the similar analysis procedure as experimental data.

Parameters of the response functions of PMTs and electronics, tuned and fixed for ^{207}Bi spectrum, were used for simulations of experimental β and background spectra obtained with neutron beam.

Data obtained in the simulations were used for simplified tracking of electron trajectories. It was oriented both for selection of relevant events needed for comparison with experimental results as well as for investigation of peculiarities realized in tracking with charge-division method (systematic enhancement of slopes of reconstructed tracks). Simplifications in the model consisted in approximation of position resolution of individual layers of the tracker as an average resolution measured experimentally for all cells of a given layer.

Presented results of initial simulations confirmed the correctness of detection geometry and materials implemented into Geant4 model of BRAND-0 and the relevance of selected physics processes. Other results of Geant4 simulation of BRAND-0 are presented together with the results of data analysis in chaprers 7 and 8.

LIST OF ABBREVIATIONS

ADC Analog to Digital Converter

AU Arbitrary Units

Back_scint Back scintillator

BSM Beyond Standard Model

CERN Conseil Européen pour la Recherche Nucléaire

HV High Voltage

IFJ PAN The Institute of Nuclear Physics, Polish Academy of Sciences, Karków

ILL Institut Laue-Langevin, Grenoble

MC Monte Carlo (simulation method)

Mott_dets Mott detectors

Mott_det1 Mott detector 1

Mott_det2 Mott detector 2

MWDC Multi Wire Drift Chamber

ODR Orthogonal Distance Regression

PCB Printed Circuit Board

PF1B Polarised cold neutron beam facility at ILL

PMT Photo-Multiplier Tube

SiPM Silicon PhotoMultiplier

SM Standard Model

TDC Time to Digital Converter

TTFA Topological Track-Finding Algorithm

JU Jagiellonian University, Kraków

Acknowledgements

I would like to take this opportunity to express my appreciation to the individuals and institutions that have supported me throughout my PhD studies.

First and foremost, I am deeply grateful to my supervisor, Prof. Krzysztof Pysz. His mentorship, guidance, and encouragement have been crusial throughout my PhD journey.

I'm truly thankful to Prof. Adam Kozela for his valuable feedbacks, discussions, and helpful critiques.

I would like to express my sincere gratitude to Prof. Kazimierz Bodek, the head of the BRAND collaboration, for his insightful discussions and expertise. I extend my acknowledgment to every member of the BRAND collaboration, with special thanks to the colleagues in Krakow: Prof. J. Zejma, Dr. D. Rozpędzik, Mr. K. Łojek, and Ghanshyam Gupta and with whom I interacted during the experiment at the Institut Laue-Langevin (ILL): Dr. D. Ries, Martin Engler, and Noah Yazdandoost for their technical support and collaboration. Special recognition goes to Dr. T. Soldner for his valuable discussions and support throughout the experiment.

The facilities provided by the Institute of Nuclear Physics, Polish Academy of Sciences (IFJ PAN), have been crucial for my research. I'm grateful for the opportunities this institution has given me. I'd also like to acknowledge the National Science Center, Poland, for financing the project (Grant No. UMO-2018/29/B/ST2/02505), and the Polish National Agency for Academic Exchange (NAWA) for the student exchange grant that supported my scientific visit to ILL, France.

I would like to take this opportunity to offer my special thanks to Prof. Pysz and Prof. Kozela for proofreading and providing invaluable input in shaping this manuscript.

I extend gratitude to my friends in Krakow for the enjoyable weekend dinners and shared laughter that brought balance to this journey. Special thanks to Arpan Das, Arvind Khuntia, Sneha, Rajeev, and Bartek – you made Kraków feel like home. Also, heartfelt gratitude to my friends in India for their unwavering encouragement.

To my dear Parents and Family, your encouragement, patience, and love which have been my driving force during tough times.

Lastly, I want to express my deepest gratitude to Himan, who has become my family away from home. Your presence has been a guiding light through the challenges, and your support has made this journey more manageable. Thank you for being there when I needed it and for reminding me to take breaks and cherish moments of respite.

In conclusion, I'm thankful for the combined effort and support that led to completing this thesis. My heartfelt gratitude goes to those mentioned earlier and to others who may not be named here but have made meaningful contributions.

Bibliography

[1] P. Langacker. *The Standard Model and Beyond*. CRC Press, 2016. DOI: https://doi.org/10.1201/b22175.

[2] J. Barranco. "Some Standard model problems and possible solutions". In: *Journal of Physics: Conference Series* 761.1 (Oct. 2016), p. 012007. DOI: 10.1088/1742-6596/761/1/012007. URL: https://dx.doi.org/10.1088/1742-6596/761/1/012007.

[3] J Iliopoulos. "Standard Model and Prospects". In: *Journal of Physics: Conference Series* 2502.1 (May 2023), p. 012001. DOI: 10.1088/1742-6596/2502/1/012001. URL: https://dx.doi.org/10.1088/1742-6596/2502/1/012001.

[4] David d'Enterria et al. "Opportunities for new physics searches with heavy ions at colliders". In: *JOURNAL OF PHYSICS G-NUCLEAR AND PARTICLE PHYSICS* 50.5 (May 2023). ISSN: 0954-3899. DOI: 10.1088/1361-6471/acc197.

[5] V. V. Shalaev, S. V. Shmatov, and CMS collaboration. "Physics of the Standard Model in the CMS Experiment at the LHC". In: *PHYSICS OF PARTICLES AND NUCLEI* 54.3 (June 2023), pp. 425–428. ISSN: 1063-7796. DOI: 10.1134/S1063779623030334.

[6] N. Severijns. "Weak interaction studies by precision experiments in nuclear beta decay". In: *Lecture Notes in Physics* 651 (2004), pp. 339–381. URL: https://api.semanticscholar.org/CorpusID:62812891.

[7] Nathal Severijns, Marcus Beck, and Oscar Naviliat-Cuncic. "Tests of the standard electroweak model in nuclear beta decay". In: *Rev. Mod. Phys.* 78 (3 Sept. 2006), pp. 991–1040. DOI: 10.1103/RevModPhys.78.991. URL: https://link.aps.org/doi/10.1103/RevModPhys.78.991.

[8] Hartmut Abele. "The neutron. Its properties and basic interactions". In: *Progress in Particle and Nuclear Physics* 60.1 (2008), pp. 1–81. ISSN: 0146-6410. DOI: https://doi.org/10.1016/j.ppnp.2007.05.002. URL: https://www.sciencedirect.com/science/article/pii/S0146641007000622.

[9] Hartmut Abele. "Neutron beta-decay and the standard model". In: *Nuclear Physics A* 721 (2003), pp. C182–C189. ISSN: 0375-9474. DOI: https://doi.org/10.1016/S0375-9474(03)01031-5. URL: https://www.sciencedirect.com/science/article/pii/S0375947403010315.

[10] T. D. Lee and C. N. Yang. "Question of Parity Conservation in Weak Interactions". In: *Phys. Rev.* 104 (1 Oct. 1956), pp. 254–258. DOI: 10.1103/PhysRev.104.254. URL: https://link.aps.org/doi/10.1103/PhysRev.104.254.

[11] T. D. Lee and C. N. Yang. "Question of Parity Conservation in Weak Interactions". In: *Phys. Rev.* 106 (6 June 1957), pp. 1371–1371. DOI: 10.1103/PhysRev.106.1371. URL: https://link.aps.org/doi/10.1103/PhysRev.106.1371.

[12] T. D. Lee and C. N. Yang. "Parity Nonconservation and a Two-Component Theory of the Neutrino". In: *Phys. Rev.* 105 (5 Mar. 1957), pp. 1671–1675. DOI: 10.1103/PhysRev.105.1671. URL: https://link.aps.org/doi/10.1103/PhysRev.105.1671.

[13] Fred L. Wilson. "Fermi's Theory of Beta Decay". In: *Am. J. Phys.* 36.12 (1968), pp. 1150–1160. DOI: 10.1119/1.1974382.

[14] G. Gamow and E. Teller. "Selection Rules for the β-Disintegration". In: *Phys. Rev.* 49 (12 June 1936), pp. 895–899. DOI: 10.1103/PhysRev.49.895. URL: https://link.aps.org/doi/10.1103/PhysRev.49.895.

[15] Chien-Shiung Wu. "The discovery of the parity violation in weak interactions and its recent developments". In: *Lect. Notes Phys.* 746 (2008), pp. 43–70. DOI: 10.1007/978-4-431-77056-5_4.

[16] R. P. Feynman and M. Gell-Mann. "Theory of the Fermi Interaction". In: *Phys. Rev.* 109 (1 Jan. 1958), pp. 193–198. DOI: 10.1103/PhysRev.109.193. URL: https://link.aps.org/doi/10.1103/PhysRev.109.193.

[17] E. C. G. Sudarshan and R. E. Marshak. "Chirality Invariance and the Universal Fermi Interaction". In: *Phys. Rev.* 109 (5 Mar. 1958), pp. 1860–1862. DOI: 10.1103/PhysRev.109.1860.2. URL: https://link.aps.org/doi/10.1103/PhysRev.109.1860.2.

[18] J. D. Jackson, S. B. Treiman, and H. W. Wyld. "Possible Tests of Time Reversal Invariance in Beta Decay". In: *Phys. Rev.* 106 (3 May 1957), pp. 517–521. DOI: 10.1103/PhysRev.106.517. URL: https://link.aps.org/doi/10.1103/PhysRev.106.517.

[19] J.D. Jackson, S.B. Treiman, and H.W. Wyld. "Coulomb corrections in allowed beta transitions". In: *Nuclear Physics* 4 (1957), pp. 206–212. ISSN: 0029-5582. DOI: https://doi.org/10.1016/0029-5582(87)90019-8. URL: https://www.sciencedirect.com/science/article/pii/0029558287900198.

[20] M.E. Ebel and G. Feldman. "Further remarks on Coulomb corrections in allowed beta transitions". In: *Nuclear Physics* 4 (1957), pp. 213–214. ISSN: 0029-5582. DOI: https://doi.org/10.1016/0029-5582(87)90020-4. URL: https://www.sciencedirect.com/science/article/pii/0029558287900204.

[21] J. Sromicki. "T Violation in the weak scalar and tensor interaction: neutron and nuclei". In: *Nuclear Instruments and Methods in Physics Research Section A: Accelerators, Spectrometers, Detectors and Associated Equipment* 440.3 (2000), pp. 609–617. ISSN: 0168-9002. DOI: https://doi.org/10.1016/S0168-9002(99)01050-5. URL: https://www.sciencedirect.com/science/article/pii/S0168900299010505.

[22] A. D. Sakharov. "Violation of CP Invariance, C asymmetry, and baryon asymmetry of the universe". In: *Pisma Zh. Eksp. Teor. Fiz.* 5 (1967), pp. 32–35. DOI: 10.1070/PU1991v034n05ABEH002497.

[23] Jeffrey S. Nico and W. Michael Snow. "FUNDAMENTAL NEUTRON PHYSICS". In: *Annual Review of Nuclear and Particle Science* 55.1 (2005), pp. 27–69. DOI: 10.1146/annurev.nucl.55.090704.151611. URL: https://doi.org/10.1146/annurev.nucl.55.090704.151611.

[24] Dirk Dubbers and Bastian Märkisch. "Precise Measurements of the Decay of Free Neutrons". In: *Annual Review of Nuclear and Particle Science* 71.1 (2021), pp. 139–163. DOI: 10.1146/annurev-nucl-102419-043156. URL: https://doi.org/10.1146/annurev-nucl-102419-043156.

[25] Bodek, K. et al. "BRAND - Search for BSM physics at TeV scale by exploring transverse polarization of electrons emitted in neutron decay". In: *EPJ Web Conf.* 219 (2019), p. 04001. DOI: 10.1051/epjconf/201921904001. URL: https://doi.org/10.1051/epjconf/201921904001.

[26] Bodek, K. et al. "BRAND - exploring transverse polarization of electrons emitted in neutron decay - Feasibility demonstration experiment". In: *EPJ Web Conf.* 262 (2022), p. 01014. DOI: 10.1051/epjconf/202226201014. URL: https://doi.org/10.1051/epjconf/202226201014.

[27] A. Kozela et al. "Measurement of the Transverse Polarization of Electrons Emitted in Free-Neutron Decay". In: *Phys. Rev. Lett.* 102 (17 May 2009), p. 172301. DOI: 10.1103/PhysRevLett.102.172301. URL: https://link.aps.org/doi/10.1103/PhysRevLett.102.172301.

[28] G. Ban et al. "A Mott polarimeter for the search of time reversal violation in the decay of free neutrons". In: *Nuclear Instruments and Methods in Physics Research Section A: Accelerators, Spectrometers, Detectors and Associated Equipment* 565 (2006), pp. 711–724. DOI: 10.1016/j.nima.2006.05.166. URL: https://hal.in2p3.fr/in2p3-00096160.

[29] D. Rozpędzik et al. "Search for BSM physics with neutron beta decay in the BRAND experiment". In: *Pos PANIC2021* 432 (2022).

[30] M. Kolodziej. "Masters thesis". In: *Jageillonian University, Krakow* (2020).

[31] Nevill Francis Mott. "The Scattering of Fast Electrons by Atomic Nuclei". In: *Proceedings of The Royal Society A: Mathematical, Physical and Engineering Sciences* 124 (1929), pp. 425–442. URL: https://api.semanticscholar.org/CorpusID:122655299.

[32] Nevill Francis Mott. "The polarisation of electrons by double scattering". In: *Proceedings of the Royal Society of London. Series A, Containing Papers of a Mathematical and Physical Character* 135.827 (1932), pp. 429–458.

[33] Noah Sherman. "Coulomb Scattering of Relativistic Electrons by Point Nuclei". In: *Phys. Rev.* 103 (6 Sept. 1956), pp. 1601–1607. DOI: 10.1103/PhysRev.103.1601. URL: https://link.aps.org/doi/10.1103/PhysRev.103.1601.

[34] Noah Sherman and Donald F. Nelson. "Determination of Electron Polarization by Means of Mott Scattering". In: *Phys. Rev.* 114 (6 June 1959), pp. 1541–1542. DOI: 10.1103/PhysRev.114.1541. URL: https://link.aps.org/doi/10.1103/PhysRev.114.1541.

[35] M. Drągowski et al. "Monte Carlo study of the effective Sherman function for electron polarimetry". In: *Nuclear Instruments and Methods in Physics Research Section B: Beam Interactions with Materials and Atoms* 389-390 (2016), pp. 48–55. ISSN: 0168-583X. DOI: https://doi.org/10.1016/j.nimb.2016.11.018. URL: https://www.sciencedirect.com/science/article/pii/S0168583X16304888.

[36] M. Drągowski et al. "Polarized electron Mott scattering model for the Geant4 Monte Carlo toolkit". In: *Nuclear Instruments and Methods in Physics Research Section B: Beam Interactions with Materials and Atoms* 488 (2021), pp. 37–42. ISSN: 0168-583X. DOI: https://doi.org/10.1016/j.nimb.2020.12.008. URL: https://www.sciencedirect.com/science/article/pii/S0168583X20305103.

[37] Kuzniak Marcin. "Analysis of experimental uncertainties in the R-correlation measurement in the decay of free neutrons". MA thesis. Kraków: Jagiellonian University.

[38] G. Gupta et al. "BRAND-Low energy proton detector". In: *Proceedings of the DAE Symp. on Nucl. Phys* (2022).

[39] K. Dhanmeher et al. "Mott polarimeter for electrons from neutron decay in BRAND experiment". In: *POS Proceedings of Science* 380 (2022).

[40] https://www.ill.eu/.

[41] H. Abele et al. "Characterization of a ballistic supermirror neutron guide". In: (2005). arXiv:nucl-ex/0510072.

[42] A.K. Petukhov et al. "A concept of advanced broad-band solid-state supermirror polarizers for cold neutrons". In: *Nuclear Instruments and Methods in Physics Research Section A: Accelerators, Spectrometers, Detectors and Associated Equipment* 838 (2016), pp. 33–38. ISSN: 0168-9002. DOI: https://doi.org/10.1016/j.nima.2016.09.023. URL: https://www.sciencedirect.com/science/article/pii/S0168900216309469.

[43] A.N. Bazhenov et al. “An adiabatic resonance spin-flipper for thermal and cold neutrons”. In: *Nuclear Instruments and Methods in Physics Research Section A: Accelerators, Spectrometers, Detectors and Associated Equipment* 332.3 (1993), pp. 534–536. ISSN: 0168-9002. DOI: https://doi.org/10.1016/0168-9002(93)90311-5. URL: https://www.sciencedirect.com/science/article/pii/0168900293903115.

[44] Constantine C Spyrakos. *Finite Element Modeling*. West Virginia Univ. Press Morgantown, WV, USA, 1994.

[45] F.B. Dunning T.J. Gay. “Mott electron polarimetry”. In: *Rev. Sci. Instrum.* (1992), pp. 1635–1651. DOI: 10.1063/1.1384229.

[46] Maciej Perkowski. “Precision measurements of the electron energy distribution in nuclear beta decays”. PhD thesis. Kraków: Jagiellonian University.

[47] M. Perkowski et al. In: *Acta Phys. Pol.* 49 (2018), p. 261.

[48] A. Kozela. “Search for Time-Reversal Violating Effects in Free Neutron Decay”. In: (2011). Habilitation thesis.

[49] S. A. Hoedl et al. “An electron transparent proton detector for neutron decay studies”. In: *Journal of App. Phys.* 99 (2006), p. 084904.

[50] https://daq-plone.triumf.ca/HR/VME/CAEN/V1190_REV13.pdf.

[51] D. R. Nygren. *Converting vice to virtue: can time-walk be used as a measure of deposited charge in silicon detectors?* Intern LBL Note. 1991.

[52] I. Kipnis et al. “A time-over-threshold machine: the readout integrated circuit for the BABAR Silicon Vertex Tracker”. In: *IEEE Trans. Nucl. Sci.* 44 (1997), p. 289.

[53] Daniel R. McAlister. *Gamma Ray Attenuation Properties of Common Shielding Materials*. PG Research Foundation, Inc. 1955 University Lane Lisle, IL 60532, USA. Revision 6.1, 2018. URL: https://www.eichrom.com/wp-content/uploads/2018/02/Gamma-Ray-Attenuation-White-Paper-by-D-M-rev-6-1-002.pdf.

[54] *Neutron scattering lengths and cross sections*. National Institute of Standards and Technology (NIST). https://www.ncnr.nist.gov/resources/n-lengths/elements/li.html.

[55] H. Abele et al. “Characterization of a ballistic supermirror neutron guide”. In: *Nuclear Instruments and Methods in Physics Research Section A: Accelerators, Spectrometers, Detectors and Associated Equipment* 562.1 (2006), pp. 407–417. ISSN: 0168-9002. DOI: https://doi.org/10.1016/j.nima.2006.03.020. URL: https://www.sciencedirect.com/science/article/pii/S0168900206005328.

[56] T. Soldner, Private comunication.

[57] A. Sharma and F. Sauli. “Low mass gas mixtures for drift chambers operation”. In: *Nuclear Instruments and Methods in Physics Research Section A: Accelerators, Spectrometers, Detectors and Associated Equipment* 350.3 (1994), pp. 470–477. ISSN: 0168-9002. DOI: https://doi.org/10.1016/0168-9002(94)91246-7. URL: https://www.sciencedirect.com/science/article/pii/0168900294912467.

[58] https://www.heraeus.com/en/hep/products$_hep/clevios/clevios_prod/clevios_1.html$.

[59] Georges Charpak and F. Sauli. “Multiwire proportional chambers and drift chambers”. In: *Nucl. Instrum. Meth.* 162 (1979), pp. 405–428. DOI: 10.1016/0029-554X(79)90726-2.

[60] Luigi Rolandi Walter Blum and Werner Riegler. *Particle detection with drift chambers. Particle Acceleration and Detection.* 2008.

[61] Ix-B García Ferreira, J García Herrera, and L Villaseñor. “The Drift Chambers Handbook, introductory laboratory course”. In: *Journal of Physics: Conference Series* 18.1 (Jan. 2005), p. 346. DOI: 10.1088/1742-6596/18/1/010. URL: https://dx.doi.org/10.1088/1742-6596/18/1/010.

[62] R. L. Workman et al. “Review of Particle Physics”. In: *PTEP* 2022 (2022), p. 083C01. DOI: 10.1093/ptep/ptac097.

[63] http://mathworld.wolfram.com/LeastSquaresFittingPerpendicularOffsets..

[64] F. James. “Function Minimization and Error Analysis, Reference Manual”. In: *CERN Program Library Long Writeup D506* (1994). URL: http://cdssls.cern.ch/record/2296388/files/minuit.pdf.

[65] M. Bellomo et al. “The barrel-inner-large tracking chambers for the ATLAS muon spectrometer: Ready for installation”. In: *Nuclear Instruments and Methods in Physics Research Section A: Accelerators, Spectrometers, Detectors and Associated Equipment* 573.3 (2007), pp. 340–360. ISSN: 0168-9002. DOI: https://doi.org/10.1016/j.nima.2006.12.044. URL: https://www.sciencedirect.com/science/article/pii/S0168900206024715.

[66] A. Breskin et al. “Further results on the operation of high-accuracy drift chambers”. In: *Nuclear Instruments and Methods* 119 (1974), pp. 9–28. ISSN: 0029-554X. DOI: https://doi.org/10.1016/0029-554X(74)90728-9. URL: https://www.sciencedirect.com/science/article/pii/0029554X74907289.

[67] https://root.cern.ch/doc/master/classTSpline.html.

[68] https://root.cern.ch/doc/master/classTGraphSmooth.html.

[69] https://root.cern.ch/doc/master/classTGraphSmooth.h.

[70] https://pdg.lbl.gov/2022/reviews/rpp2022-rev-passage-particles-matter.pdf.

[71] https://www-user.rhrk.uni-kl.de/~apelster/Vorlesungen/WS2021/v11.pdf.

[72] Jiangshan Lan et al. “A Generalized Model for Light Transport in Scintillators”. In: (Oct. 2017). arXiv: 1710.11291 `[physics.ins-det]`.

[73] A. K. Petoukhov et al. “Realization of an advanced super-mirror solid-state neutron polarizer for the instrument PF1B at the Institut Laue–Langevin”. In: *Review of Scientific Instruments* 94.2 (2023), p. 023304. DOI: 10.1063/5.0123419. eprint: https://doi.org/10.1063/5.0123419. URL: https://doi.org/10.1063/5.0123419.

[74] Database. *Thermal Neutron Capture gamma's*. https://www.nndc.bnl.gov/capgam/. URL: https://www.nndc.bnl.gov/capgam/.

[75] M A Ali et al. “Properties of the 158Gd compound state gamma-decay cascades”. In: *Journal of Physics G: Nuclear and Particle Physics* 20.12 (Dec. 1994), p. 1943. DOI: 10.1088/0954-3899/20/12/010. URL: https://dx.doi.org/10.1088/0954-3899/20/12/010.

[76] Rene Brun and Fons Rademakers. “ROOT — An object oriented data analysis framework”. In: *Nuclear Instruments and Methods in Physics Research Section A: Accelerators, Spectrometers, Detectors and Associated Equipment* 389.1 (1997). New Computing Techniques in Physics Research V, pp. 81–86. ISSN: 0168-9002. DOI: https://doi.org/10.1016/S0168-9002(97)00048-X. URL: https://www.sciencedirect.com/science/article/pii/S016890029700048X.

[77] C. S. Wu et al. “Experimental Test of Parity Conservation in Beta Decay”. In: *Phys. Rev.* 105 (4 Feb. 1957), pp. 1413–1415. DOI: 10.1103/PhysRev.105.1413. URL: https://link.aps.org/doi/10.1103/PhysRev.105.1413.

[78] B. Erozolimsky et al. “Corrigendum: Corrected value of the beta-emission asymmetry in the decay of polarized neutrons measured in 1990”. In: (1997). [Erratum: Phys.Lett.B 412, 240–241 (1997)]. DOI: 10.1016/S0370-2693(97)01004-6.

[79] P. Liaud et al. “The measurement of the beta asymmetry in the decay of polarized neutrons”. In: *Nucl. Phys. A* 612 (1997), pp. 53–81. DOI: 10.1016/S0375-9474(96)00325-9.

[80] D. Mund et al. "Determination of the Weak Axial Vector Coupling $\lambda{=}g_A/g_V$ from a Measurement of the β-Asymmetry Parameter A in Neutron Beta Decay". In: *Phys. Rev. Lett.* 110 (17 Apr. 2013), p. 172502. DOI: 10.1103/PhysRevLett.110.172502. URL: https://link.aps.org/doi/10.1103/PhysRevLett.110.172502.

[81] M. P. Mendenhall et al. "Precision measurement of the neutron β-decay asymmetry". In: *Phys. Rev. C* 87 (3 Mar. 2013), p. 032501. DOI: 10.1103/PhysRevC.87.032501. URL: https://link.aps.org/doi/10.1103/PhysRevC.87.032501.

[82] M. A.-P. Brown et al. "New result for the neutron β-asymmetry parameter A_0 from UCNA". In: *Phys. Rev. C* 97 (3 Mar. 2018), p. 035505. DOI: 10.1103/PhysRevC.97.035505. URL: https://link.aps.org/doi/10.1103/PhysRevC.97.035505.

[83] A. Kozela et al. "Measurement of the Transverse Polarization of Electrons Emitted in Free-Neutron Decay". In: *Phys. Rev. Lett.* 102 (17 May 2009), p. 172301. DOI: 10.1103/PhysRevLett.102.172301. URL: https://link.aps.org/doi/10.1103/PhysRevLett.102.172301.

[84] G. Ban et al. "A Mott polarimeter for the search of time reversal violation in the decay of free neutrons". In: *Nuclear Instruments and Methods in Physics Research Section A: Accelerators, Spectrometers, Detectors and Associated Equipment* 565.2 (2006), pp. 711–724. ISSN: 0168-9002. DOI: https://doi.org/10.1016/j.nima.2006.05.166. URL: https://www.sciencedirect.com/science/article/pii/S0168900206009090.

[85] K. Bodek and A. Kozela. "Measurement of the transverse polarization of electrons emitted in neutron decay – nTRV experiment". In: *SciPost Physics Proceedings* (2021). URL: https://api.semanticscholar.org/CorpusID:235358614.

[86] J. Allison et al. "Recent developments in Geant4". In: *Nuclear Instruments and Methods in Physics Research Section A: Accelerators, Spectrometers, Detectors and Associated Equipment* 835 (2016), pp. 186–225. ISSN: 0168-9002. DOI: https://doi.org/10.1016/j.nima.2016.06.125. URL: https://www.sciencedirect.com/science/article/pii/S0168900216306957.

[87] J. Allison et al. "Geant4 developments and applications". In: *IEEE Transactions on Nuclear Science* 53.1 (2006), pp. 270–278. DOI: 10.1109/TNS.2006.869826.

[88] S. Agostinelli et al. "Geant4—a simulation toolkit". In: *Nuclear Instruments and Methods in Physics Research Section A: Accelerators, Spectrometers, Detectors and Associated Equipment* 506.3 (2003), pp. 250–303. ISSN: 0168-9002. DOI: https://doi.org/10.1016/S0168-9002(03)01368-8. URL: https://www.sciencedirect.com/science/article/pii/S0168900203013688.